(NASA-TM-81790) WIND-TUNNEL INVESTIGATION OF LONGITUDINAL AND LATERAL-DIRECTIONAL STABILITY AND CONTROL CHARACTERISTICS OF A 0.237-SCALE MODEL OF A REMOTELY PILOTED RESEARCH VEHICLE WITH A THICK. (NASA) 218 p G3/08

N83-11142

Unclas
32178

NASA Technical Memorandum 81790

Wind-Tunnel Investigation of Longitudinal and Lateral-Directional Stability and Control Characteristics of a 0.237-Scale Model of a Remotely Piloted Research Vehicle With a Thick, High-Aspect-Ratio Supercritical Wing (U)

Thomas A. Byrdsong and Cuyler W. Brooks, Jr.
Langley Research Center
Hampton, Virginia

National Aeronautics
and Space Administration

**Scientific and Technical
Information Office**

1980

(U) SUMMARY (U)

(U) An experimental investigation has been conducted in the Langley 8-Foot Transonic Pressure Tunnel of a 0.237-scale force model of a remotely piloted research vehicle. The model was equipped with a thick, high-aspect-ratio supercritical wing and employed elevons for pitch and roll control. The purpose of the investigation was to provide experimental data for a prediction of the static stability and control characteristics of the research vehicle. In addition, the purpose was to provide an estimate of vehicle flight characteristics for a computer simulation program used in the planning and execution of specific flight-research mission. The wind-tunnel test conditions were for a Reynolds number of 16.5×10^6 per meter at Mach numbers from 0.30 to 0.92. The model test variables were as follows: symmetric and asymmetric elevon deflection angles from -9° to 6°; rudder deflection angles from -9° to 0°; sideslip angles from 0° to 6°; and angles of attack from -4° to 18°. Three model configurations that differed only with the addition of two ventral pod designs were investigated.

(U) At some test conditions the model exhibited longitudinal instability characterized by a "pitch-up" behavior. An adequate margin of the stability was determined for a cruise condition. The pitch-control effectiveness was shown to be sufficient to trim the model at all Mach numbers tested. The model also had positive roll-control effectiveness, positive yaw-control effectiveness, positive effective dihedral, and directional stability.

(U) INTRODUCTION (U)

(U) The Drones for Aerodynamic and Structural Testing (DAST) project (ref. 1) is a NASA flight program which uses a modified Firebee II target drone vehicle as a test-bed aircraft for testing aeroelastic research wings (ARW). In the integrated design of the second wing (ARW-2), the structural integrity of the wing depends on the successful operation of several active control systems. The ARW-2 design includes active controls for maneuver load alleviation, gust load alleviation, relaxed static stability, and flutter suppression.

(U) This vehicle will be flight tested with simultaneous operation of all active control systems. The successful conduct of this flight-test program depends to some degree on prior prediction of the performance, flightworthiness, and stability and control characteristics of the research vehicle. Wind-tunnel investigations are used to predict these characteristics. In addition, the wind-tunnel data are used to provide an estimate of vehicle flight characteristics for a computer simulation program. The simulation program is used in the planning and execution of specific flight-research missions and as an aid in the prediction of structural loadings at critical points in the flight envelope.

(U) Results, with limited analysis, of wind-tunnel measurements of the total aerodynamic forces and moments for a 0.237-scale model of the Firebee II aircraft (ref. 2) equipped with a thick, high-aspect-ratio supercritical wing (fig. 1) are documented in this paper. Three configurations of the wind-tunnel model were tested. Each configuration differed only by the absence or addition of one of two ventral pods that were designed to house instrumentation and ballast weights for the flight-test vehicle. The wind-tunnel tests were conducted in the Langley 8-Foot Transonic Pressure Tunnel at Mach numbers from 0.30 to 0.92, angles of attack from approximately -4° to 18°, angles of sideslip from approximately 0° to 6°, and a Reynolds number of approximately 16.5×10^6 per meter.

(U) SYMBOLS (U)

(U) The results presented herein are referred to the stability-axis system for the longitudinal aerodynamic characteristics and to the body-axis system for the lateral-directional aerodynamic characteristics (ref. 3). Force and moment data have been reduced to conventional coefficient form based on the geometry of the reference wing planform (i.e., the planform generated by extending the straight leading and trailing edges of the outboard sections of the wing to the fuselage centerline). Moments are referenced to the quarter-chord point of the mean geometric chord of the reference wing panel (model station 1.06, fig. 2). All dimensional values are given in SI units; however, measurements and calculations were made in U.S. Customary Units.

b wing span

c streamwise local chord of wing (includes trailing-edge extension)

$\bar{c}$ wing mean geometric chord

$\bar{c}_t$ elevon mean geometric chord

C_D drag coefficient (corrected for fuselage base pressure), $\frac{\text{Drag}}{qS}$

C_{D_α} slope of drag curve, per deg

$C_{D_{\delta_e}}$ elevon effectiveness in drag parameter, $\frac{\partial C_D}{\partial \delta_e}$, per deg

C_L lift coefficient, $\frac{\text{Lift}}{qS}$

$C_{L,0}$ lift coefficient at zero angle of attack

C_{L_α} lift-curve slope, per deg

$C_{L_{\delta_e}}$ elevon effectiveness in lift parameter, $\frac{\partial C_L}{\partial \delta_e}$, per deg

C_l rolling-moment coefficient, $\frac{\text{Rolling moment}}{qSb}$

C_{l_β} effective dihedral parameter, $\frac{\Delta C_l}{\Delta \beta}$, per deg

$C_{l_{\delta_a}}$ asymmetric elevon effectiveness parameter, $\frac{\partial C_l}{\partial \delta_a}$, per deg

$C_{l_{\delta_r}}$ effect of rudder deflection on rolling-moment coefficient, $\frac{\partial C_l}{\partial \delta_r}$, per deg

C_m pitching-moment coefficient, $\frac{\text{Pitching moment}}{qS\bar{c}}$

$C_{m,0}$ pitching-moment coefficient at zero lift

C_{m_α} slope of pitching-moment coefficient against angle-of-attack curve, per deg $\left(C_{m_\alpha} < 0 \text{ indicates stability}\right)$

$C_{m_{\delta_e}}$ elevon effectiveness in pitch parameter, $\frac{\partial C_m}{\partial \delta_e}$, per deg

C_n yawing-moment coefficient, $\frac{\text{Yawing moment}}{qSb}$

C_{n_β} directional-stability parameter, $\frac{\Delta C_n}{\Delta \beta}$, per deg $\left(C_{n_\beta} > 0 \text{ indicates stability}\right)$

$C_{n_{\delta_a}}$ effect of asymmetric elevon deflection on yawing-moment coefficient, $\frac{\partial C_n}{\partial \delta_a}$, per deg

$C_{n_{\delta_r}}$ rudder-effectiveness parameter, $\frac{\partial C_n}{\partial \delta_r}$, per deg

C_Y side-force coefficient, $\frac{\text{Side force}}{qS}$

C_{Y_β} side-force parameter, $\frac{\Delta C_Y}{\Delta \beta}$, per deg

$C_{Y_{\delta_a}}$ effect of asymmetric elev. deflection on side-force coefficient, $\frac{\partial C_Y}{\partial \delta_a}$, per deg

$C_{Y_{\delta_r}}$ effect of rudder deflection on side-force coefficient, $\frac{\partial C_Y}{\partial \delta_r}$, per deg

M free-stream Mach number

$M\left(\frac{L}{D}\right)$ aerodynamic range parameter, product of M and $\left(\frac{C_L}{C_D}\right)$

M_{DD} Mach number at which $\frac{\partial C_D}{\partial M} = 0.10$ (drag divergence)

q free-stream dynamic pressure

R radius

S planform area of basic wing panels (including fuselage intercept)

t local wing section thickness

x streamwise distance measured from leading edge of wing, positive toward wing trailing edge

y spanwise distance measured normal to model plane of symmetry, zero at fuselage centerline

z vertical distance measured normal to x, positive upward

α angle of attack, deg

$\alpha_{0,L}$ zero-lift angle of attack, deg

β angle of sideslip, deg

δ_a effective asymmetric elevon deflection angle (positive, right wing down), $\frac{\delta_{HL} - \delta_{HR}}{2}$, deg

δ_e symmetric elevon deflection angle (positive trailing edge down), deg

δ_{e_α} symmetric pitch-control index, $\frac{C_{m_\alpha}}{C_{m_{\delta_e}}}$

δ_{HL} left elevon deflection angle (positive trailing edge down), deg

δ_{HR} right elevon deflection angle (positive trailing edge down), deg

δ_r rudder deflection angle (positive trailing edge left), deg

δ_{r_β} rudder-control index, $-\frac{C_{n_\beta}}{C_{n_{\delta_r}}}$

ε angle of twist of local airfoil section (angle between the wing reference plane and a line through the leading edge and a point midway between the upper and lower surfaces at the airfoil maximum thickness), deg

Abbreviations:

M.S. model station, m

W.L. water line, m

Subscript:

max maximum value

(U) APPARATUS AND PROCEDURE (U)

(U) MODEL DESCRIPTION (U)

(U) The wind-tunnel investigation was conducted using a 0.237-scale model of the test-bed aircraft, a modified Firebee II target drone (ref. 2), equipped with a thick, high-aspect-ratio supercritical wing. The general arrangement of the basic wind-tunnel model (configuration A) is shown in figure 1 and the model planform with selected geometric data is shown in figure 2.

(U) The supercritical wing was constructed of stainless steel and mounted in a high-wing position. The wing reference plane had an incidence angle of 0°

with respect to the fuselage centerline. The wing had approximately 4.4° of twist (washout) in the unloaded condition. The spanwise twist distribution and the maximum thickness-to-chord ratio for the wing are shown in figures 3 and 4, respectively. The reference wing (excluding the trailing-edge extension) had an aspect ratio of 10.3, a taper ratio of 0.40, a quarter-chord sweep angle of 27° and a dihedral angle of 0°. The area of the reference wing planform, including the fuselage intercept, was 0.183 m^2, the mean geometric chord of the reference wing panel was 14.15 cm, and the span was 1.37 m. Nondimensional wing airfoil coordinates at the wing-fuselage junction, the wing-planform break, and the wing tip are presented in table I. The wing reference plane was located at W.L. = -0.013.

(U) The model fuselage was constructed of fiberglass skin, aluminum bulkheads and a steel beam 1.282 m in length (from M.S. = 0.433 to M.S. = 1.715) to provide for a large degree of rigidity. Protuberances for angle-of-attack and angle-of-sideslip measurements were not included on the model fuselage. The abrupt change in fuselage area at the inlet duct on the flight configuration (ref. 4) was modified to provide a smooth contour on the model for attached flow conditions. A sketch of the air inlet-duct area is shown in figure 5. Indicated on the sketch is a faired line of the revised contour for the wind-tunnel model. The exit-duct area was covered by a flat surface having a rectangular clearance hole that provided access to the fuselage cavity for the model support system. Cross-sectional views of the model fuselage geometry are presented in figure 6. Static-pressure tubes were positioned at selected locations in the fuselage to provide for base-pressure corrections to the test data.

(U) The tail surfaces of the model were constructed of stainless steel. The rudder was attached to the vertical fin by a hinge bracket that was fabricated to provide rudder deflection angles from -12° to 0° in increments of 3°. Elevons (all-movable, differentially operating horizontal-tail surfaces), which provide for pitch and roll control, were attached in a manner which allowed for independent deflection angles from -15° to 9° in increments of 3°. The ranges of rudder and elevon deflection angles for the full-scale vehicle were from -10° to 10° and from -12° to 7°, respectively.

(U) Three configurations of the wind-tunnel model were used during the test program. The configurations, designated A, B, and C, differed only by the absence or addition of one of two pod designs to the fuselage lower surface. Configuration A refers to the basic wind-tunnel model shown in figure 1. Configuration B refers to the basic wind-tunnel model with the addition of the pod design shown in figures 7 and 8. Configuration C refers to the basic wind-tunnel model with the addition of the pod shown in figures 9 and 10. Dimensional data for the pod designs of configurations B and C are included in figures 7 and 9 along with their location on the fuselage. As indicated in the sketch of figures 7 and 9, the primary difference in the pods of configurations B and C is the fairing located downstream of model station 1.108.

(U) TEST FACILITY (U)

(U) The investigation was conducted in the Langley 8-Foot Transonic Pressure Tunnel. This facility is a continuous-flow, single-return, slotted-throat

tunnel having controls that allow for the independent variation of Mach number, density, temperature, and dewpoint. The test section is square in cross section with the upper and lower walls axially slotted (each wall having an open ratio of approximately 0.06) to permit changing the test-section Mach number continuously through the transonic speed range. The stagnation pressures in the tunnel can be varied from a minimum value of approximately 0.25 atm at all test Mach numbers to a maximum value of approximately 1.5 atm at transonic Mach numbers and to approximately 2.0 atm at Mach numbers of 0.40 or less (1 atm = 101.3 kPa). A more detailed description of the tunnel may be found in reference 5.

(U) BOUNDARY-LAYER TRANSITION STRIPS (U)

(U) Boundary-layer transition strips were placed on all model components for the entire investigation. All transition strips were 0.3-cm wide and were made of carborundum grit. The size and location of each strip were determined by the techniques of references 6 and 7 and from experiences gained by putting transition strips on similar wind-tunnel models (e.g., ref. 8). The strips were fixed at the location shown in figure 11. The model surface forward of the strips was kept smooth to maintain laminar flow.

(U) MEASUREMENTS AND TEST CONDITIONS (U)

(U) Six-component force and moment data were obtained with an electrical strain-gage balance housed within the fuselage. Angle of attack was measured by means of a ±10g linear servo accelerometer that was also housed within the fuselage and aligned with the pitch reference axis (1g = 9.8 m/sec^2). Model static pressures were measured in the vicinity of the strain-gage balance and in the sting clearance opening at the aft fuselage.

(U) Measurements were taken over a Mach number range from about 0.30 to 0.92 for angles of attack that varied from about -4° to 18° at sideslip angles from 0° to 6° at a Reynolds number of approximately 16.5×10^6 per meter. The entire investigation was conducted at a stagnation temperature of 322 K and at a dewpoint low enough to avoid significant condensation effects (see ref. 9).

(U) Basic longitudinal and lateral data were obtained for all undeflected control surfaces. Yaw-control data were obtained by rudder deflections, and pitch- and roll-control data were obtained by symmetric and asymmetric elevon deflections, respectively.

(U) ACCURACIES AND CORRECTIONS (U)

(U) The maximum allowable loadings for the six-component force balance used in this investigation were as follows: normal force, 11.1 kN; axial force, 2.22 kN; side force, 1.78 kN; pitching moment, 1130 N-m; rolling moment, 848 N-m; and yawing moment, 508 N-m. The model sting support, however, had a maximum allowable loading of 8.90 kN, which was used as the limiting normal force. The accuracy of each component of the balance was estimated to be one-half of one percent of the maximum value.

(U) The angle of attack of the model was corrected for flow angularity in the tunnel test section. Sideslip angle was corrected for sting bending. Lift, drag, and pitching-moment coefficients were corrected to a condition of free-stream static pressure at the base using the static pressures measured in the balance cavity and in the sting access opening at the aft fuselage. No corrections have been applied to the data for sting interference effects or for the effects of either solid wake blockage or lift interference due to wall effects. The estimated accuracy of Mach number was 0.003. The accuracy for the angular deflection of the elevon and rudder was estimated to be within approximately $\pm 1^{\circ}$ and $\pm 0.1^{\circ}$, respectively. It is believed that angle of attack and angle of sideslip are accurate to $\pm 0.1^{\circ}$.

(U) PRESENTATION OF RESULTS (U)

(U) The results of this investigation are presented in the following figures:

(C) DISCUSSION OF RESULTS (U)

(U) Measurements of the basic data for the longitudinal and lateral-directional characteristics were obtained in different angle-of-attack ranges for the three model configurations. The initial tests were made using model configuration B to determine a "well-defined" maximum value for the lift coefficient. During these tests, severe buffeting and/or rolling moments were encountered at the higher angles of attack and Mach numbers. To avoid possible damage to the model or instrumentation, the angle-of-attack range for subsequent tests of model configurations A and C was limited by buffet onset or balance off-scale loading. Also, comparable data at selected Mach numbers were not obtained for all configurations. This additional limitation on the data of the test program was considered to have a negligible effect on the test results.

(U) The resulting data from the wind-tunnel tests (figs. 12 to 14 and 29 to 32) were reduced to coefficient form and fitted with a smooth curve generated by a tension-spline computer program (ref. 10). The computer program was also used to generate the interpolated data for the summary of the longitudinal aerodynamic characteristics (i.e., figs. 15 to 18) and for the derivatives of the summary (i.e., figs. 19, 21 to 24, and 37 to 39). A linear least-square fit based on the method of reference 11 was used for the derivatives of figures 25 to 27 and figures 35 and 36. The derivatives of figures 33 and 34 were obtained from calculations of the incremental changes of the variables.

(C) LONGITUDINAL AERODYNAMIC CHARACTERISTICS (U)

(U) Basic Characteristics (U)

(U) The effect of model configuration on the longitudinal aerodynamic characteristics is indicated in figure 12. Data are presented for model configurations A, B, and C at a sideslip angle of 0°, at a symmetric elevon deflection of 0°, and at Mach numbers from 0.300 to 0.920. The data indicate similar variations of the longitudinal characteristics for each model configuration. At $M = 0.860$ and above, the configurations with pods have increasingly greater drag with increasing Mach number, and somewhat lower lift at corresponding angles of attack. The effect of the pods on pitching moment is not consistent with increased drag below the moment center, indicating that there may be other interference effects due to the presence of the pod.

(U) The effect of sideslip on the longitudinal aerodynamic characteristics is indicated in figure 13. Data are presented for model configuration C at three sideslip angles (nominal values of 0°, 2.5°, and 5.0°), a symmetric elevon deflection of 0°, and for Mach numbers from 0.300 to 0.920. At a Mach number of 0.300, pitching-moment coefficient increased as sideslip was increased for the range of angles of attack. At the higher Mach numbers ($M \geq 0.700$), the data show a "cross-over" angle of attack where the pitching-moment coefficient decreased with increased sideslip. This cross-over angle of attack decreased as Mach number increased from Mach 0.700 to 0.900. A secondary effect of sideslip is best illustrated at Mach 0.800 by the small reduction in the magnitude of the lift coefficient at an angle of attack of 2°. The effect of sideslip on the lift coefficient appears to be associated with the larger increments in pitching-moment coefficient due to sideslip. In general, the data indicate a substantial effect of sideslip on the pitching-moment coefficient, and a small or negligible effect of sideslip on the lift and drag coefficients.

(U) The effect of pitch control (symmetric elevon deflection) on the longitudinal aerodynamic characteristics is presented in figure 14. Data are presented for model configuration C at five symmetric elevon deflections (-9°, -6°, -3°, 0°, and 3°) and for the tail-off condition at a sideslip angle of 0° for Mach numbers from 0.300 to 0.900. As elevon deflection was varied from -9° to 3°, the data indicate that the lift coefficient increased and that the pitching-moment coefficient decreased for each Mach number. In general, the results indicate that the model could have been trimmed throughout the ranges of Mach number and angle of attack with a relatively small symmetric deflection angle. For a given angle of attack, more negative symmetric elevon deflection is required with increasing Mach number.

(C) Summary Characteristics (U)

(U) Variations of the zero-lift angle of attack, the zero-angle-of-attack lift coefficient, and the zero-lift pitching-moment coefficient with Mach number are presented in figures 15 to 17, respectively, for model configurations A, B, and C with symmetric elevon deflection of 0°. Small changes in the values of the zero-lift angle of attack (fig. 15), the zero-angle-of-attack lift coefficient (fig. 16), and the zero-lift pitching-moment coefficient (fig. 17) are

indicated for the lower Mach numbers ($M \leq 0.750$ or 0.800). At the higher Mach numbers, all parameters changed rapidly with Mach number. For each model configuration, a positive value for the zero-lift pitching moment is also indicated throughout the range of Mach numbers. In general, the data of figures 15 to 17 indicate only small changes due to changes in model configuration, but significant variations with increasing Mach number at the high Mach numbers.

(U) The drag characteristics for each model configuration are presented in figure 18. For each lift coefficient, the data show a characteristic drag rise at Mach numbers from about 0.80 to 0.92. The data also show a significant effect of model configuration. For a given Mach number, the smallest drag coefficients were usually obtained for configuration A, whereas the largest drag coefficients were usually obtained for configuration B. The improvement (reduction) in the drag coefficients of configuration C compared with that of configuration B is attributed to the longer aft pod fairing of configuration C (fig. 9). This longer, more streamlined pod had a smaller "dead-air" region behind it than the relatively blunt-ended pod of configuration B.

(C) The drag-divergence Mach number M_{DD} is presented as a function of lift coefficient in figure 19 for each configuration. The data show that a maximum value for the drag-divergence Mach number was obtained at a lift coefficient of 0.20 for configurations A and B, and at a lift coefficient of 0.30 for configuration C. The highest drag-divergence Mach number ($M_{DD} = 0.832$) was obtained for configuration A.

(U) Variations in the aerodynamic range parameter $M(L/D)$ with Mach number are presented in figure 20 for all model configurations and for lift coefficients from 0.30 to 0.70. The range parameter, which is proportional to the range of the full-scale flight vehicle, was computed for each configuration by obtaining the product of Mach number and lift-drag ratio C_L/C_D at each lift coefficient. The data of figure 20 may be used to obtain an estimate of a cruise flight condition (the flight condition for maximum range in the absence of propulsive and structural trade-offs). An obvious choice is the flight condition associated with the highest value of $M(L/D)$. The combinations of Mach number and lift coefficient for maximum $M(L/D)$ are different for each configuration. However, with only one exception, all curves in figure 20 peak at a Mach number of approximately 0.80 ($M = 0.80 \pm 0.02$). Since only an estimate is sought, a Mach number of 0.80 is a reasonable single choice which applies to the three model configurations. A lift coefficient of 0.60 results in the largest value of $M(L/D)$ at a Mach number of 0.80 for all configurations. However, for this combination of Mach number and lift coefficient, the data in figure 12(e) exhibit a pronounced change in the slopes (breaks) of the lift and pitching-moment curves. These breaks are usually indicative of buffet onset and stability problems $\left(C_{m_\alpha} \geq 0\right)$. Thus, a lift coefficient of 0.50 was chosen to provide some margin prior to the occurrence of buffet and instability. For each model configuration, the data of figure 20 indicate a reduction of only 5 to 6 percent in the value of the range parameter $M(L/D)$ at a Mach number of 0.80 when the lift coefficient changes from 0.60 to 0.50. Accordingly, the estimate for an efficient cruise flight condition is a lift coefficient of 0.50 at a Mach number of 0.80. This flight condition agrees well with the cruise

flight condition reported in reference 12 for a wind-tunnel investigation of a similar high-aspect-ratio supercritical wing mounted on a wide-body type fuselage.

(U) Variations of the lift-curve slope with Mach number are presented in figure 21 for model configurations A, B, and C. Data are presented for the results of figure 12 at angles of attack from -4° to 3° in the range of test Mach numbers. The effect of model configuration on the variation of lift-curve slope was generally small or insignificant. The data of figure 21 show that the lift-curve slope gradually increased to a peak value and, thereafter, decreased rapidly as the Mach number was increased. Significant differences in the magnitude of the lift-curve slope are indicated after the peak.

(U) Variations of the static stability derivative with Mach number are presented in figure 22 for model configurations A, B, and C. Data are presented for the results of figure 12 for angles of attack from -4° to 3° in the range of test Mach numbers. The data indicate that the model configurations were statically stable $\left(C_{m_{\alpha}} < 0\right)$ from a Mach number of about 0.30 up to a Mach number which varied from 0.75 to 0.90 depending on angle of attack and model configuration.

(U) The stability boundaries for model configurations A, B, and C are presented in figure 23 based on the information of figure 22. The figure presents boundaries in terms of Mach number and angle of attack and in terms of Mach number and lift coefficient. The dashed lines represent the combination of either Mach number and angle of attack or Mach number and lift coefficient for which the longitudinal static stability derivative has the largest negative value.

(U) Variations of the drag-curve slope $C_{D_{\alpha}}$ with Mach number are presented in figure 24 for model configurations A, B, and C. Data are presented for the appropriate slopes from the data of figure 12 for lift coefficients from 0.0 to 0.60. The data indicate similar trends for each model configuration in the range of test Mach numbers. At Mach numbers above 0.80, large variations of the drag-curve slope are indicated. As lift coefficient was increased, the variations of the drag-curve slopes became more severe. Both lift coefficient and Mach number have considerable effect on the drag-curve slope. For lift coefficients at and below 0.40, the effect of model configuration on the drag-curve slope is, in general, secondary.

(U) Variations of elevon effectiveness with Mach number are presented in figures 25 to 27. The data are presented for model configuration C at angles of attack from 0° to 3° in figures 25 and 26, and for lift coefficients from 0.00 to 0.60 in figure 27. Symmetric elevon deflections were varied from -9° to 3°. The elevon effectiveness in lift (fig. 25) and the elevon effectiveness in drag (fig. 27) were essentially unchanged in the Mach number range from 0.30 to approximately 0.70, and small changes gradually developed at Mach numbers from about 0.70 to 0.90. The effect of angle of attack on elevon effectiveness in lift or the effect of lift coefficient on elevon effectiveness in drag was, in general, insigificant for the range of test variables. A small increase of

elevon effectiveness in pitching moment (fig. 26) was obtained as Mach number was varied from 0.30 to 0.90. It is apparent that the effect of angle of attack on the elevon effectiveness in pitching moment was insignificant.

(U) The variation of the pitch-control index δ_{e_α} with Mach number is presented in figure 28. Data are presented for model configuration C at angles of attack from 0° to 3°. The data show substantial variations of the pitch-control index for Mach numbers above 0.70. The excursions of the pitch-control index are associated with changes in the longitudinal static stability of the model (figs. 22 and 23) at the higher Mach numbers. At Mach numbers from 0.73 to 0.86, the pitch-control index decreased rapidly as angle of attack was increased from 1° to 3°, and at Mach numbers from 0.86 to 0.90, the pitch-control index increased rapidly for angles of attack from 0° to 3°. The data of figure 28 indicate that, in general, pitch-control index was significantly affected by angle of attack and Mach number for Mach numbers above 0.70.

(U) LATERAL-DIRECTIONAL AERODYNAMIC CHARACTERISTICS (U)

(U) Basic Characteristics (U)

(U) The effect of model configuration on the lateral-directional aerodynamic characteristics is presented in figure 29. Data are presented for model configurations A, B, and C at a sideslip angle of 0°. The data indicate that the lateral-directional characteristics were essentially unchanged at the lower Mach number of 0.300 and for angles of attack in the range from about -4° to 8°. As Mach number was increased, the angle-of-attack range for very small or insignificant changes increased for the yawing-moment and side-force coefficients, and decreased for the rolling-moment coefficients. At Mach numbers above about 0.800, the rolling-moment coefficient oscillates with increasing angle of attack. A significant effect of model configuration is also indicated on the rolling-moment coefficient for the higher Mach numbers of 0.900 and 0.920. The change in rolling-moment coefficient is probably associated with an asymmetric loss of lift at the higher angles of attack.

(U) The effect of sideslip on the lateral-directional aerodynamic characteristics is presented in figure 30 for model configuration C at nominal sideslip angles of 0°, 2.5°, and 5.0°. For all three sideslip angles, the data show a significant effect of angle of attack on the rolling-moment coefficient. As sideslip angle increased the effect of angle of attack on the rolling moment became more pronounced. Significant negative and positive rolling moments are indicated for Mach numbers of 0.700 and 0.840 (figs. 30(b) and 30(e)). A negligible effect of angle of attack on the yawing-moment coefficient is indicated throughout the Mach number range, except at a Mach number of 0.300 for an angle of attack of 10° where data were obtained at a longitudinally unstable, pitch-up condition. The side-force coefficient generally shows a small or negligible effect of angle of attack for a sideslip angle of 0°. For a sideslip angle of 2.5° at Mach numbers above 0.900 (fig. 30(g)) and for a sideslip angle of 5.0° at Mach numbers above 0.860 (fig. 30(f)), the data show that as angle of attack was increased the side-force coefficient increased significantly in the negative direction.

(U) The effect of roll control on the lateral-directional aerodynamic characteristics is presented in figure 31. These data were obtained for model configuration C with asymmetric elevon deflections of -6°, -3°, -1.5°, 0°, and 3°. The data show significant nonlinear variation of the rolling-moment coefficients near angles of attack corresponding to the longitudinally unstable condition. These variations (also obtained in the investigation of ref. 13) are considered to be primarily associated with asymmetric wing stall and occur at lift coefficients that are well beyond the operating range of the flight vehicle. The effects of angle of attack and Mach number on the yawing-moment and side-force coefficients are not considered significant.

(U) The effect of directional control on the lateral-directional aerodynamic characteristics is presented in figure 32. The data were obtained for model configuration C with rudder deflection angles of 0°, -3°, -6°, and -9° (trailing edge to the right). The primary effect of rudder deflection is indicated by the relatively large positive yawing-moment coefficient and the associated negative side-force coefficient for the ranges of angle of attack and Mach number. The data also indicate a small effect of rudder deflection on the rolling-moment coefficient at angles of attack where the model was stable (fig. 32(c)), and that there was a negligible effect of angle of attack and Mach number on the yawing-moment and side-force coefficients. In general, the results indicate that rudder deflection provides a significant positive directional control, a significant side effect on side force, and a small side effect on rolling moment.

(U) Summary Characteristics (U)

(U) Variations of the lateral-directional static stability characteristics with lift coefficient are presented in figure 33. Data are presented for model configuration C over two ranges of sideslip angle for the range of test Mach numbers. The lower range of sideslip angles had nominal values from 0° to 2.5°, and the upper range of sideslip angles had nominal values from 2.5° to 5.0°. The actual values of the ranges of sideslip angle are indicated on the figure. The rolling-moment derivative (dihedral effect) is shown in figure 33(a), the yawing-moment derivative (directional stability) is shown in figure 33(b), and the side-force derivative is shown in figure 33(c). Positive effective dihedral $\left(C_{l_\beta} < 0\right)$ was obtained for Mach numbers up to 0.80 for both ranges of sideslip angle. Both positive and negative effective dihedral are shown for the higher Mach numbers ($M > 0.80$) at selected lift coefficients and sideslip angles. The reversal of dihedral effect $\left(C_{l_\beta} > 0\right)$ is attributed to asymmetric wing stall.

In figure 33(b), the data indicate that the model was directionally stable $\left(C_{n_\beta} > 0\right)$ for all test conditions. The directional stability was significantly larger for the upper range of sideslip angles than for the lower range of sideslip angles. Although the effect of lift coefficient was not consistent in the range of Mach numbers, the largest effect occurred at a Mach number of 0.84 and is indicated by a gradual increase in directional stability of approximately 31 percent for the upper range of sideslip angles and 73 percent for the lower range of sideslip angles. The data of figure 33(c) indicate that lift coeffi-

cient has a small effect on the side-force derivative for both the upper and the lower ranges of sideslip angle. The near-linear reduction in the value of the side-force derivative for the upper range of sideslip angles varied from about 15 percent at a Mach number of 0.30 to about 14 percent at a Mach number of 0.92 in the range of lift coefficients. The side-force derivative was always smaller for the upper range of sideslip angles for the range of test conditions.

(U) Variations of the lateral-directional static stability characteristics with Mach number are presented in figure 34. The data, which are cross plots of the results of figure 33, are presented for model configuration C at lift coefficients from 0.0 to 0.50 for two ranges of sideslip angle. One range of sideslip angles had nominal values from 0° to 2.5°, and the other range had nominal values from 2.5° to 5.0°. The actual values of the ranges of sideslip angle are indicated on the figure. The rolling-moment derivative (dihedral effect) is shown in figure 34(a), the yawing-moment derivative (directional stability) is shown in figure 34(b), and the side-force derivative is shown in figure 34(c). In figure 34(a), large excursions of the dihedral effect are indicated at Mach numbers above 0.80. The data also indicate that an unstable dihedral effect $\left(C_{l_\beta} > 0\right)$ occurred for both ranges of sideslip angle. For the lower Mach numbers (0.30 to 0.70), small or insignificant changes in the dihedral effect are indicated for both ranges of sideslip angle. The data of figure 34(b) indicate that the model was directionally stable $\left(C_{n_\beta} > 0\right)$ at all test conditions. The data also indicate that the model had more directional stability at the upper range of sideslip angles than at the lower range of sideslip angles. A significant increase of directional stability occurred at the higher Mach numbers (above 0.80) for both ranges of sideslip angle. The data of figure 34(c) indicate that the side-force derivative was negative for all test conditions. As Mach number was increased, larger negative values of the side-force derivative were obtained.

(U) Variations of the roll-control derivatives (asymmetric elevon deflection) with lift coefficient are presented in figure 35 for model configuration C. These data were obtained for asymmetric elevon deflections of -6° ($\delta_{HL} = -9^{\circ}$, $\delta_{HR} = 3^{\circ}$), -3° ($\delta_{HL} = 0^{\circ}$, $\delta_{HR} = 6^{\circ}$), -1.5° ($\delta_{HL} = -3^{\circ}$, $\delta_{HR} = 0^{\circ}$), 0° ($\delta_{HL} = 0^{\circ}$, $\delta_{HR} = 0^{\circ}$), and 3° ($\delta_{HL} = -3^{\circ}$, $\delta_{HR} = -9^{\circ}$). The data of figure 35 show that the roll-control effectiveness was positive (positive values of the rolling-moment derivative). The effect of lift coefficient on the roll-control effectiveness was significant but not consistent at all test Mach numbers. The largest effect, however, is indicated for a Mach number of 0.90 where the roll-control effectiveness increased approximately 94 percent over the range of lift coefficients (0 to 0.6). The data also indicate a near-linear reduction of the yawing-moment derivative with increasing lift coefficient for the test Mach numbers. In the range of lift coefficients, a reduction of about 65 percent is indicated for a Mach number of 0.30, and reductions of about 31 percent and 34 percent are indicated for Mach numbers of 0.80 and 0.90, respectively. The side-force derivative due to asymmetric elevon deflection increased (became less negative) with lift coefficient for the test Mach numbers. The increase of the side-force derivative was nearly linear with lift coefficient and the slopes

were approximately equal for the test Mach numbers. The largest increase of side-force derivative (38 percent) was for a Mach number of 0.90 over the range of lift coefficients.

(U) Variations of the roll-control derivatives (asymmetric elevon deflection) with Mach number are presented in figure 36 for model configuration C. These data are cross plots of figure 35 for a range of lift coefficients from 0.0 to 0.60. The data show that there was a small or negligible effect of Mach number on the roll-control effectiveness up to a Mach number of approximately 0.70. The data show (depending on lift coefficient) changes of roll-control effectiveness as Mach number was increased from 0.70 to 0.90. A pronounced effect of Mach number is indicated for the yawing-moment and side-force derivatives. As Mach number was increased, the yawing-moment derivative increased and the side-force derivative decreased for all lift coefficients. The results of figure 35 show that Mach number and lift coefficient had a significant effect on the roll-control derivatives; however, Mach numbers up to about 0.70 had only a minimal effect on the roll-control effectiveness.

(U) Variations of the rudder-control derivatives with rudder-deflection angle are presented in figure 37 for model configuration C. These data were obtained from cross plots of the results of figure 32. The data of figure 37(a) show that the rudder deflection had a considerable effect on the rolling-moment derivative. The most pronounced effect of rudder deflection is indicated for a Mach number of 0.90, where the largest effect of lift coefficient is also indicated. The data of figure 37(b) show the effect of rudder deflection on the yawing-moment derivative (directional-control derivative). The salient feature of these data is the nonlinear variation of directional control with rudder deflection. A small change (increase) in directional control is indicated for rudder deflection angles from 0° to about -3° or -4°, and the more significant levels of directional control occurred at the largest deflection angles. The data of figure 37(c) show the effect of rudder deflection on the side-force derivative. In general, the maximum (positive) values of the side-force derivative occurred near a rudder deflection angle of -8° and the minimal values occurred at rudder deflection angles from 0° to about -3° or -4°, depending on Mach number and lift coefficient. Values of the side-force derivative were consistently positive for all test variables.

(U) Variations of the rudder-control derivatives with Mach number are presented in figure 38 for model configuration C at four rudder deflection angles. These data are cross plots of the results of figure 37. The data of figure 38(a) show characteristic reversals of the rolling-moment derivative at Mach numbers above 0.70 for rudder deflection angles of -9°, -3°, and 0°. The data also indicate that the direction and severity of the reversals for the rolling-moment derivative are dependent on lift coefficient and rudder deflection angle. The data of figures 38(b) and 38(c) show variations of the yawing-moment derivative (directional-control derivative) and side-force derivative with Mach number, respectively. These data indicate that the effects of Mach number (and lift coefficient) were relatively small on the directional-control and side-force derivatives. The data also indicate that rudder deflection provides significant directional control and side force.

(U) Variations of the rudder-control index with lift coefficient are presented in figure 39 for model configuration C at four rudder deflection angles. Data are included for the upper and the lower ranges of sideslip angle, and the actual values of sideslip angle are shown in the figure. The data show that the rudder-control index was not significantly affected by lift coefficient for most test conditions. The largest change in rudder-control index is shown for a Mach number of 0.840 at the lower rudder deflection angles. Decreased rudder-control sensitivity is also indicated as the rudder deflection angle was varied from 0° to -9°. At corresponding test conditions, the rudder-control index is substantially larger for the upper range of sideslip angles than for the lower range of sideslip angles.

(U) Variations of the rudder-control index with Mach number are presented in figure 40 for model configuration C and at rudder deflection angles. These data are cross plots of the results of figure 39. Data are included for the upper and the lower ranges of sideslip angle, and the actual values of sideslip angle are shown in the figure. The data show that the rudder-control index was relatively insensitive to Mach numbers in the Mach number range from 0.30 to 0.80. A significant increase of rudder-control index is also shown as Mach number was varied from 0.80 to 0.90 for all lift coefficients.

(U) CONCLUDING REMARKS (U)

(U) A wind-tunnel investigation has been conducted to determine the longitudinal and lateral-directional static stability and control characteristics of a 0.237-scale force model of a remotely piloted research vehicle with a thick, high-aspect-ratio supercritical wing. Three configurations of the model were tested at Mach numbers from 0.30 to 0.92, at angles of attack from about -4° to 18°, and at angles of sideslip from 0° to 6°. Regions of longitudinal instability were identified for the model. The horizontal-tail effectiveness in pitch was shown to be sufficient to trim the model for Mach numbers up to 0.90. The model had positive effective dihedral for Mach numbers up to about 0.82. In addition, the model was directionally stable, had positive effectiveness of roll control, and had positive effectiveness of yaw control for Mach numbers up to 0.90.

(U) Limit performance analysis indicated that maximum values of the drag-divergence Mach number occurred at lift coefficients between 0.20 and 0.30 for the model configurations. A cruise condition based on the aerodynamic range parameter was identified to be a lift coefficient of approximately 0.50 and a Mach number of 0.80.

Langley Research Center
National Aeronautics and Space Administration
Hampton, VA 23665
April 16, 1980

(U) REFERENCES (U)

1. Murrow, H. N.; and Eckstrom, C. V.: Drones for Aerodynamic and Structural Testing (DAST) - A Status Report. J. of Aircr., vol. 16, no. 8, Aug. 1979, pp. 521-526.

2. Eckstrom, Clinton V.; and Peele, Ellwood L.: Flight Assessment of a Large Supersonic Drone Aircraft for Research Use. NASA TM X-3259, 1975.

3. Gainer, Thomas G.; and Hoffman, Sherwood: Summary of Transformation Equations and Equations of Motion Used in Free-Flight and Wind-Tunnel Data Reduction and Analysis. NASA SP-3070, 1972.

4. Byrdsong, Thomas A.: Flight Measurements of Lifting Pressures for a Thin Low-Aspect-Ratio Wing at Subsonic, Transonic, and Low Supersonic Speeds. NASA TM X-3405, 1977.

5. Schaefer, William T., Jr.: Characteristics of Major Active Wind Tunnels at the Langley Research Center. NASA TM X-1130, 1965.

6. Braslow, Albert L.; and Knox, Eugene C.: Simplified Method for Determination of Critical Height of Distributed Roughness Particles for Boundary-Layer Transition at Mach Numbers from 0 to 5. NACA TN-4363, 1958.

7. Blackwell, James A., Jr.: Preliminary Study of Effects of Reynolds Number and Boundary-Layer Transition Location on Shock-Induced Separation. NASA TN D-5003, 1969.

8. Bartlett, Dennis W.: Wind-Tunnel Investigation of Several High Aspect-Ratio Supercritical Wing Configurations on a Wide-Body-Type Fuselage. NASA TM X-71996, 1977.

9. Jordan, Frank L., Jr.: Investigation at Near-Sonic Speed of Some Effects of Humidity on the Longitudinal Aerodynamic Characteristics of an NASA Supercritical-Wing Research Airplane Model. NASA TM X-2618, 1972.

10. Cline, Alan K.: Curve Fitting Using Splines Under Tension. Atmos. Technol., Sept. 1973, pp. 60-65.

11. Mode, Elmer B.: Elements of Statistics. Second ed. Prentice-Hall, Inc., c.1951.

12. Bartlett, Dennis W.; Harris, Charles D.; and Kelly, Thomas C.: Wind-Tunnel Development of Underwing Leading-Edge Vortex Generators on an NASA Supercritical-Wing Research Airplane Configuration. NASA TM X-2808, 1973.

13. Byrdsong, Thomas A.; and Hallissy, James B.: Longitudinal and Lateral Static Stability and Control Characteristics of a 1/6-Scale Model of a Remotely Piloted Research Vehicle With a Supercritical Wing. NASA TP-1360, 1979.

(C) TABLE I.- STREAMWIDE AIRFOIL COORDINATES (U)

(a) $\frac{y}{b/2} = 0.071$ (wing-fuselage junction)

x/c	z/c	
	Upper surface	Lower surface
0.00000	-.00149	-.00149
.00200	.00989	-.01321
.00500	.01616	-.01929
.01000	.02306	-.02631
.02000	.03193	-.03487
.03000	.03711	-.04052
.04000	.04118	-.04506
.05000	.04433	-.04900
.06000	.04696	-.05242
.07000	.04917	-.05555
.08000	.05107	-.05847
.09000	.05277	-.06119
.10000	.05415	-.06371
.11000	.05533	-.06601
.12000	.05629	-.06821
.13000	.05715	-.07020
.14000	.05791	-.07209
.15000	.05857	-.07388
.16000	.05912	-.07545
.17000	.05957	-.07692
.18000	.06003	-.07826
.19000	.06026	-.07954
.20000	.06040	-.08069
.21000	.06043	-.08174
.22000	.06047	-.08268
.23000	.06039	-.08352
.24000	.06032	-.08425
.25000	.06014	-.08487

x/c	z/c	
	Upper surface	Lower surface
.26000	.05997	-.08550
.27000	.05969	-.08602
.28000	.05942	-.08643
.29000	.05904	-.08686
.30000	.05867	-.08717
.31000	.05829	-.08748
.32000	.05781	-.08781
.33000	.05734	-.08802
.34000	.05675	-.08825
.35000	.05617	-.08836
.36000	.05548	-.08848
.37000	.05479	-.08849
.38000	.05412	-.08850
.39000	.05332	-.08841
.40000	.05254	-.08832
.41000	.05175	-.08813
.42000	.05086	-.08782
.43000	.04997	-.08753
.44000	.04908	-.08713
.45000	.04809	-.08662
.46000	.04710	-.08612
.47000	.04611	-.08552
.48000	.04502	-.08481
.49000	.04392	-.08411
.50000	.04283	-.08319
.51000	.04164	-.08229
.52000	.04044	-.08128
.53000	.03925	-.08017
.54000	.03794	-.07907

TABLE I.- Continued (U)

(a) Concluded

x/c	z/c	
	Upper surface	Lower surface
.55000	.03664	-.07775
.56000	.03536	-.07644
.57000	.03395	-.07503
.58000	.03255	-.07363
.59000	.03116	-.07213
.60000	.02978	-.07063
.61000	.02828	-.06914
.62000	.02679	-.06755
.63000	.02530	-.06596
.64000	.02382	-.06437
.65000	.02223	-.06280
.66000	.02086	-.06122
.67000	.01906	-.05966
.68000	.01737	-.05819
.69000	.01569	-.05675
.70000	.01401	-.05541
.71000	.01234	-.05407
.72000	.01056	-.05273
.73000	.00878	-.05150
.74000	.00701	-.05039
.75000	.00514	-.04927
.76000	.00327	-.04815
.77000	.00140	-.04714
.78000	-.00046	-.04624
.79000	-.00242	-.04543
.80000	-.00438	-.04461
.81000	-.00634	-.04390
.82000	-.00840	-.04329

x/c	z/c	
	Upper surface	Lower surface
.83000	-.01045	-.04278
.84000	-.01250	-.04236
.85000	-.01455	-.04204
.86000	-.01658	-.04181
.87000	-.01839	-.04167
.88000	-.02064	-.04162
.89000	-.02265	-.04176
.90000	-.02466	-.04180
.91000	-.02667	-.04213
.92000	-.02866	-.04254
.93000	-.03065	-.04303
.94000	-.03264	-.04372
.95000	-.03461	-.04449
.96000	-.03658	-.04534
.97000	-.03854	-.04638
.98000	-.04048	-.04761
.99000	-.04240	-.04903
1.00000	-.04431	-.05064

c = 24.87 cm

$\varepsilon = 2.45^{o}$

ORIGINAL PAGE IS
OF POOR QUALITY

[redacted] TABLE I.- Continued (U)

(b) $\frac{y}{b/2}$ = 0.426 (planform break)

x/c	z/c	
	Upper surface	Lower surface
0.00000	-.00436	-.00436
.00200	.00499	-.01319
.00500	.00990	-.01822
.01000	.01482	-.02312
.02000	.02111	-.02925
.03000	.02559	-.03359
.04000	.02896	-.03682
.05000	.03165	-.03935
.06000	.03403	-.04156
.07000	.03611	-.04348
.08000	.03800	-.04520
.09000	.03968	-.04672
.10000	.04126	-.04813
.11000	.04265	-.04935
.12000	.04393	-.05056
.13000	.04522	-.05168
.14000	.04640	-.05269
.15000	.04749	-.05361
.16000	.04847	-.05443
.17000	.04946	-.05524
.18000	.05034	-.05595
.19000	.05113	-.05667
.20000	.05191	-.05728
.21000	.05260	-.05790
.22000	.05329	-.05841
.23000	.05397	-.05883
.24000	.05456	-.05924
.25000	.05514	-.05966

x/c	z/c	
	Upper surface	Lower surface
.26000	.05563	-.05997
.27000	.05612	-.06028
.28000	.05660	-.06050
.29000	.05698	-.06072
.30000	.05737	-.06093
.31000	.05765	-.06105
.32000	.05794	-.06106
.33000	.05823	-.06108
.34000	.05851	-.06109
.35000	.05870	-.06110
.36000	.05888	-.06102
.37000	.05907	-.06093
.38000	.05915	-.06085
.39000	.05924	-.06066
.40000	.05933	-.06047
.41000	.05941	-.06019
.42000	.05940	-.05991
.43000	.05939	-.05952
.44000	.05937	-.05913
.45000	.05935	-.05865
.46000	.05924	-.05816
.47000	.05913	-.05758
.48000	.05901	-.05690
.49000	.05880	-.05621
.50000	.05859	-.05543
.51000	.05837	-.05454
.52000	.05816	-.05366
.53000	.05784	-.05267
.54000	.05753	-.05159

(C) TABLE I.- Continued (U)

(b) Concluded

x/c	z/c	
	Upper surface	Lower surface
.55000	.05721	-.05050
.56000	.05680	-.04922
.57000	.05639	-.04793
.58000	.05597	-.04655
.59000	.05551	-.04506
.60000	.05494	-.04357
.61000	.05433	-.04198
.62000	.05371	-.04040
.63000	.05310	-.03871
.64000	.05238	-.03702
.65000	.05167	-.03523
.66000	.05085	-.03344
.67000	.05004	-.03155
.68000	.04913	-.02966
.69000	.04821	-.02777
.70000	.04730	-.02588
.71000	.04629	-.02399
.72000	.04527	-.02210
.73000	.04416	-.02021
.74000	.04304	-.01832
.75000	.04183	-.01643
.76000	.04062	-.01454
.77000	.03930	-.01265
.78000	.03809	-.01086
.79000	.03678	-.00917
.80000	.03537	-.00758
.81000	.03395	-.00599
.82000	.03244	-.00450
.83000	.03093	-.00311
.84000	.02942	-.00183
.85000	.02781	-.00064
.86000	.02620	.00035
.87000	.02449	.00114
.88000	.02277	.00172
.89000	.02096	.00221
.90000	.01915	.00249
.91000	.01724	.00258
.92000	.01533	.00236
.93000	.01332	.00195
.94000	.01131	.00133
.95000	.00921	.00042
.96000	.00710	-.00079
.97000	.00489	-.00220
.98000	.00258	-.00392
.99000	.00017	-.00593
1.00000	-.00234	-.00813
c = 14.18 cm $\varepsilon = -0.53^{o}$		

[redacted]

(C) TABLE I.- Continued (U)

(c) $\frac{Y}{b/2} = 1.000$ (wing tip)

x/c	z/c	
	Upper surface	Lower surface
0.00000	-.01350	-.01350
.00200	-.00506	-.02081
.00500	-.00074	-.02531
.01000	.00356	-.02946
.02000	.00925	-.03467
.03000	.01327	-.03823
.04000	.01640	-.04088
.05000	.01899	-.04295
.06000	.02127	-.04472
.07000	.02332	-.04625
.08000	.02518	-.04758
.09000	.02690	-.04878
.10000	.02845	-.04981
.11000	.02989	-.05077
.12000	.03128	-.05167
.13000	.03261	-.05247
.14000	.03384	-.05317
.15000	.03503	-.05383
.16000	.03612	-.05440
.17000	.03715	-.05490
.18000	.03814	-.05536
.19000	.03904	-.05576
.20000	.03993	-.05612
.21000	.04073	-.05648
.22000	.04162	-.05675
.23000	.04232	-.05698
.24000	.04302	-.05715
.25000	.04372	-.05731

x/c	z/c	
	Upper surface	Lower surface
.26000	.04438	-.05744
.27000	.04498	-.05751
.28000	.04558	-.05754
.29000	.04614	-.05757
.30000	.04664	-.05755
.31000	.04711	-.05748
.32000	.04758	-.05738
.33000	.04804	-.05722
.34000	.04844	-.05705
.35000	.04881	-.05688
.36000	.04918	-.05662
.37000	.04955	-.05635
.38000	.04988	-.05608
.39000	.05014	-.05572
.40000	.05041	-.05535
.41000	.05068	-.05495
.42000	.05091	-.05449
.43000	.05108	-.05399
.44000	.05125	-.05349
.45000	.05142	-.05290
.46000	.05155	-.05230
.47000	.05162	-.05162
.48000	.05168	-.05048
.49000	.05173	-.05009
.50000	.05176	-.04926
.51000	.05179	-.04834
.52000	.05176	-.04741
.53000	.05170	-.04639
.54000	.05164	-.04533

[redacted]

TABLE I.- Concluded (U)

(c) Concluded

x/c	z/c	
	Upper surface	Lower surface
.55000	.05156	-.04420
.56000	.05141	-.04295
.57000	.05125	-.04163
.58000	.05108	-.04020
.59000	.05088	-.03874
.60000	.05062	-.03721
.61000	.05033	-.03564
.62000	.05004	-.03401
.63000	.04974	-.03235
.64000	.04935	-.03068
.65000	.04895	-.02892
.66000	.04846	-.02715
.67000	.04796	-.02529
.68000	.04744	-.02342
.69000	.04685	-.02156
.70000	.04625	-.01962
.71000	.04563	-.01768
.72000	.04494	-.01574
.73000	.04421	-.01380
.74000	.04342	-.01186
.75000	.04259	-.00992
.76000	.04170	-.00799
.77000	.04080	-.00605
.78000	.03982	-.00421
.79000	.03883	-.00240
.80000	.03780	-.00062
.81000	.03671	.00101
.82000	.03559	.00255

x/c	z/c	
	Upper surface	Lower surface
.83000	.03440	.00398
.84000	.03321	.00532
.85000	.03193	.00655
.86000	.03063	.00765
.87000	.02925	.00855
.88000	.02786	.00931
.89000	.02644	.00991
.90000	.02496	.01030
.91000	.02344	.01050
.92000	.02186	.01046
.93000	.02024	.01023
.94000	.01856	.00972
.95000	.01685	.00899
.96000	.01506	.00803
.97000	.01318	.00687
.98000	.01120	.00541
.99000	.00905	.00366
1.00000	.00680	.00164
c = 7.62 cm		
$\varepsilon = -1.57^{o}$		

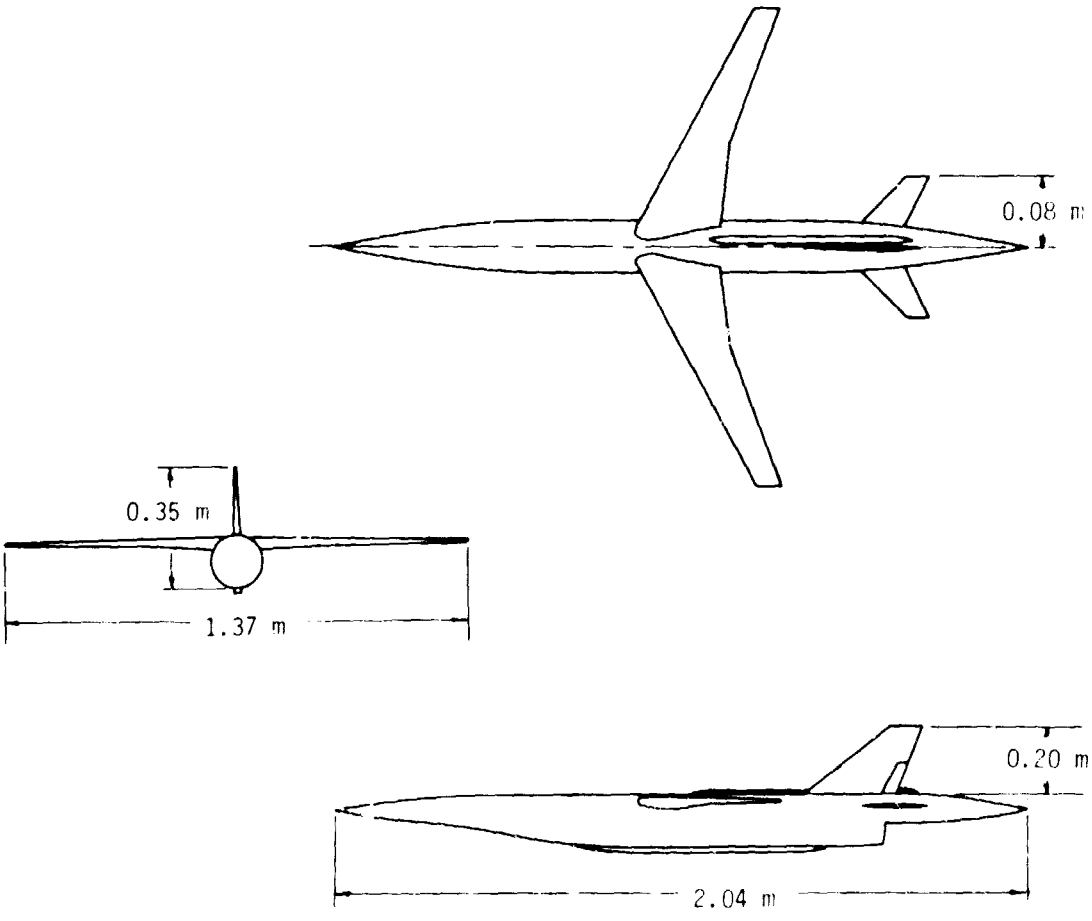

(U) Figure 1.- Basic wind-tunnel model (configuration A). (U)

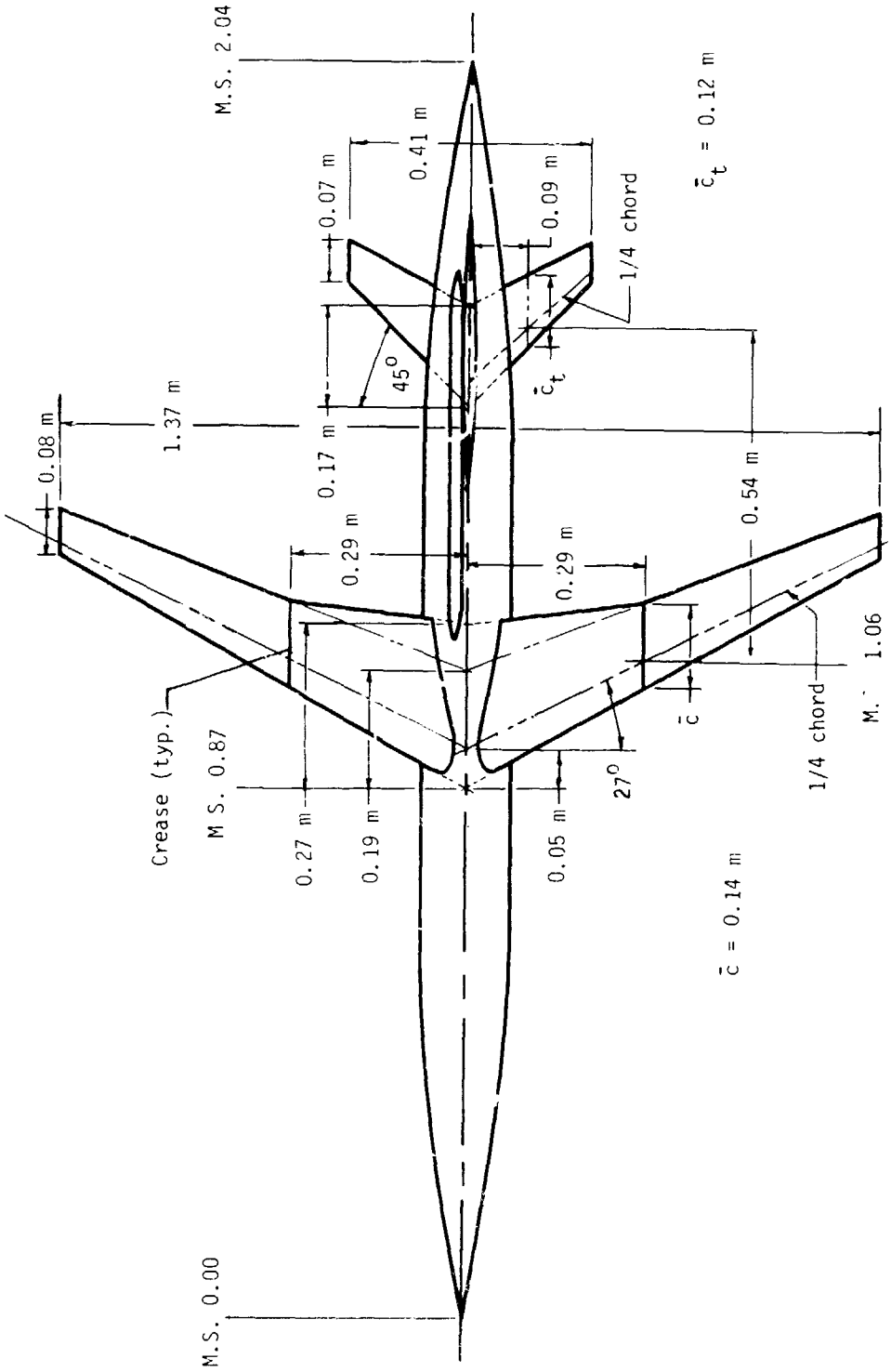

(U) Figure 2.- Model planform. (U)

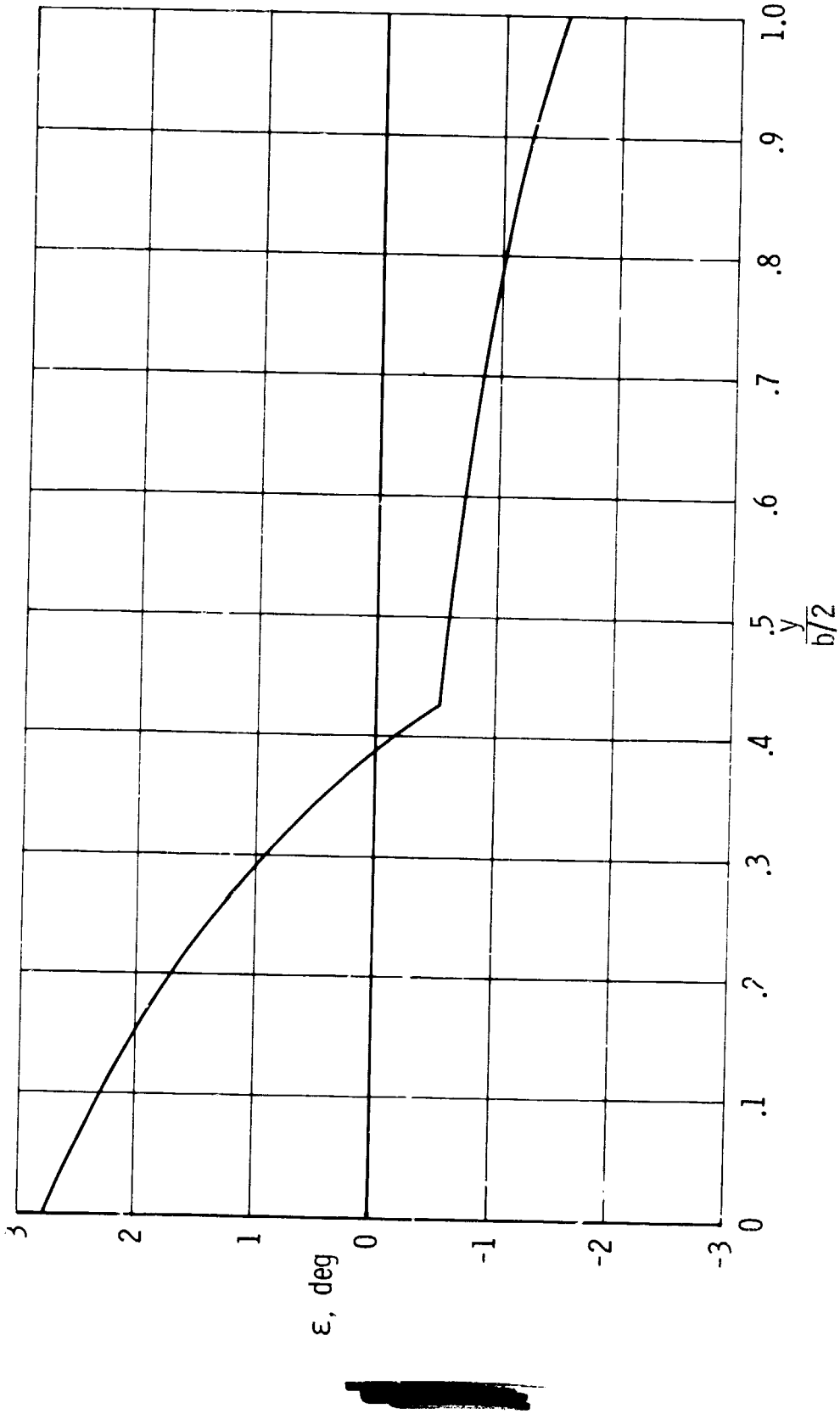

(C) Figure 3.- Wing twist distribution relative to wing reference plane. (U)

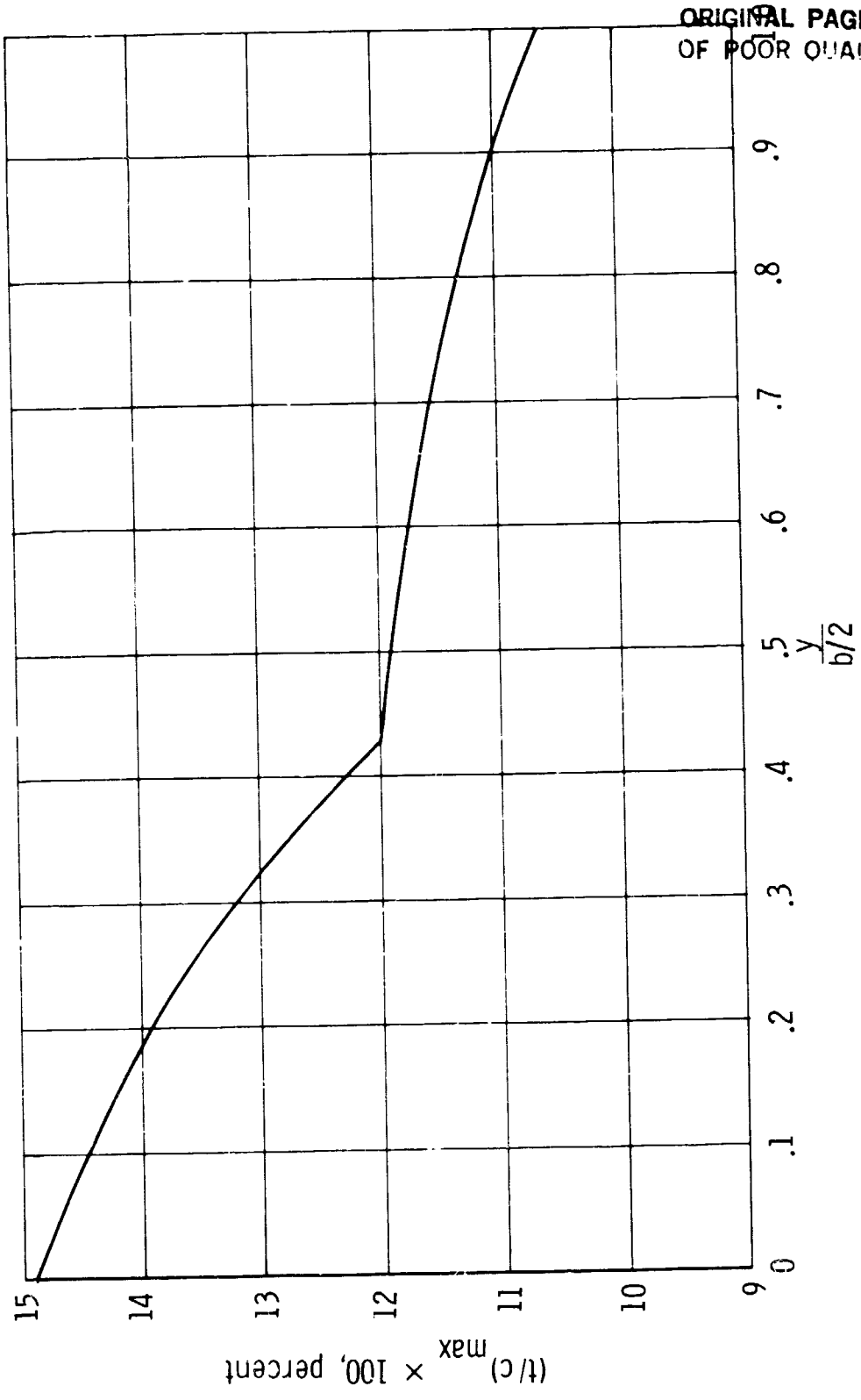

(U) Figure 4.- Wing maximum thickness distribution. (U)

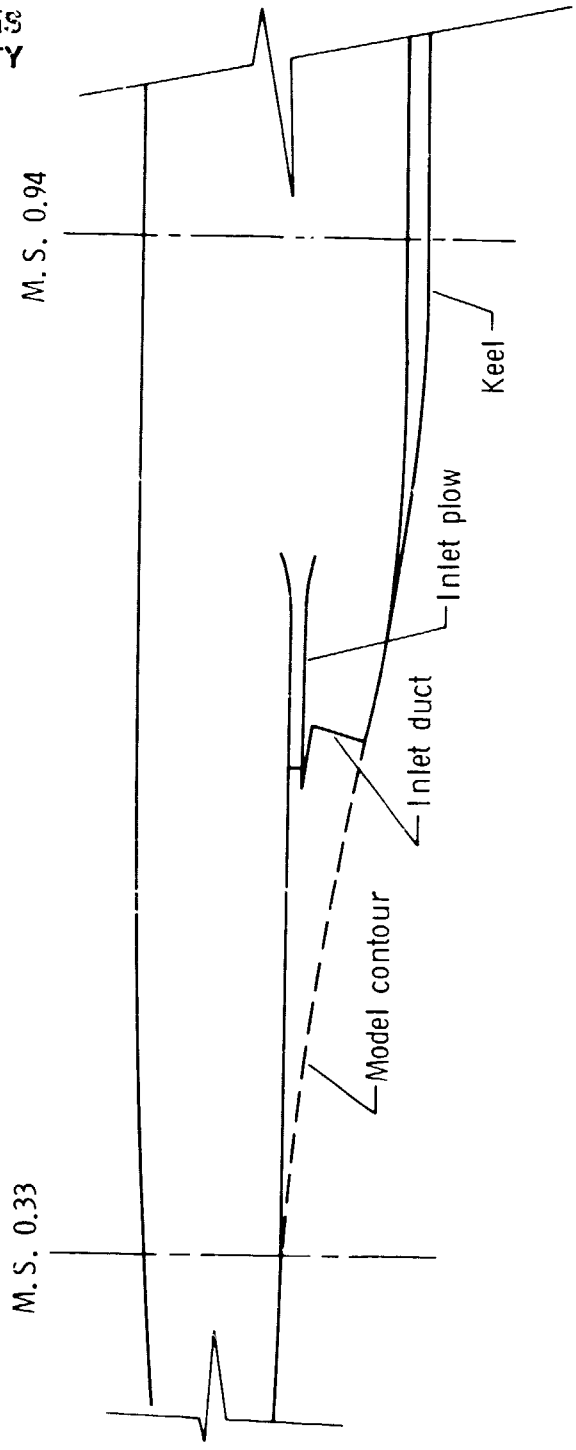

(U) Figure 5.- Engine air-inlet elevation (ref. 13). (U)

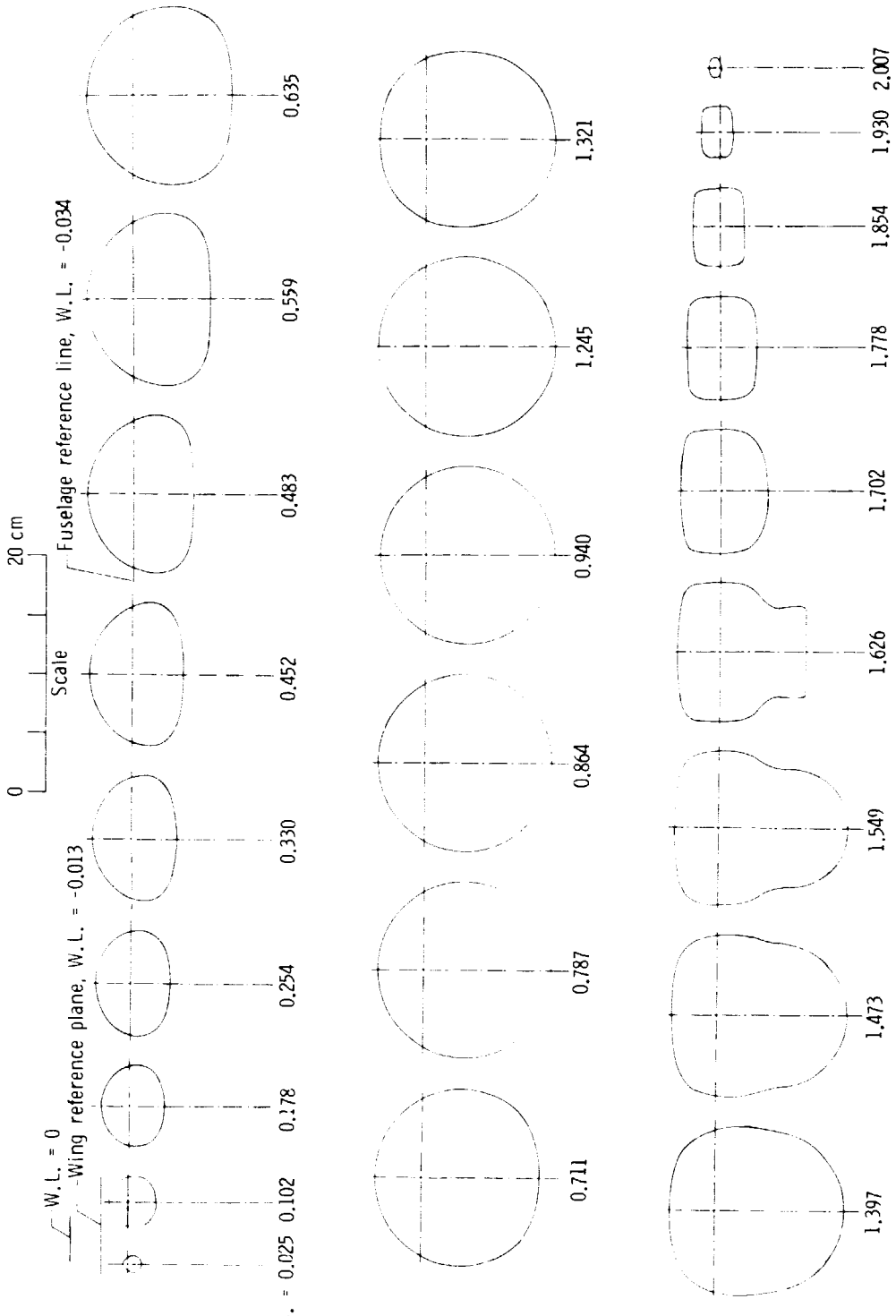

(U) Figure 6.- Cross-sectional views of fuselage geometry. (U)

ORIGINAL PAGE IS
OF POOR QUALITY

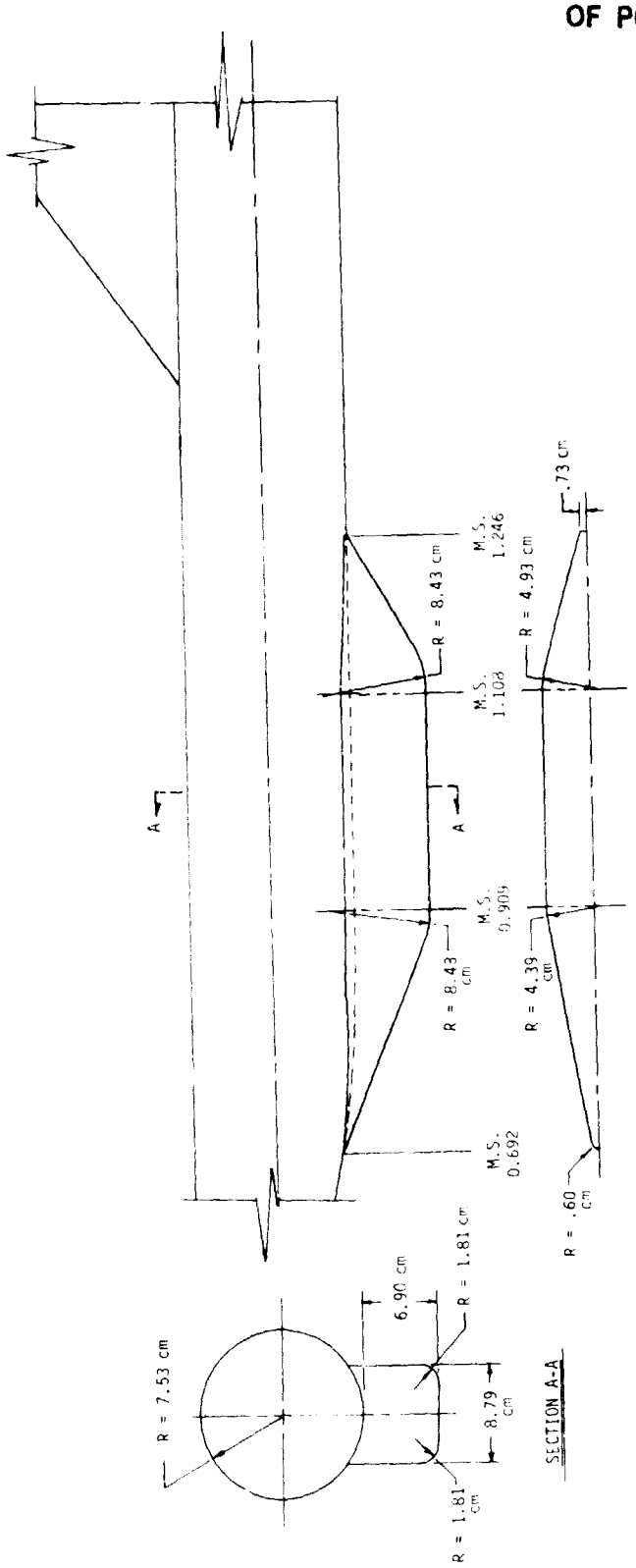

(U) Figure 7.- Sketch of pod design for model configuration B. (U)

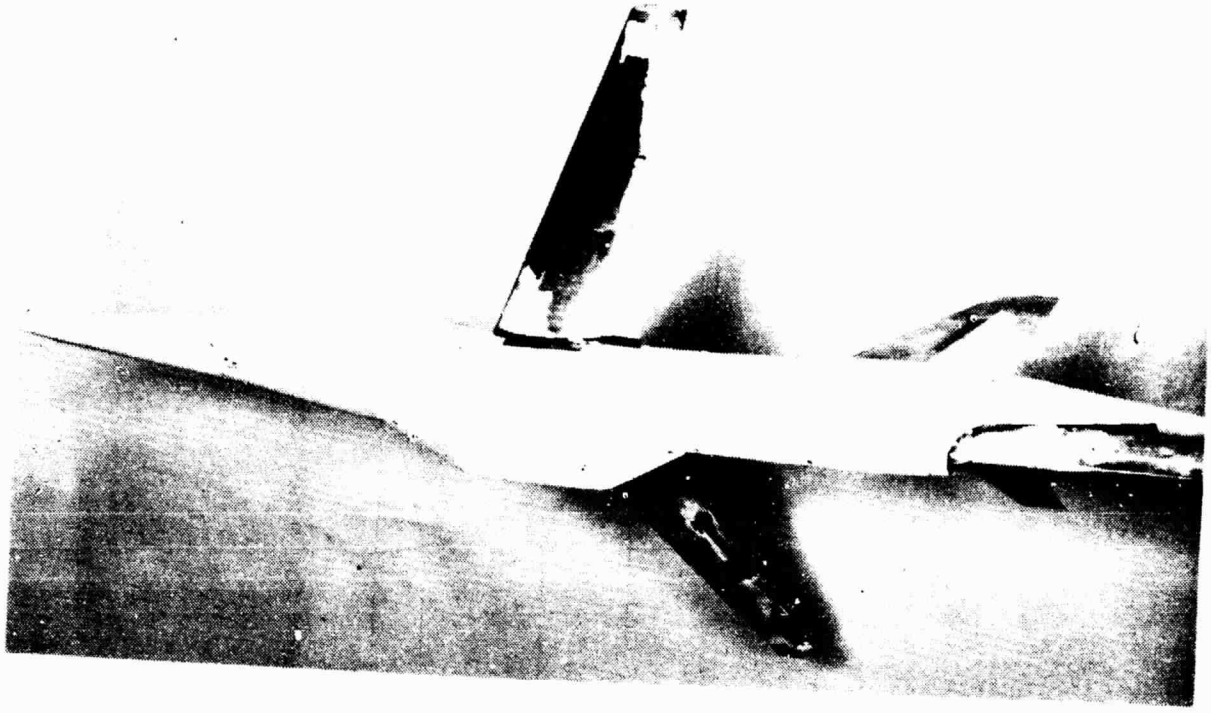

L-77-7242

(U) Figure 8.- Photographs of model configuration B. (U) L-77-7241

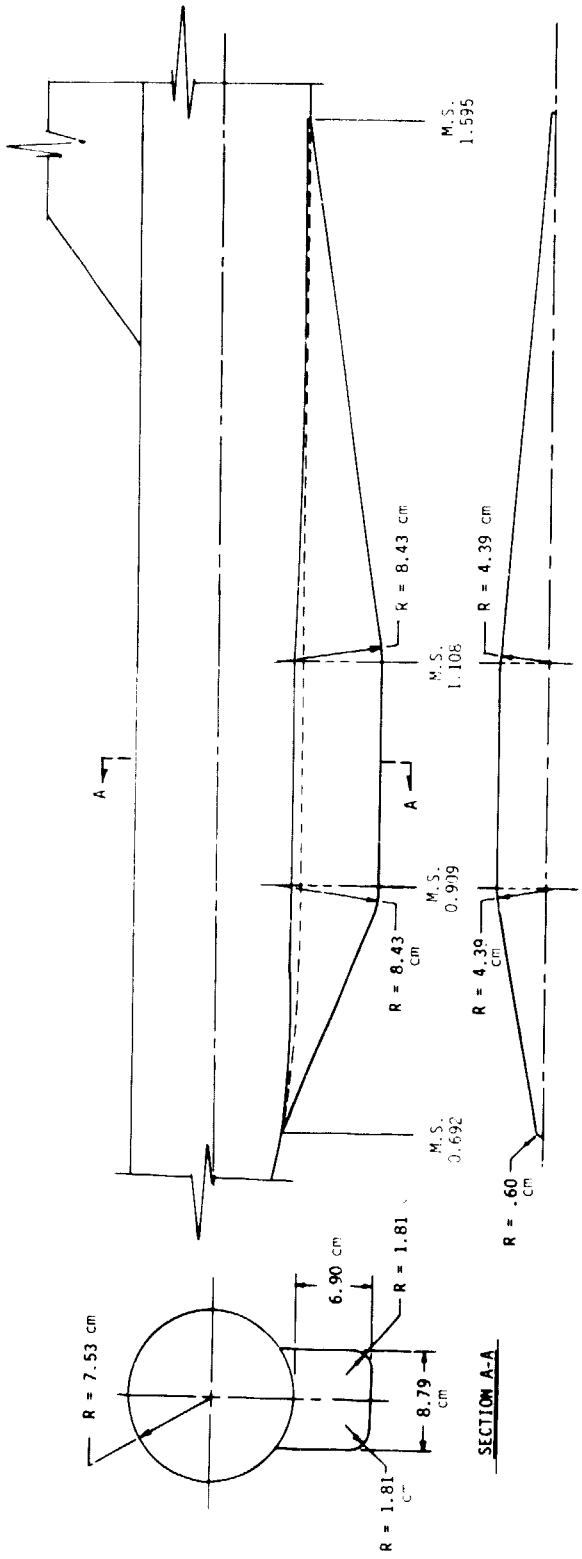

(U) Figure 9.- Sketch of pod design for model configuration C. (U)

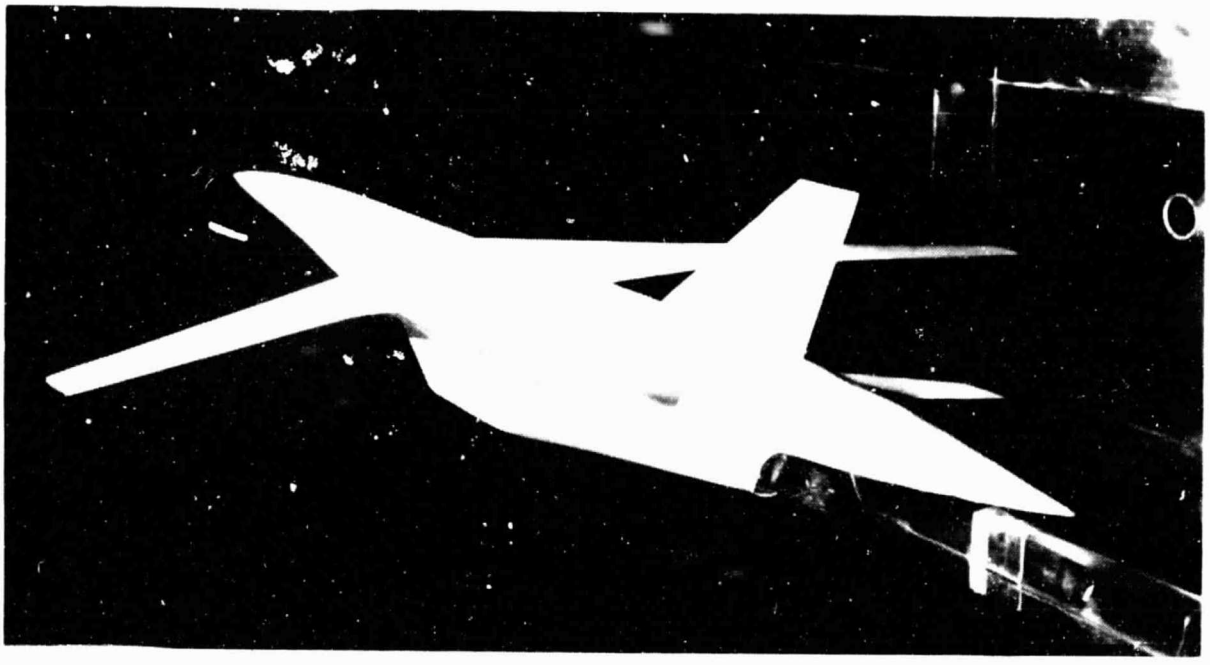

L-77-7506

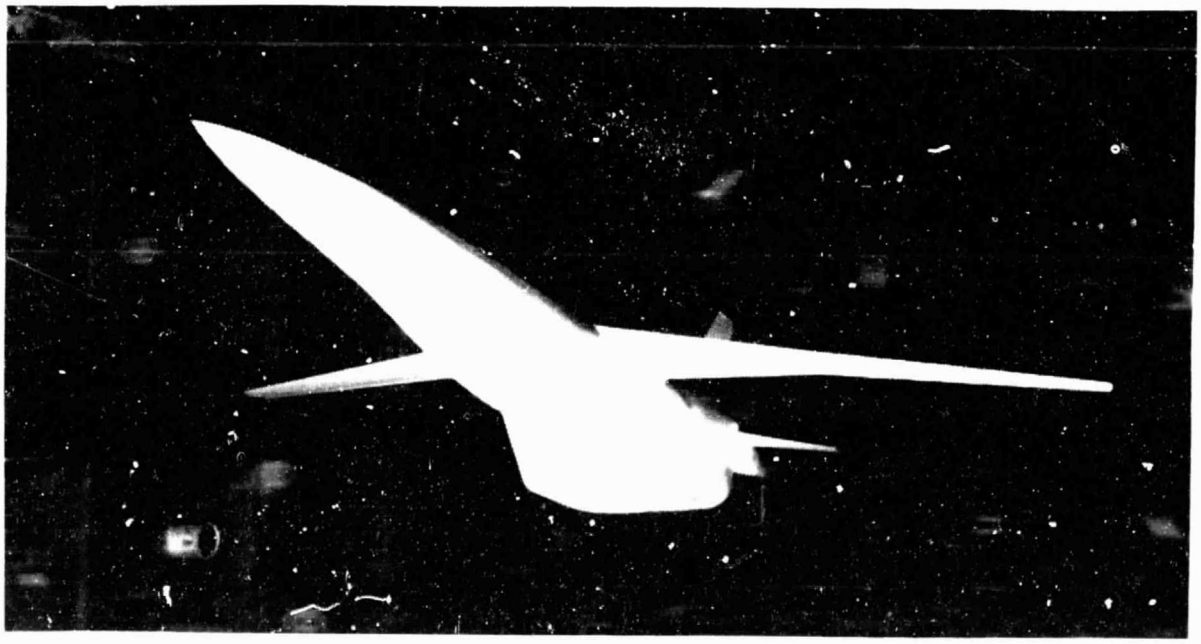

L-77-7505

(U) Figure 10.- Photographs of model configuration C. (U)

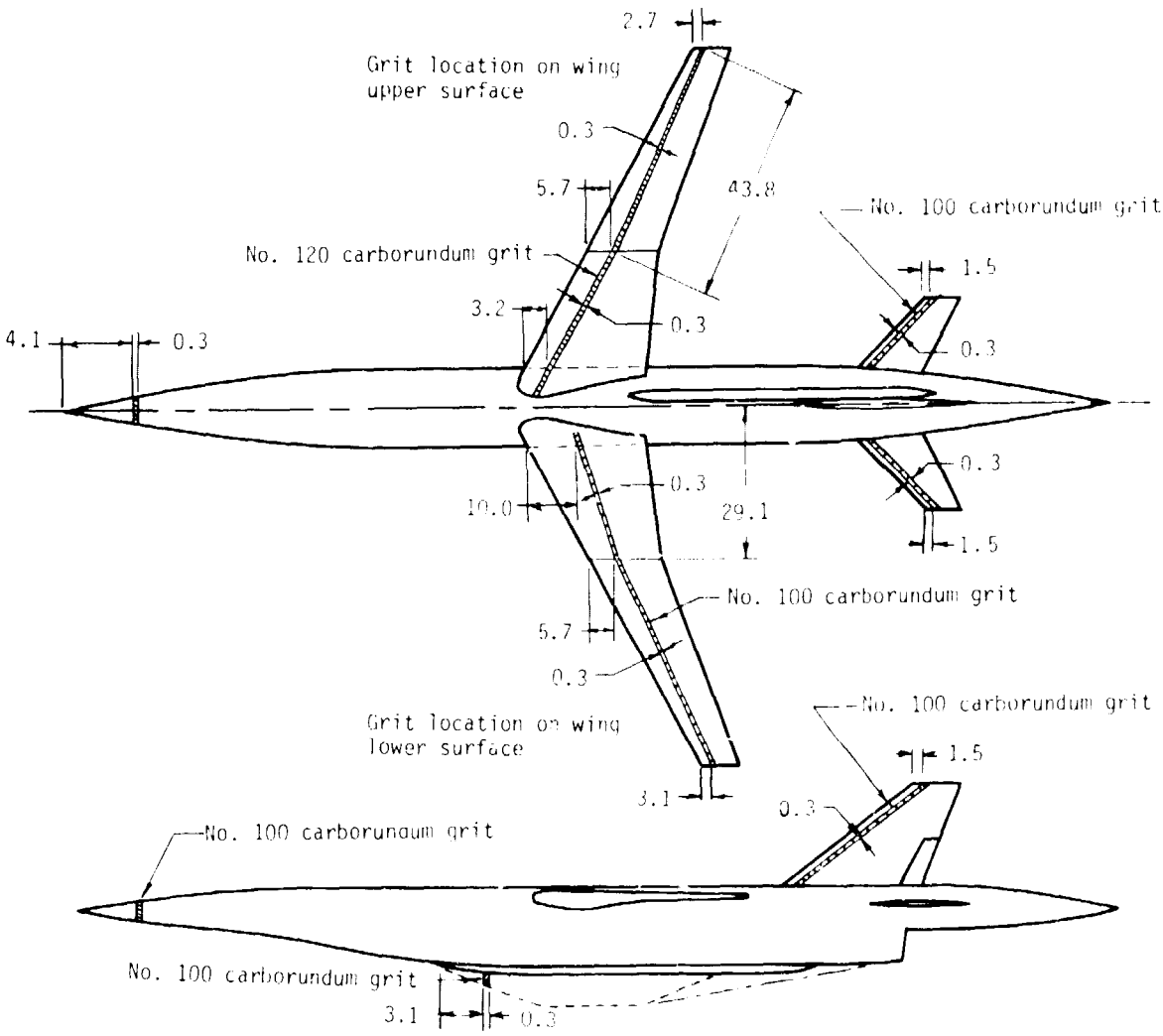

(C) Figure 11.- Model carborundum grit size and location. (Dimensions are in centimeters.) (U)

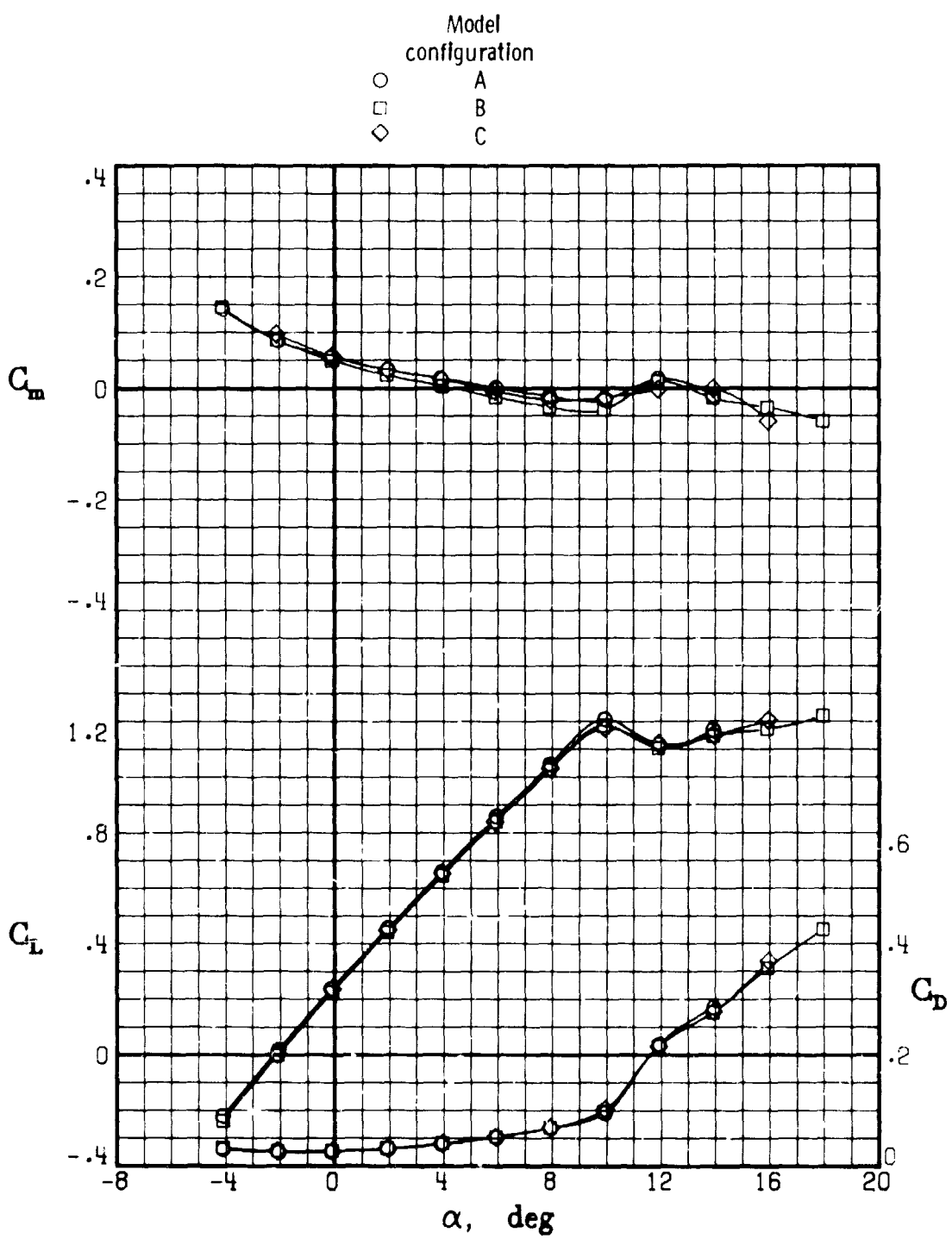

(a) M = 0.300.

(C) Figure 12.- Effect of model configuration on longitudinal aerodynamic characteristics. $\beta = 0^o$; $\delta_e = 0^o$. (U)

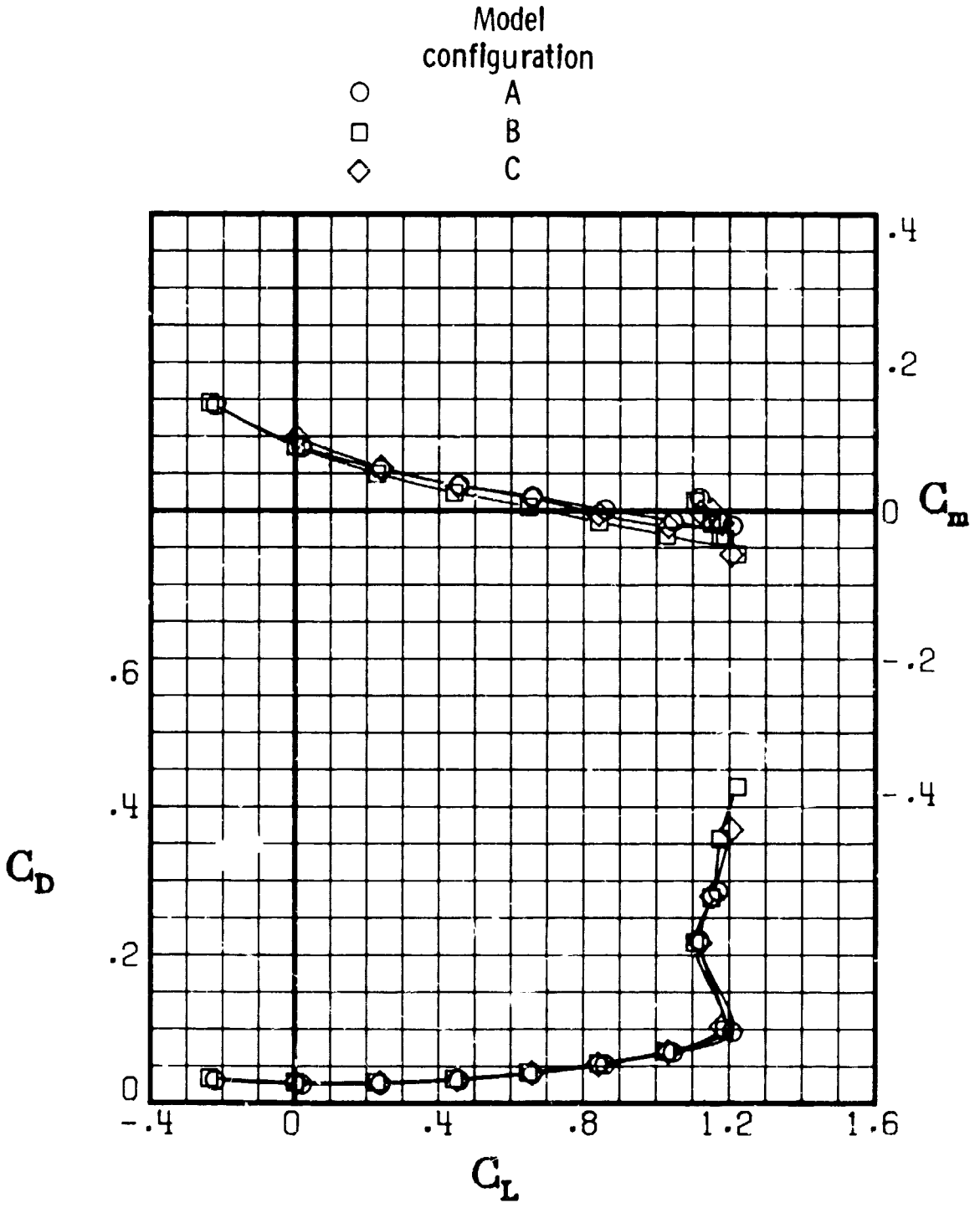

(a) Concluded.

(C) Figure 12.- Continued. (U)

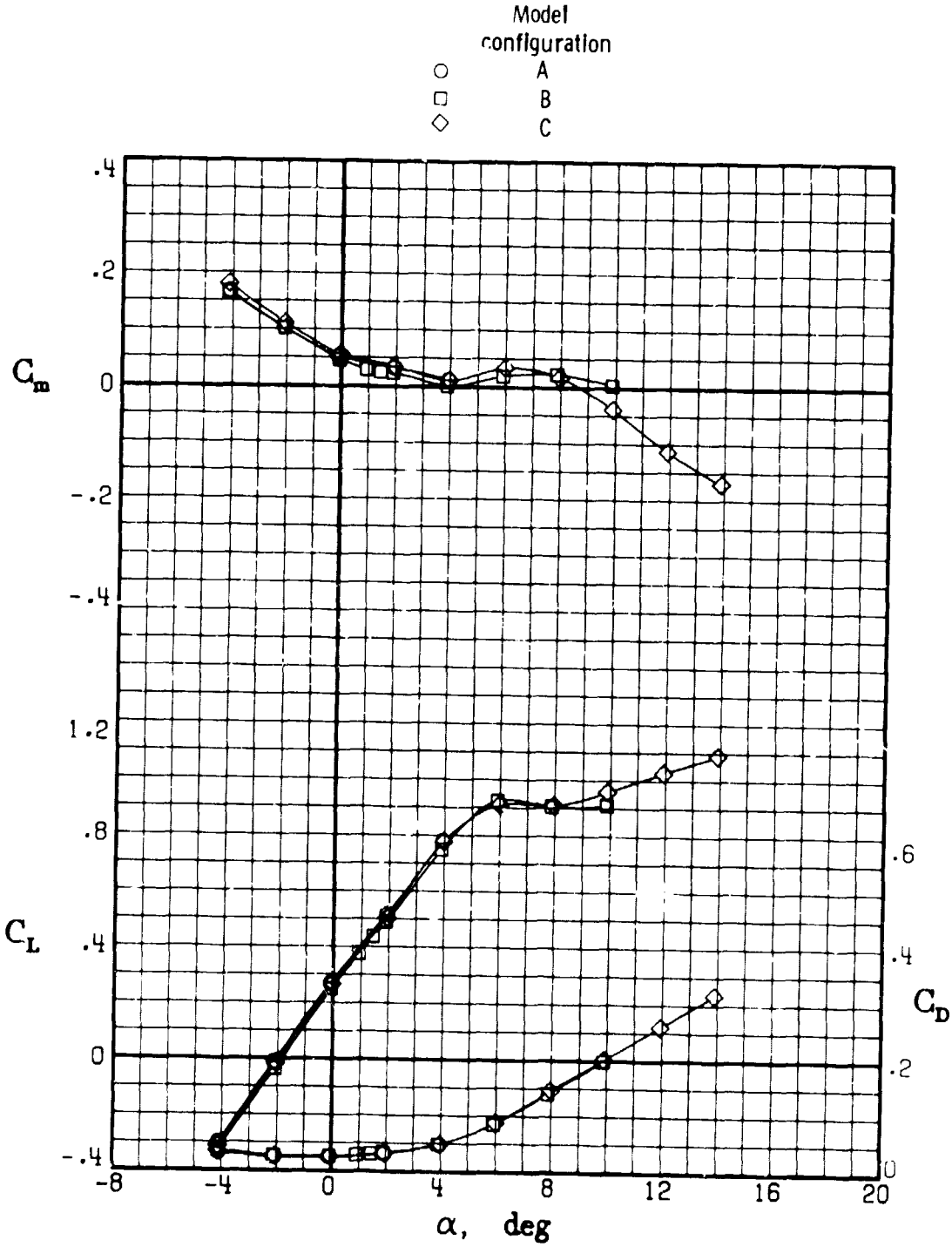

(b) M = 0.700.

Figure 12.- Continued. (U)

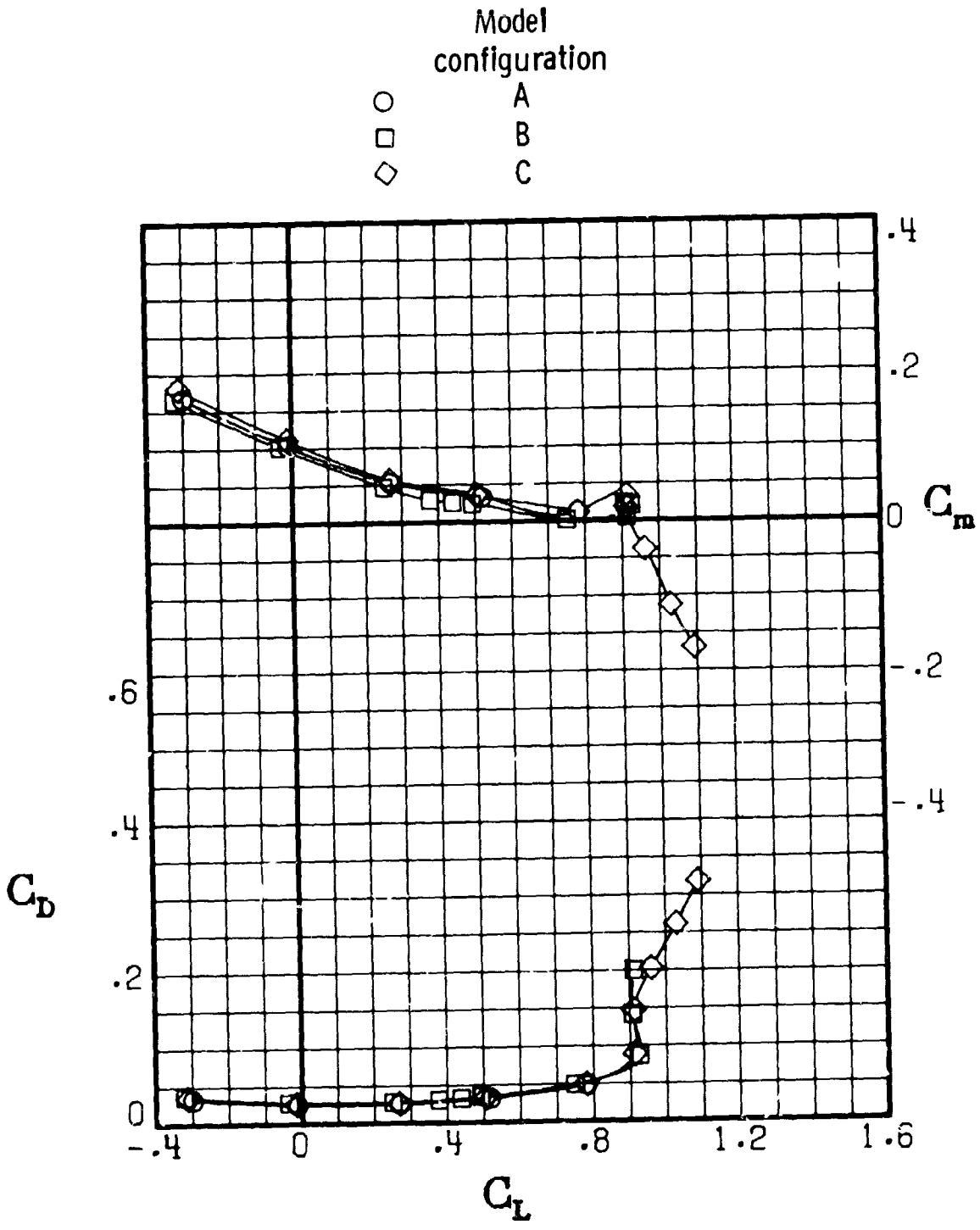

(b) Concluded.

Figure 12.- Continued. (U)

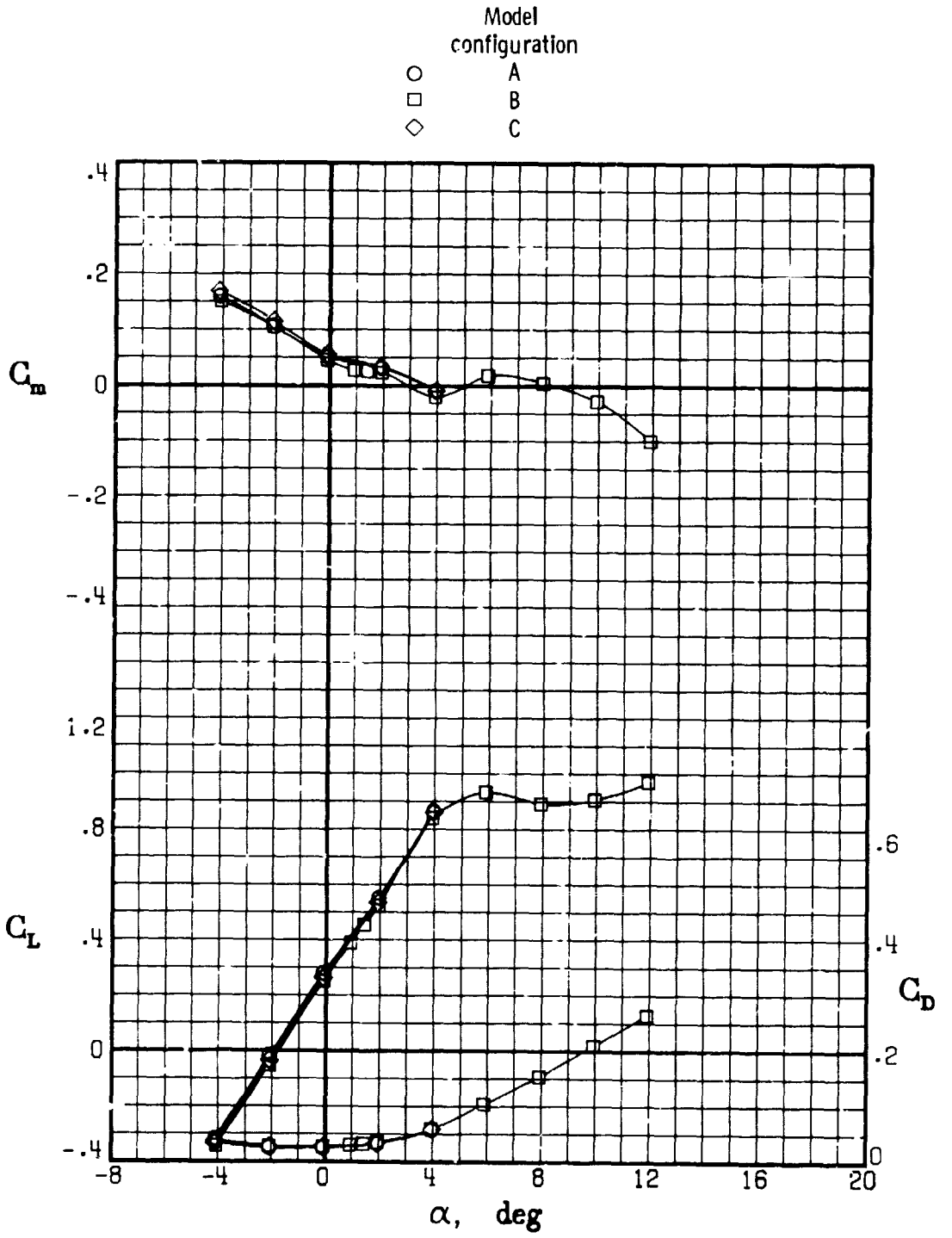

(c) M = 0.750.

Figure 12.- Continued. (U)

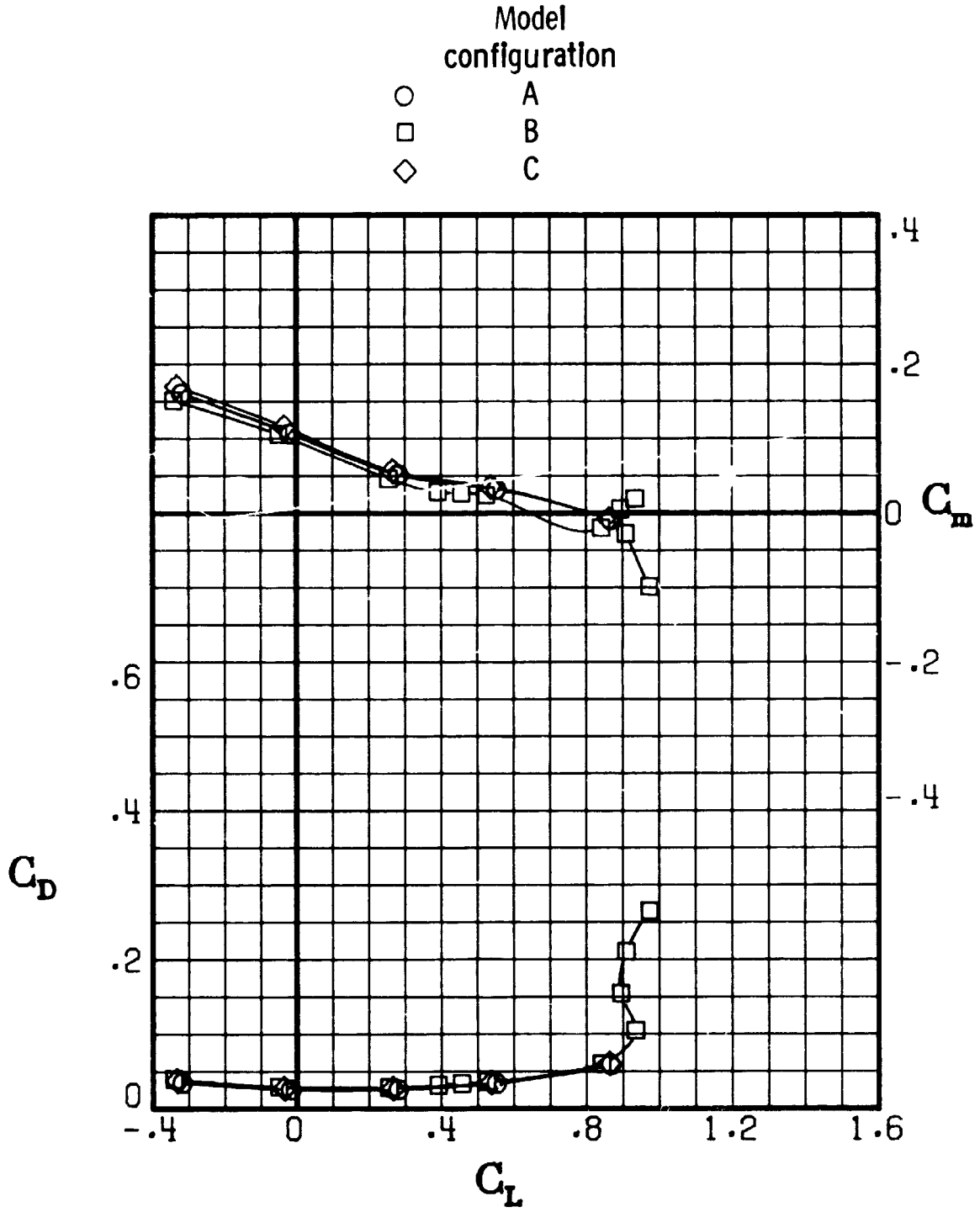

(c) Concluded.

Figure 12.- Continued. (U)

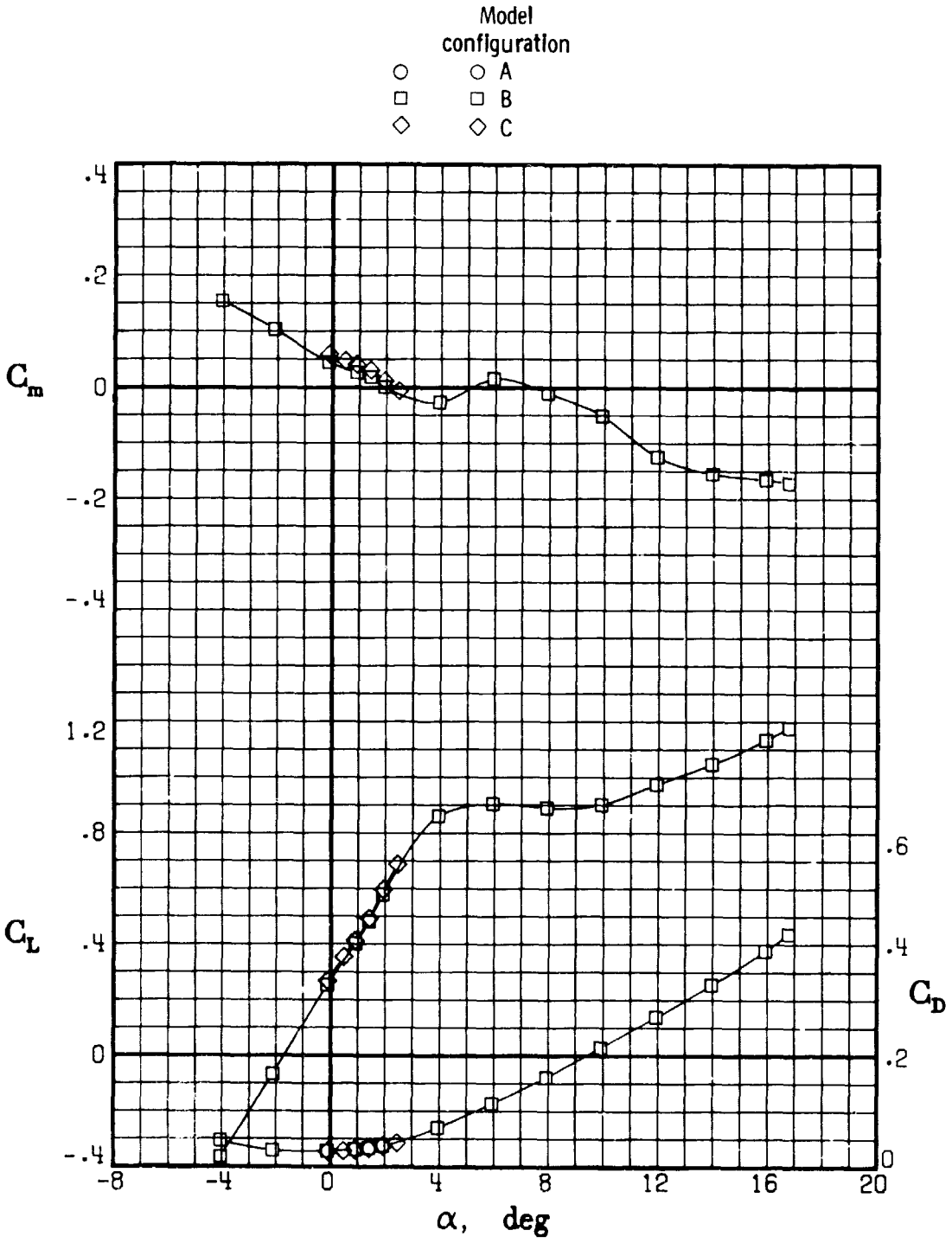

(d) M = 0.780.

(C) Figure 12.- Continued. (U)

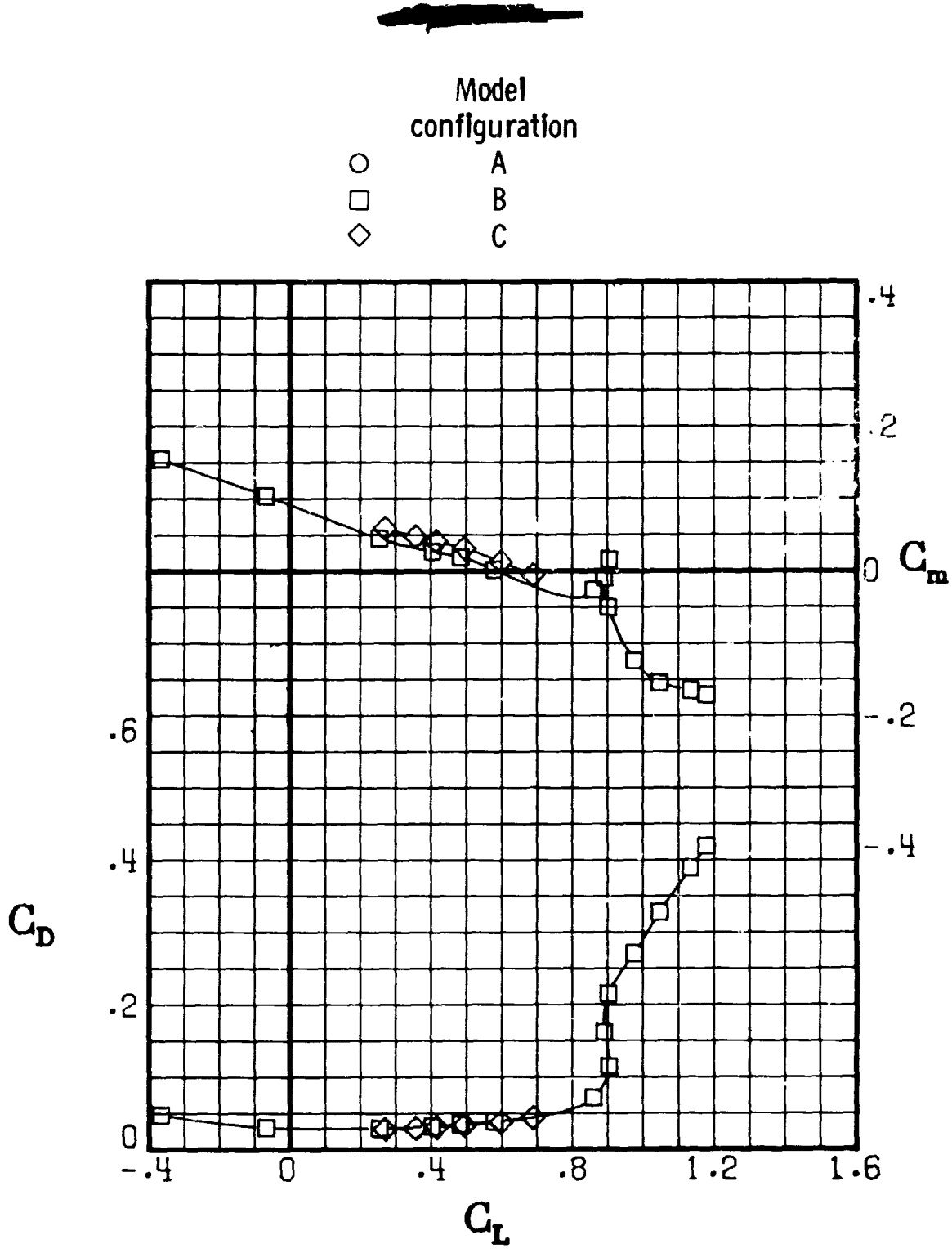

(d) Concluded.

(C) Figure 12.- Continued. (U)

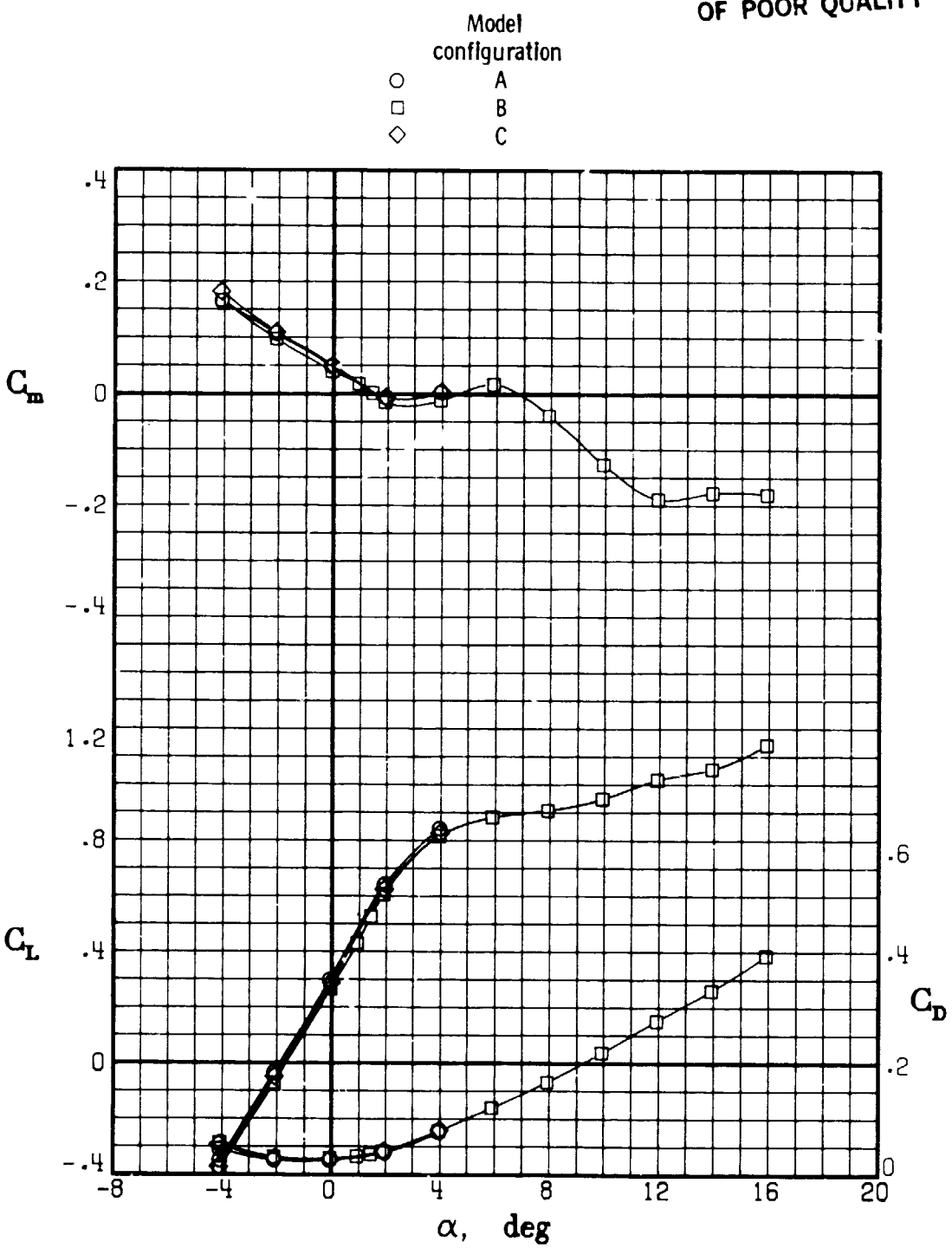

(e) M = 0.800.

Figure 12.- Continued. (U)

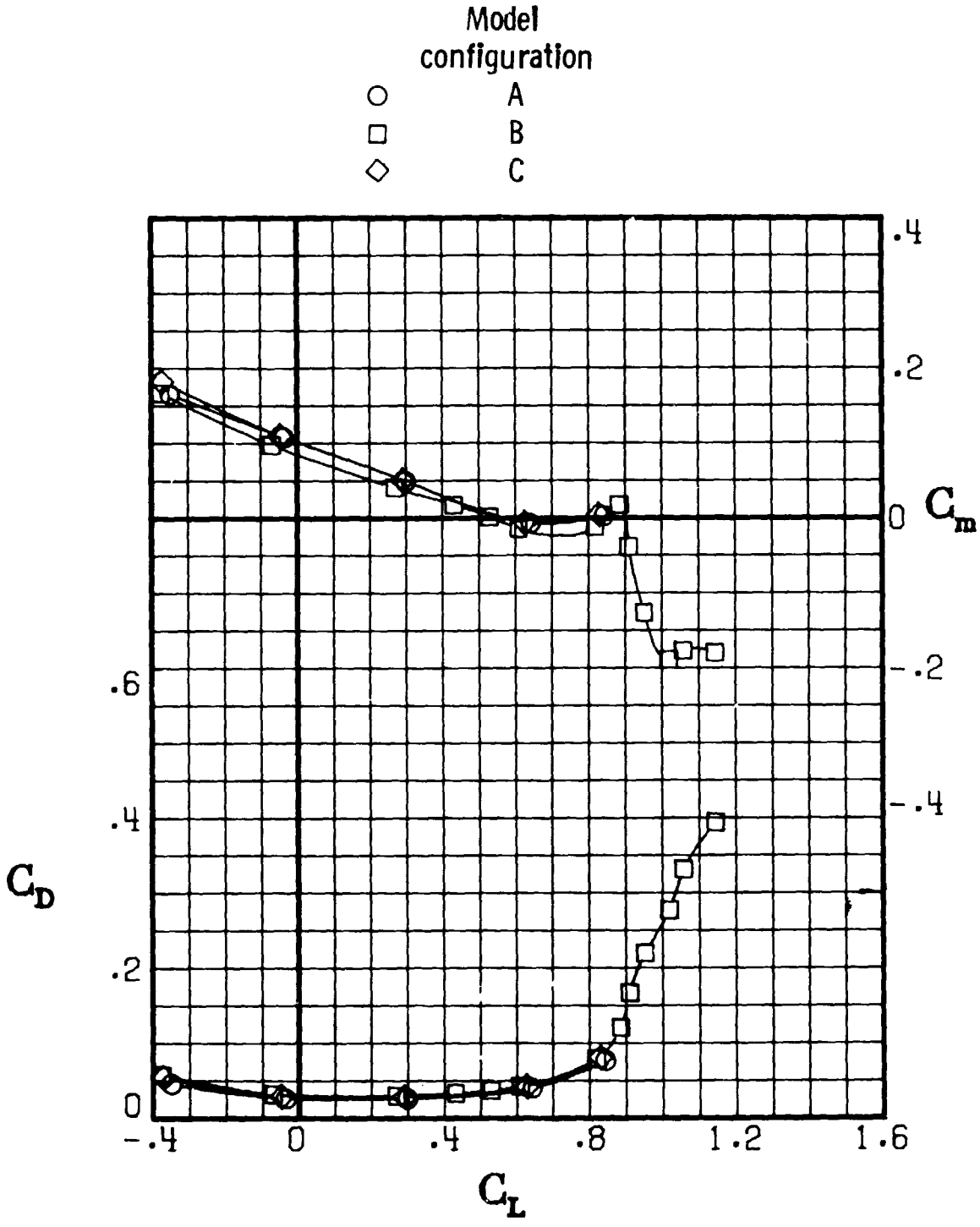

(e) Concluded.

Figure 12.- Continued. (U)

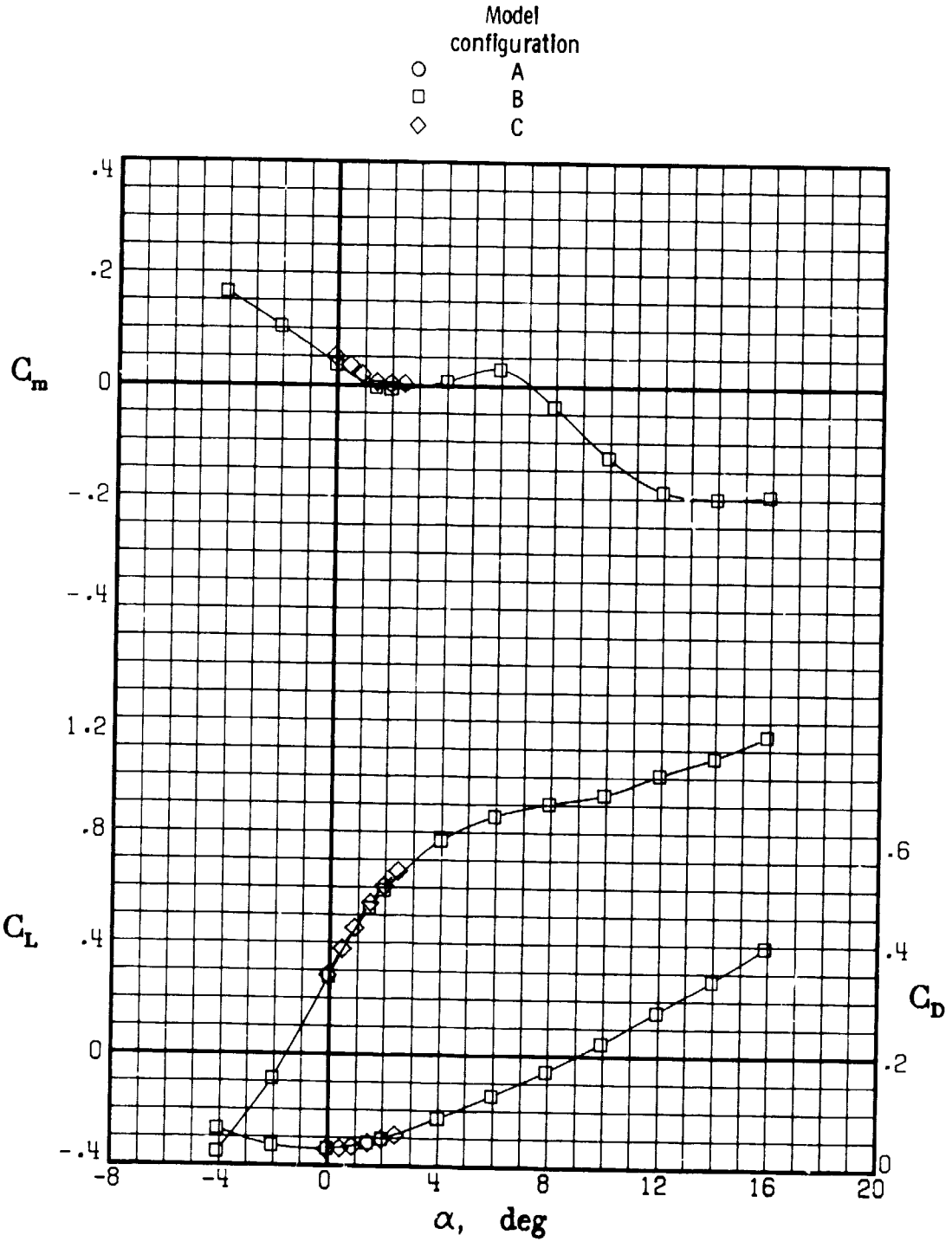

(f) M = 0.820.

Figure 12.- Continued. (U)

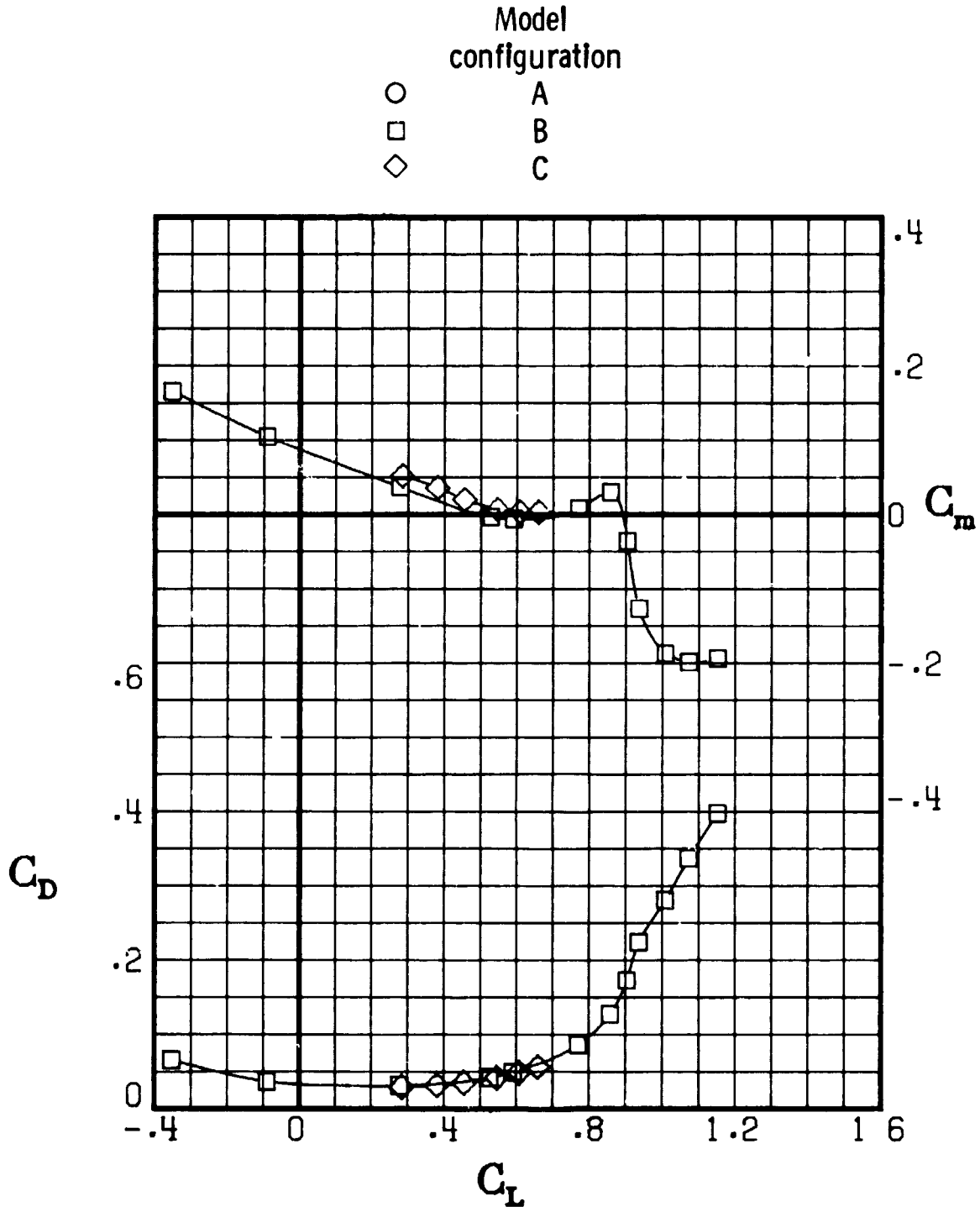

(f) Concluded.

Figure 12.- Continued. (U)

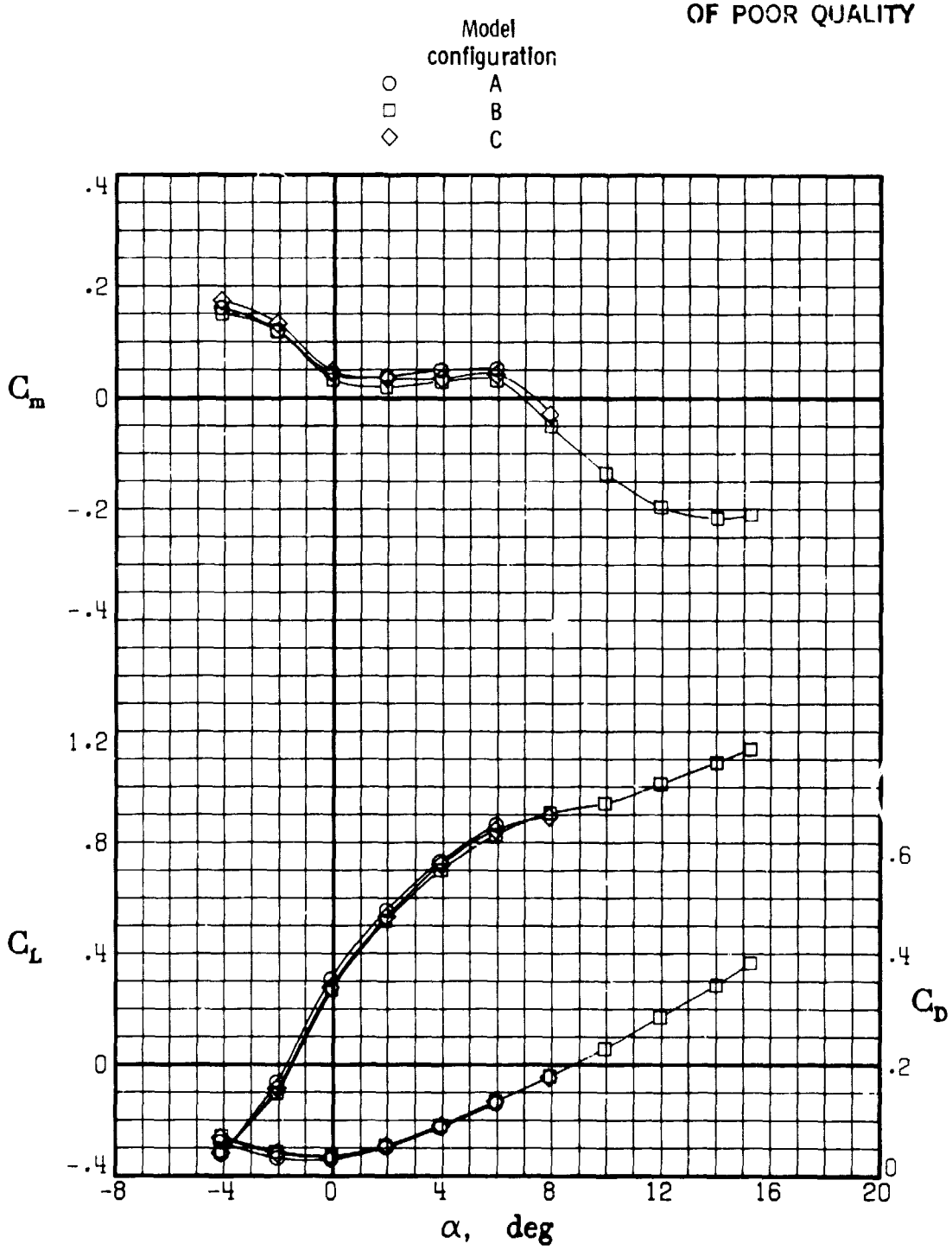

(g) M = 0.840.

Figure 12.- Continued. (U)

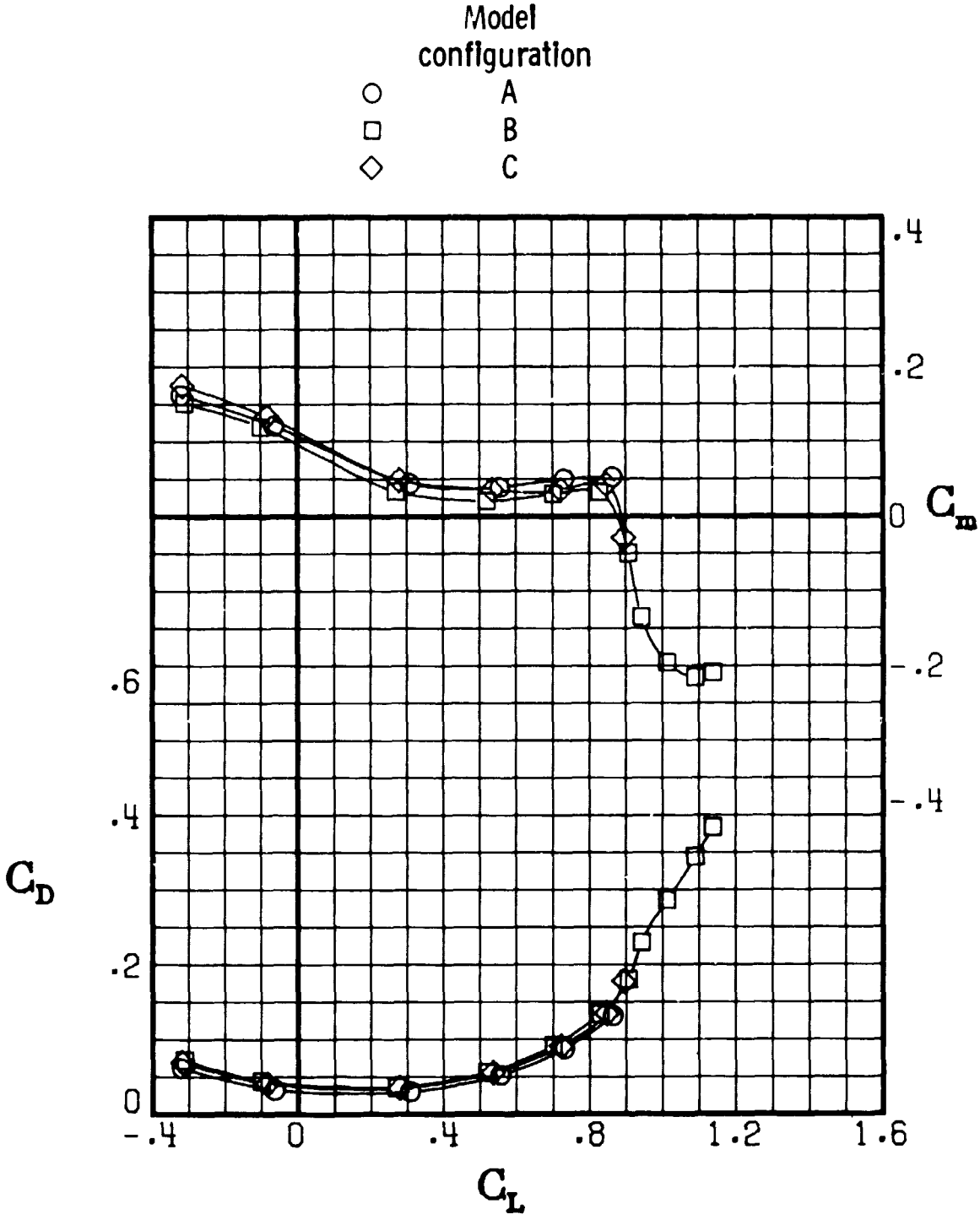

(g) Concluded.

Figure 12.- Continued. (U)

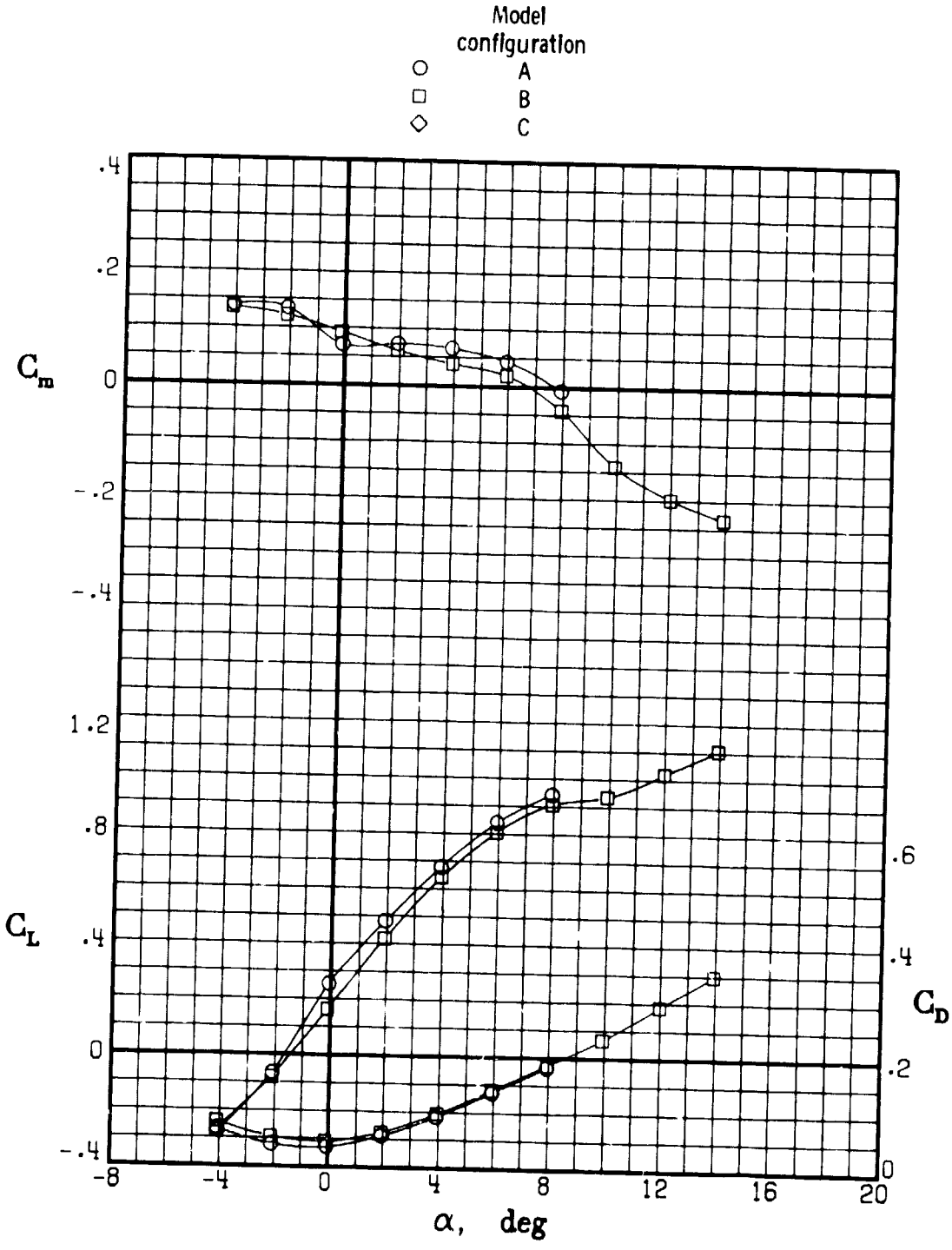

(h) M = 0.860.

Figure 12.- Continued. (u)

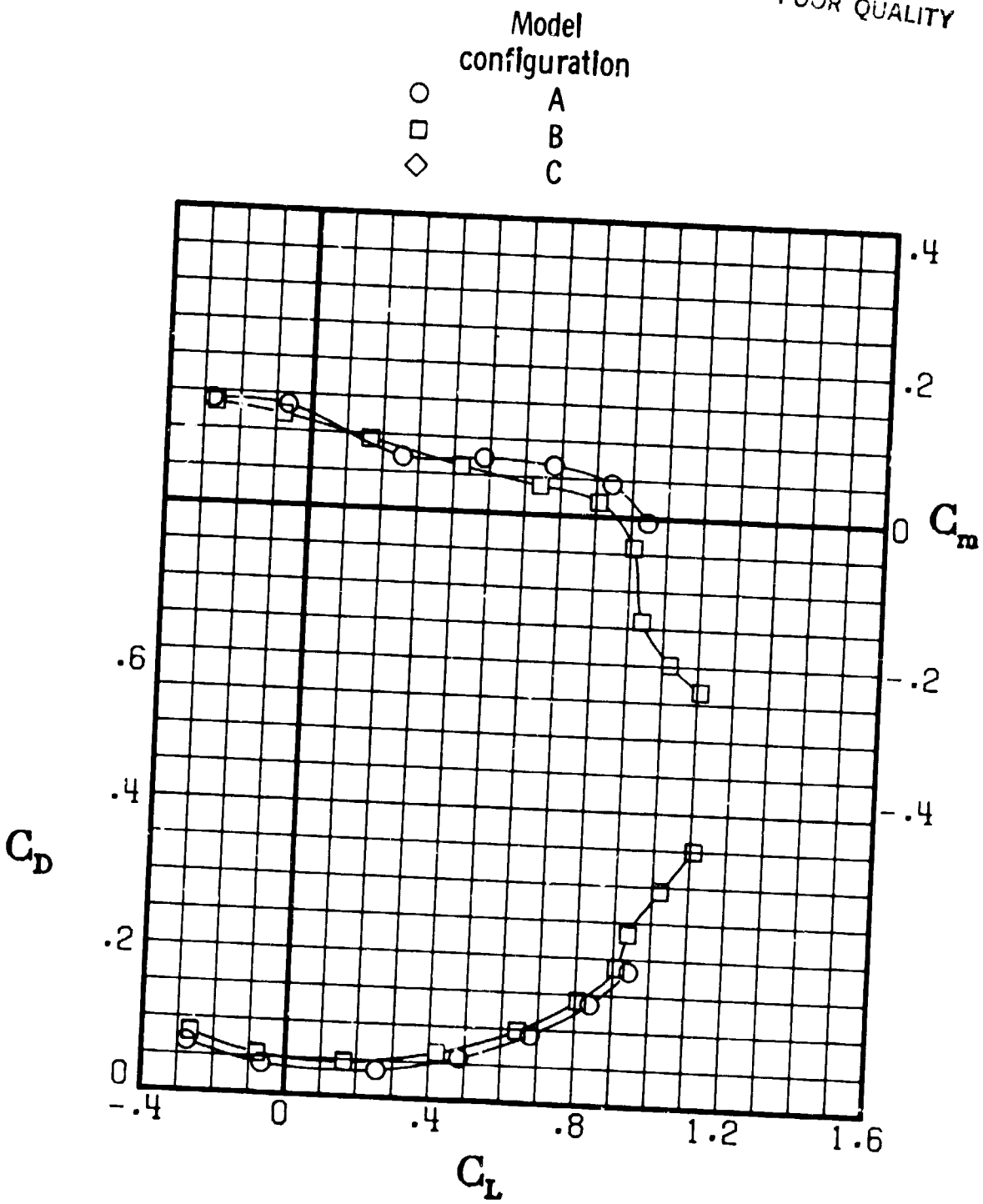

(h) Concluded.

Figure 12.- Continued.

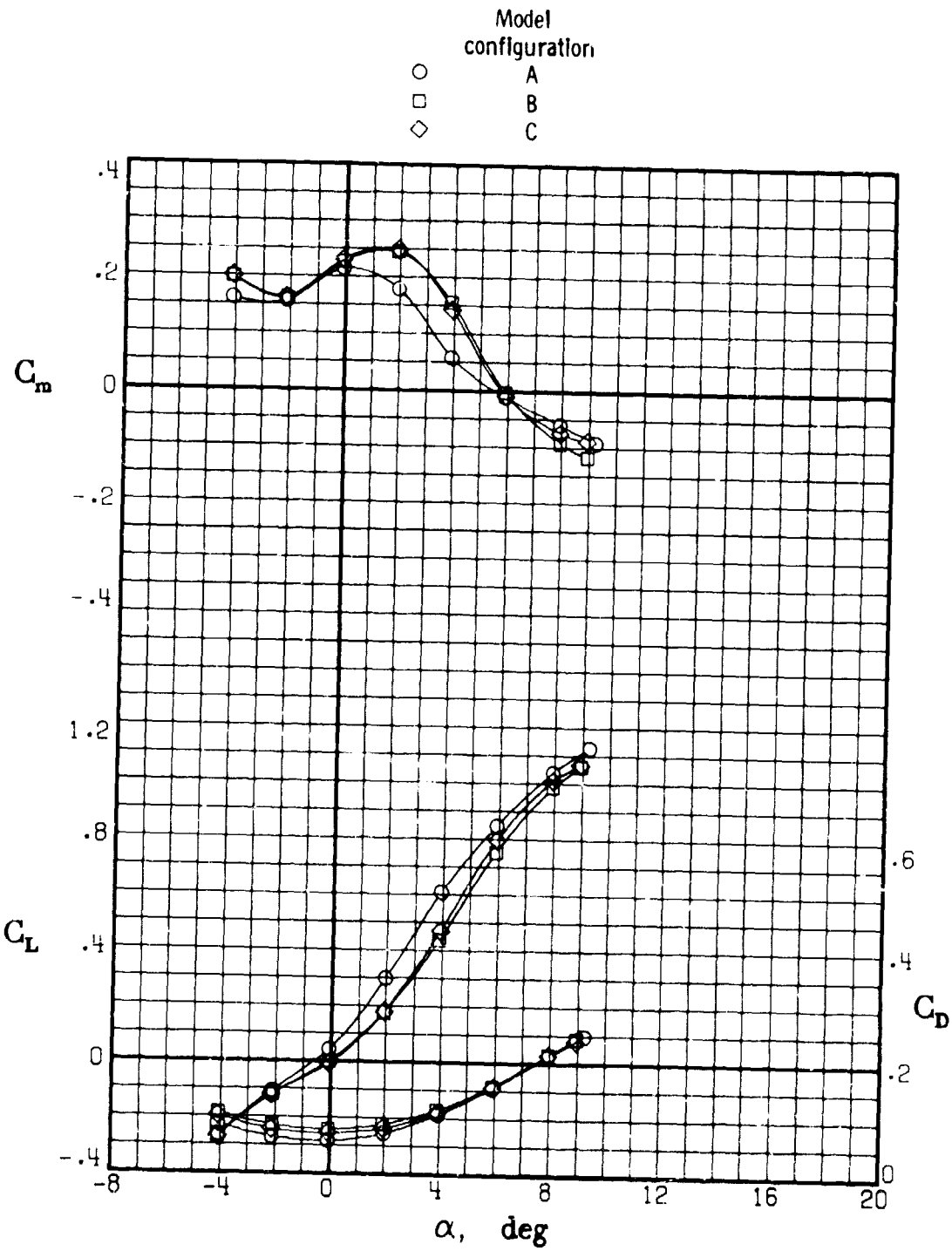

(i) M = 0.900.

Figure 12.- Continued. (U)

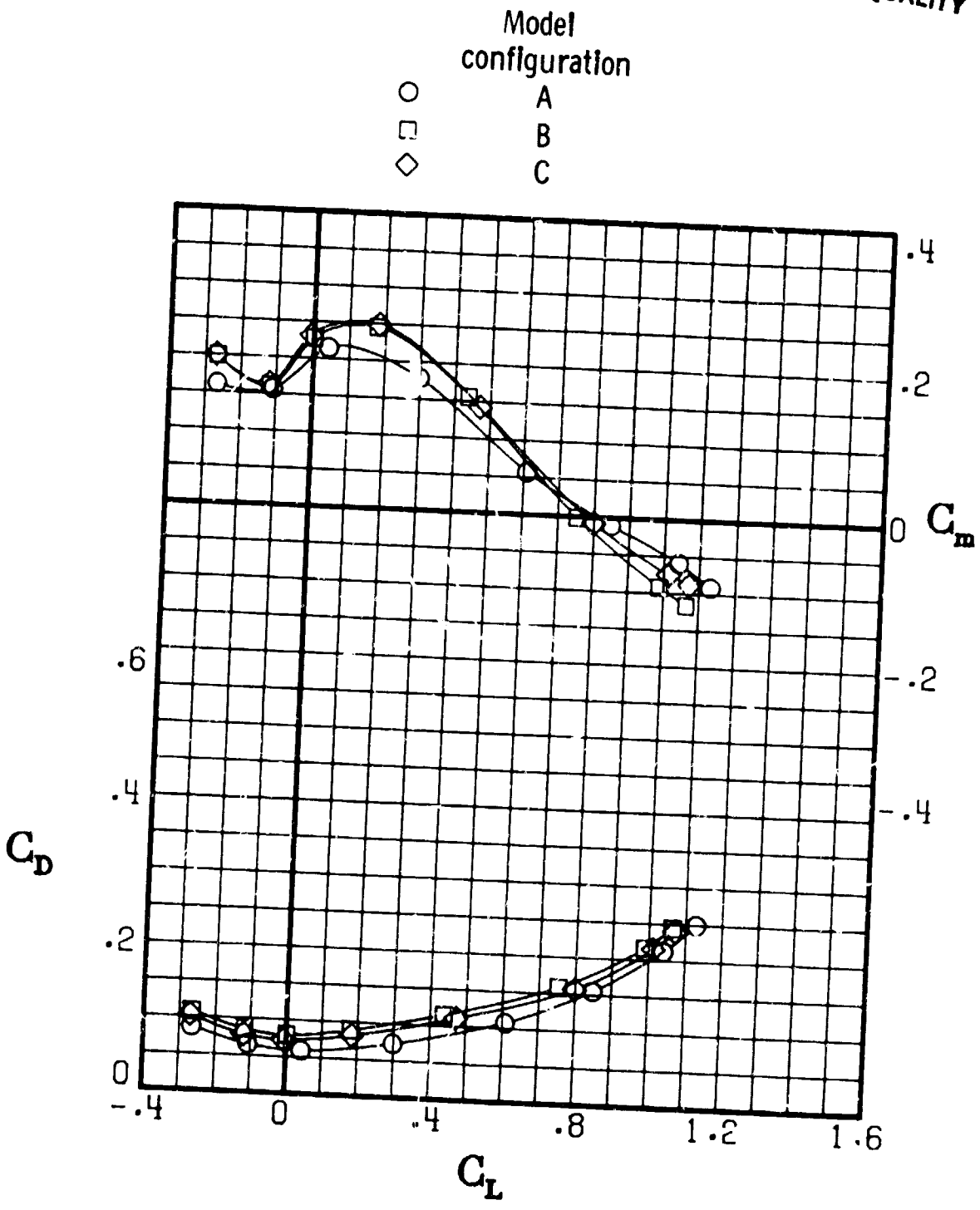

(i) Concluded.

Figure 12.- Continued. (U)

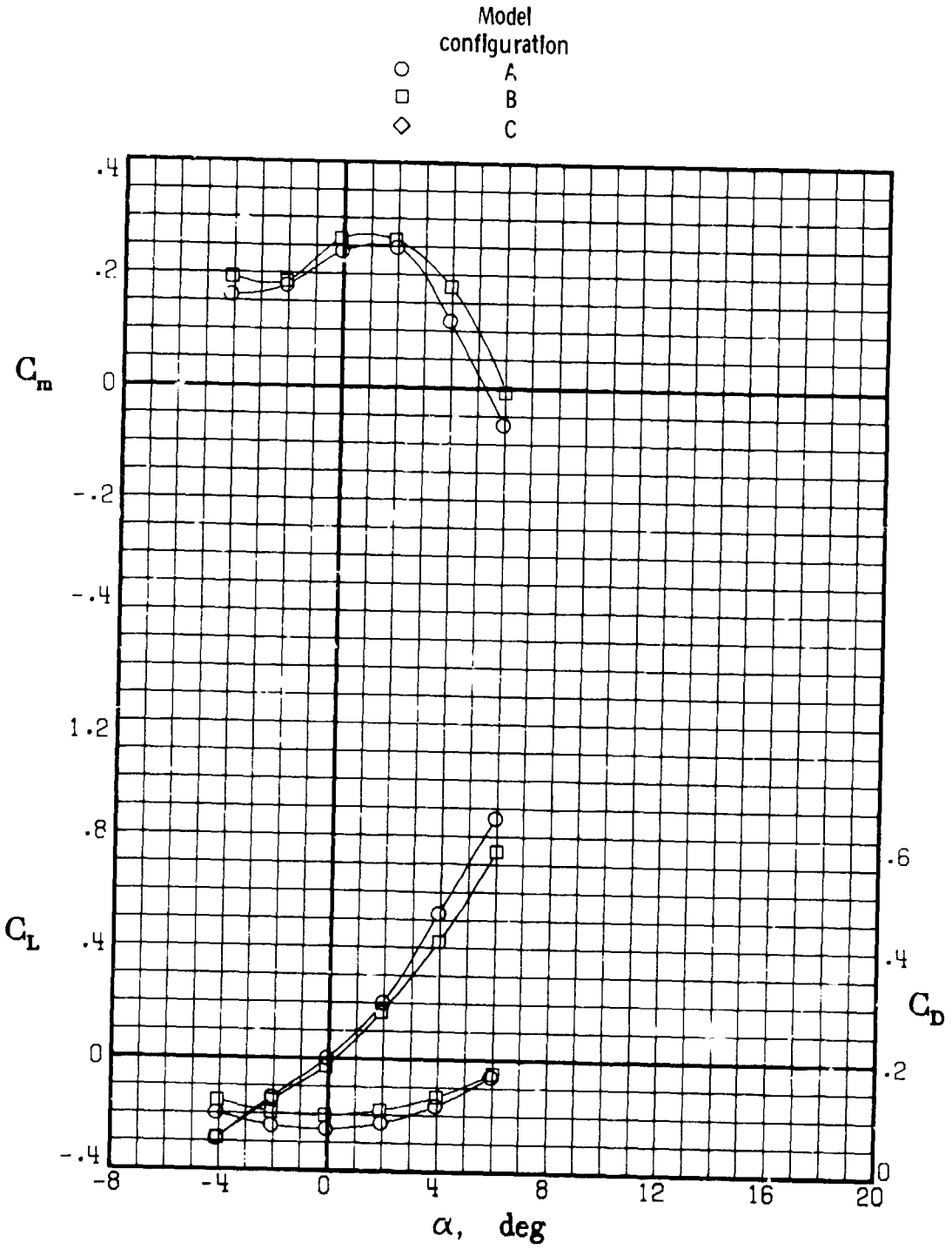

(j) M = 0.920.

Figure 12.- Continued. (U)

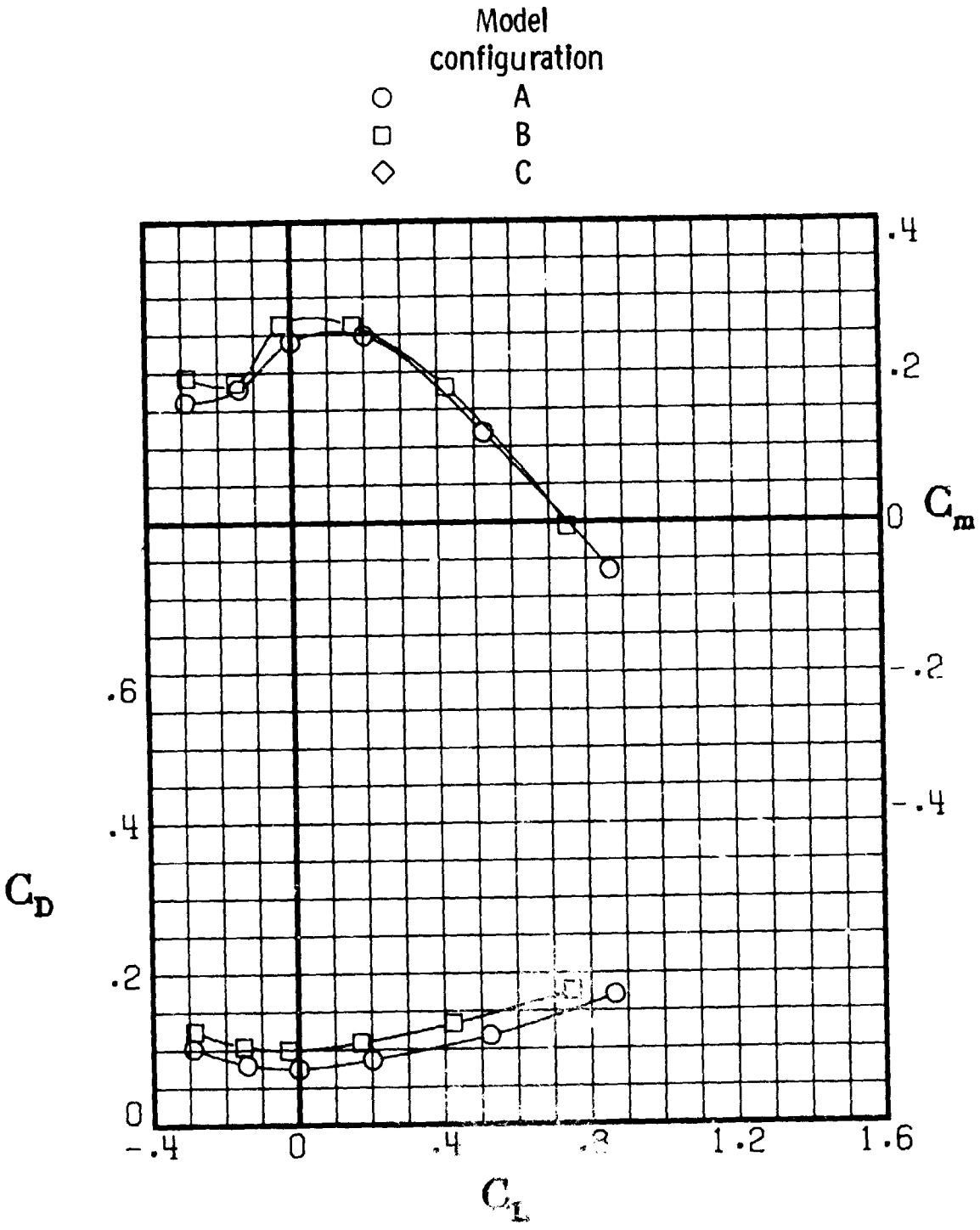

(j) Concluded.

Figure 12.- Concluded. (U)

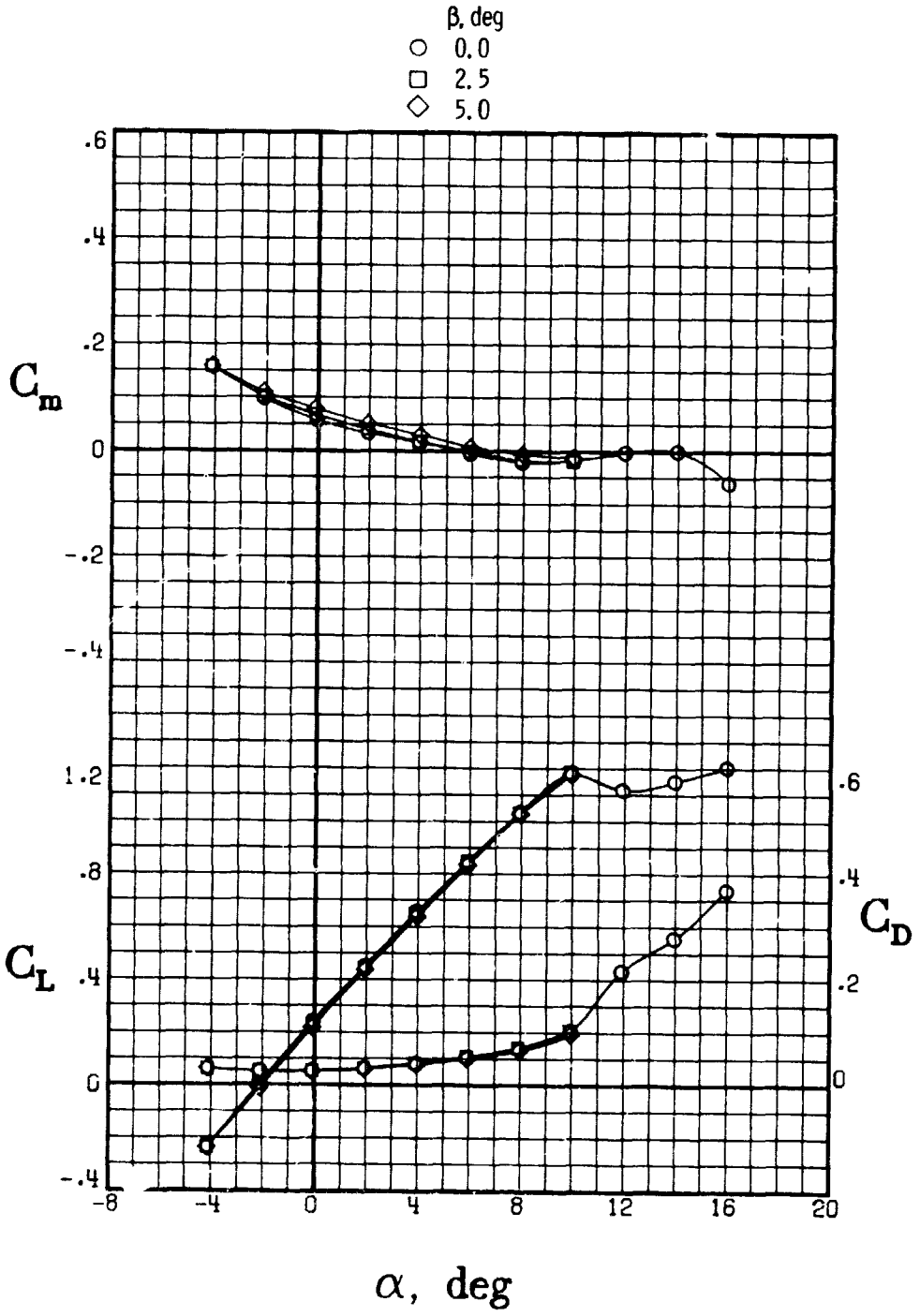

(a) M = 0.300.

Figure 13.- Effect of sideslip on longitudinal aerodynamic characteristics for model configuration C. $\delta_e = 0^o$. (U)

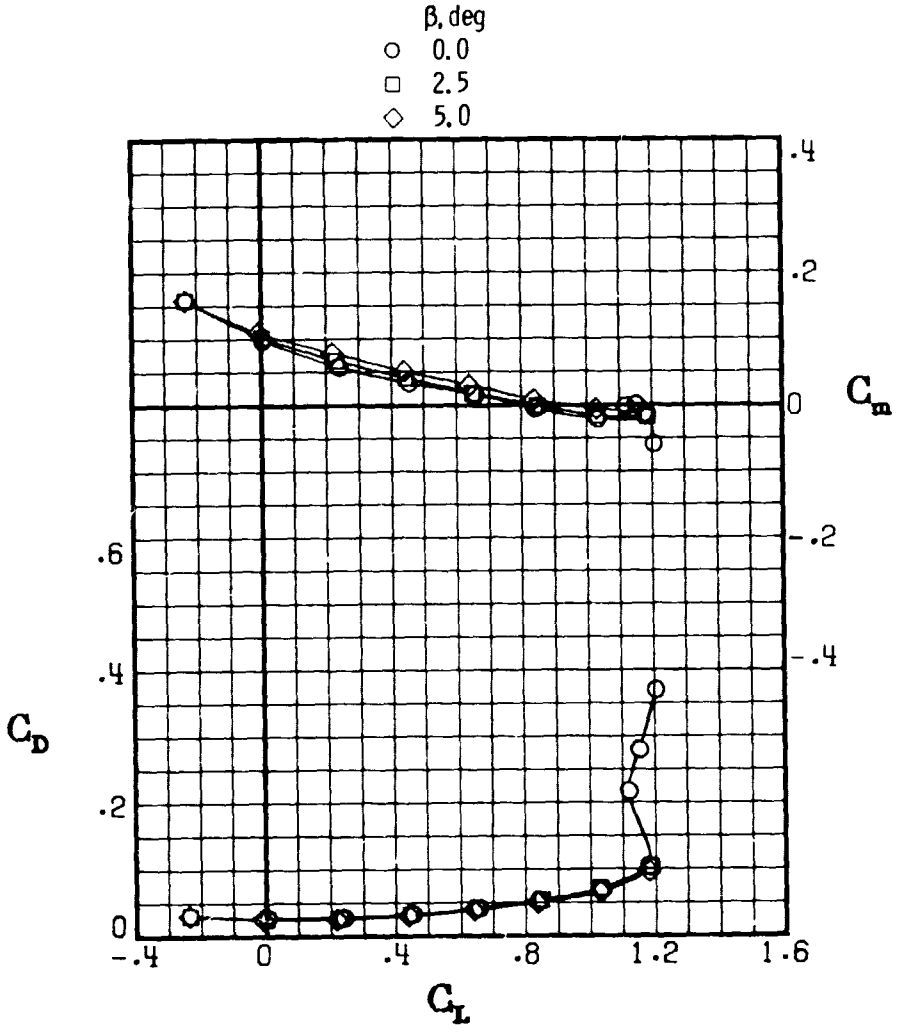

(a) Concluded.

Figure 13.- Continued. (U)

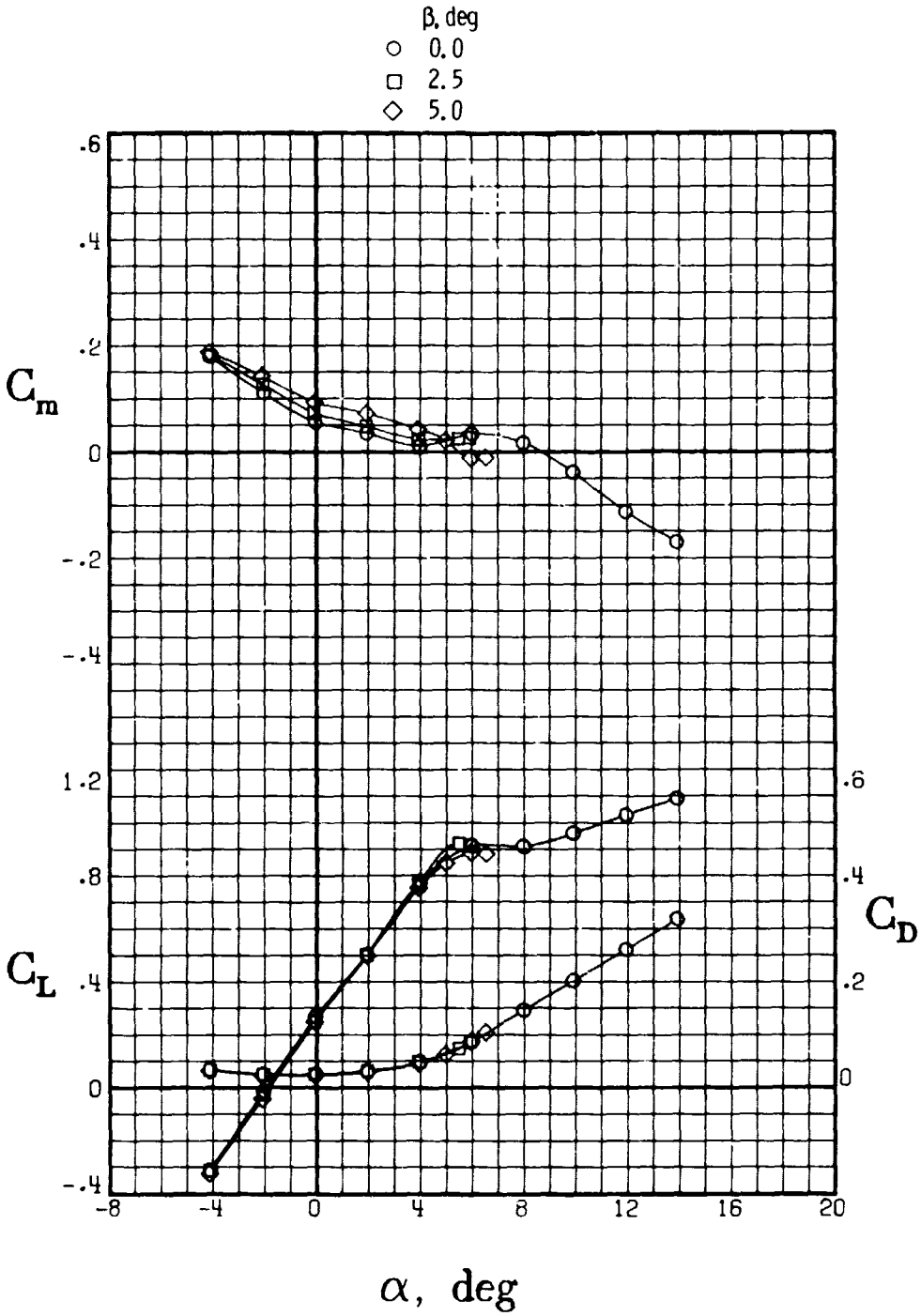

(b) M = 0.700.

Figure 13.- Continued. (U)

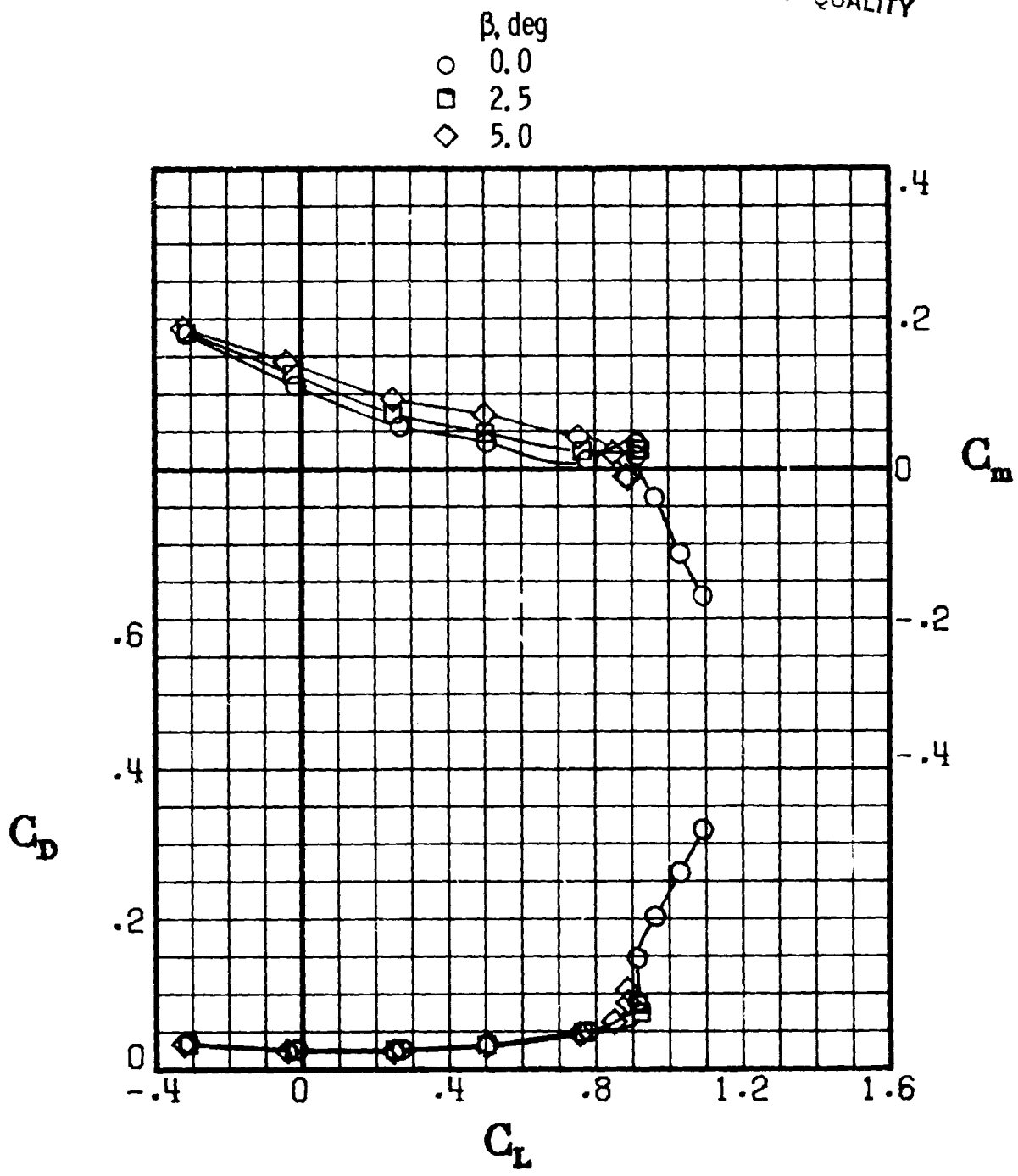

(b) Concluded.

Figure 13.- Continued. (U)

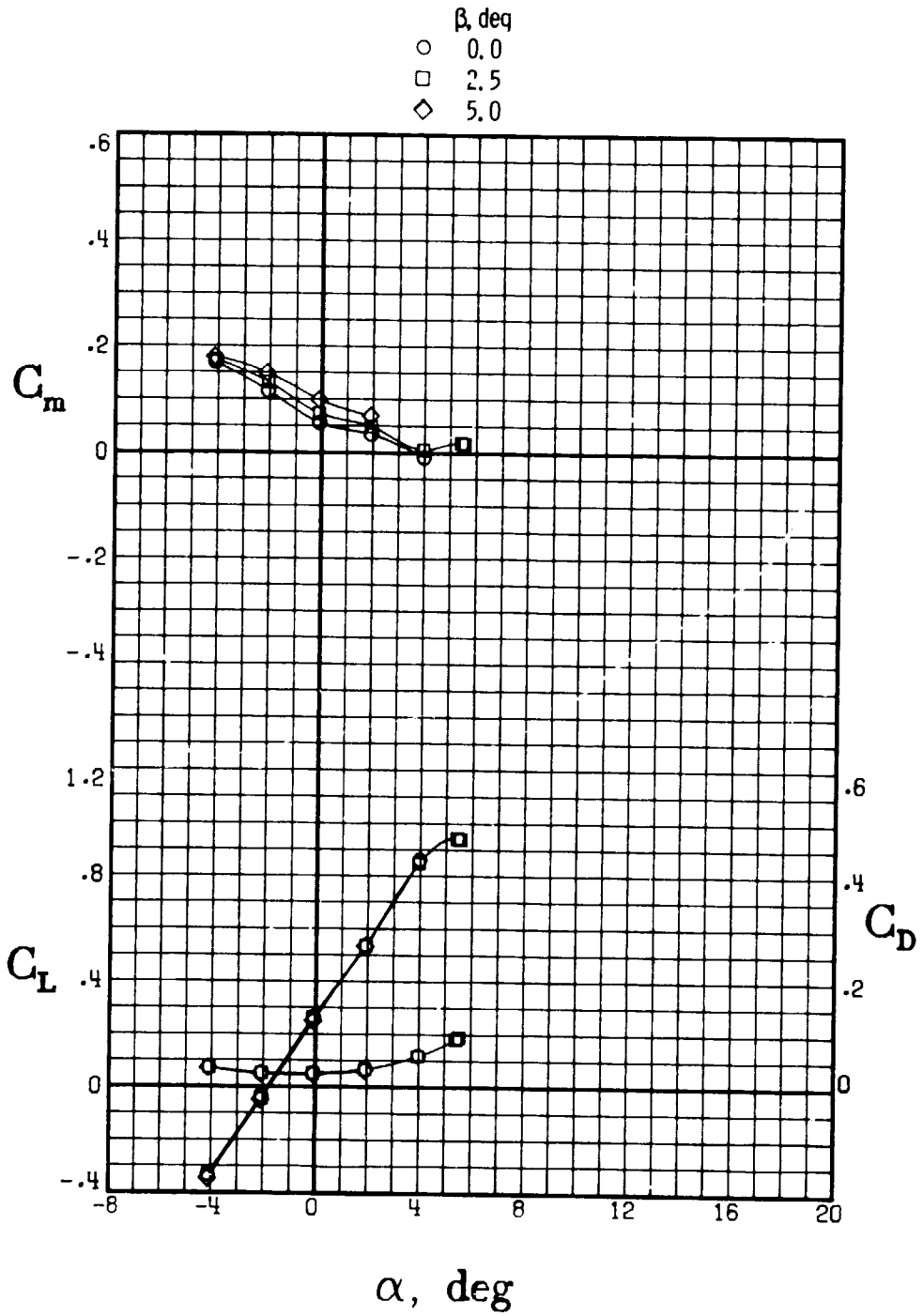

(c) M = 0.750.

Figure 13.- Continued. (U)

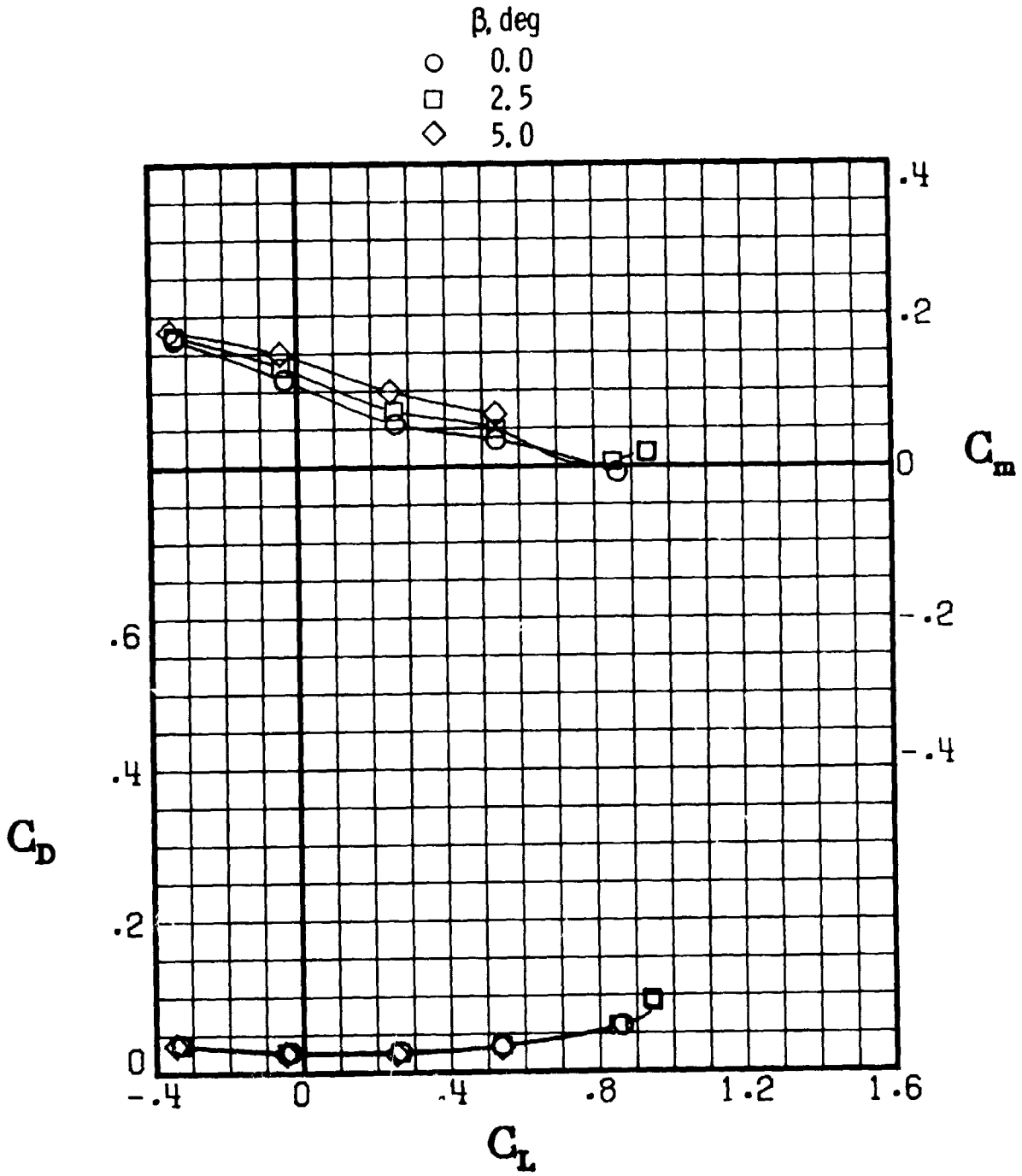

(c) Concluded.

Figure 13.- Continued. (U)

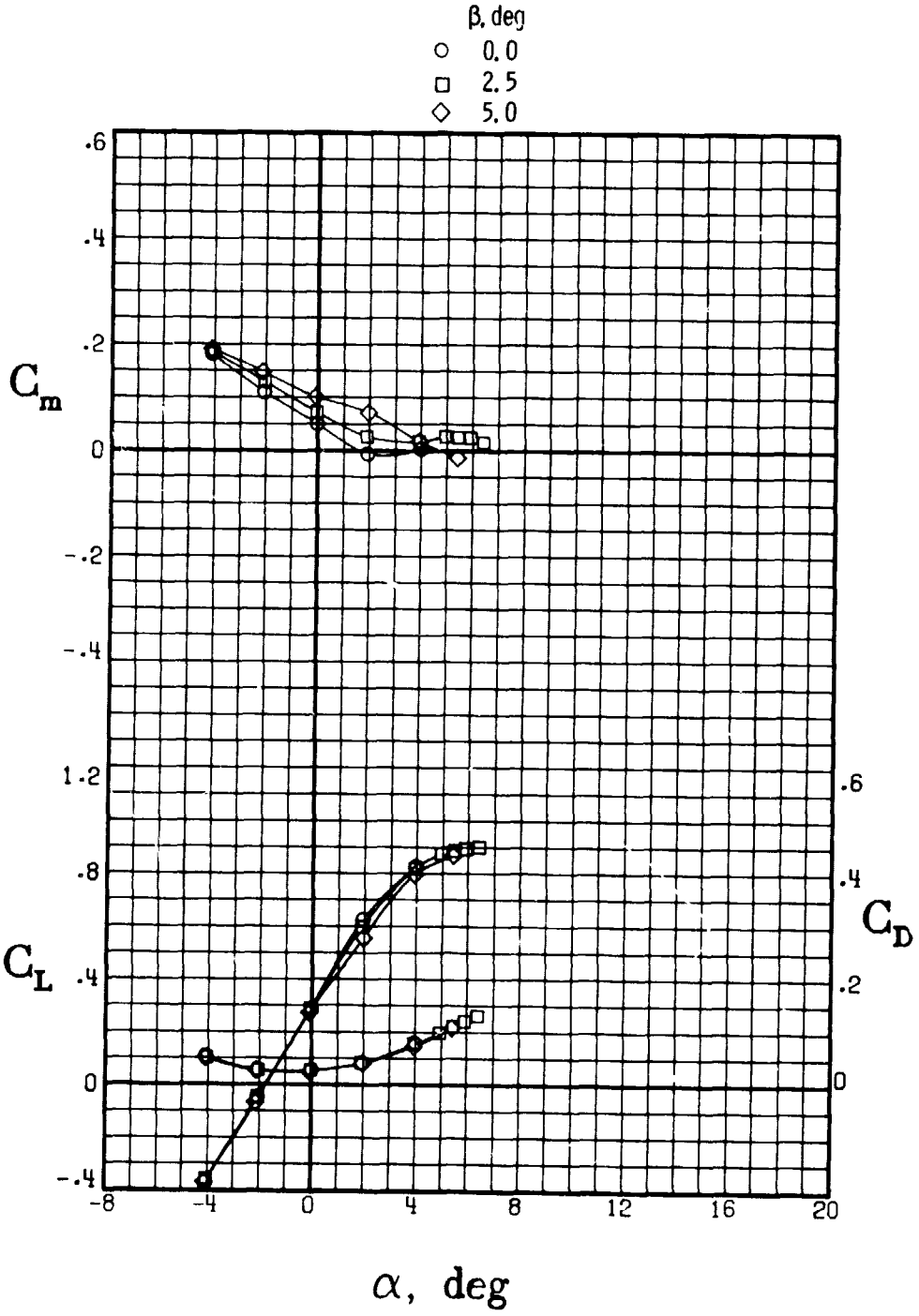

(d) M = 0.800.

Figure 13.- Continued. (U)

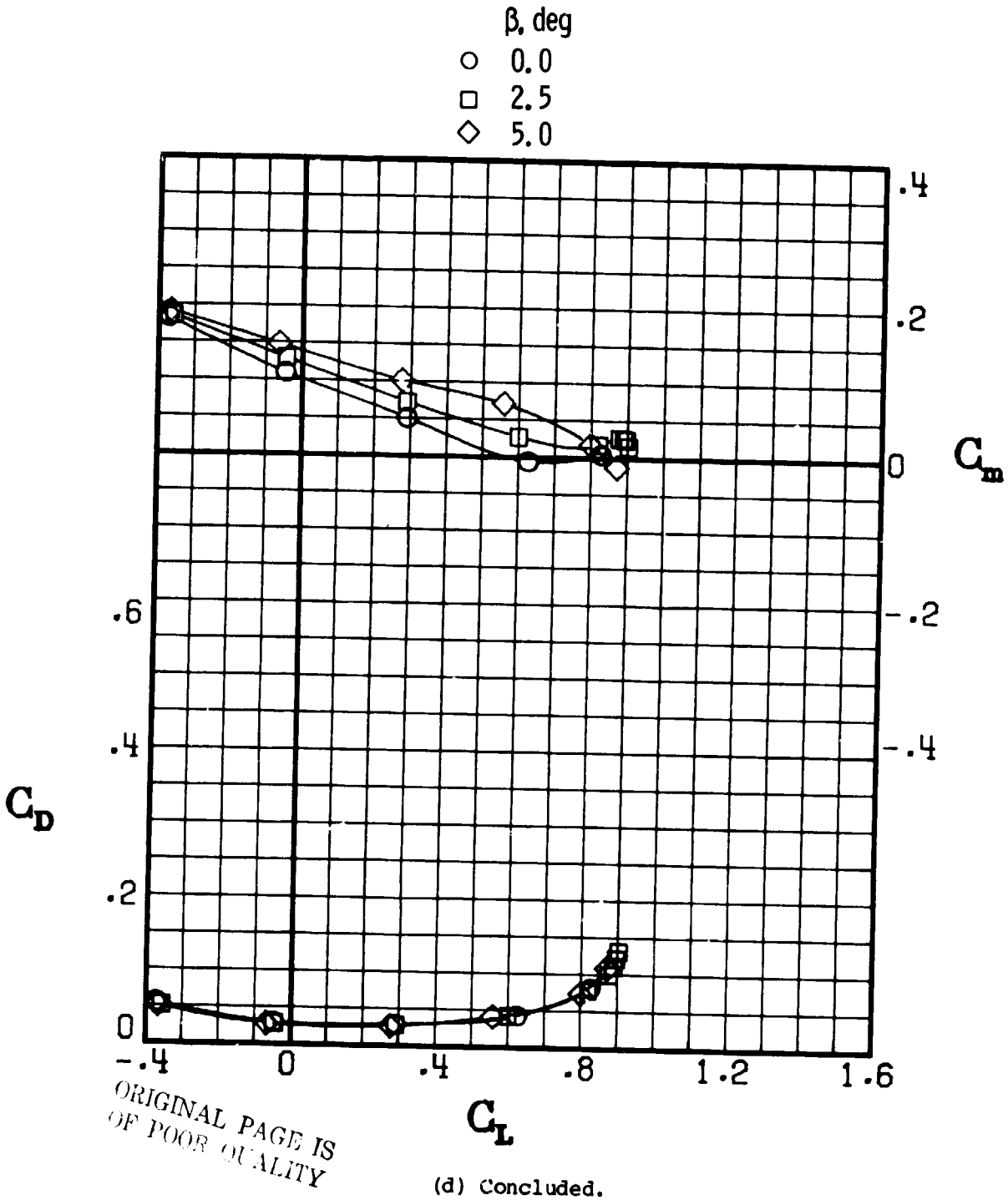

(d) Concluded.

Figure 13.- Continued. (U)

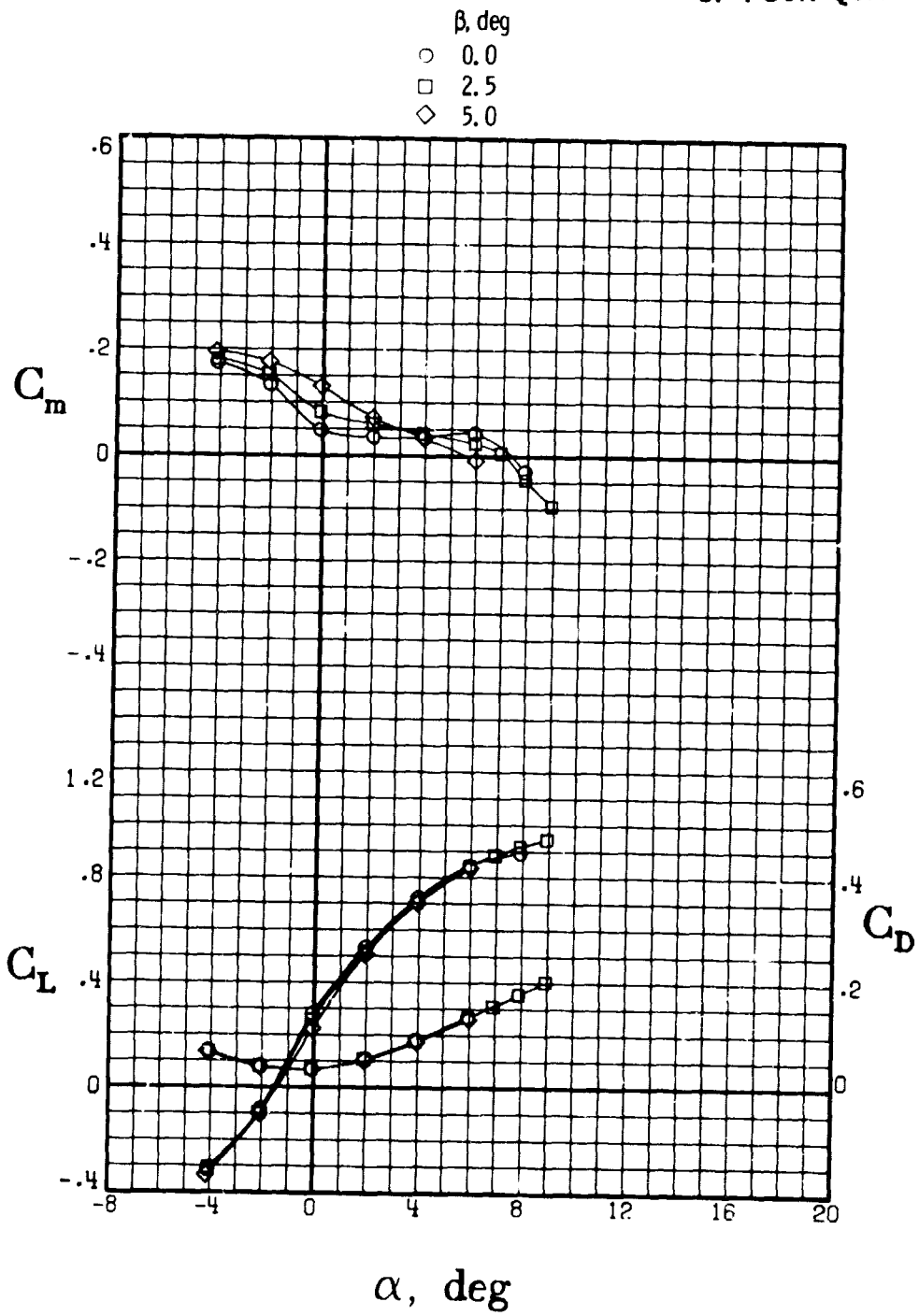

(e) M = 0.840.

(C) Figure 13.- Continued. (U)

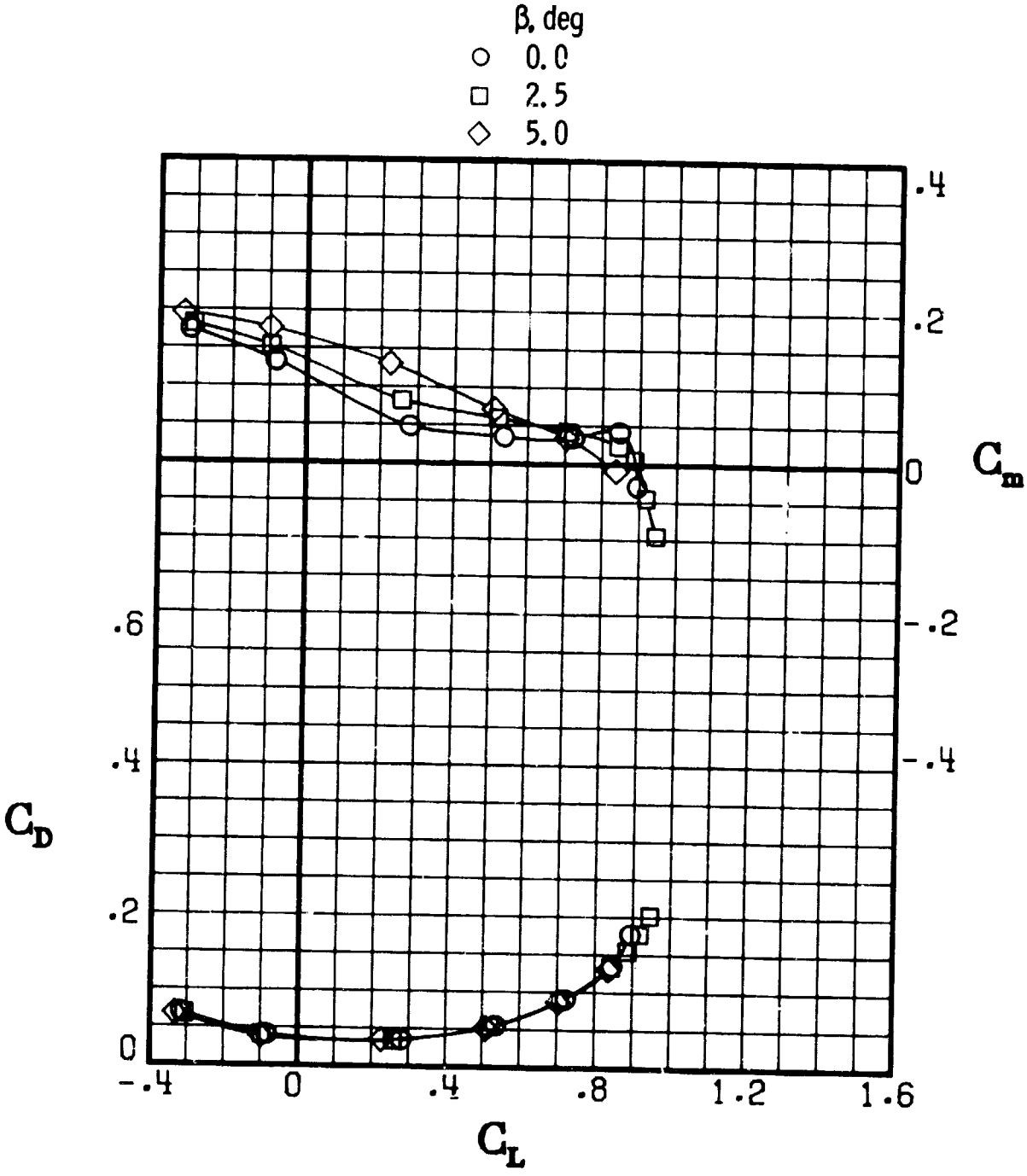

(e) Concluded.

Figure 13.- Continued. (U)

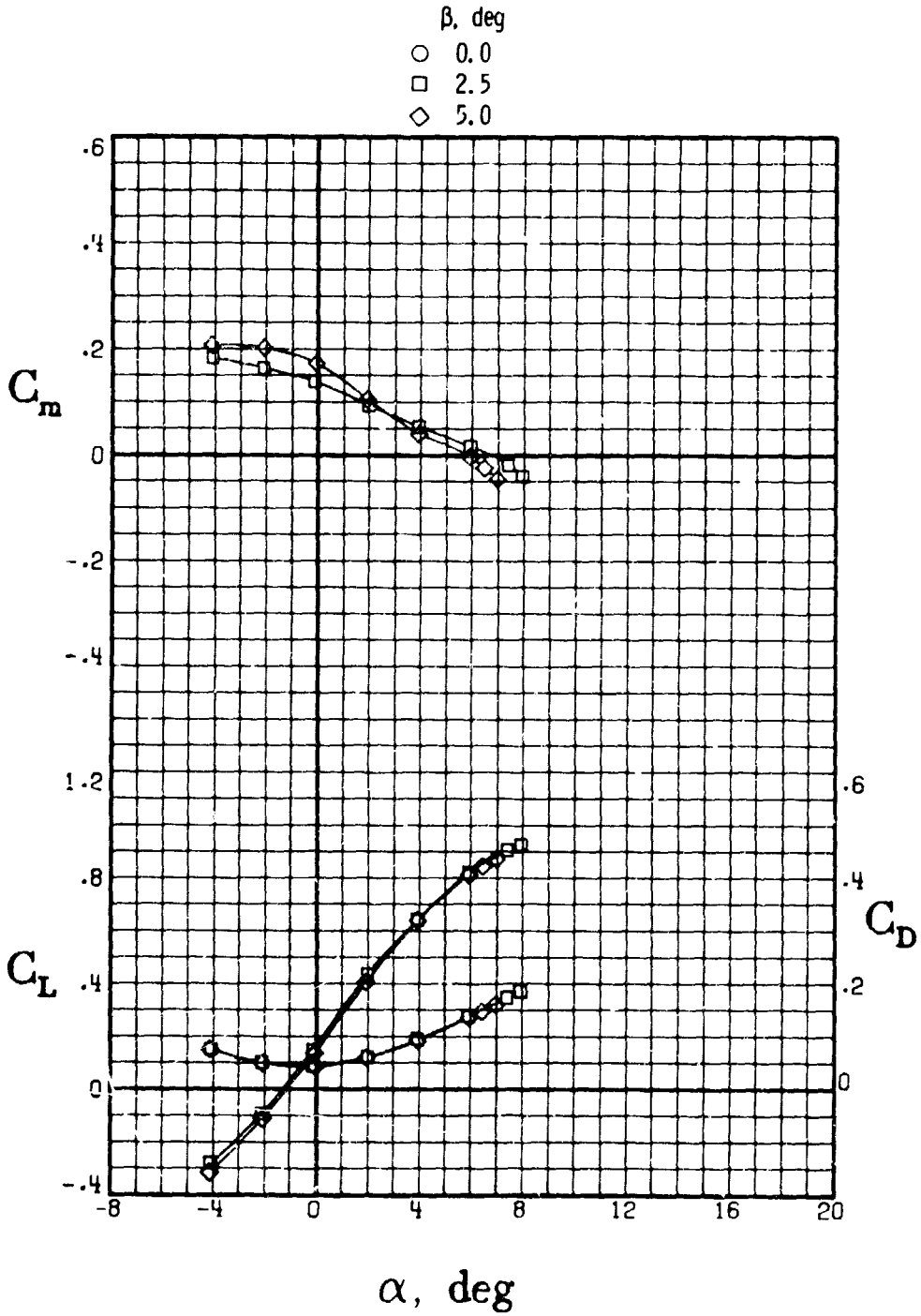

(f) M = 0.860.

(C) Figure 13.- Continued. (U)

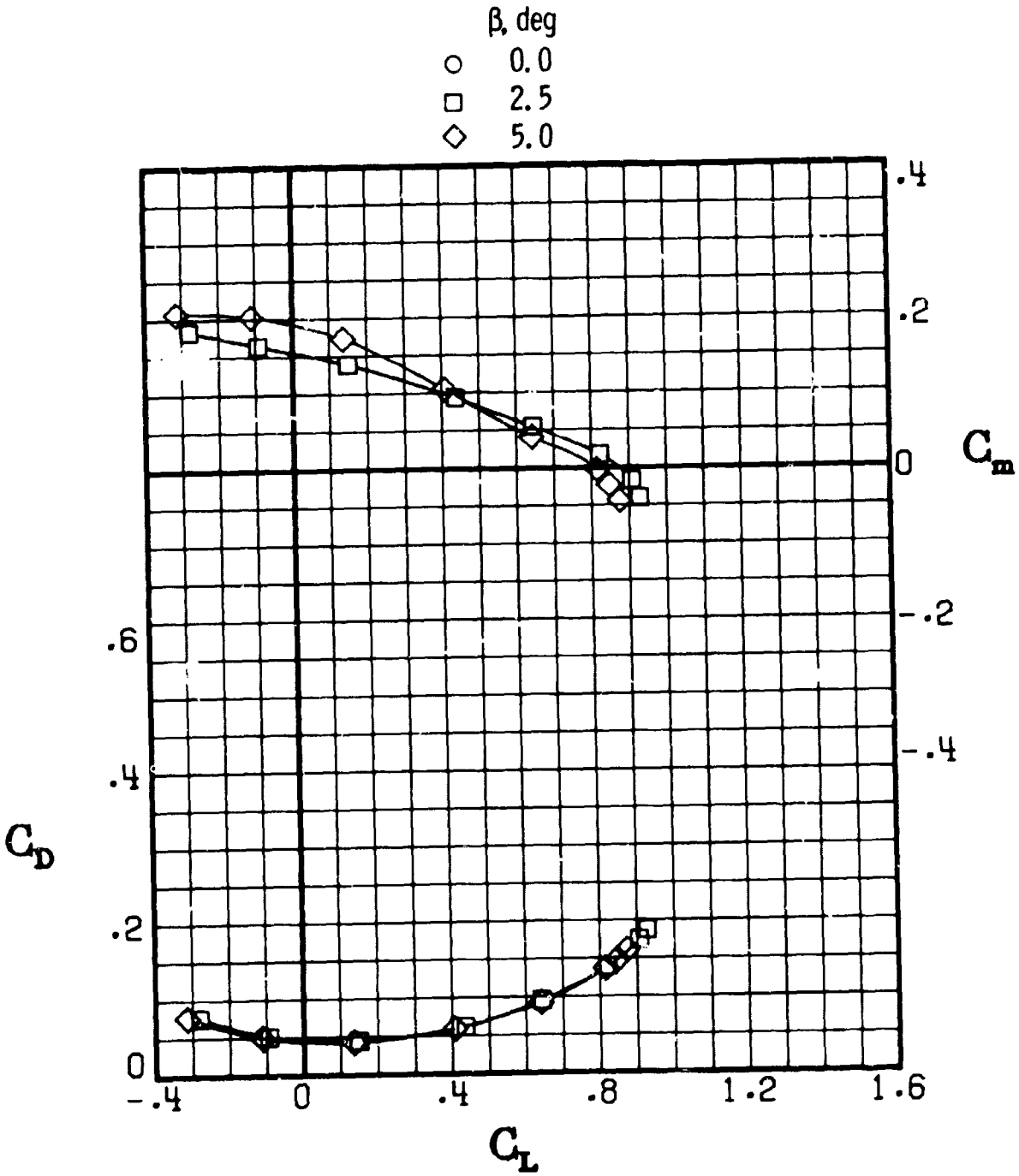

(f) Concluded.

Figure 13.- Continued. (U)

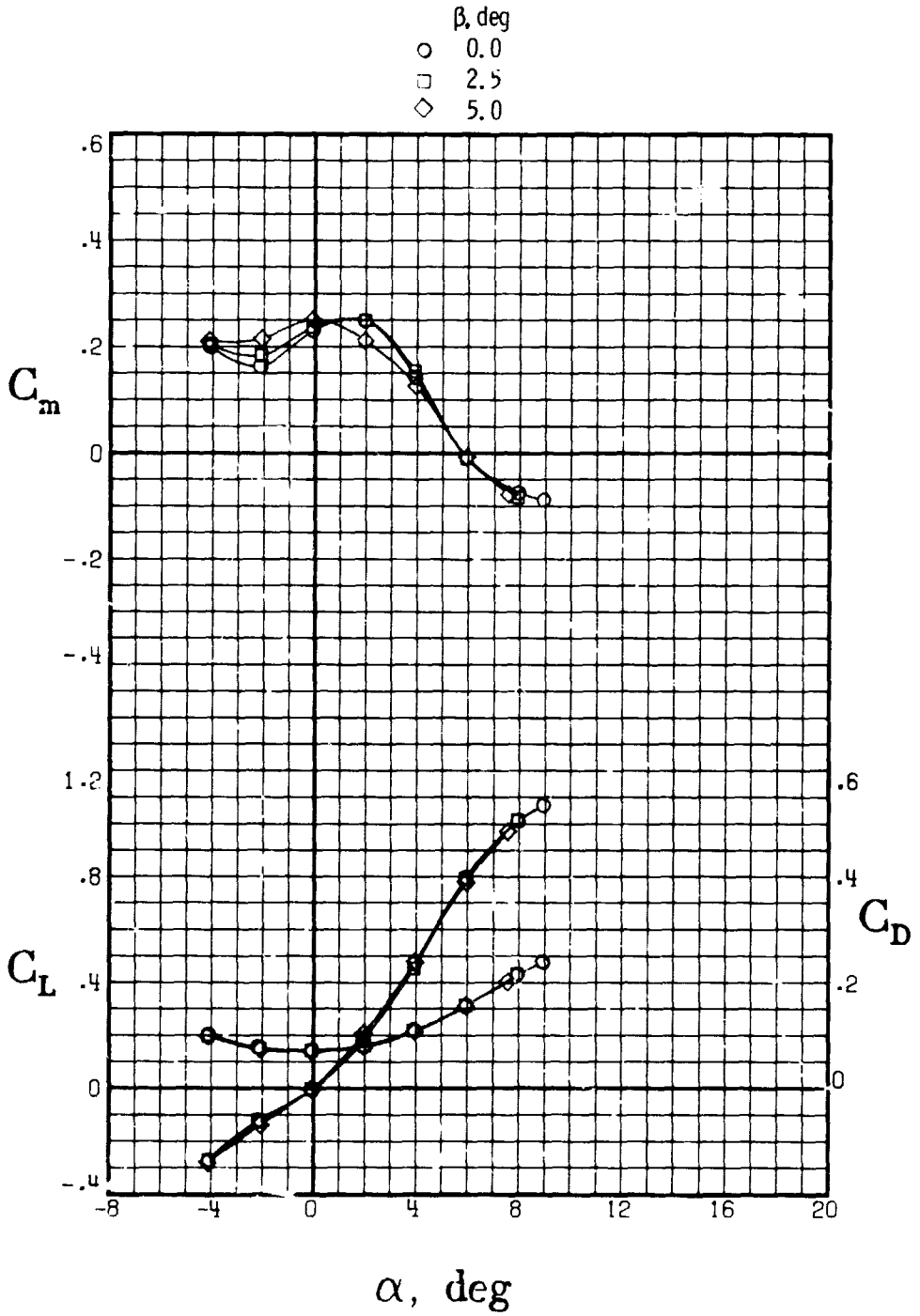

(g) M = 0.900.

Figure 13.- Continued. (U)

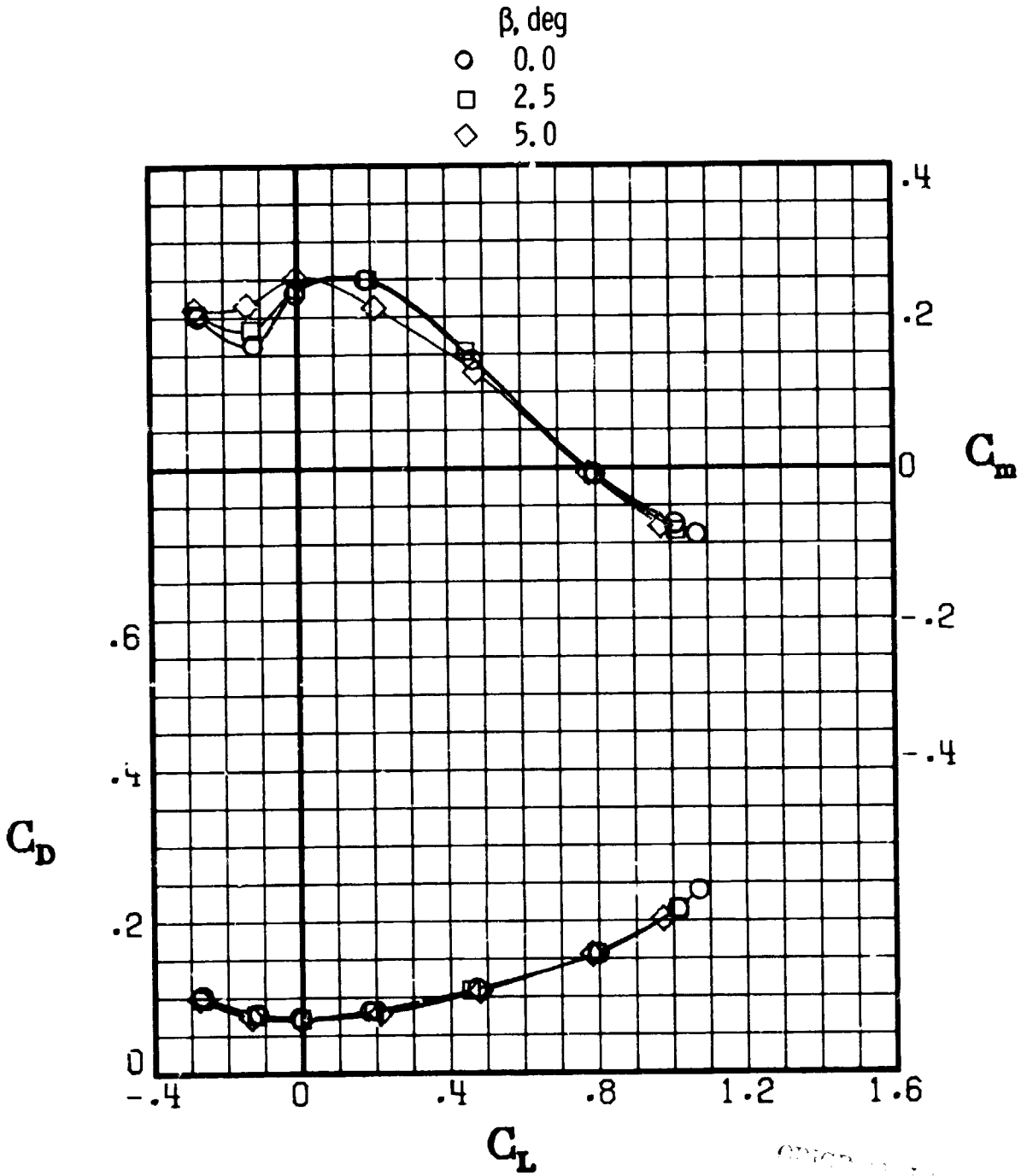

(g) Concluded.

Figure 13.- Continued. (U)

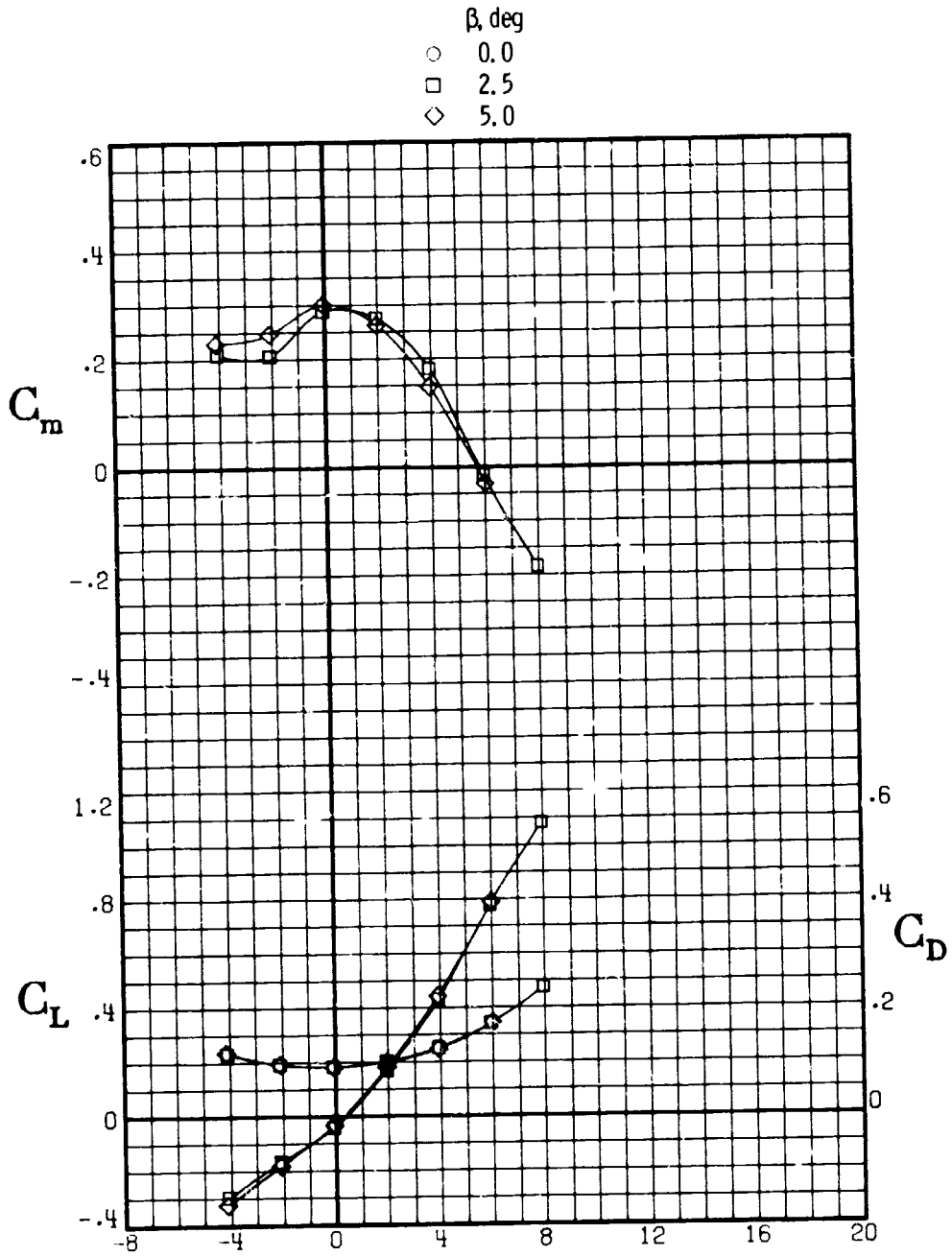

(h) M = 0.920.

Figure 13.- Continued. (U)

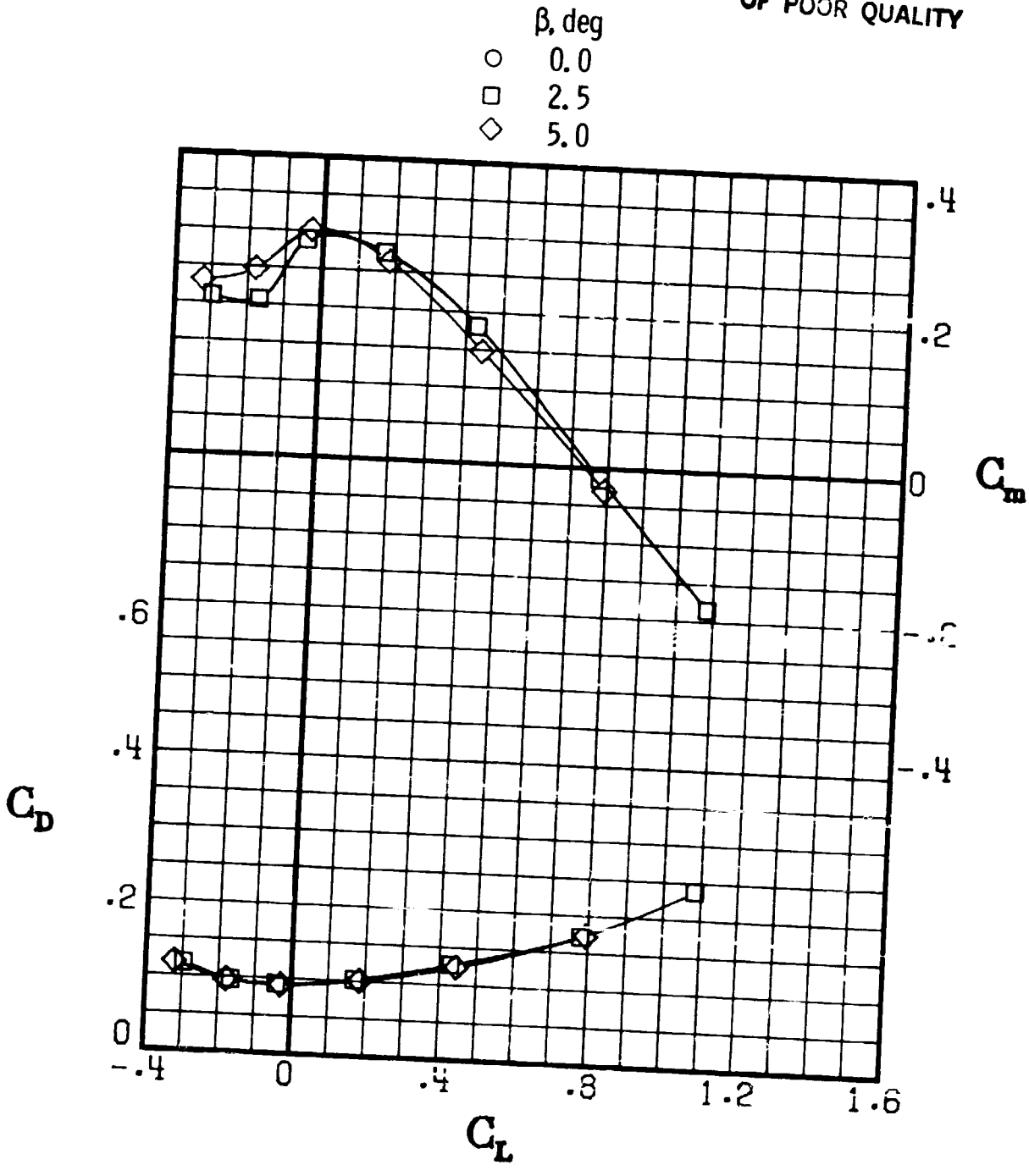

(h) Concluded.

Figure 13.- Concluded. (U)

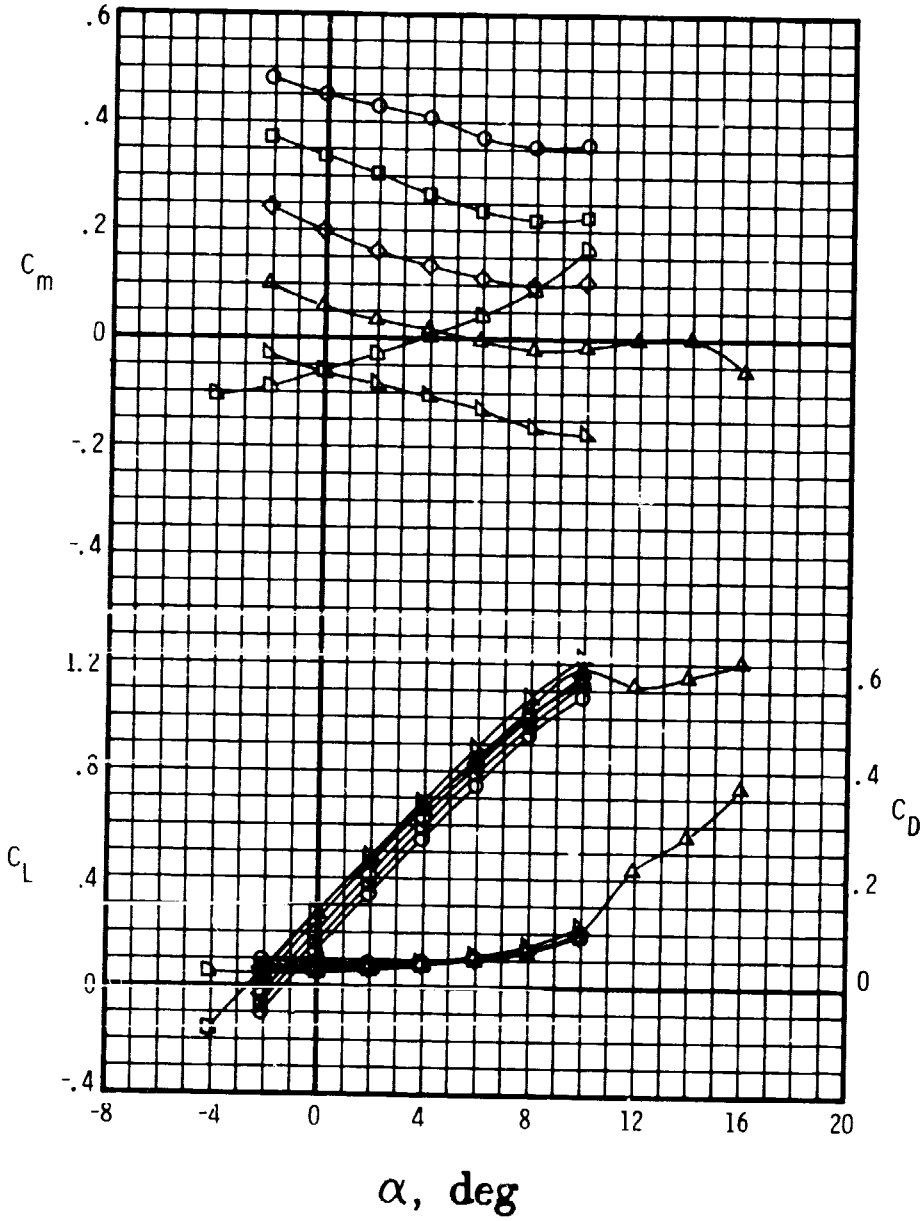

(a) M = 0.300.

Figure 14.- Effect of pitch control on longtiudinal aerodynamic characteristics for model configuration C. $\beta = 0^o$. (U)

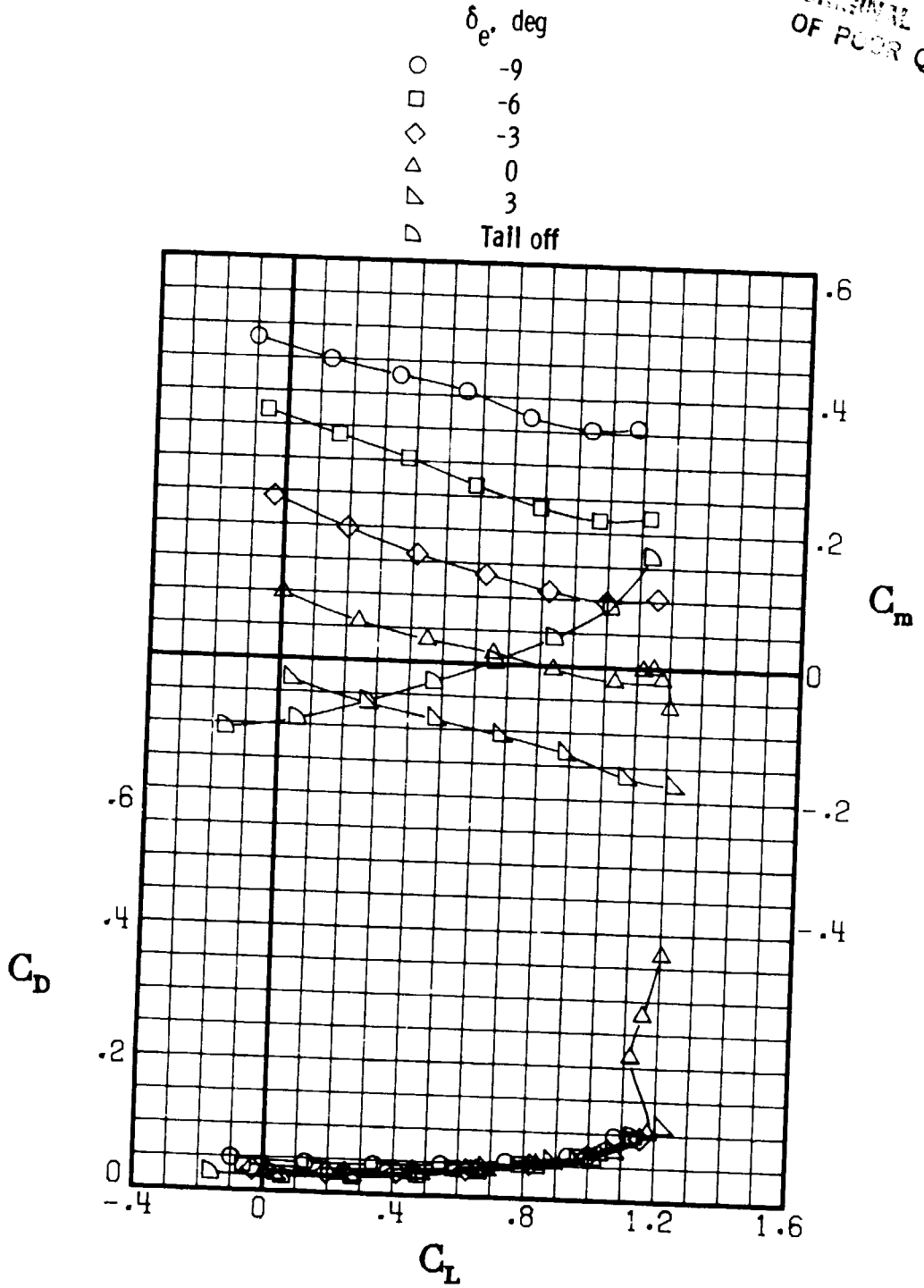

(a) Concluded.

Figure 14.- Continued. (U)

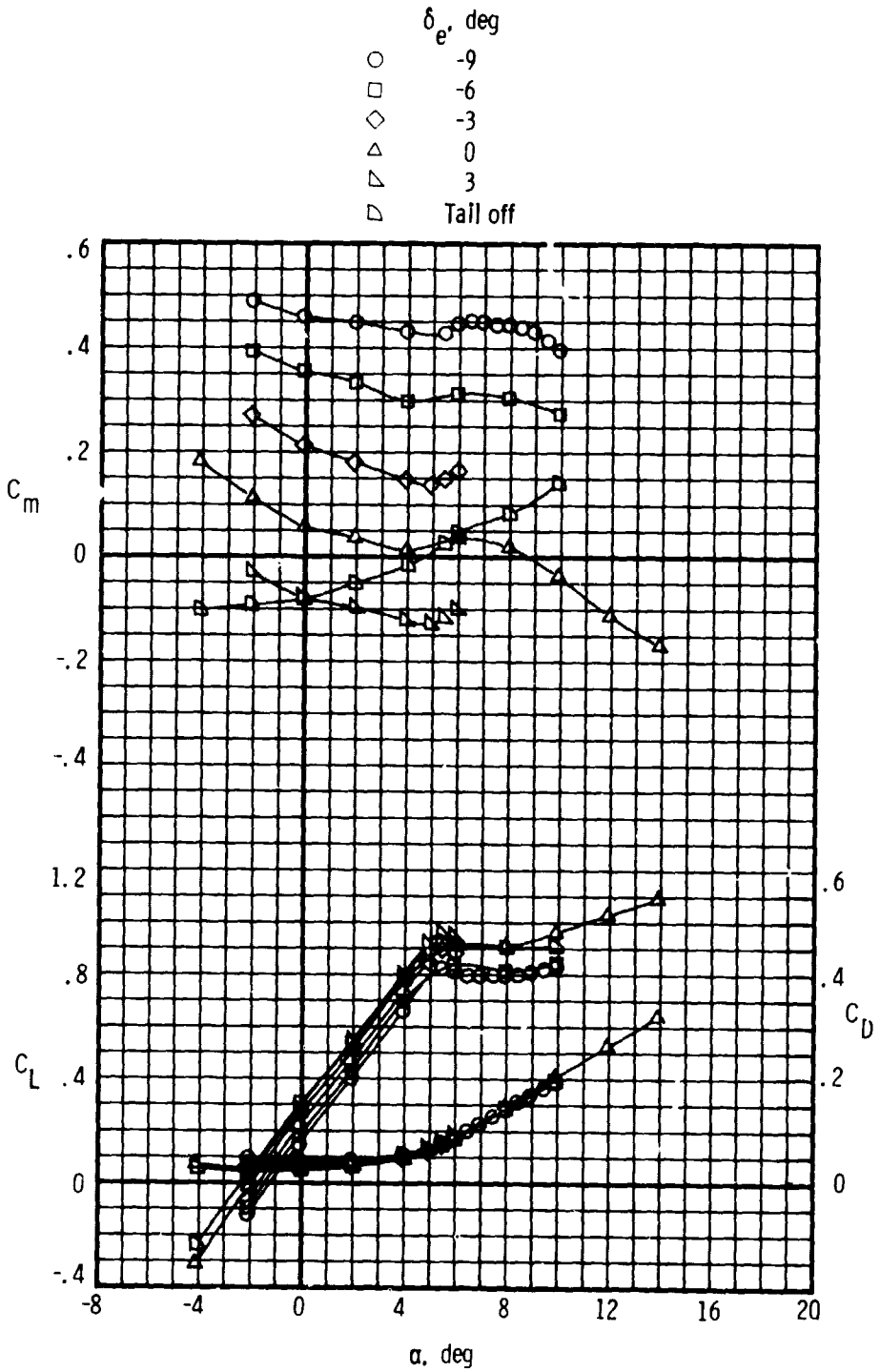

(b) M = 0.700.

Figure 14.- Continued. (U)

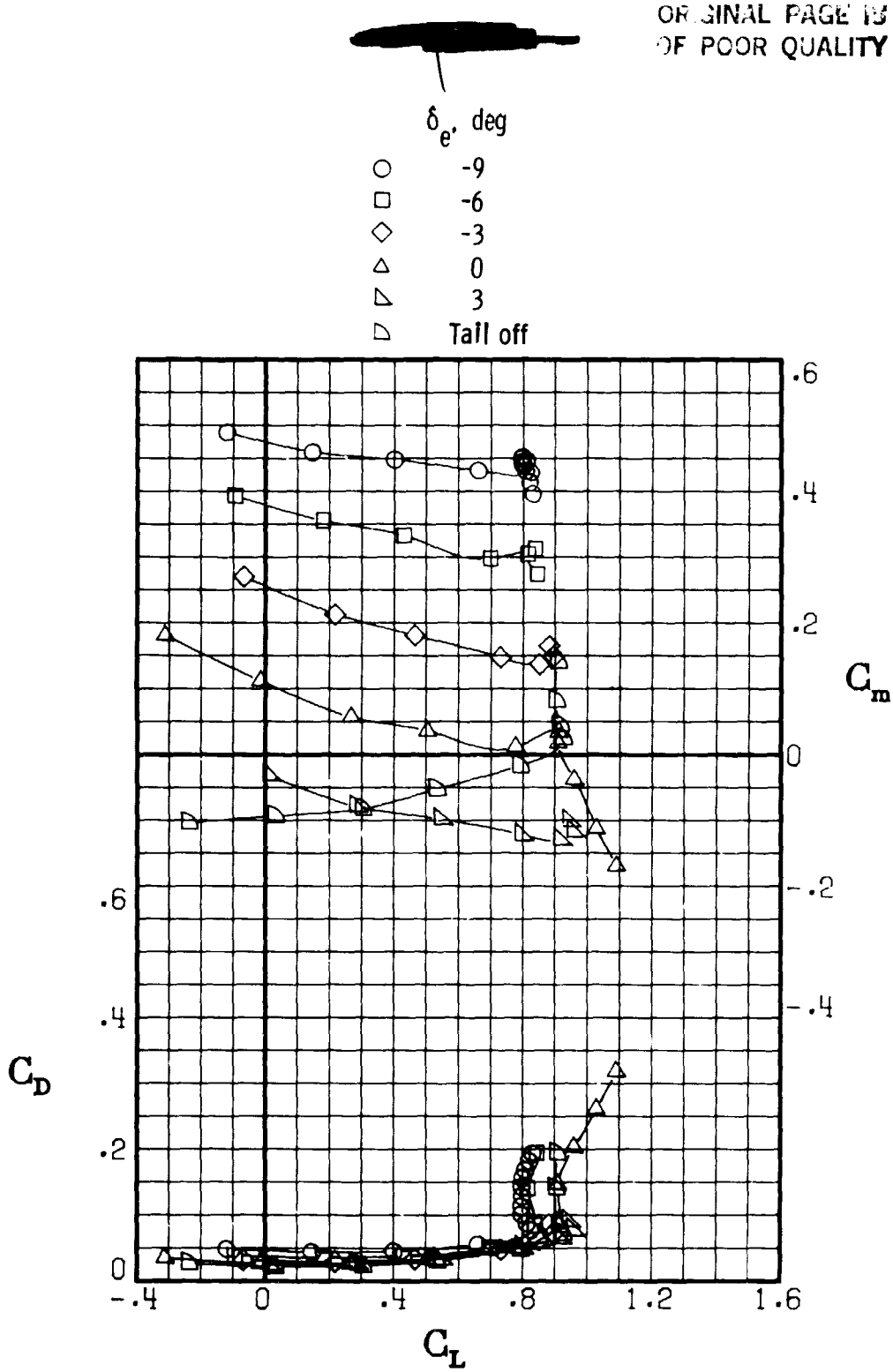

(b) Concluded.

Figure 14.- Continued. (U)

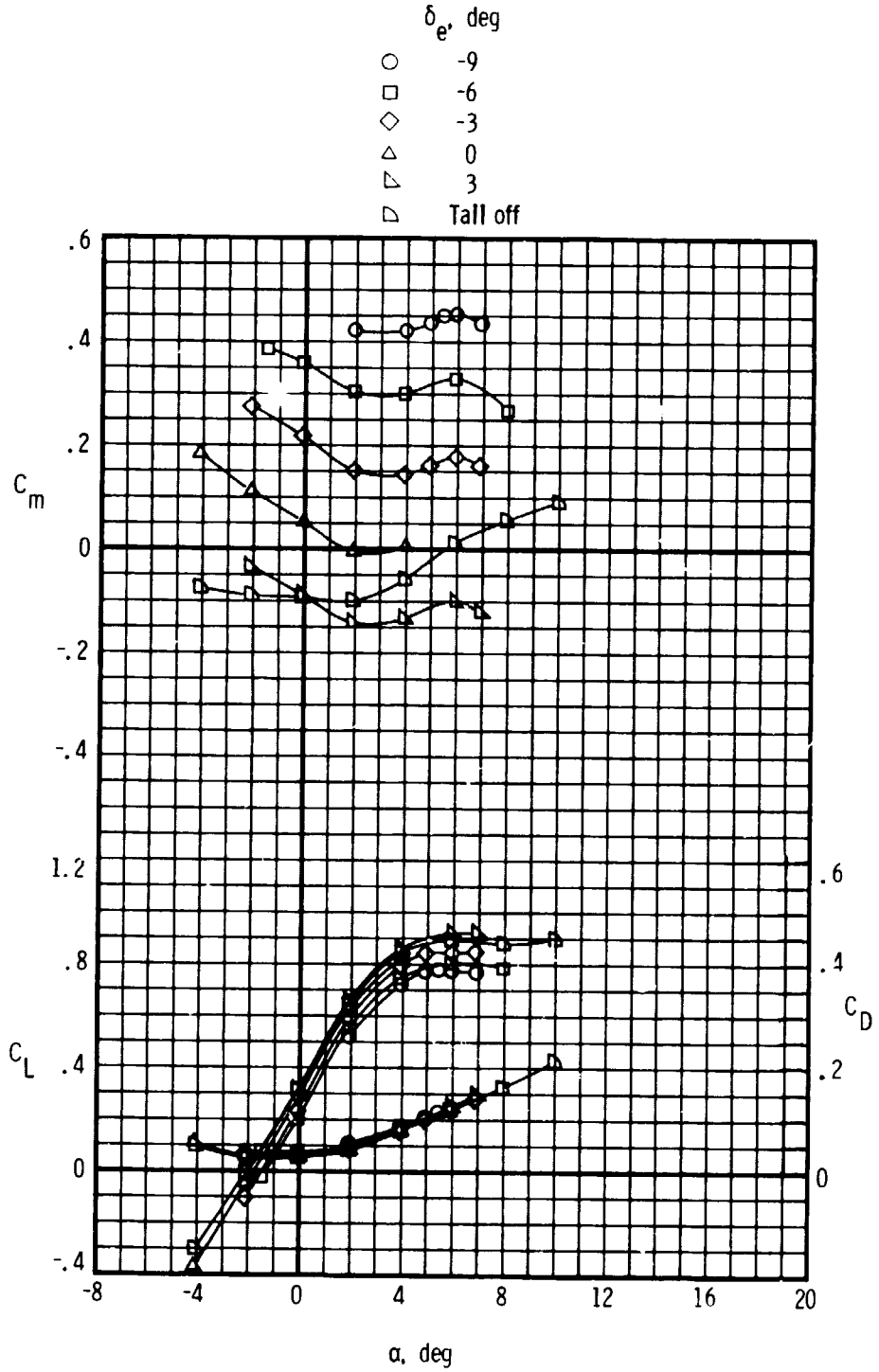

(c) M = 0.800.

Figure 14.- Continued. (U)

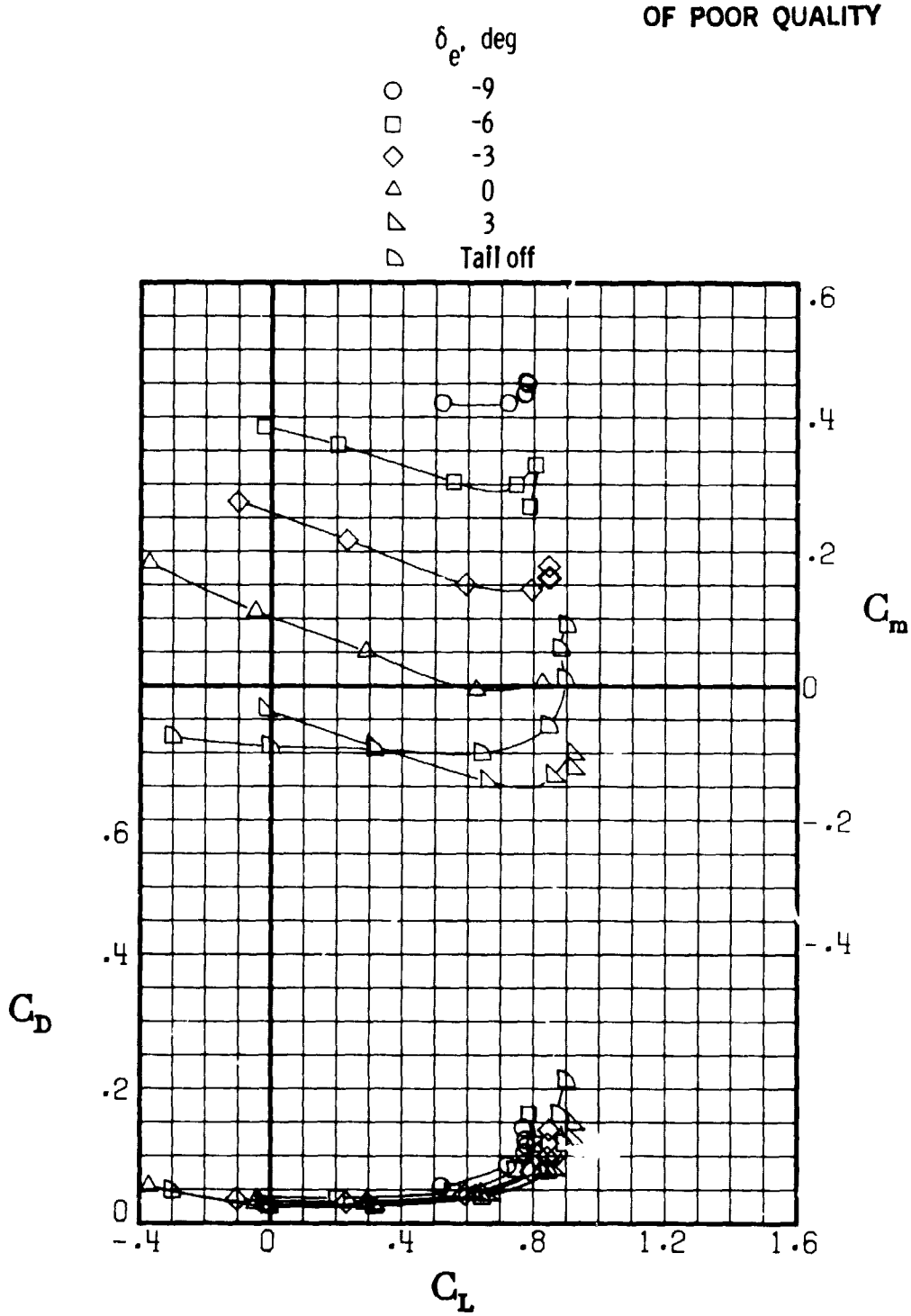

(c) Concluded.

Figure 14.- Continued. (U)

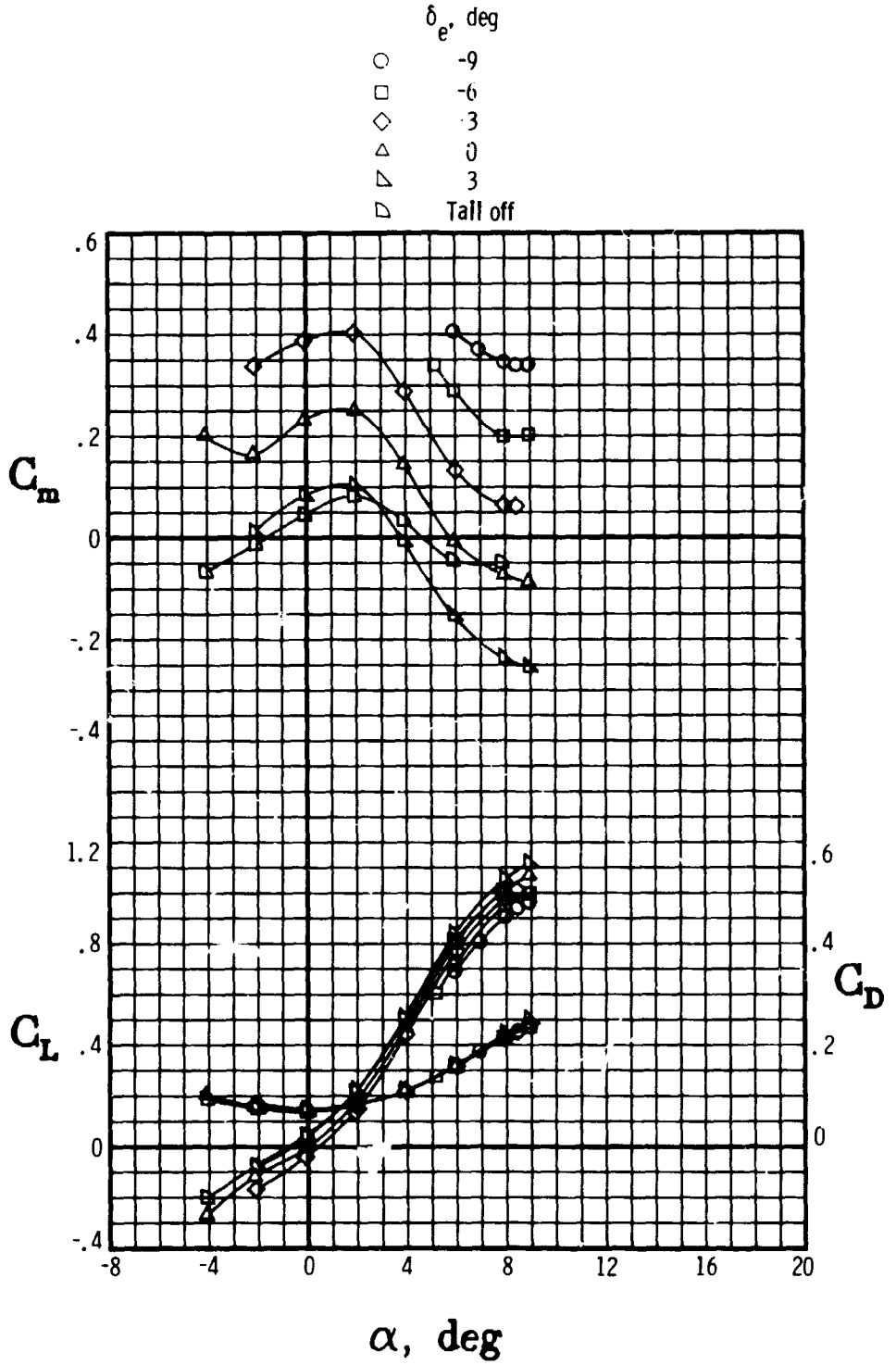

(d) M = 0.900.

Figure 14.- Continued. (U)

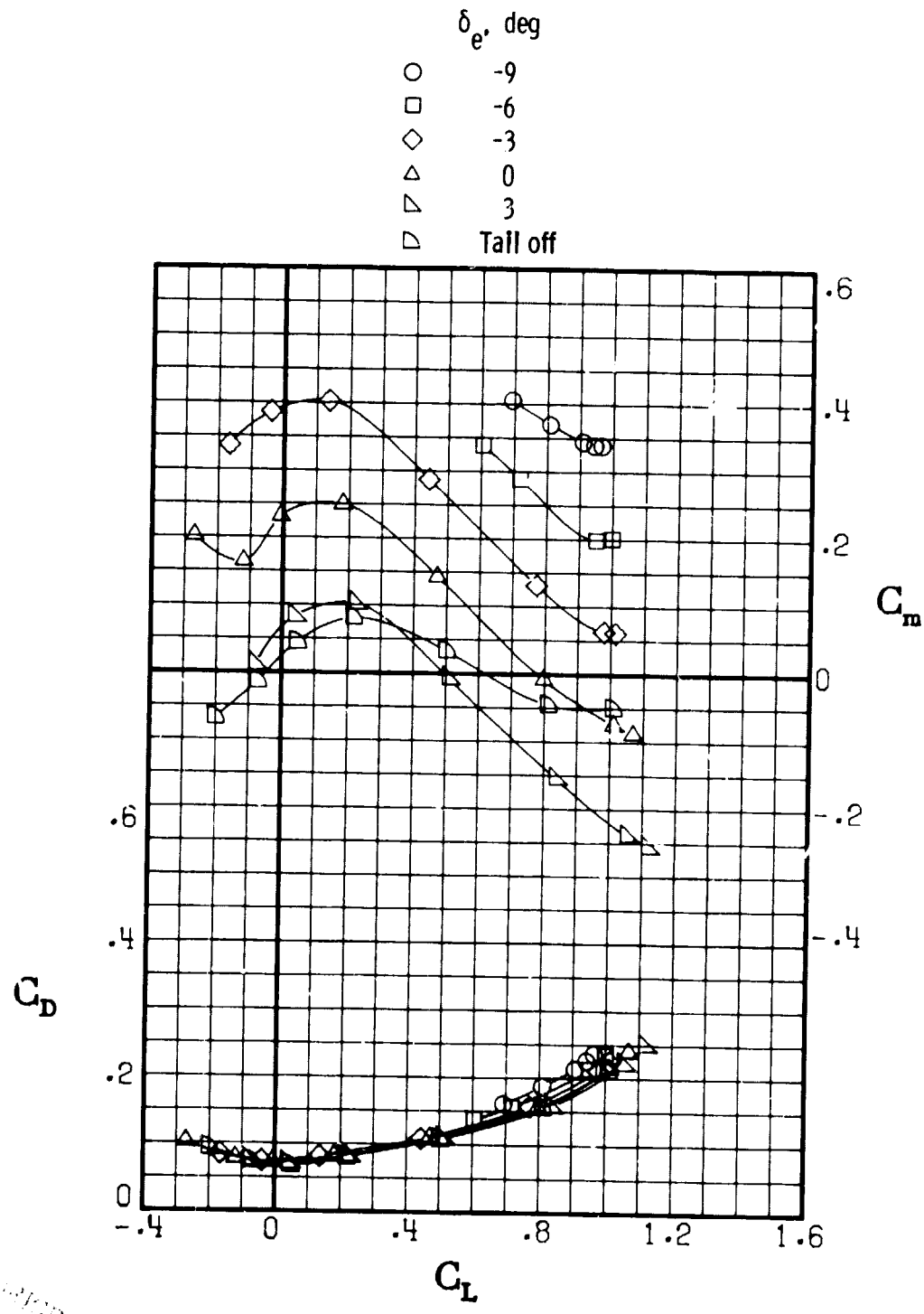

(d) Concluded.

Figure 14.- Concluded. (U)

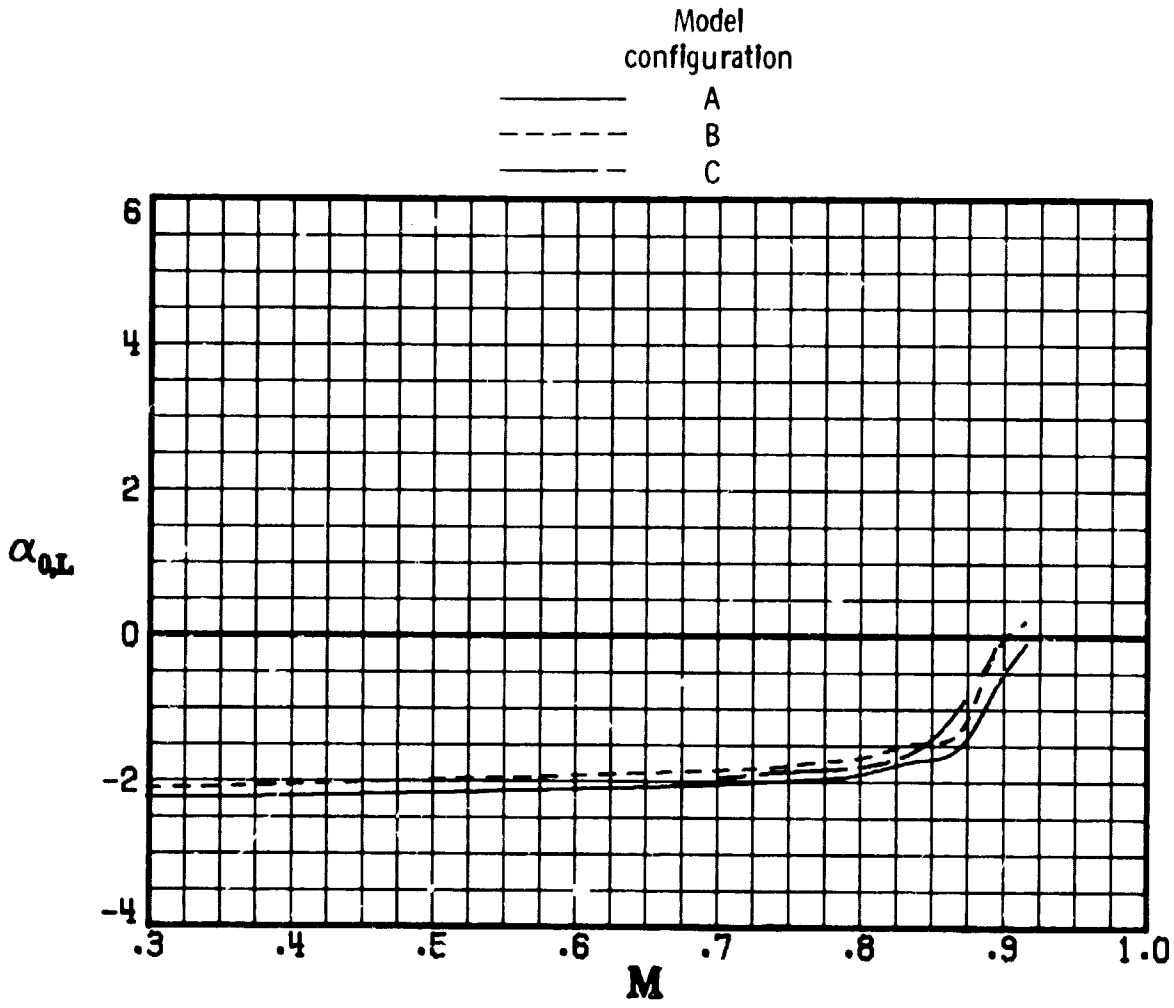

(C) Figure 15.- Variation of zero-lift angle of attack with Mach number for model configurations A, B, and C. $\delta_e = 0^o$. (U)

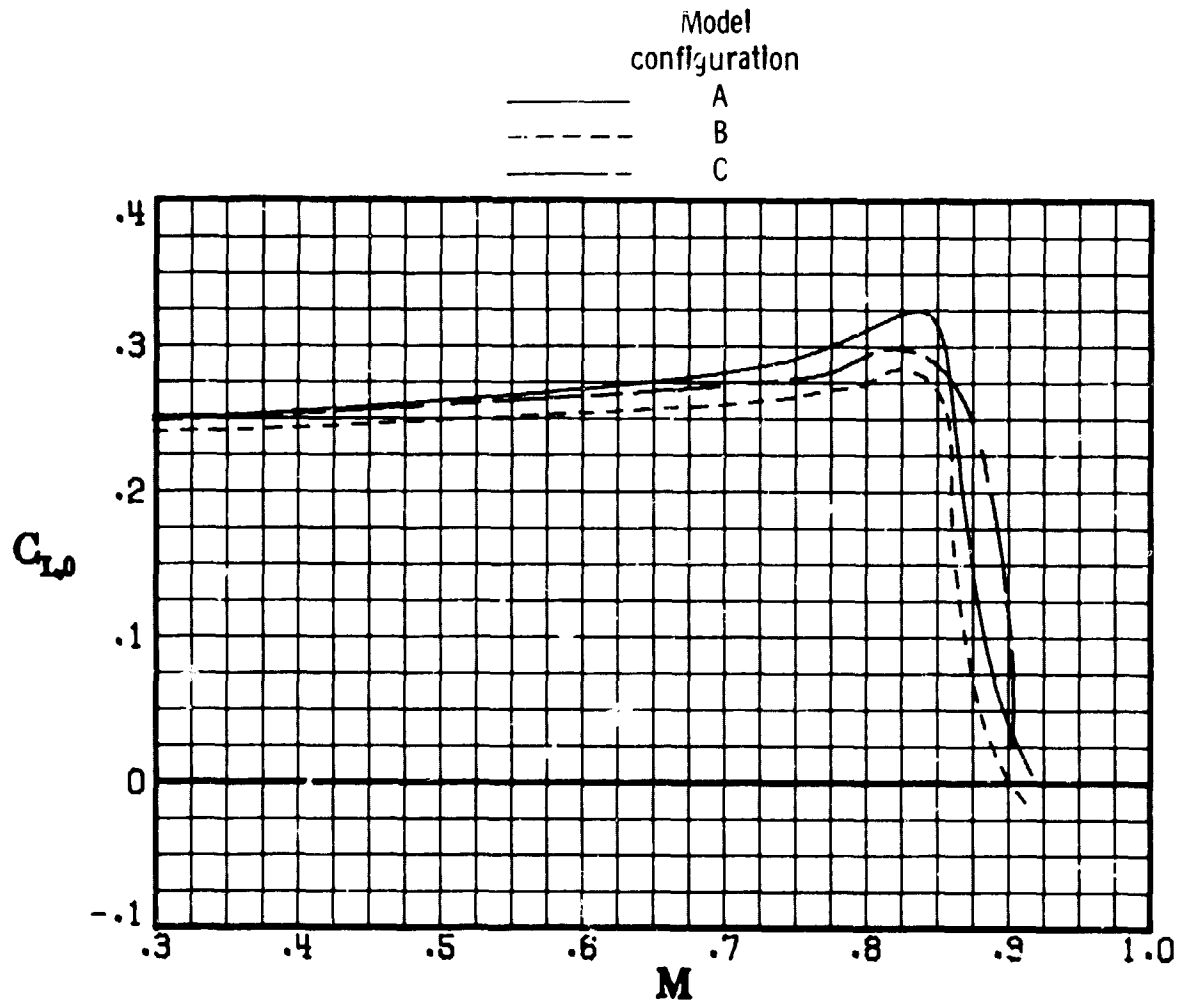

(C) Figure 16.- Variation of lift coefficient at $\alpha = 0^{o}$ with Mach number for model configurations A, B, and C. $\delta_e = 0^{o}$. (U)

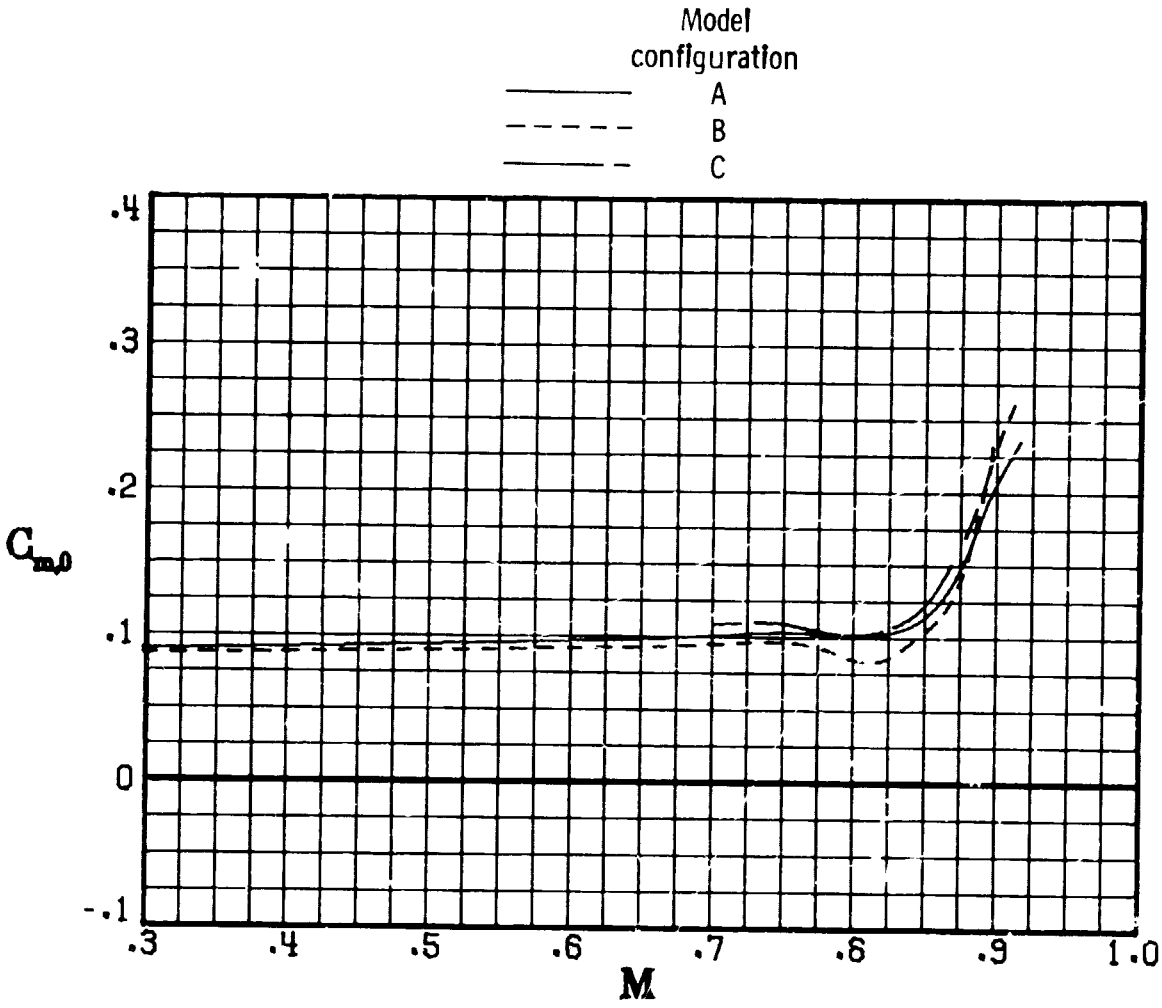

Figure 17.- Variation of zero-lift pitching-moment coefficient with Mach number for model configurations A, B, and C. $\delta_e = 0^o$. (U)

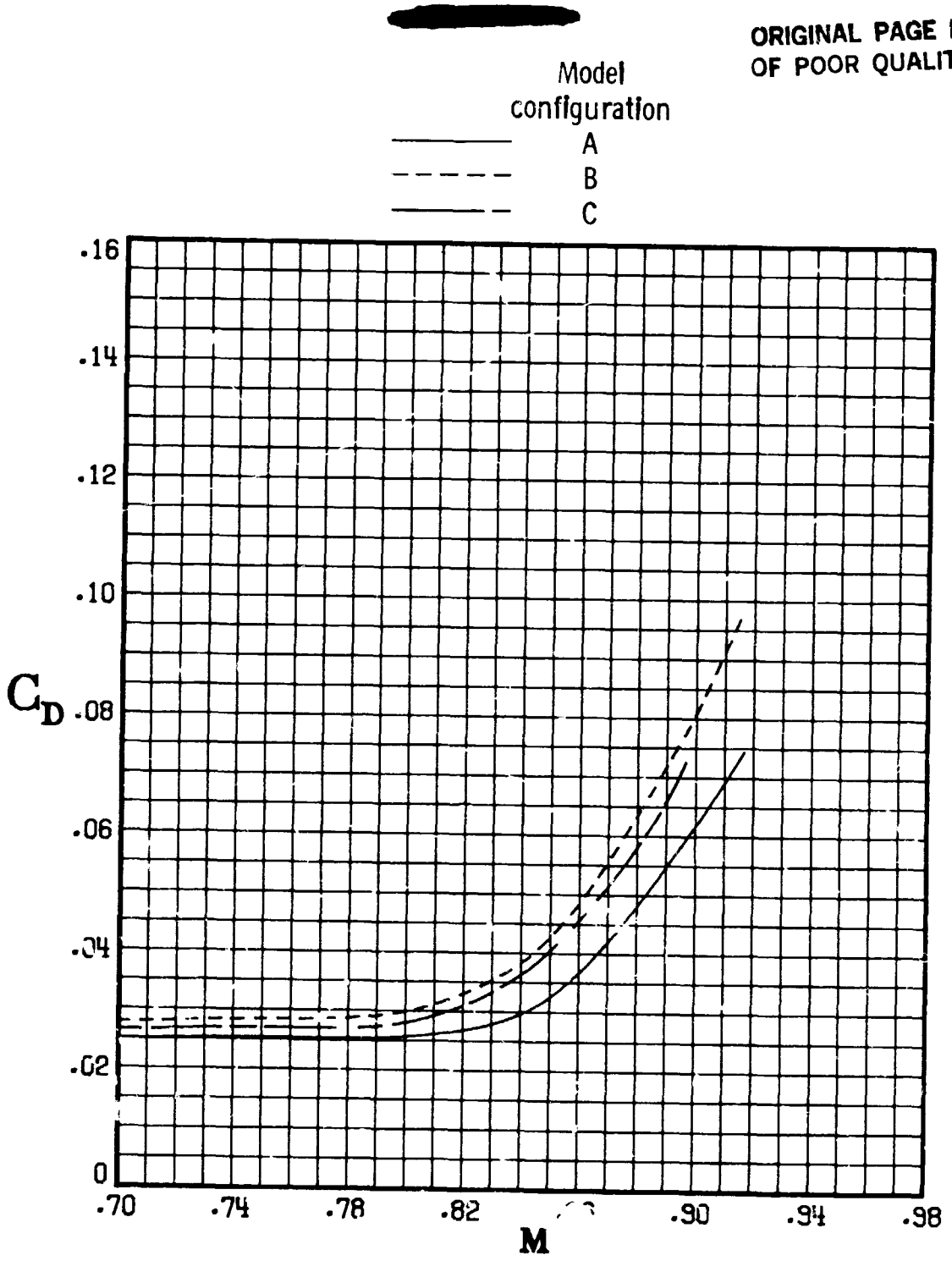

(a) $C_L = 0.0$.

(C) Figure 18.- Variation of drag coefficient with Mach number for model configurations A, B, and C for several lift coefficients. $\delta_e = 0^o$; $\beta = 0^o$. (U)

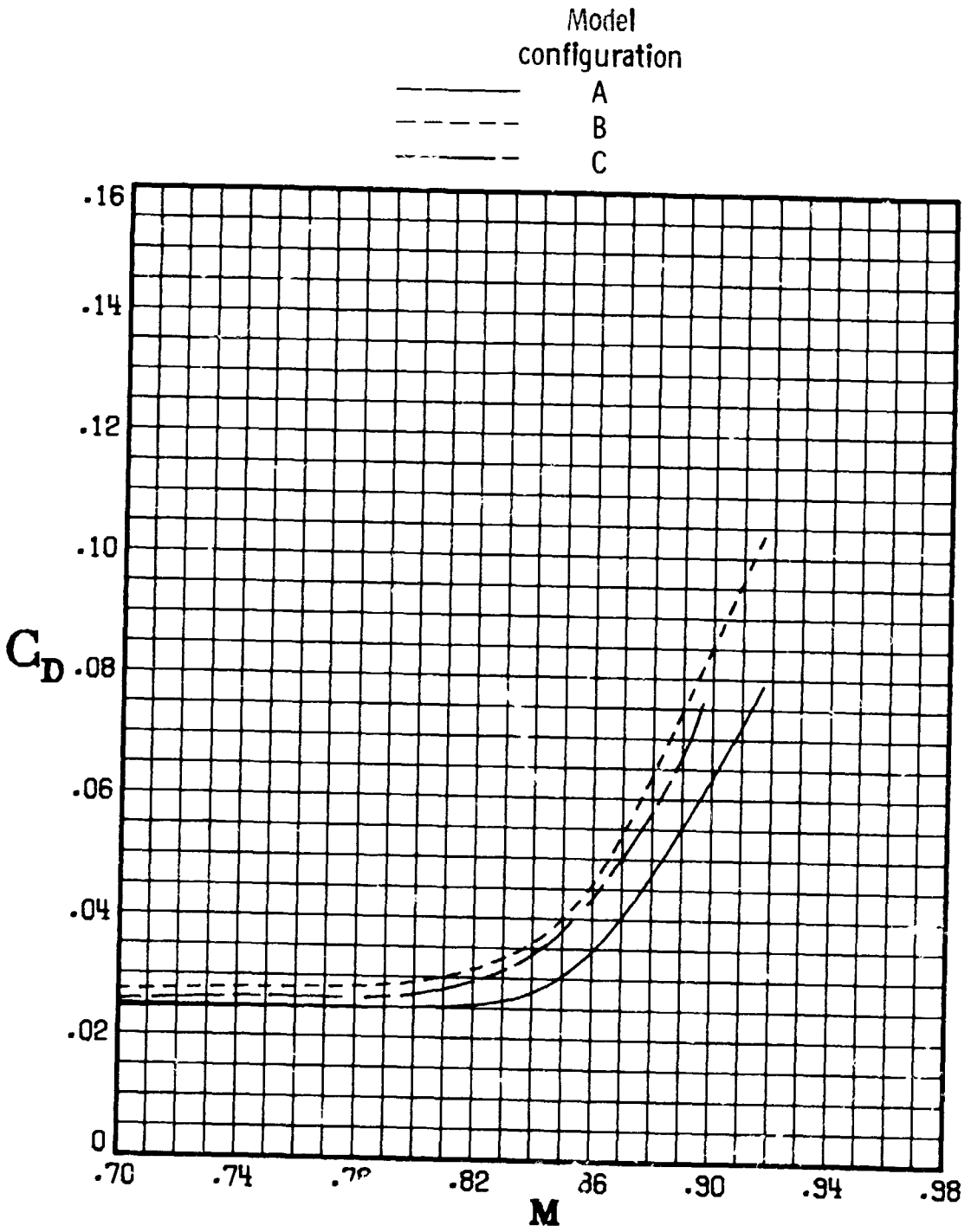

(b) $C_L = 0.1$.

Figure 18.- Continued. (U)

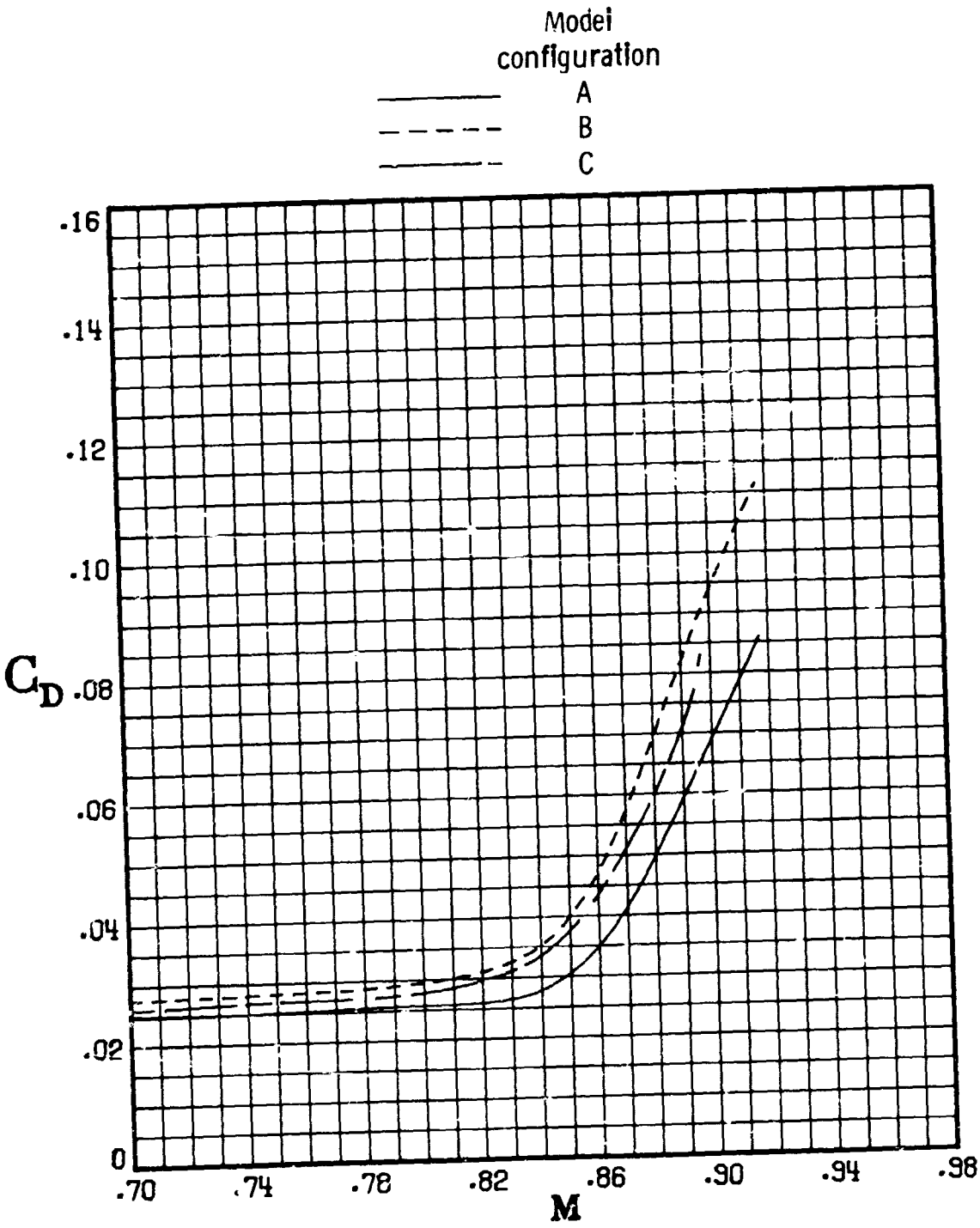

(c) $C_L = 0.2$

Figure 18.- Continued. (U)

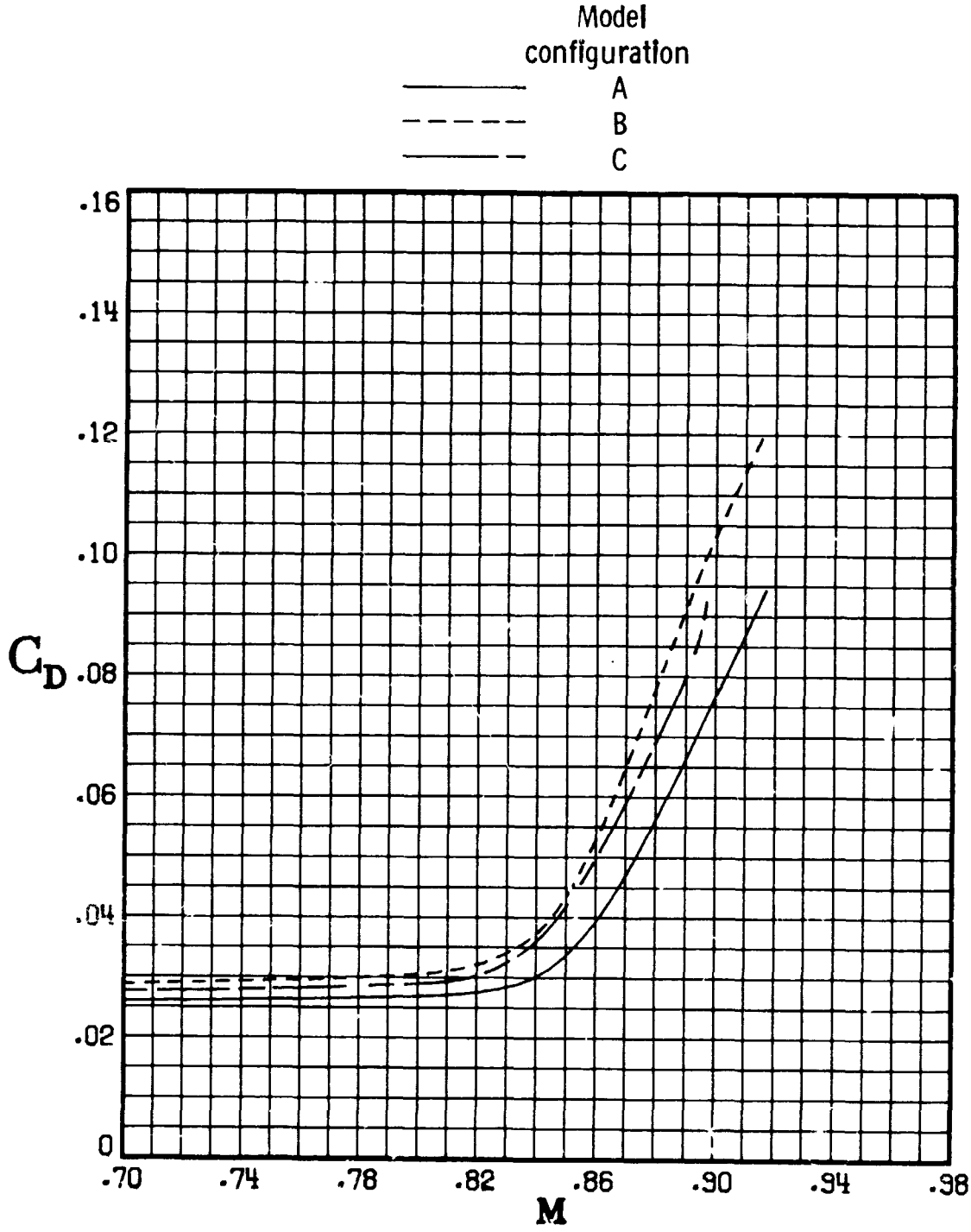

(d) $C_L = 0.3$.

Figure 18.- Continued. (U)

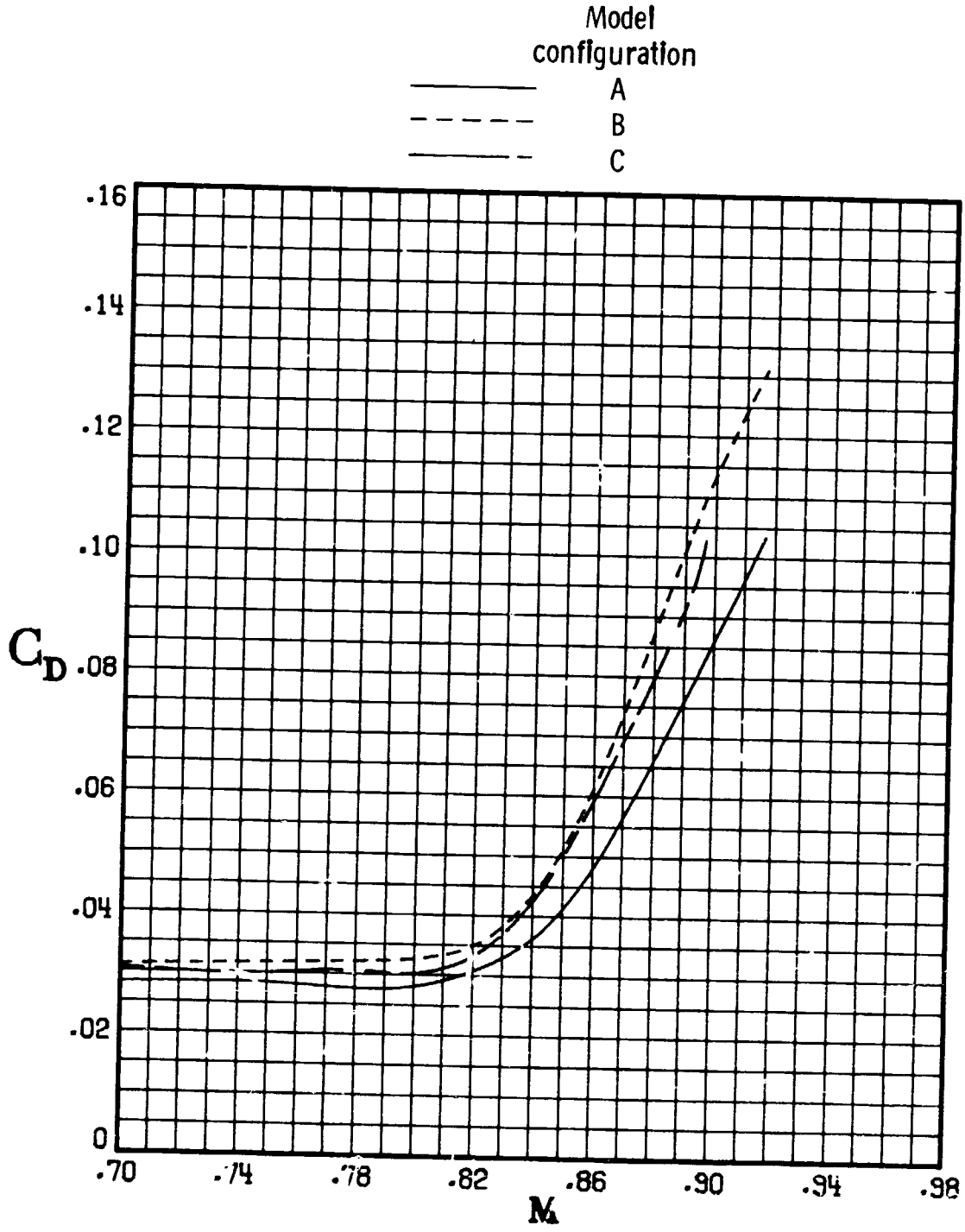

(e) $C_L = 0.4$.

Figure 18.- Continued. (U)

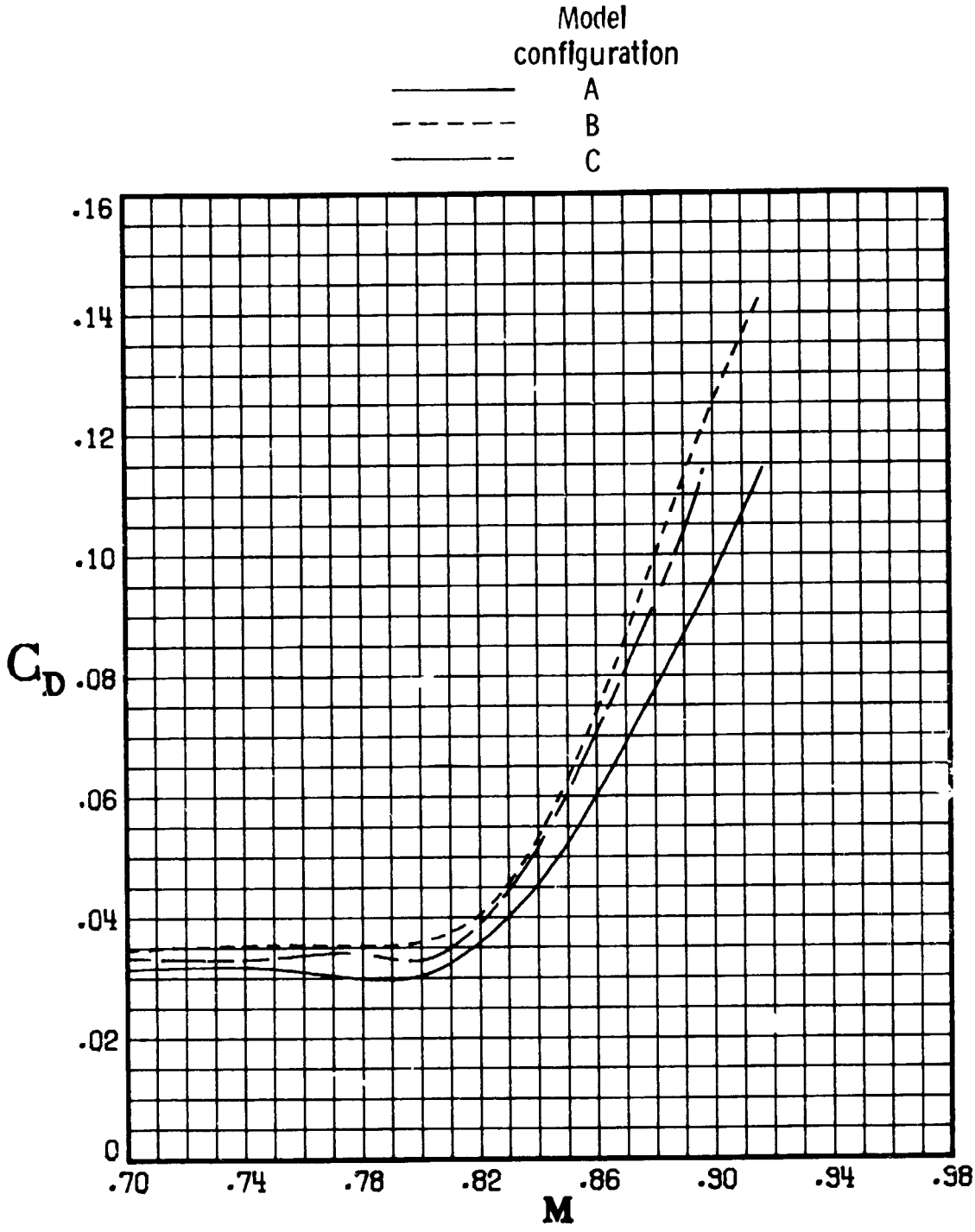

(f) $C_L = 0.5$.

Figure 18.- Continued. (U)

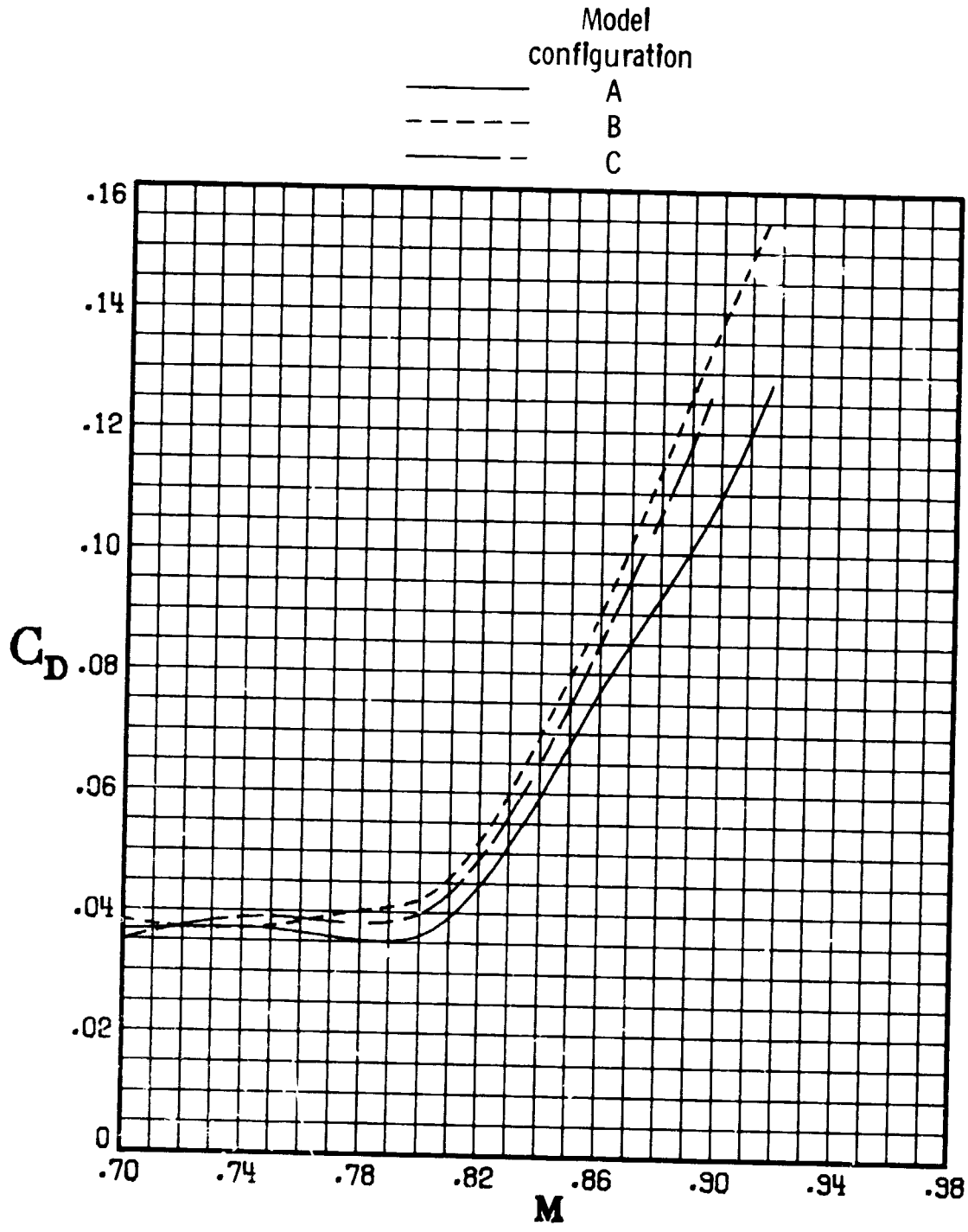

(g) $C_L = 0.6$.

Figure 18.- Concluded. (U)

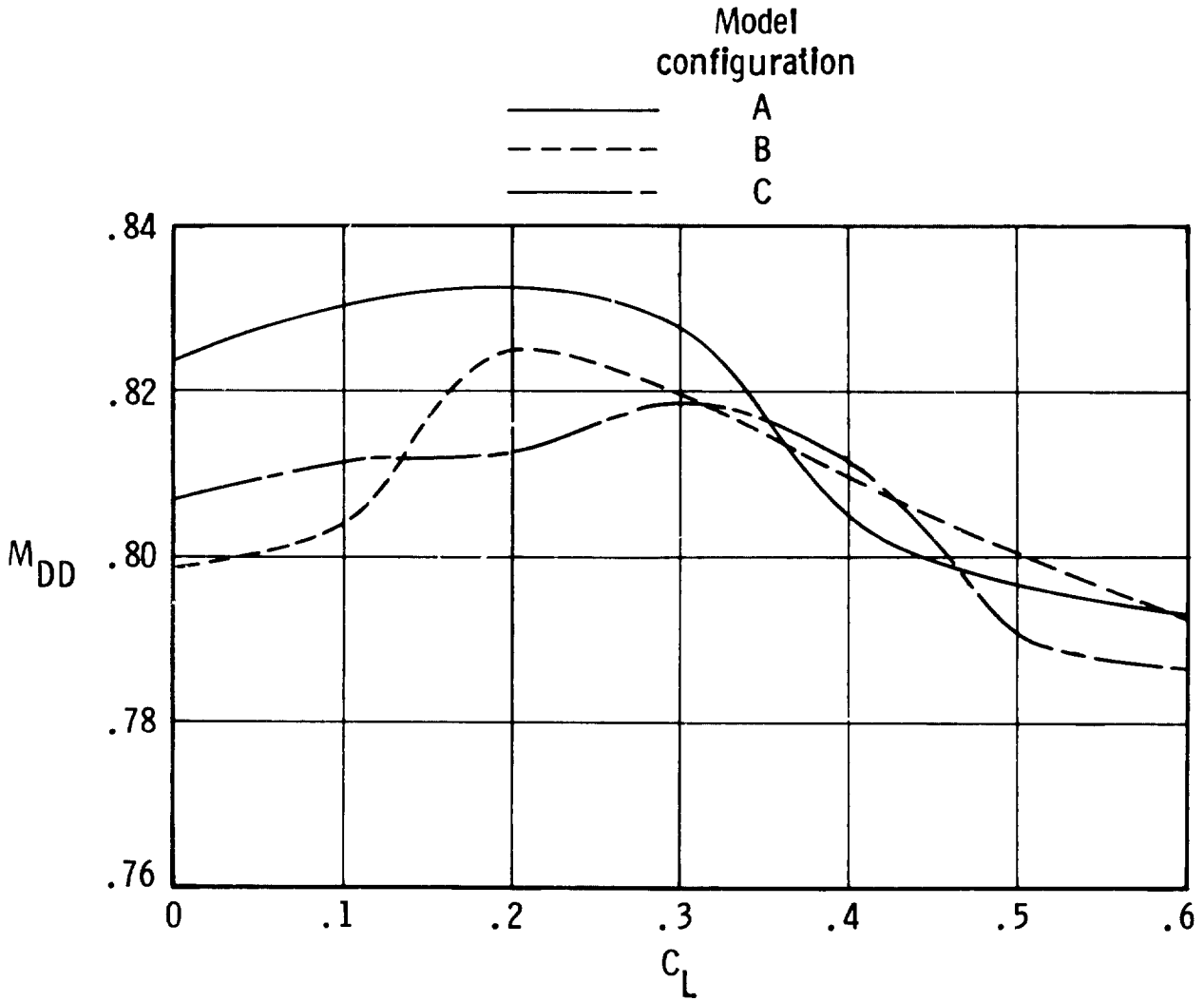

(C) Figure 19.- Variation of drag-divergence Mach number with lift coefficient for model configurations A, B, and C. (U)

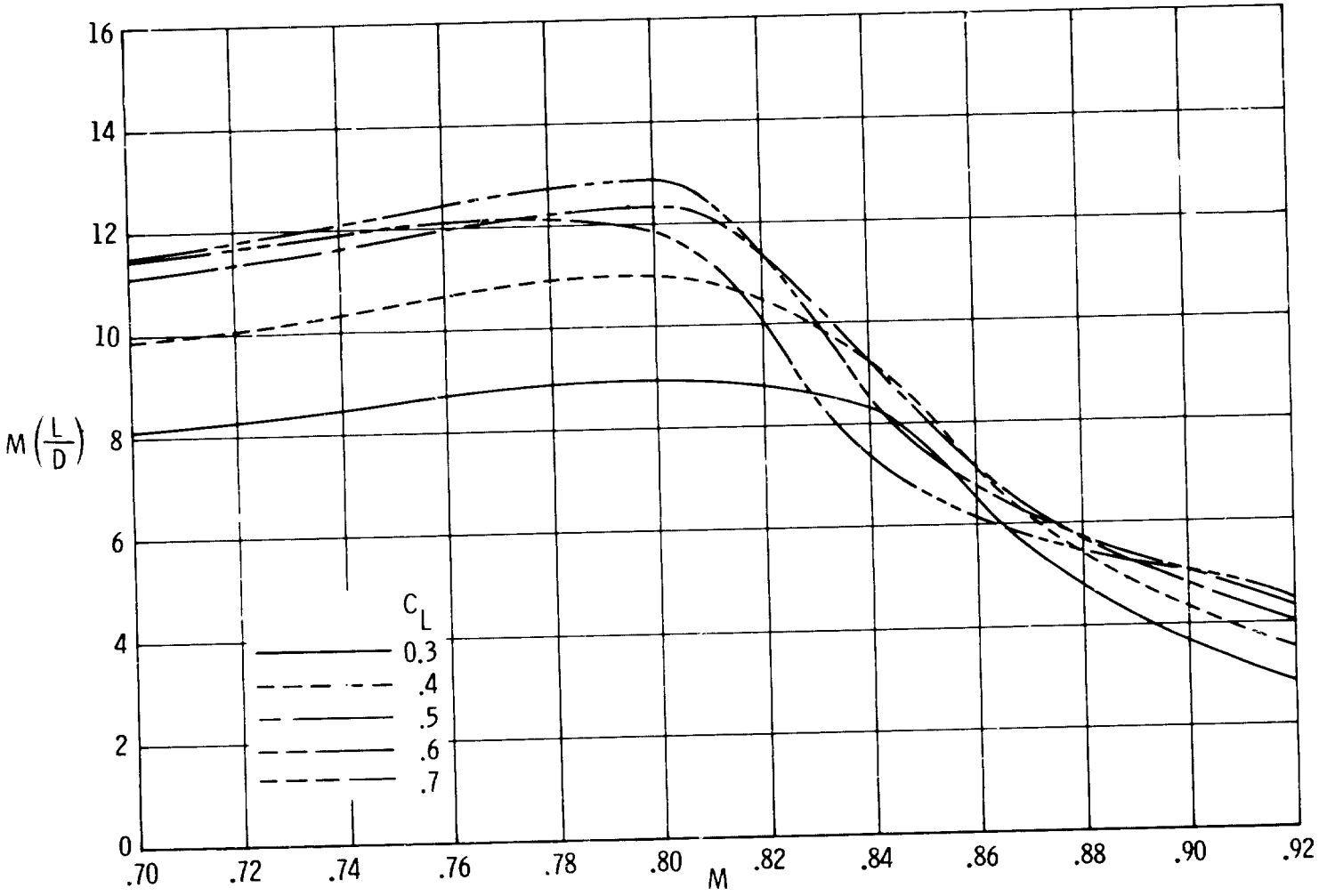

(a) Model configuration A.

(C) Figure 20.- Variation of aerodynamic range parameter with Mach number for five lift coefficients. (U)

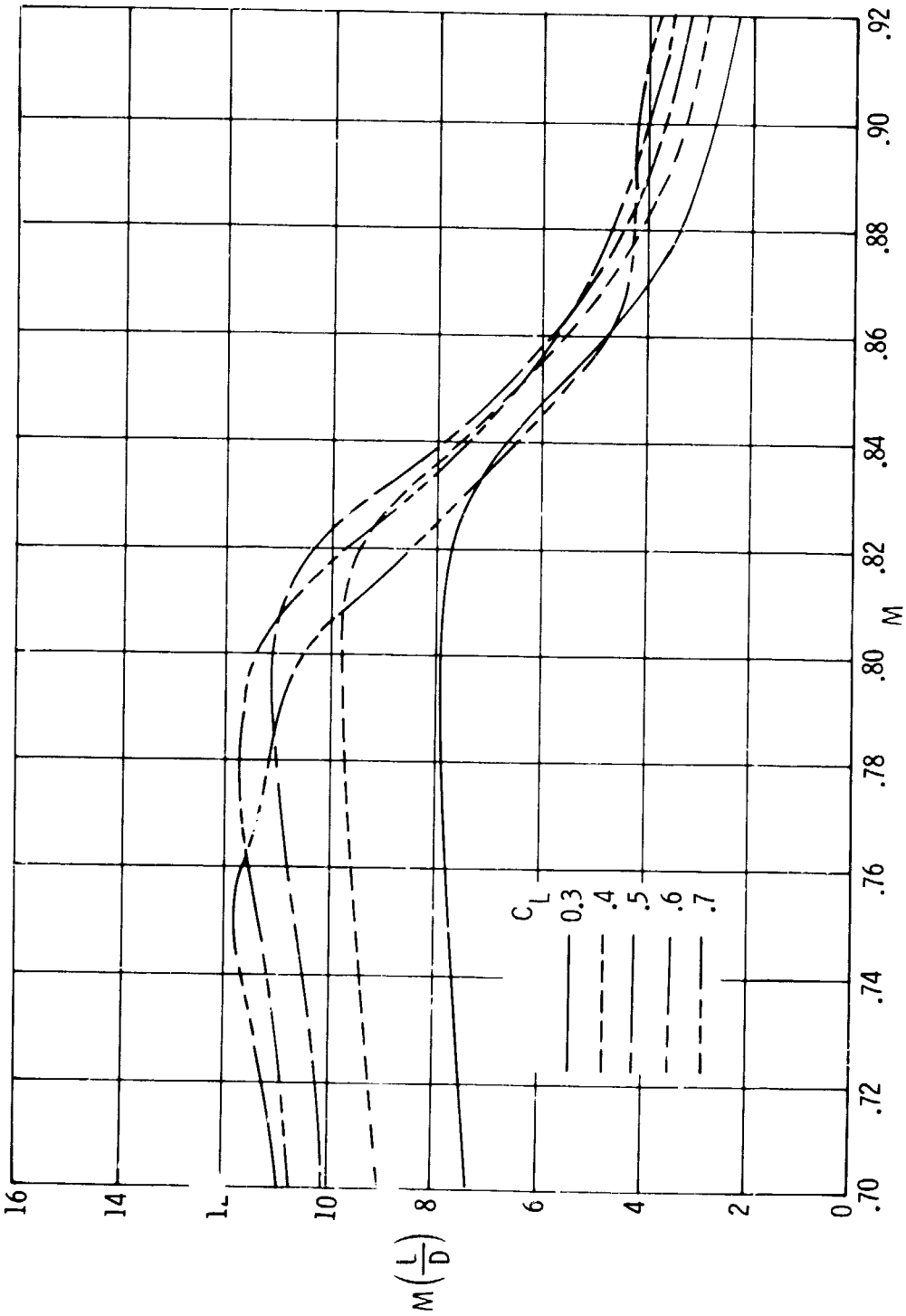

(b) Model configuration B.

(C) Figure 20.- Continued. (U)

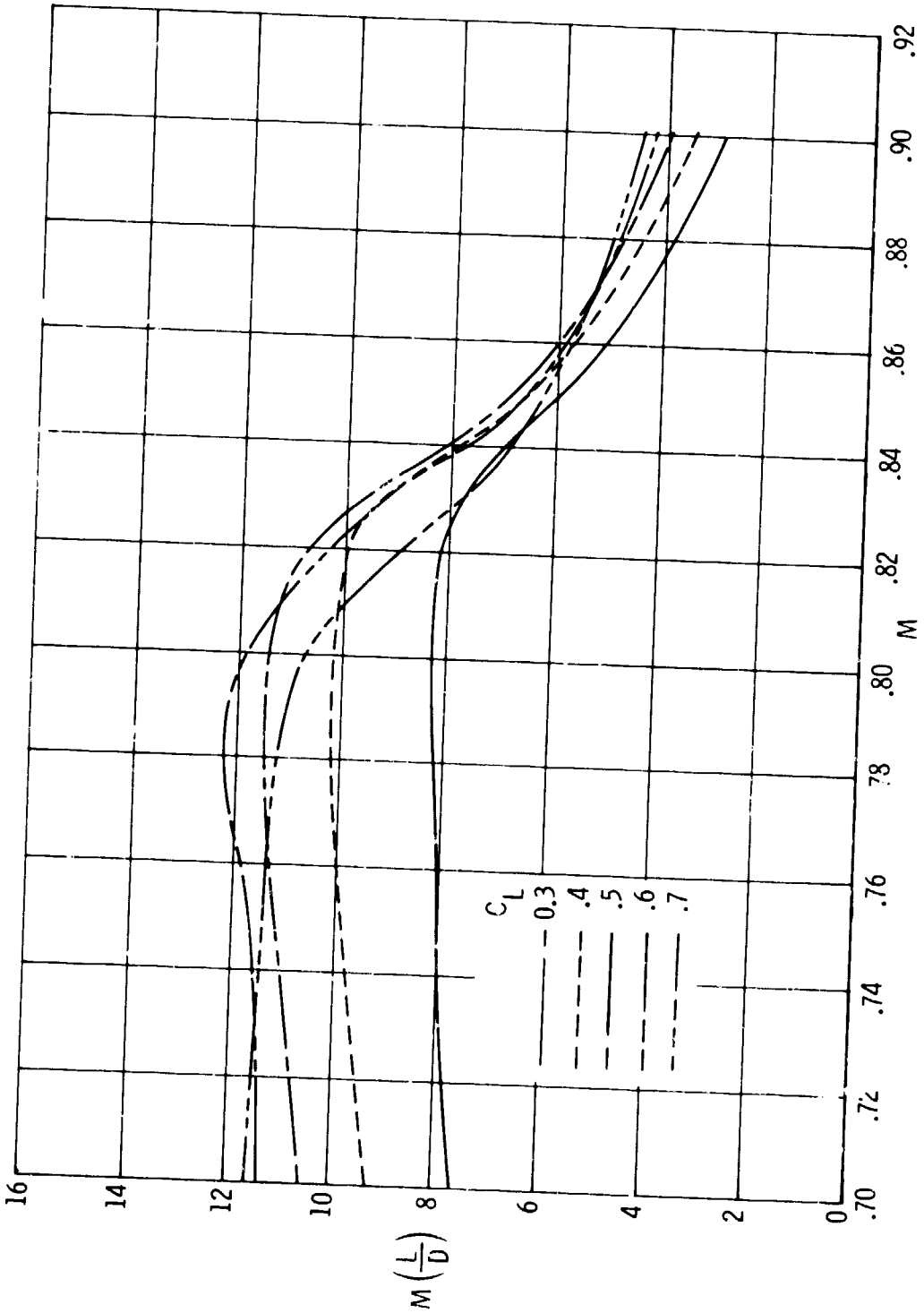

(c) Model configuration C.

(C) Figure 20.- Concluded. (U)

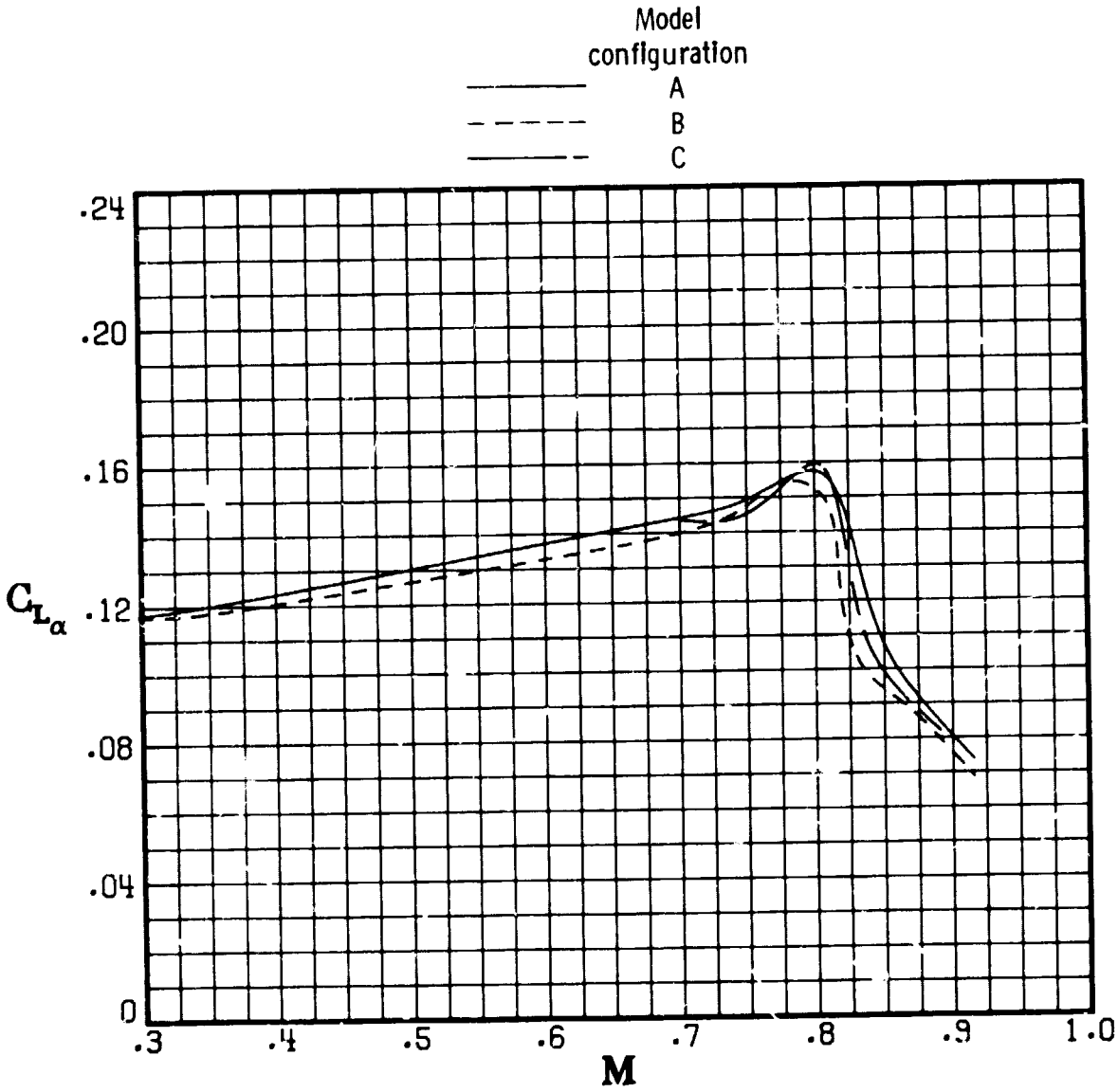

(a) $\alpha = -4^{\circ}$.

(C) Figure 21.- Variation of lift-curve slope with Mach number for model configurations A, B, and C. $\delta_e = 0^{\circ}$; $\beta = 0^{\circ}$. (U)

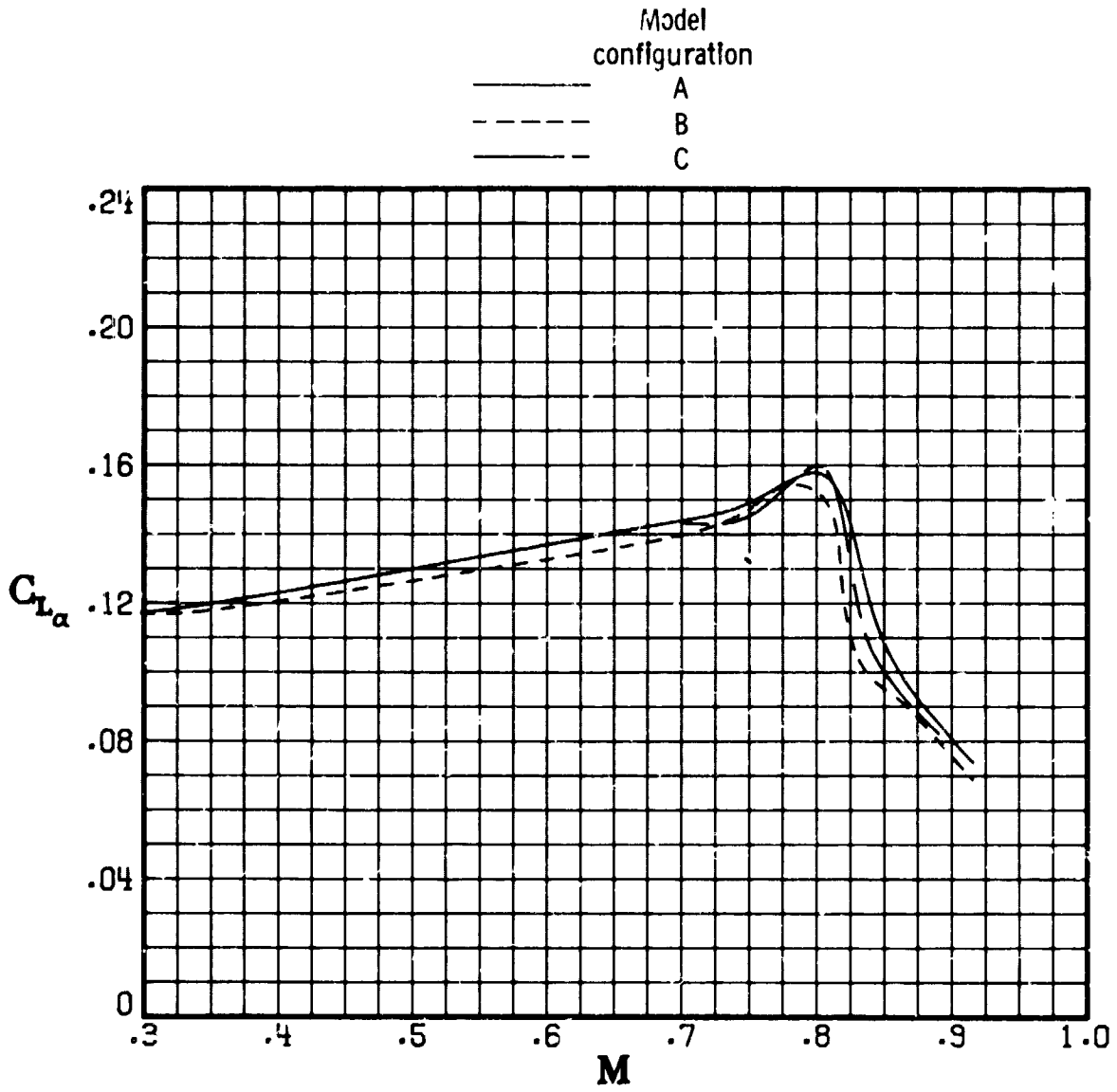

(b) $\alpha \approx -3^{\circ}$.

(C) Figure 21.- Continued. (U)

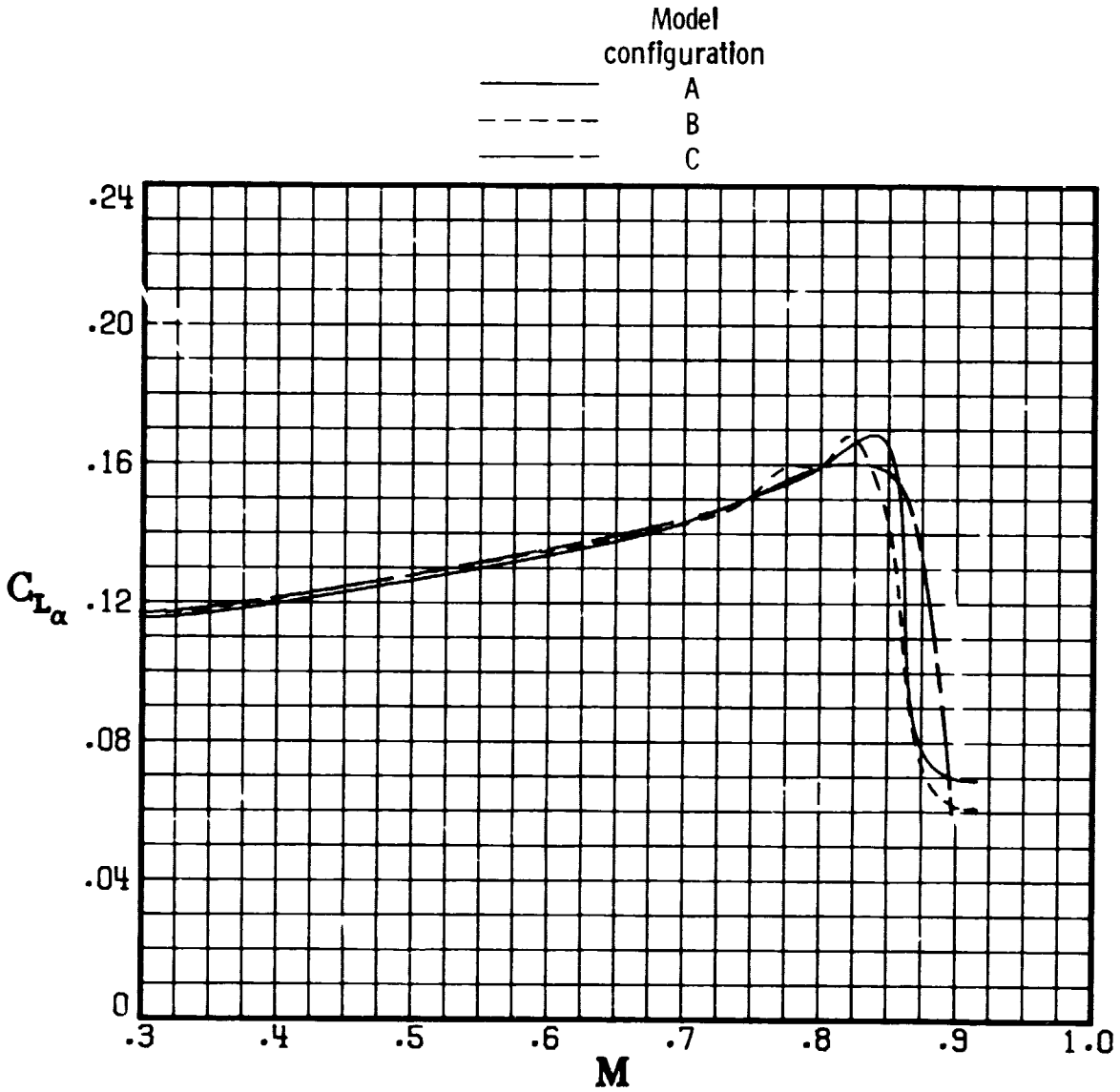

(c) $\alpha = -2^{\circ}$.

(C) Figure 21.- Continued. (U)

C-2

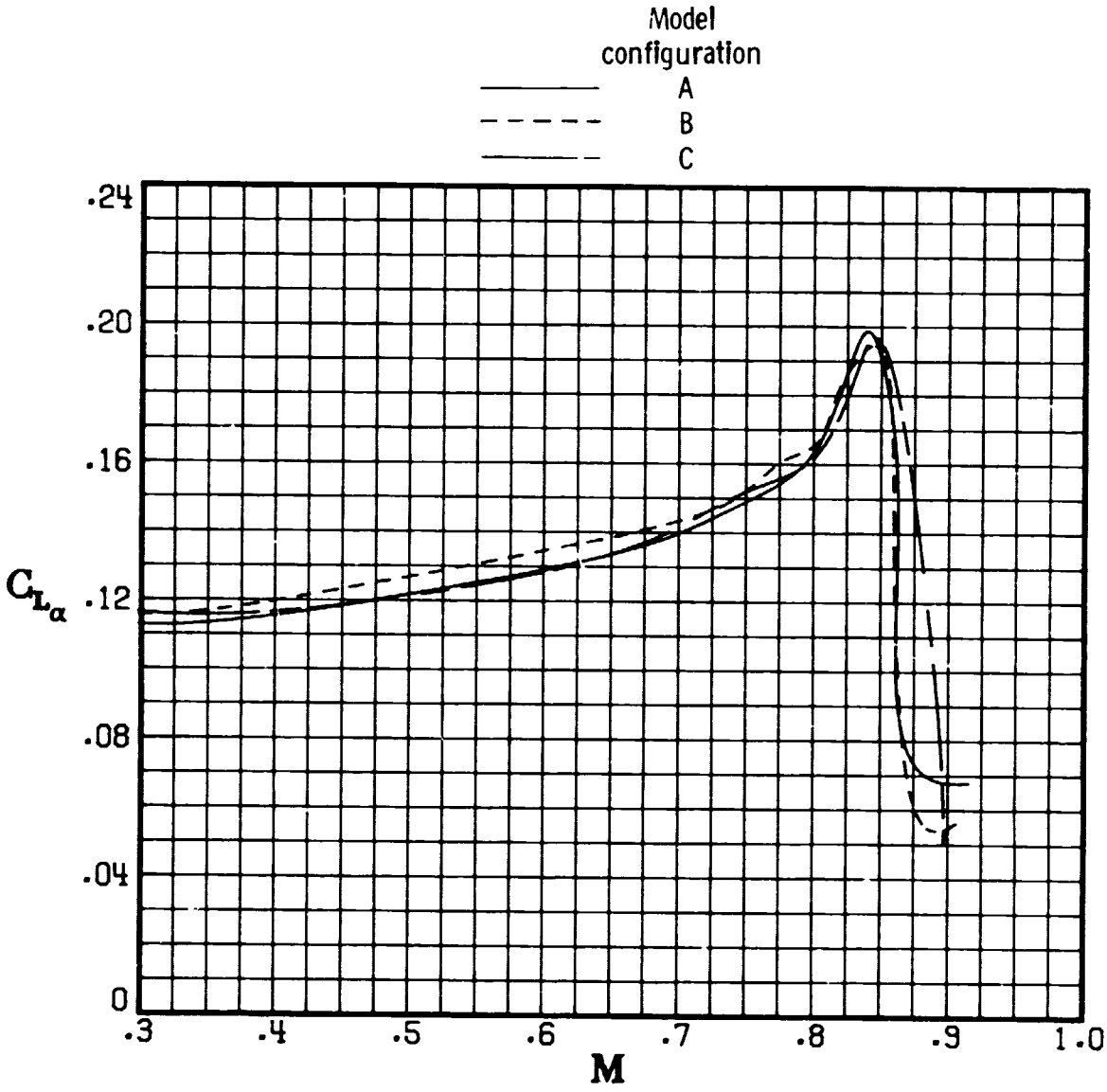

(d) $\alpha = -1^{\circ}$.

(C) Figure 21.- Continued. (U)

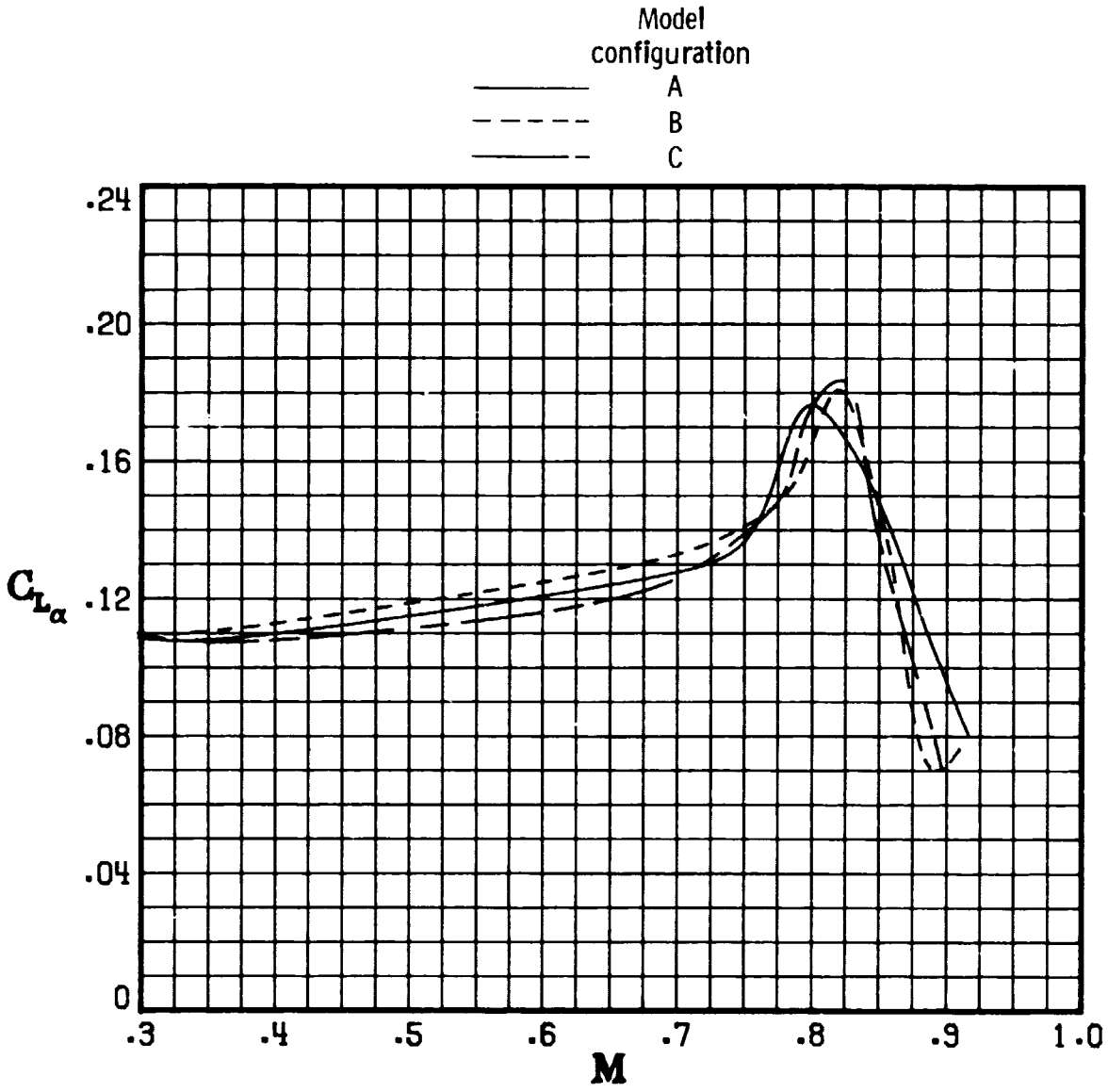

(e) $\alpha = 0^{o}$.

(U) Figure 21.- Continued. (U)

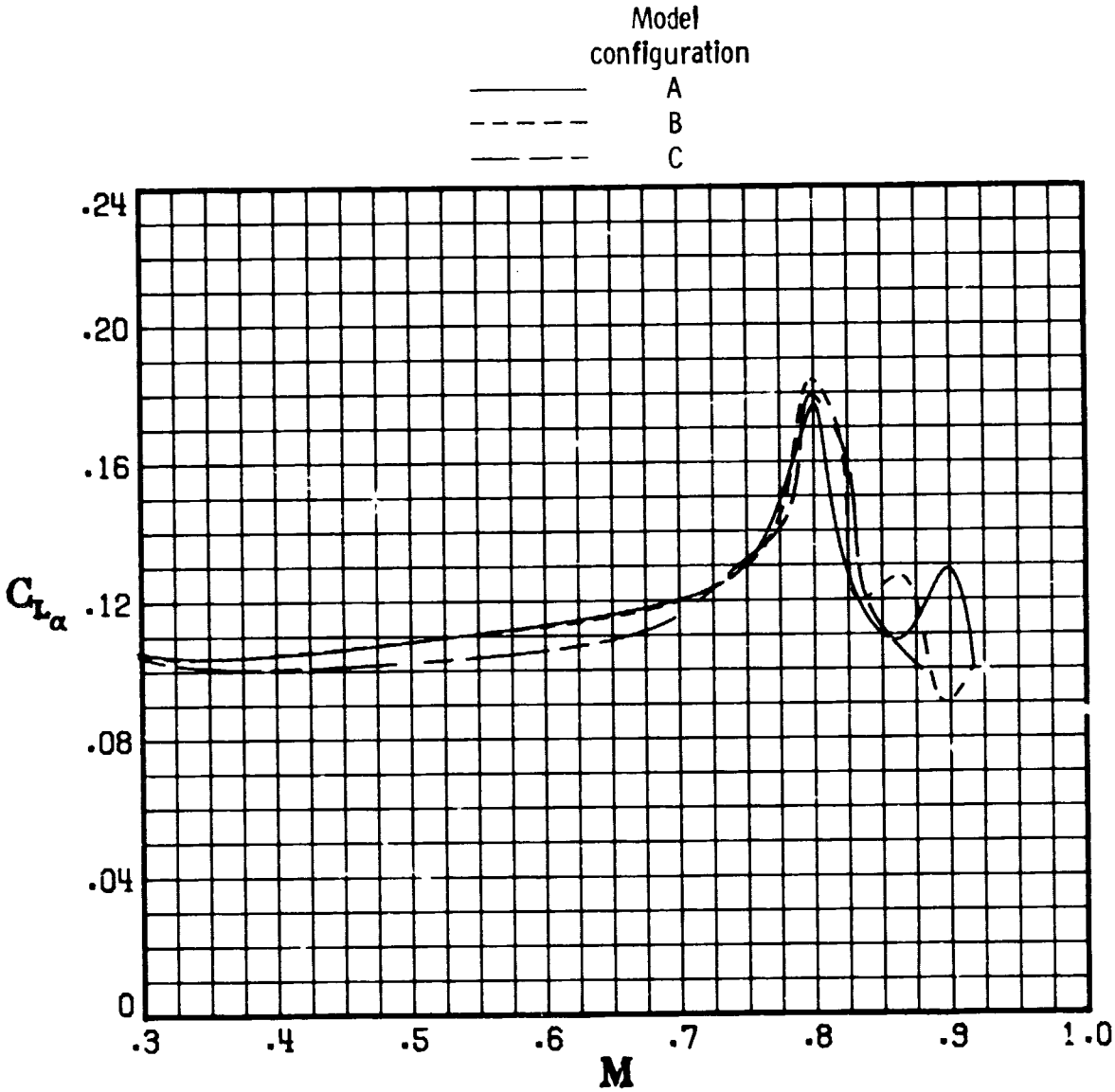

(f) $\alpha = 1^{\circ}$.

Figure 21.- Continued. (U)

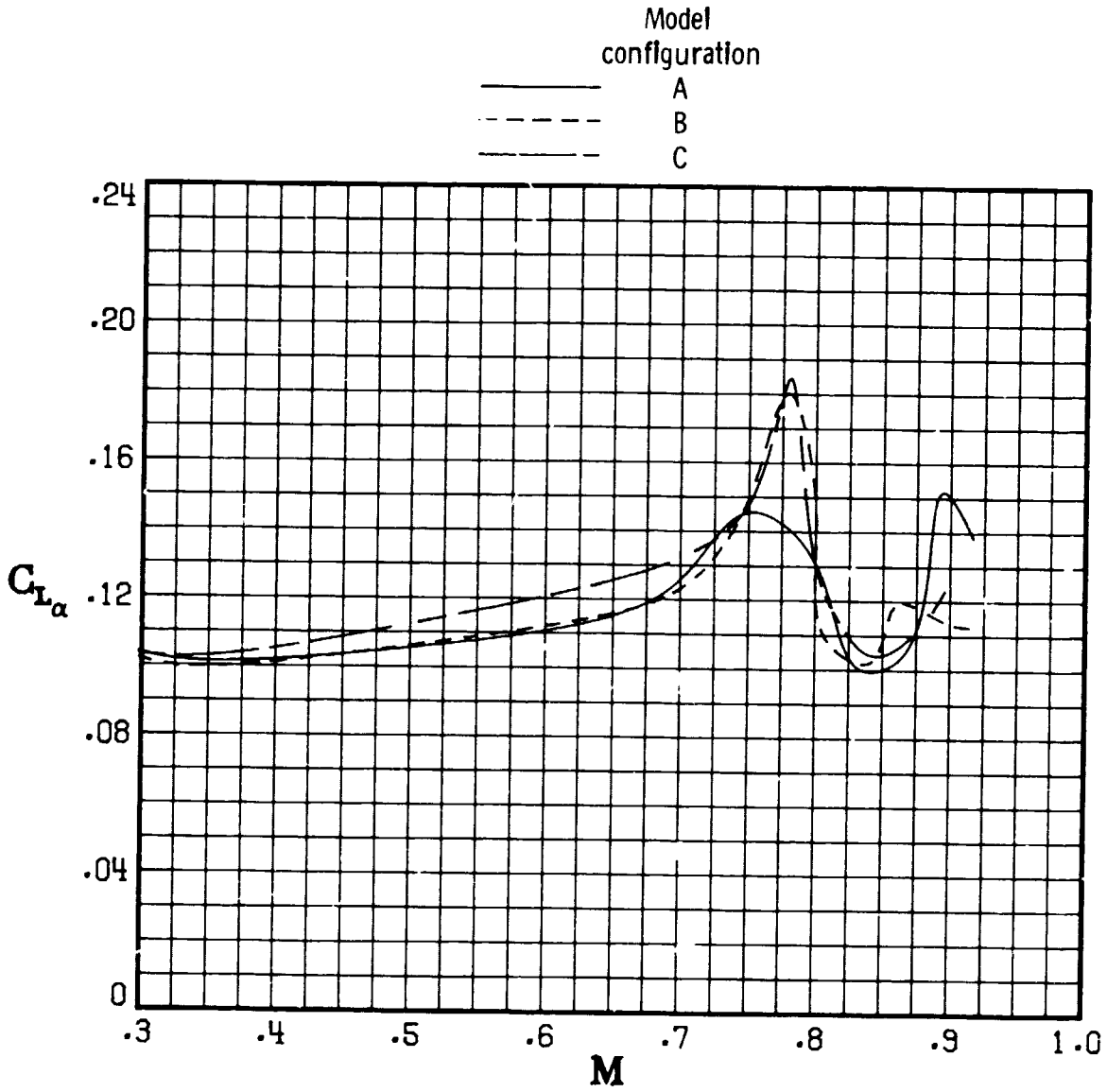

(g) $\alpha = 2^{o}$.

(C) Figure 21.- Continued. (U)

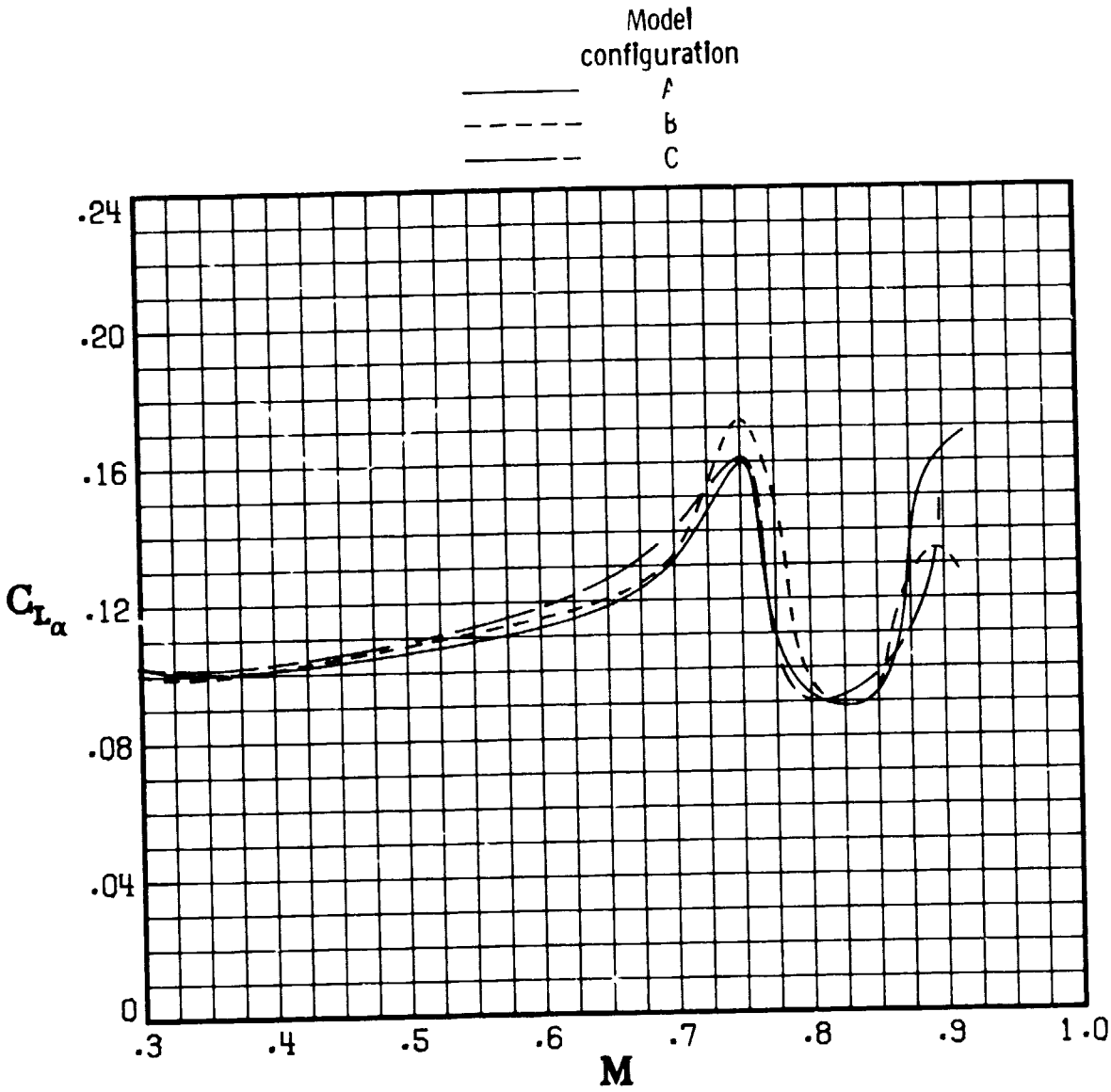

(h) $\alpha = 3^{o}$.

Figure 21.- Concluded. (U)

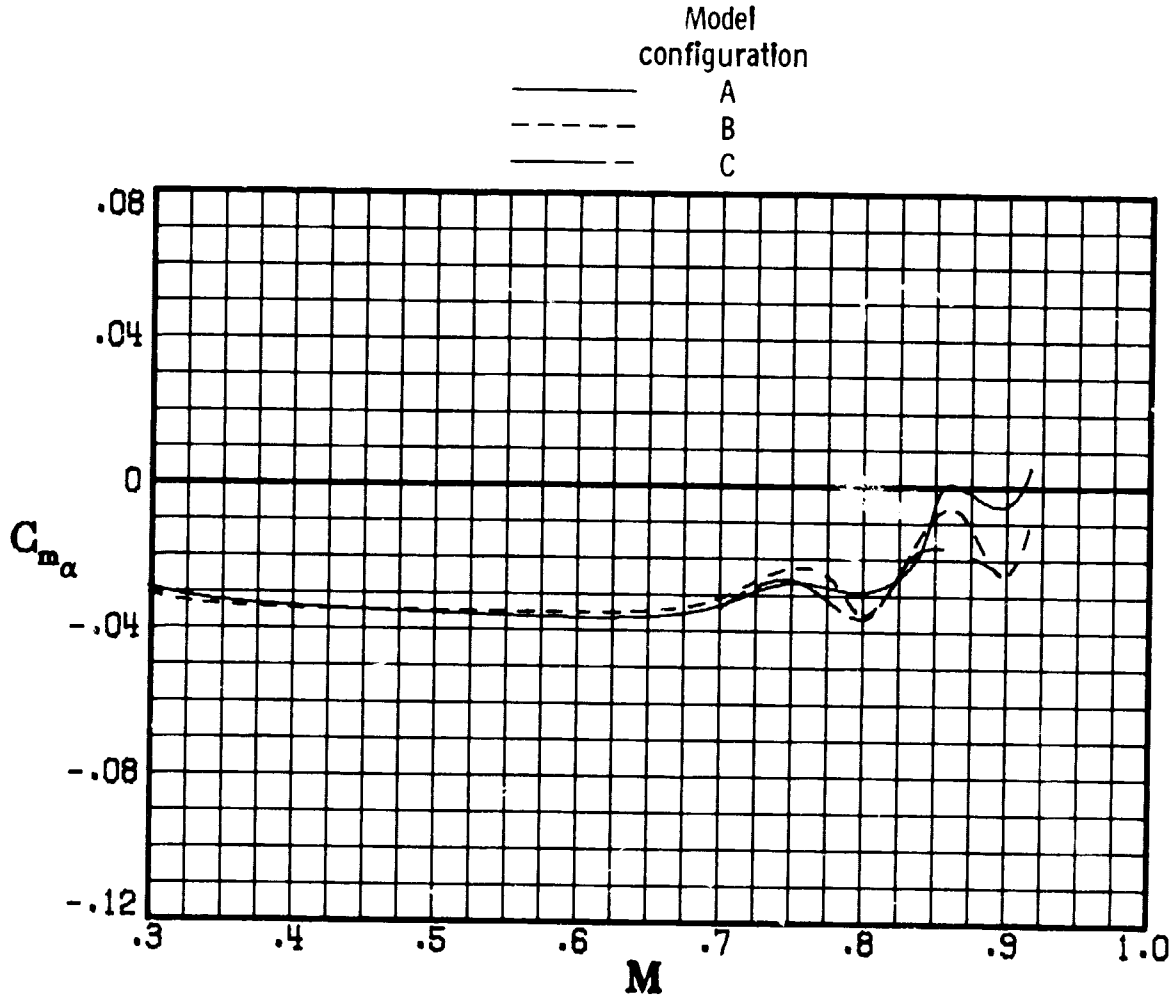

(a) $\alpha = -4^{\circ}$.

(C) Figure 22.- Variation of static stability derivative with Mach number for model configurations A, B, and C. $\delta_e = 0^{\circ}$; $\beta = 0^{\circ}$. (U)

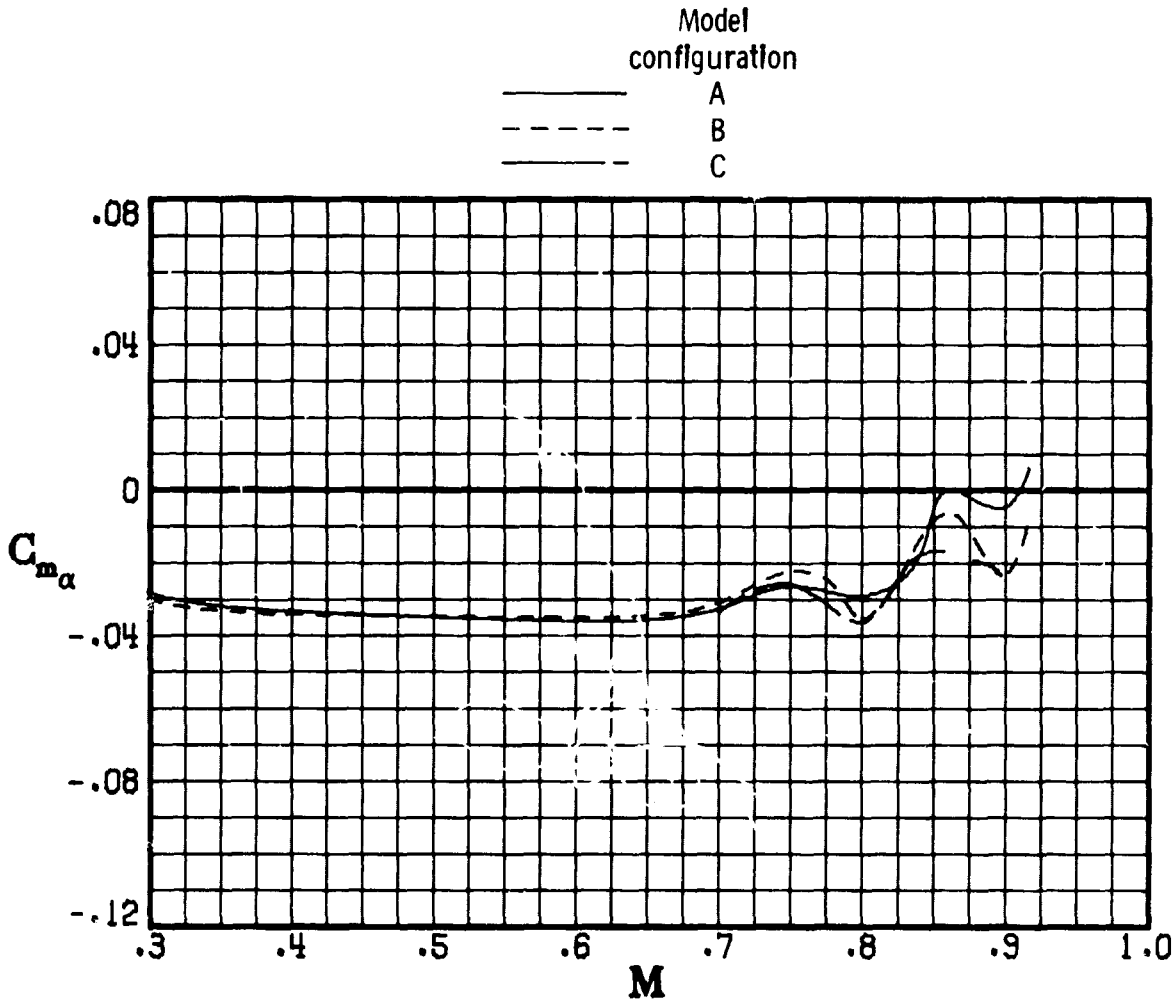

(b) $\alpha = -3^{o}$.

(C) Figure 22.- Continued. (U)

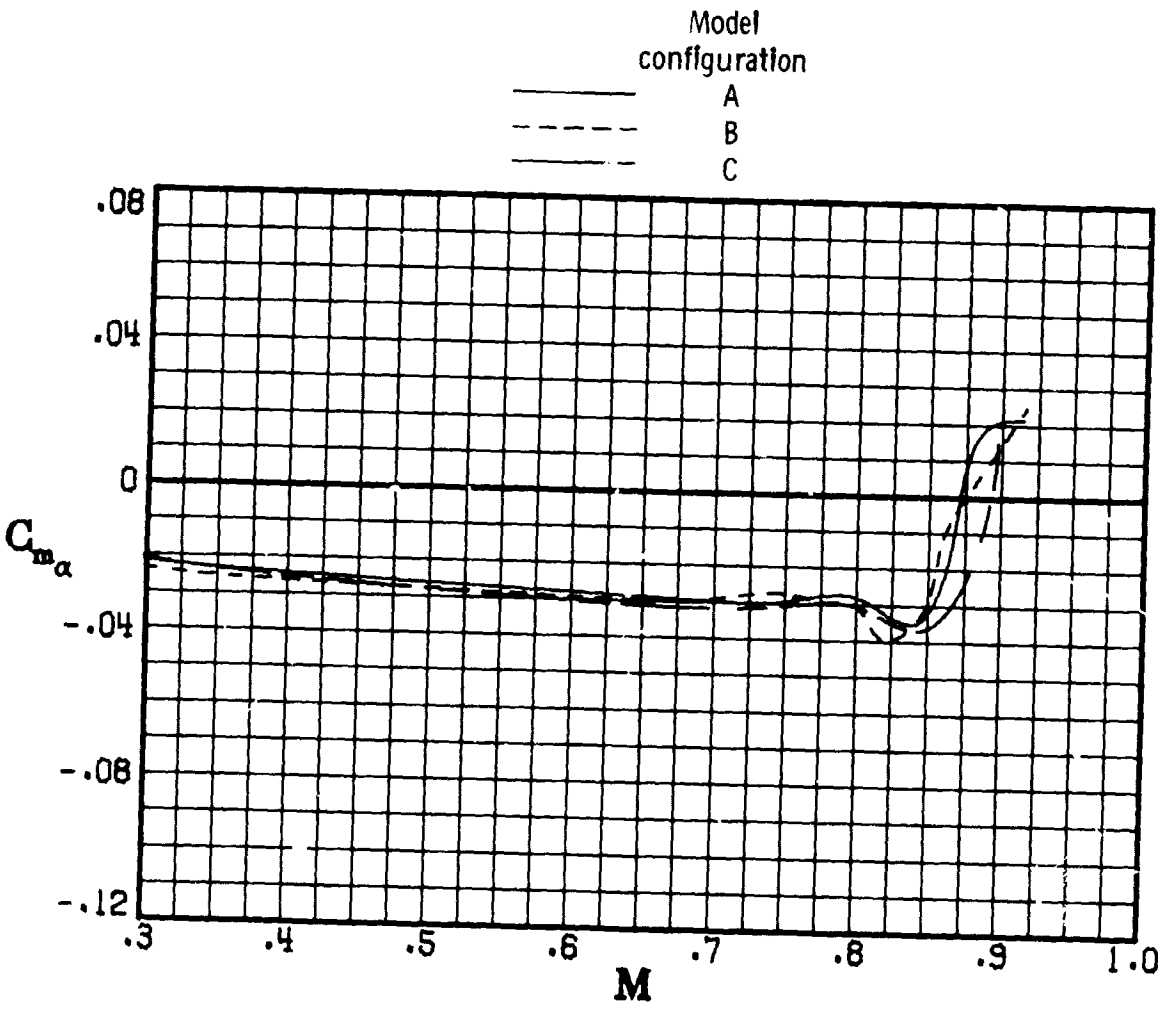

(c) $\alpha = -2^{\circ}$.

Figure 22.- Continued. (U)

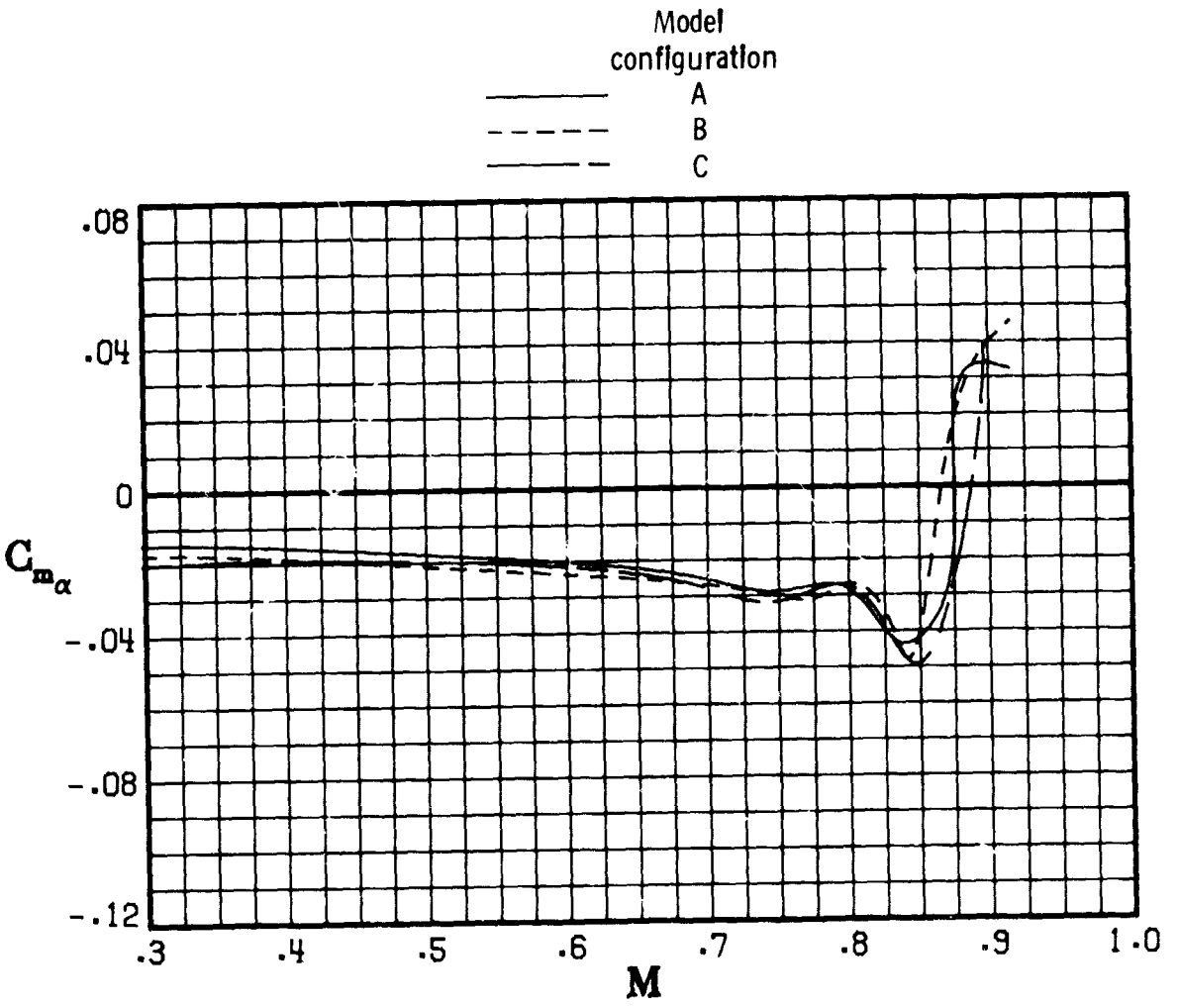

(d) $\alpha = -1^{\circ}$.

Figure 22.- Continued. (U)

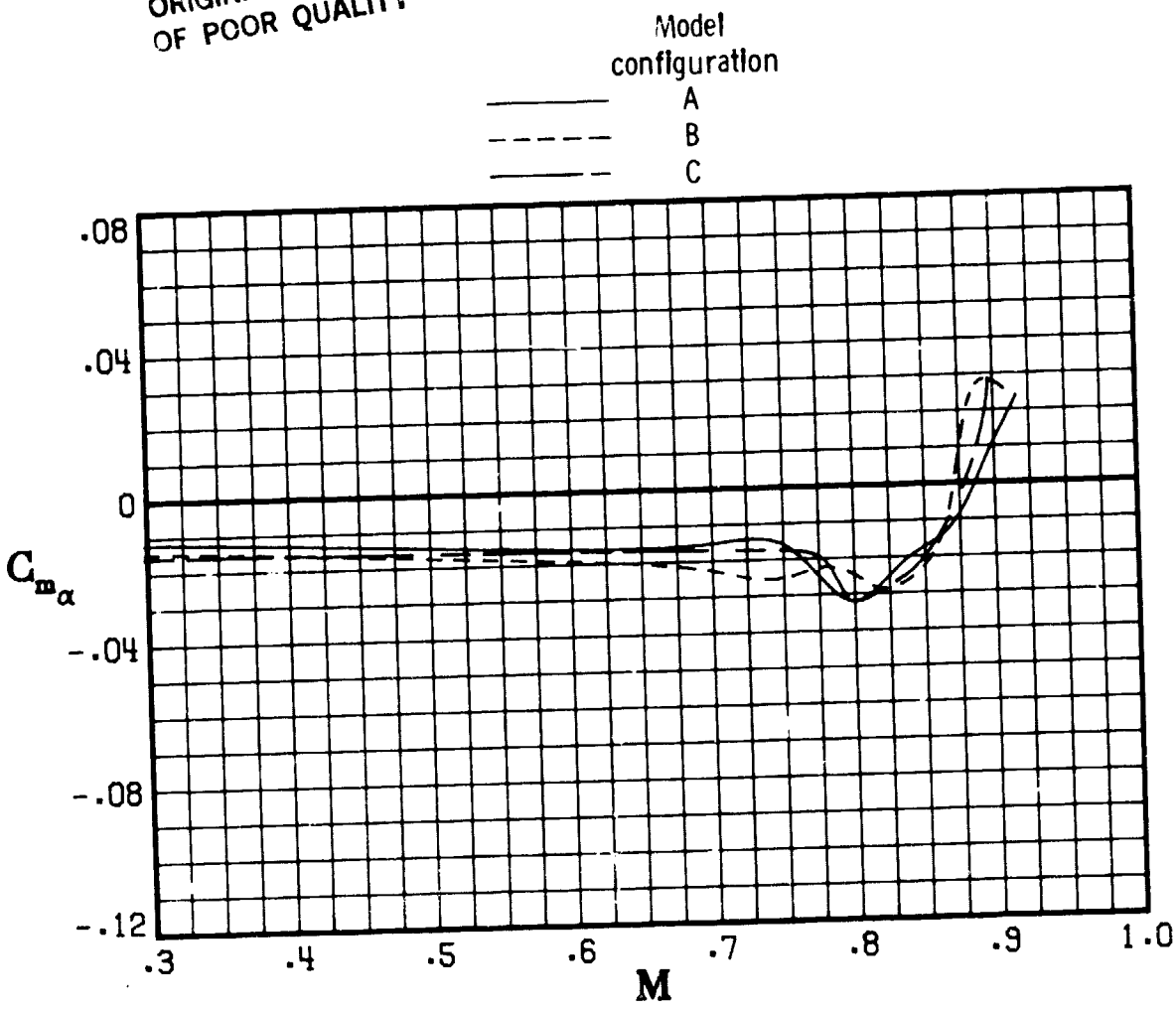

(e) $\alpha = 0^{o}$.

Figure 22.- Continued. (U)

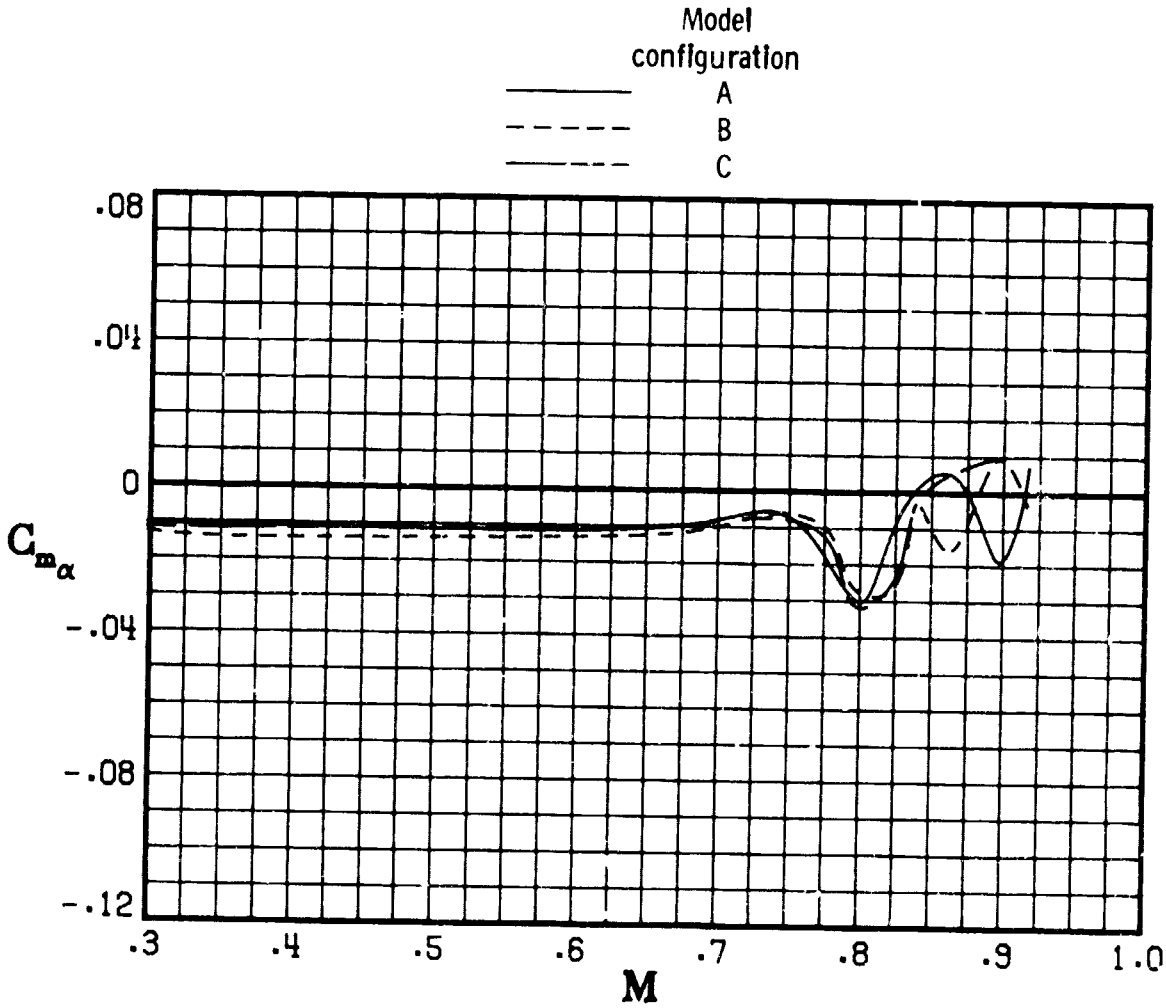

(f) $\alpha = 1^{\circ}$.

Figure 22.- Continued. (U)

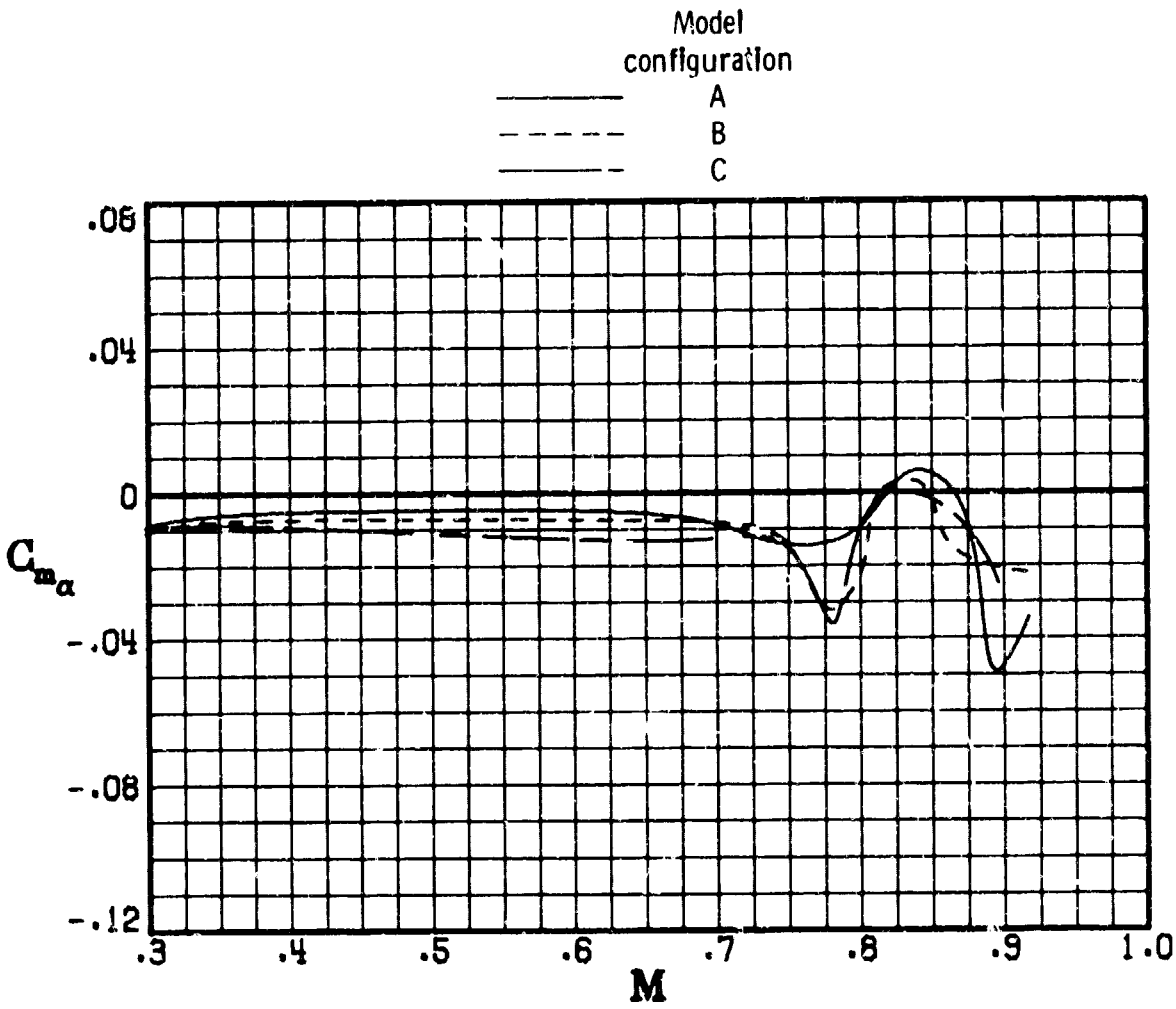

(g) $\alpha = 2^{o}$.

Figure 22.- Continued. (U)

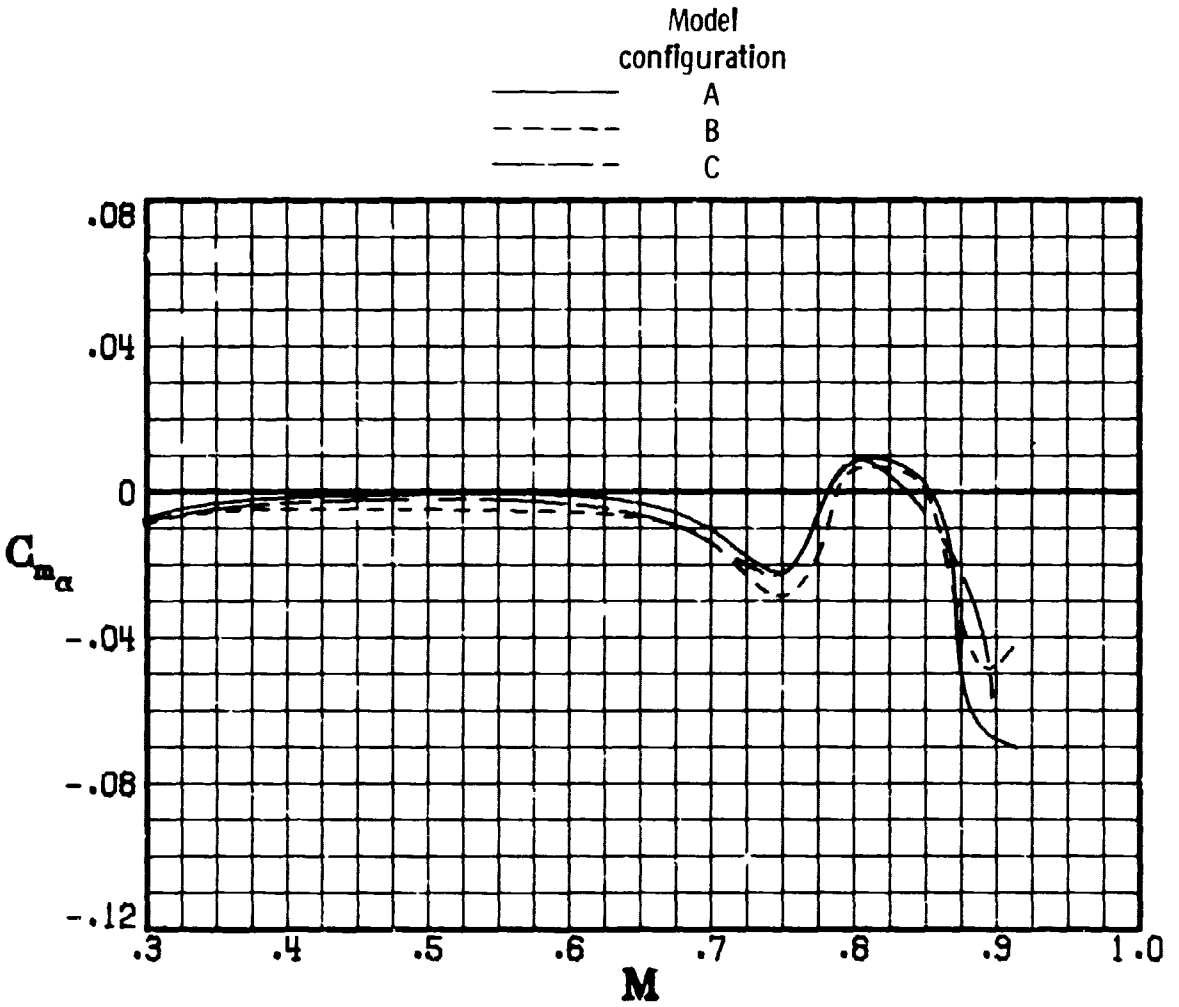

(h) $\alpha = 3^{\circ}$.

Figure 22.- Concluded. (U)

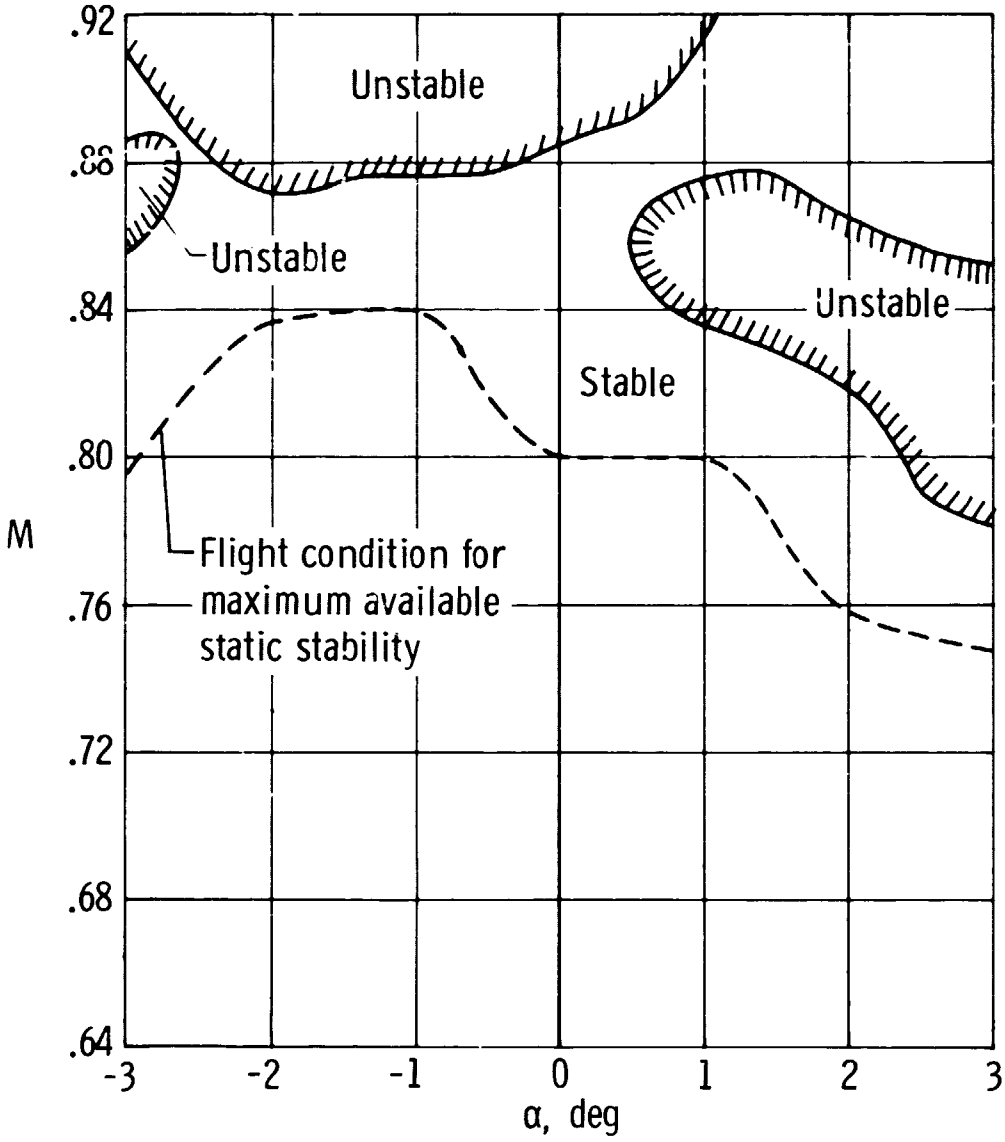

(a) Model configuration A.

Figure 23.- Longitudinal static stability boundaries. (U)

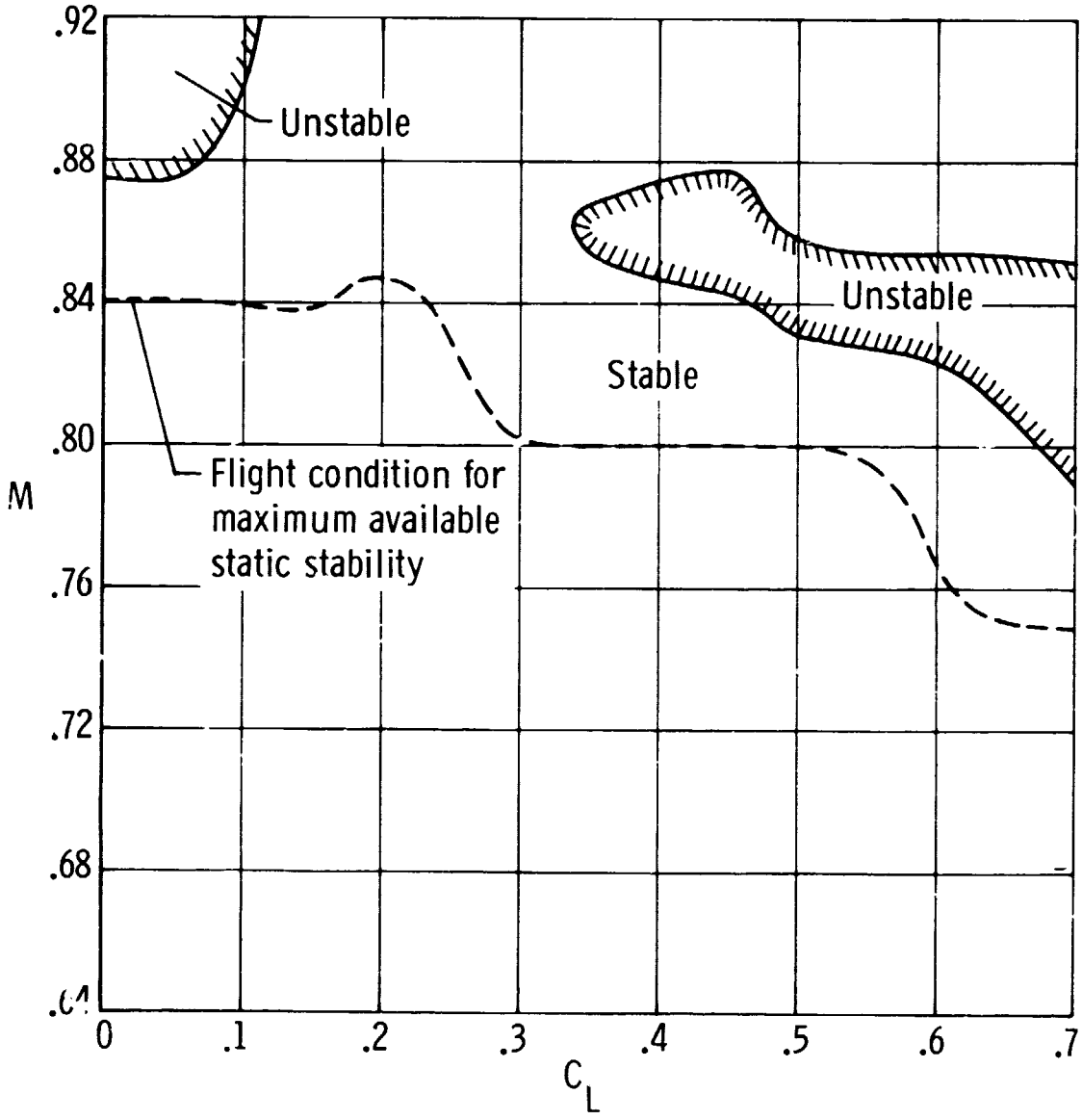

(a) Concluded.

Figure 23.–Continued. (U)

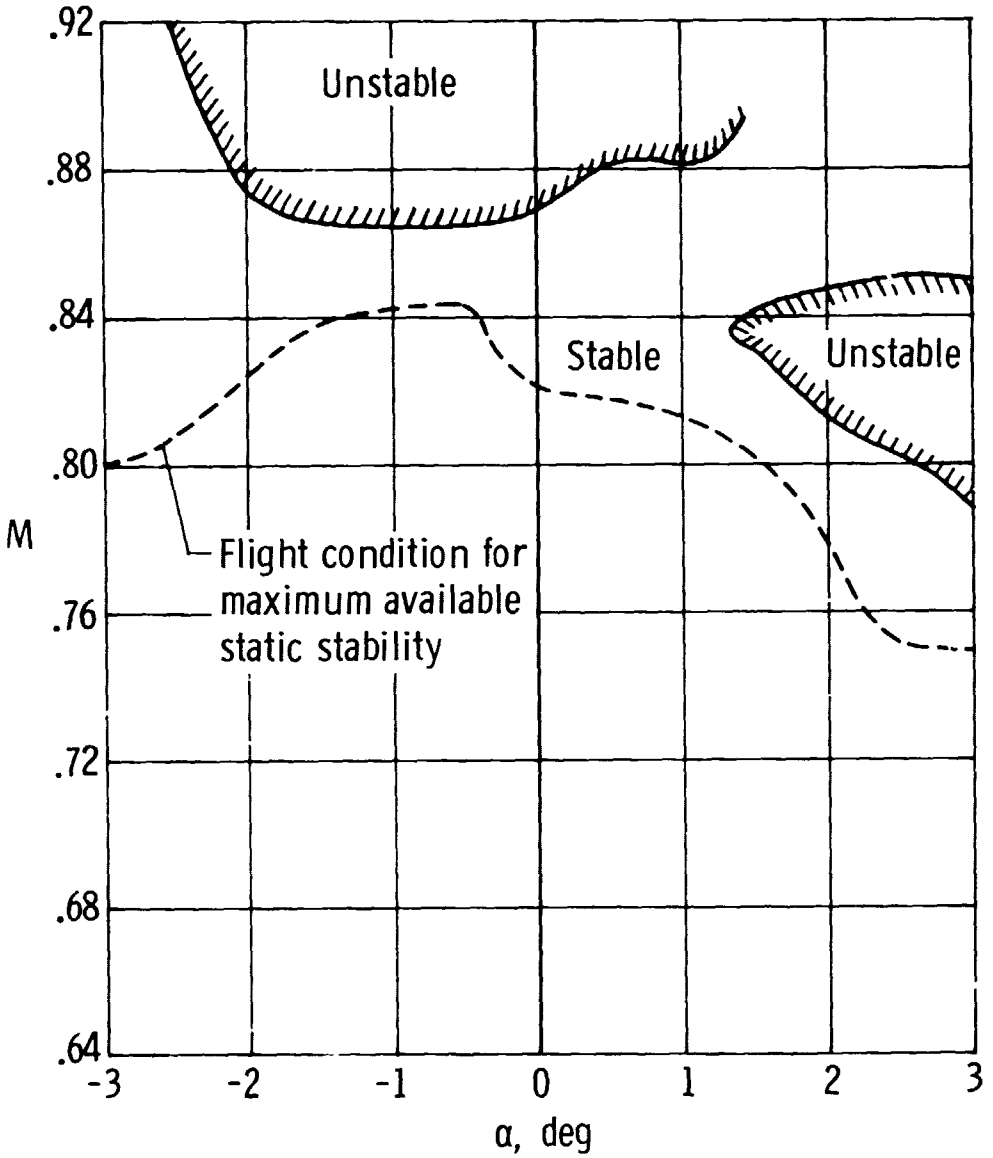

(b) Model configuration B.

(C) Figure 23.- Continued. (U)

[redacted]

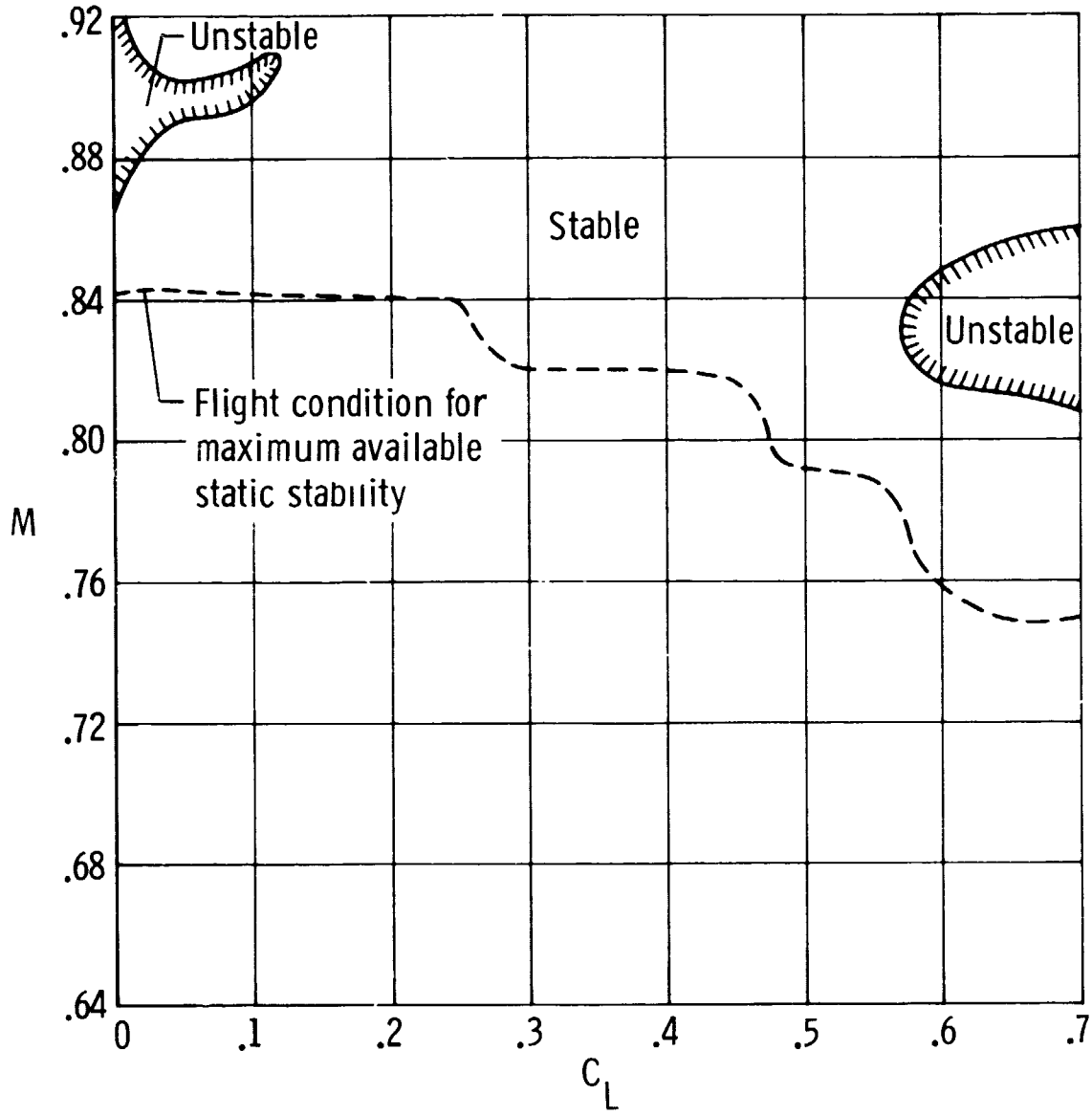

(b) Concluded.

(C) Figure 23.- Continued. (U)

[redacted]

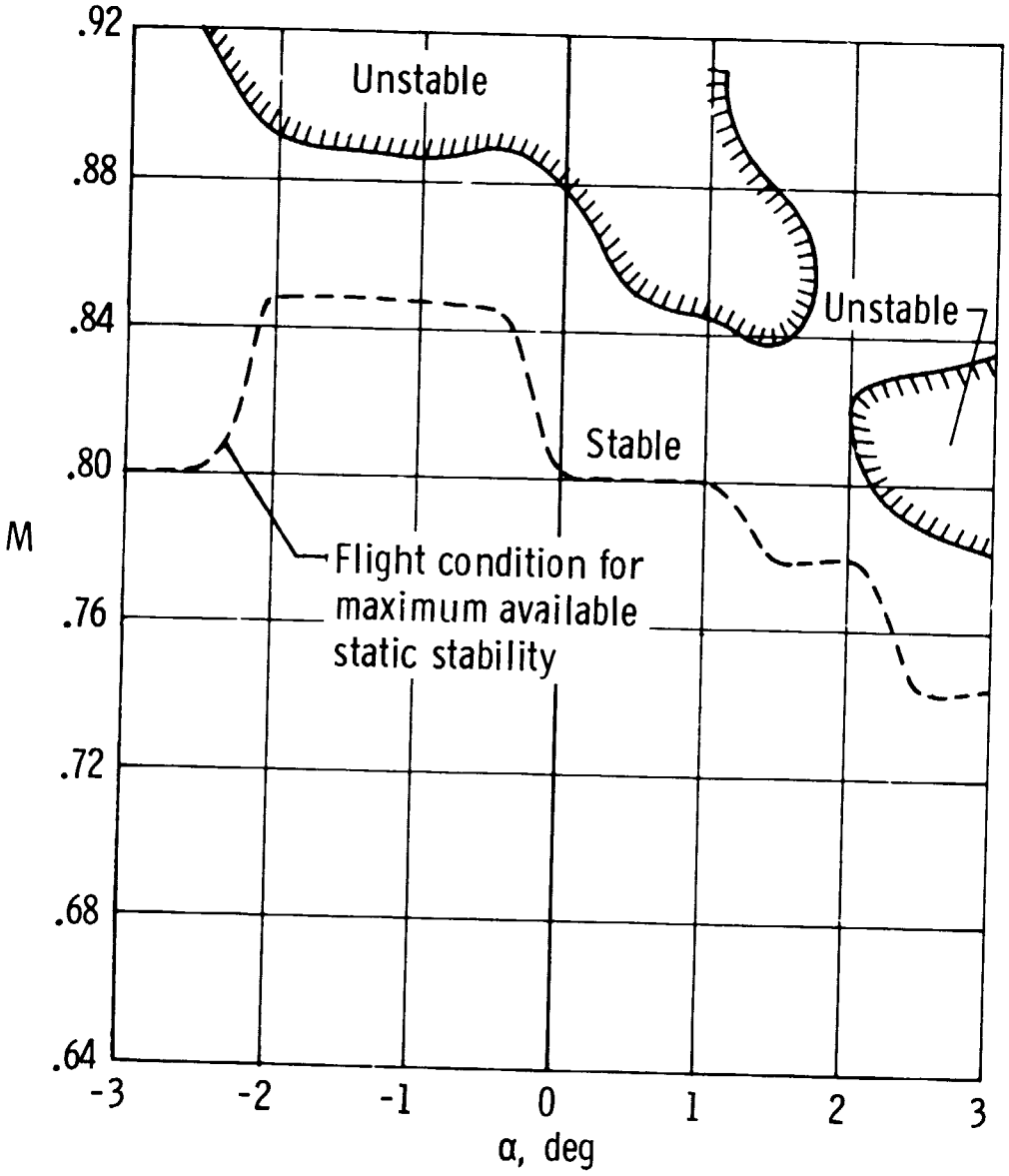

(c) Model configuration C.

Figure 23.- Continued. (U)

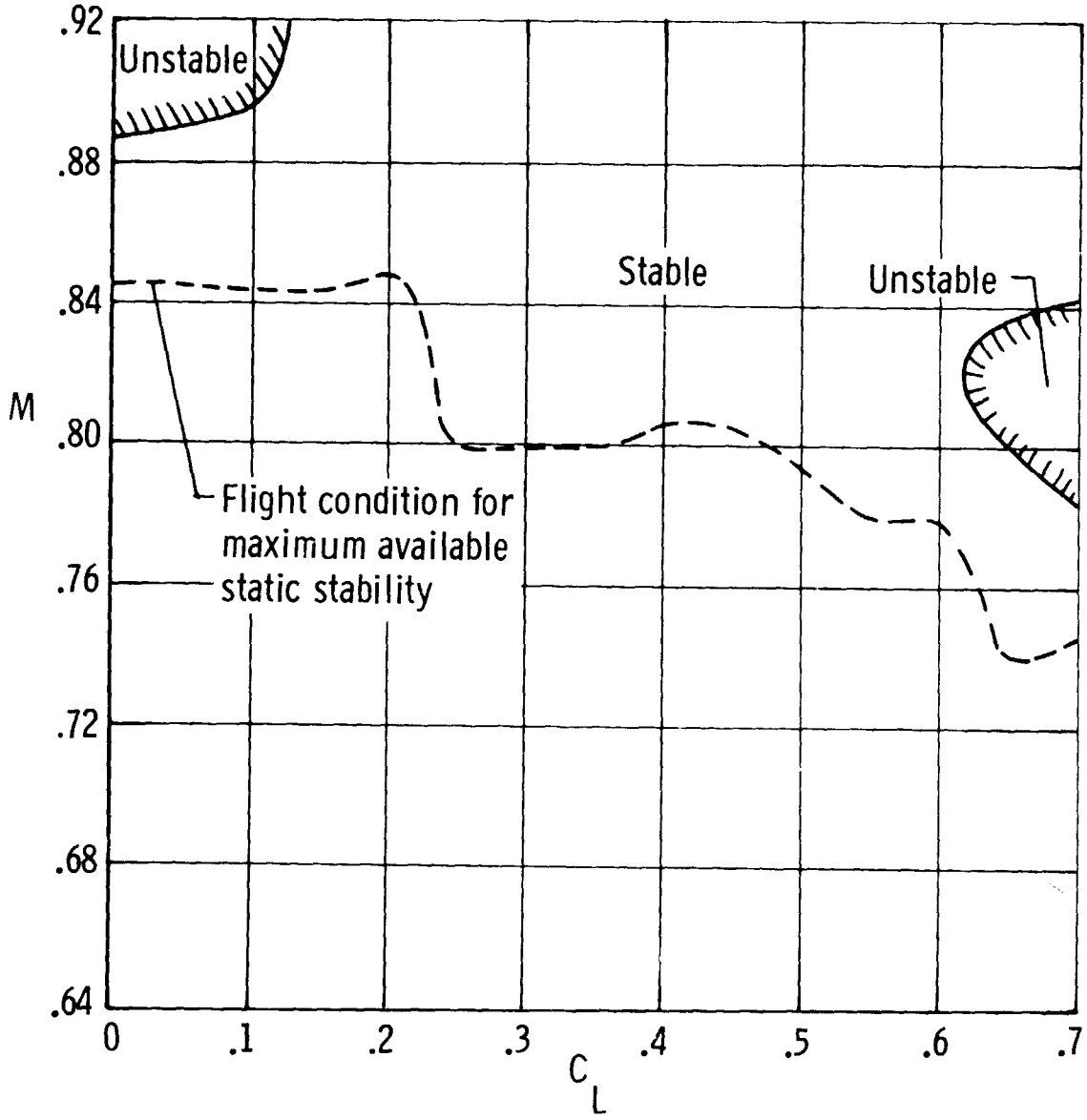

(c) Concluded.

Figure 23.- Concluded. (U)

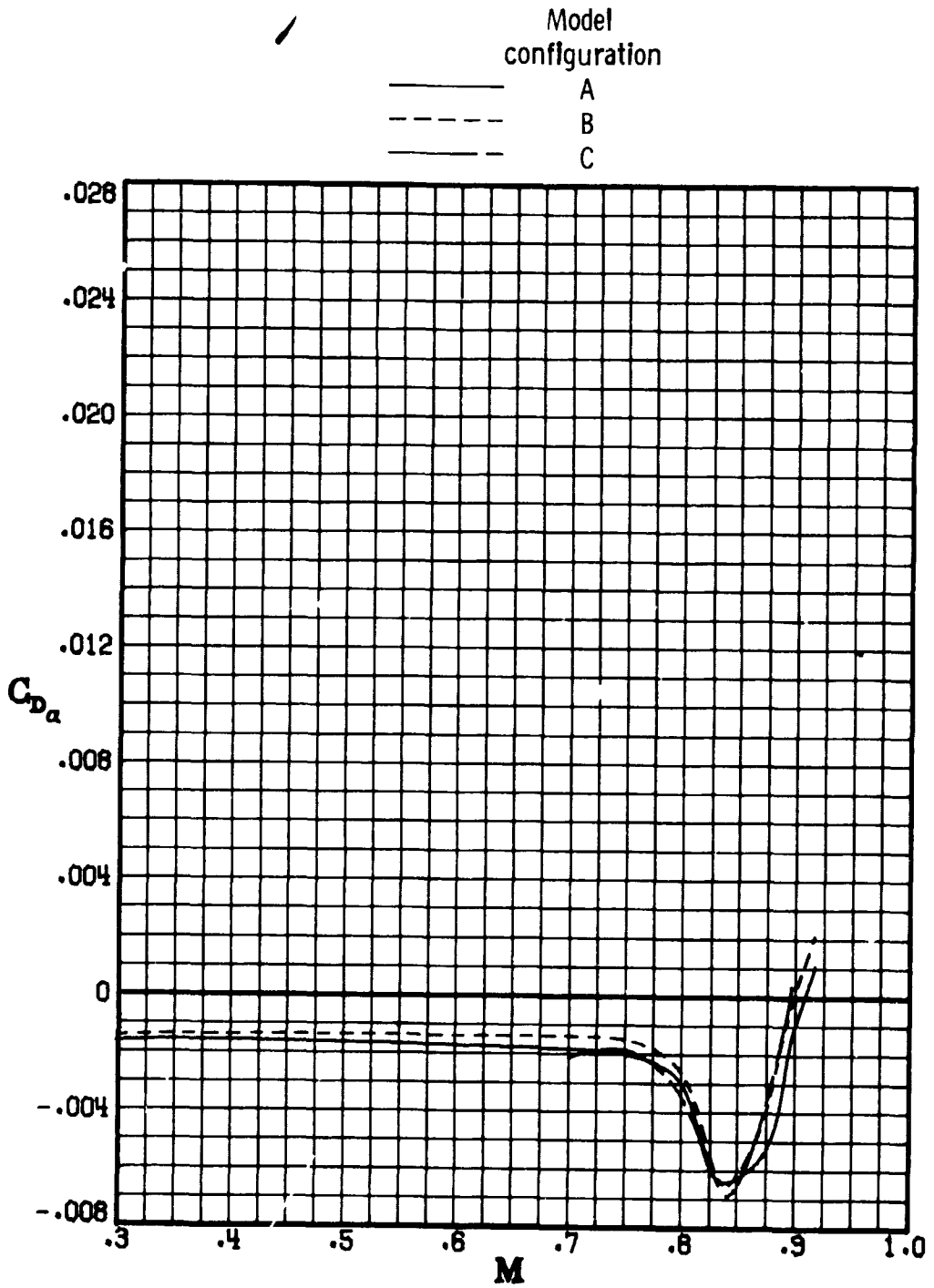

(a) $C_L = 0.0$.

Figure 24.- Variation of drag-curve slope with Mach number for model configurations A, B, and C. $\delta_e = 0^o$; $\beta = 0^o$. (U)

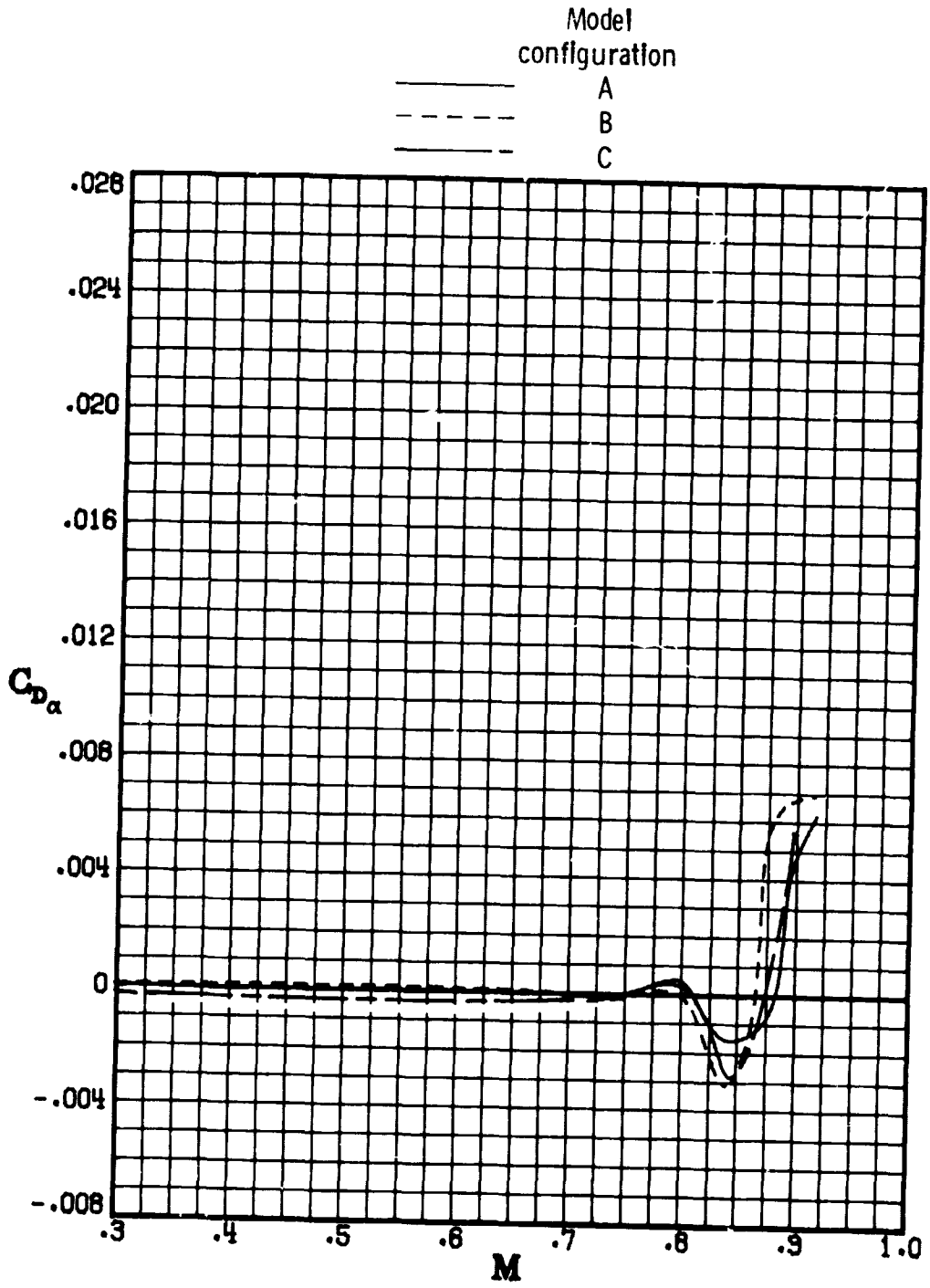

(b) $C_L = 0.1$.

Figure 24.- Continued. (U)

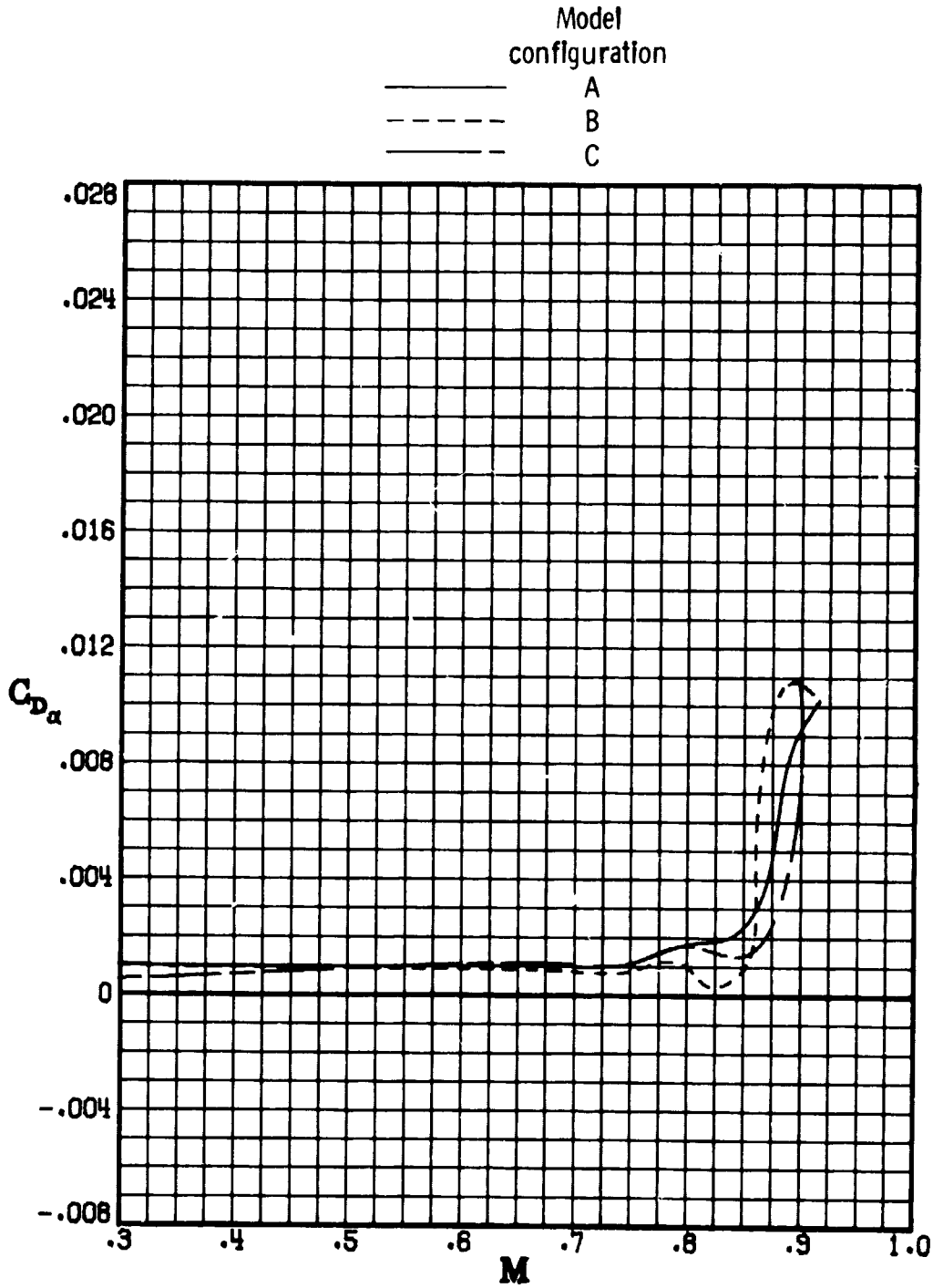

(c) $C_L = 0.2$.

Figure 24.- Continued. (U)

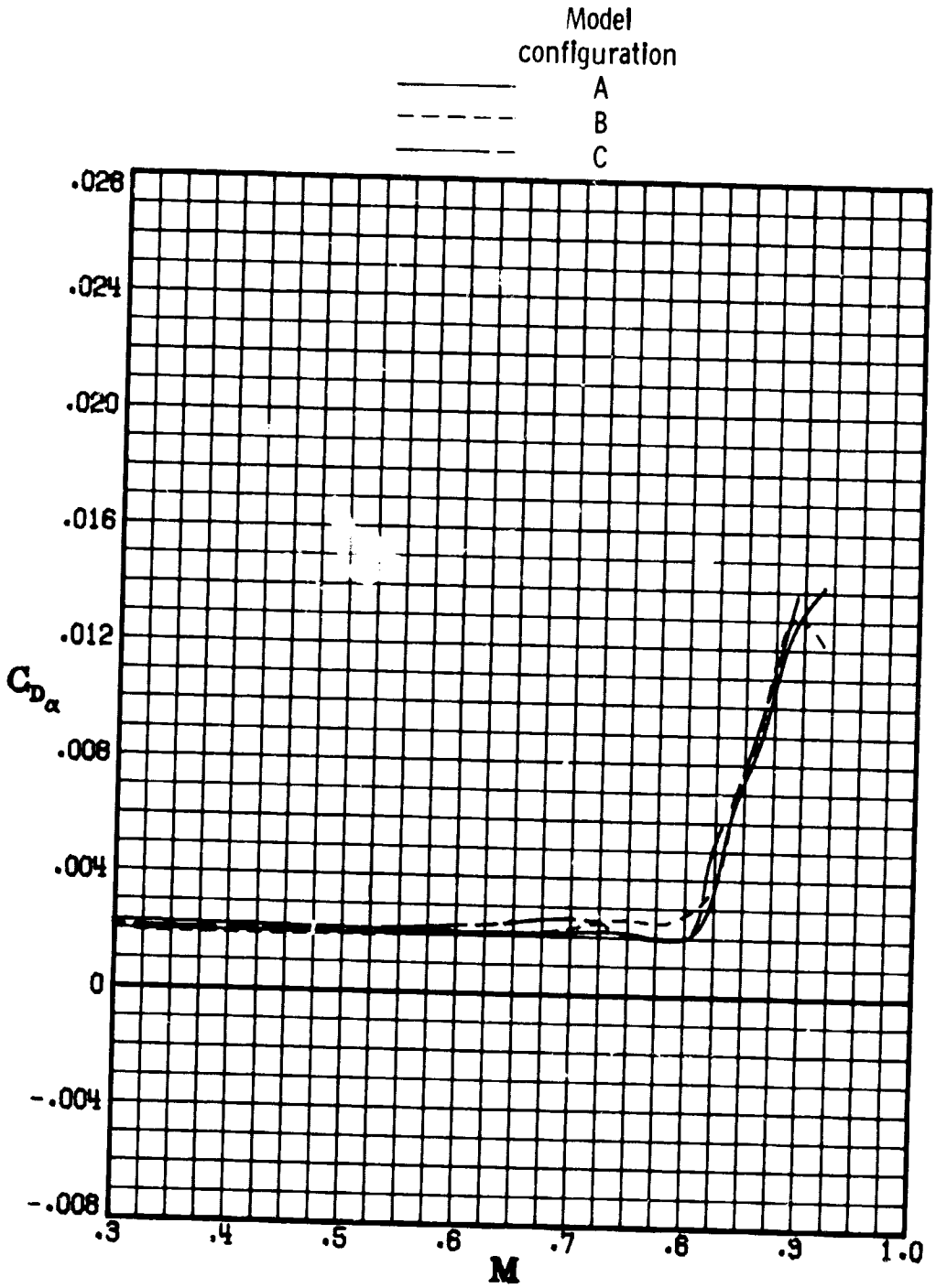

(d) $C_L = 0.3$.

Figure 24.- Continued. (U)

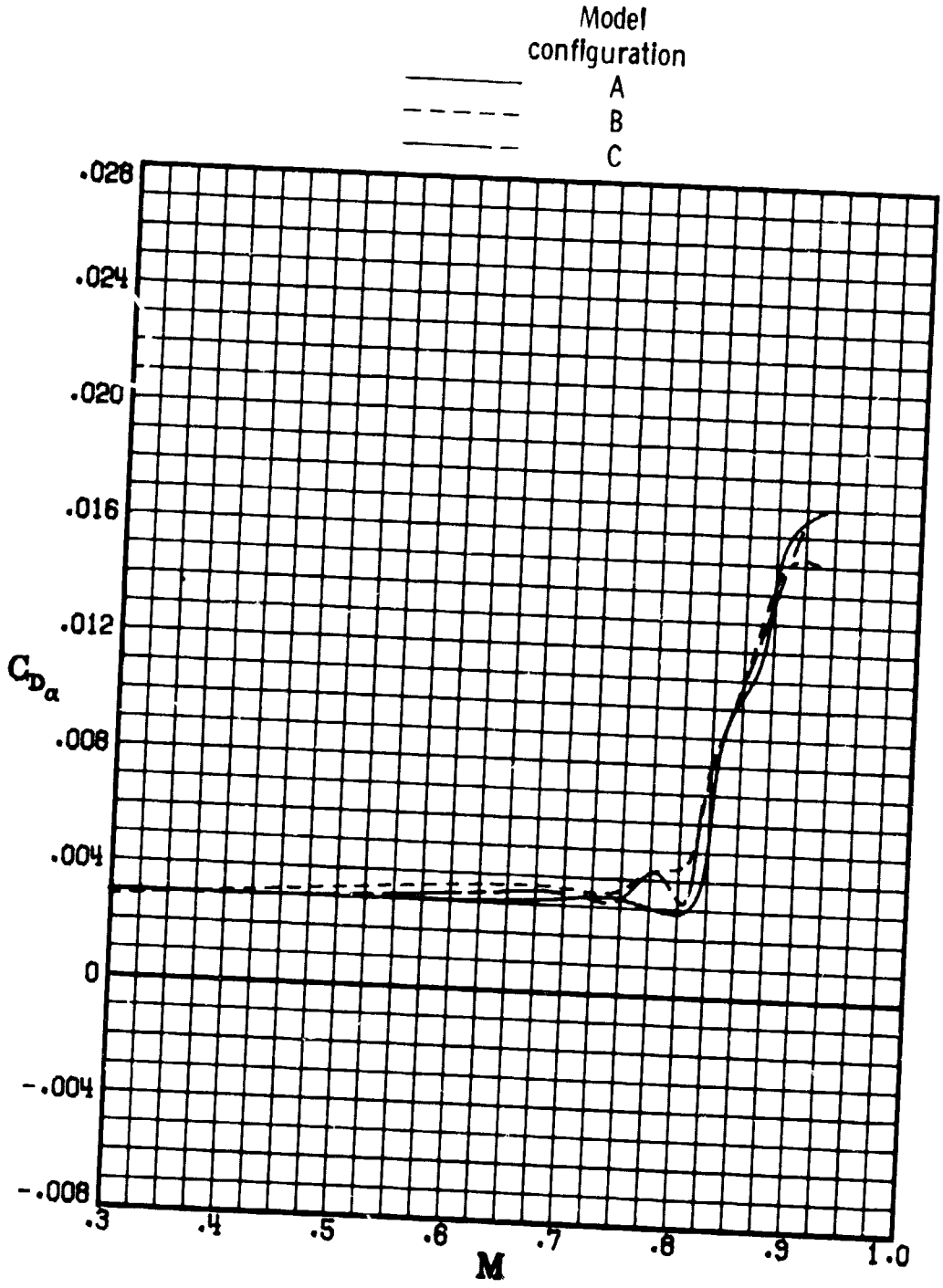

(e) $C_L = 0.4$.

Figure 24.- Continued. (U)

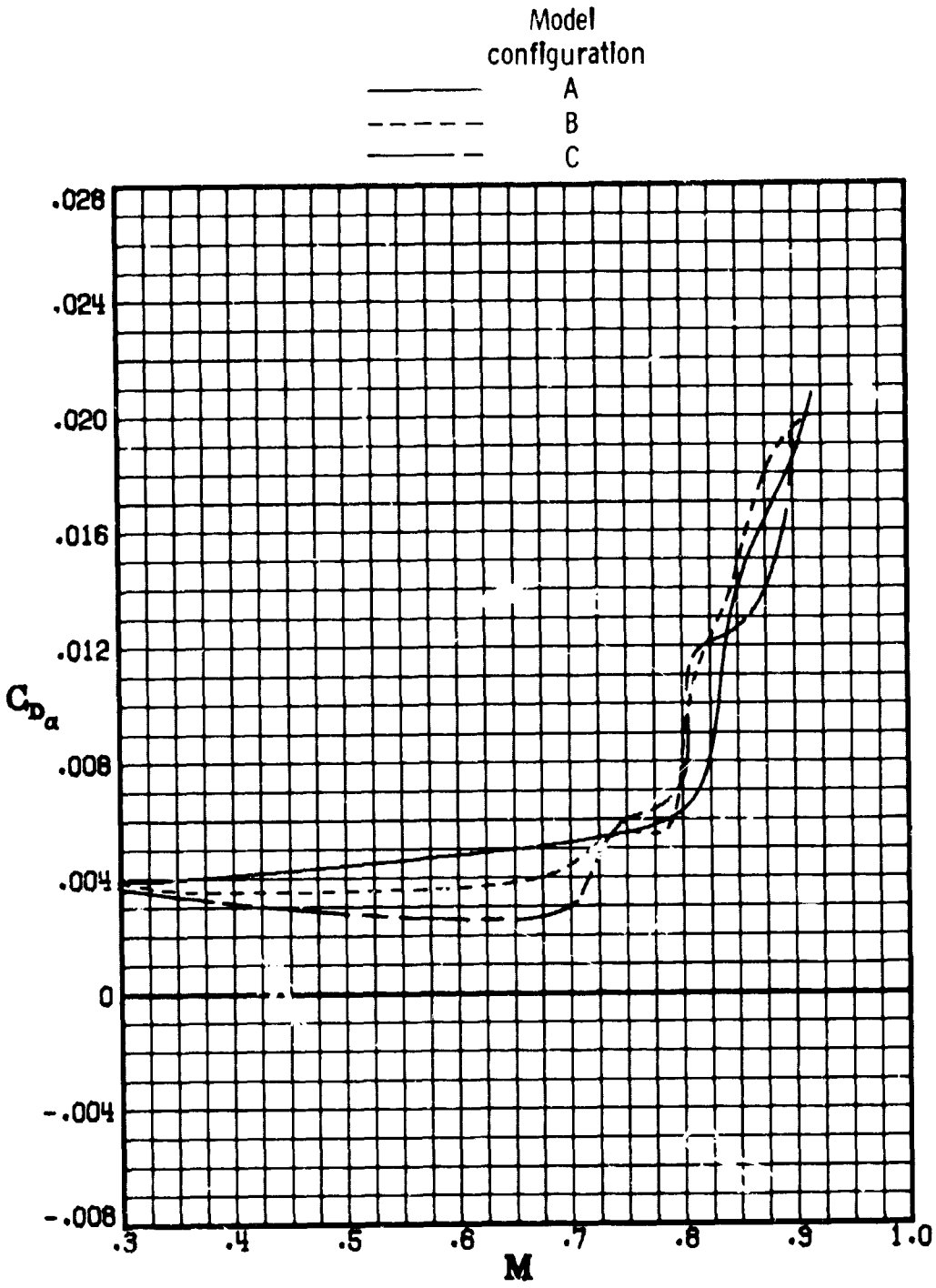

(f) $C_L = 0.5$.

Figure 24.- Continued. (U)

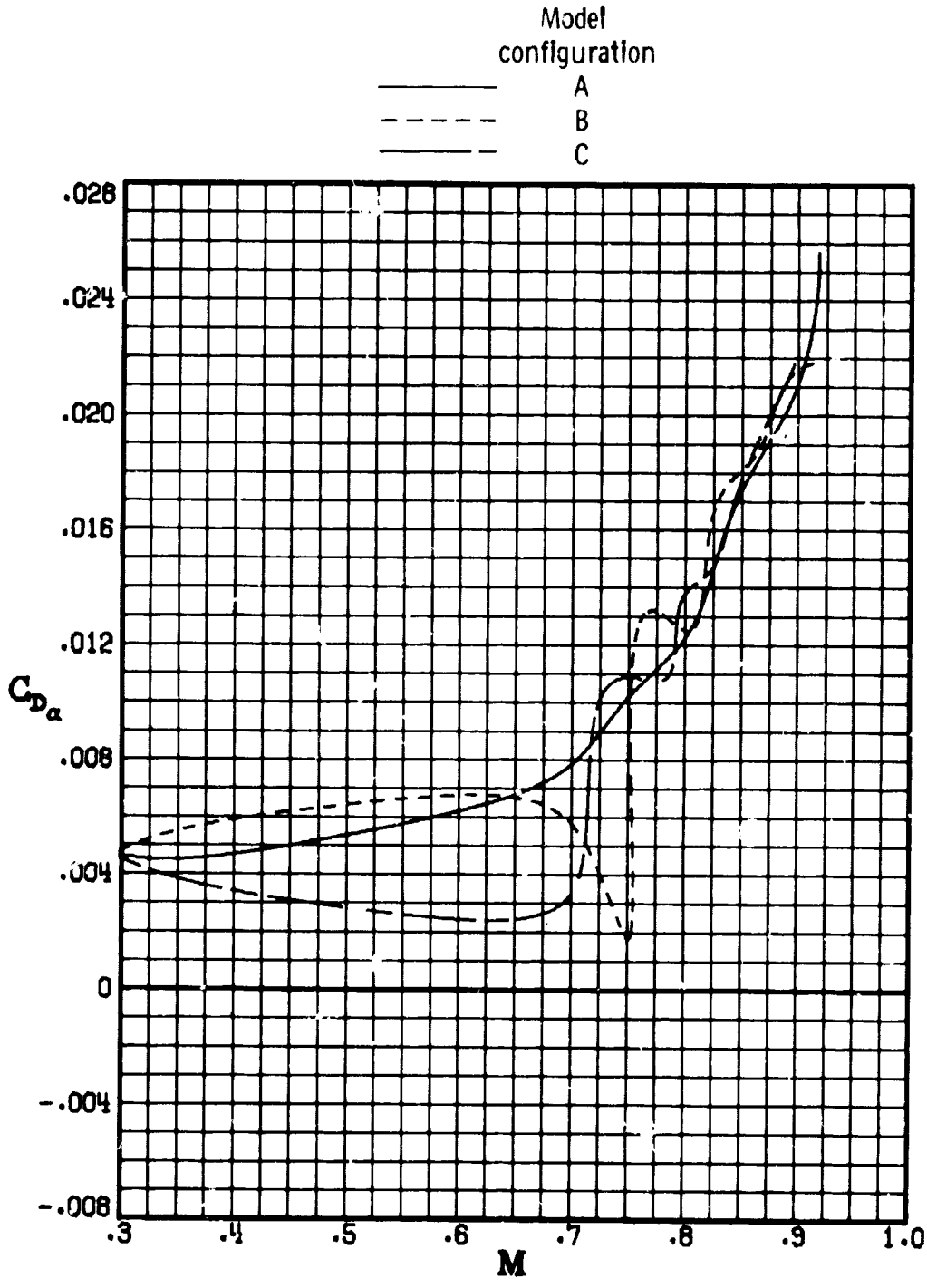

(g) $C_L \approx 0.6$.

Figure 24.- Concluded. (U)

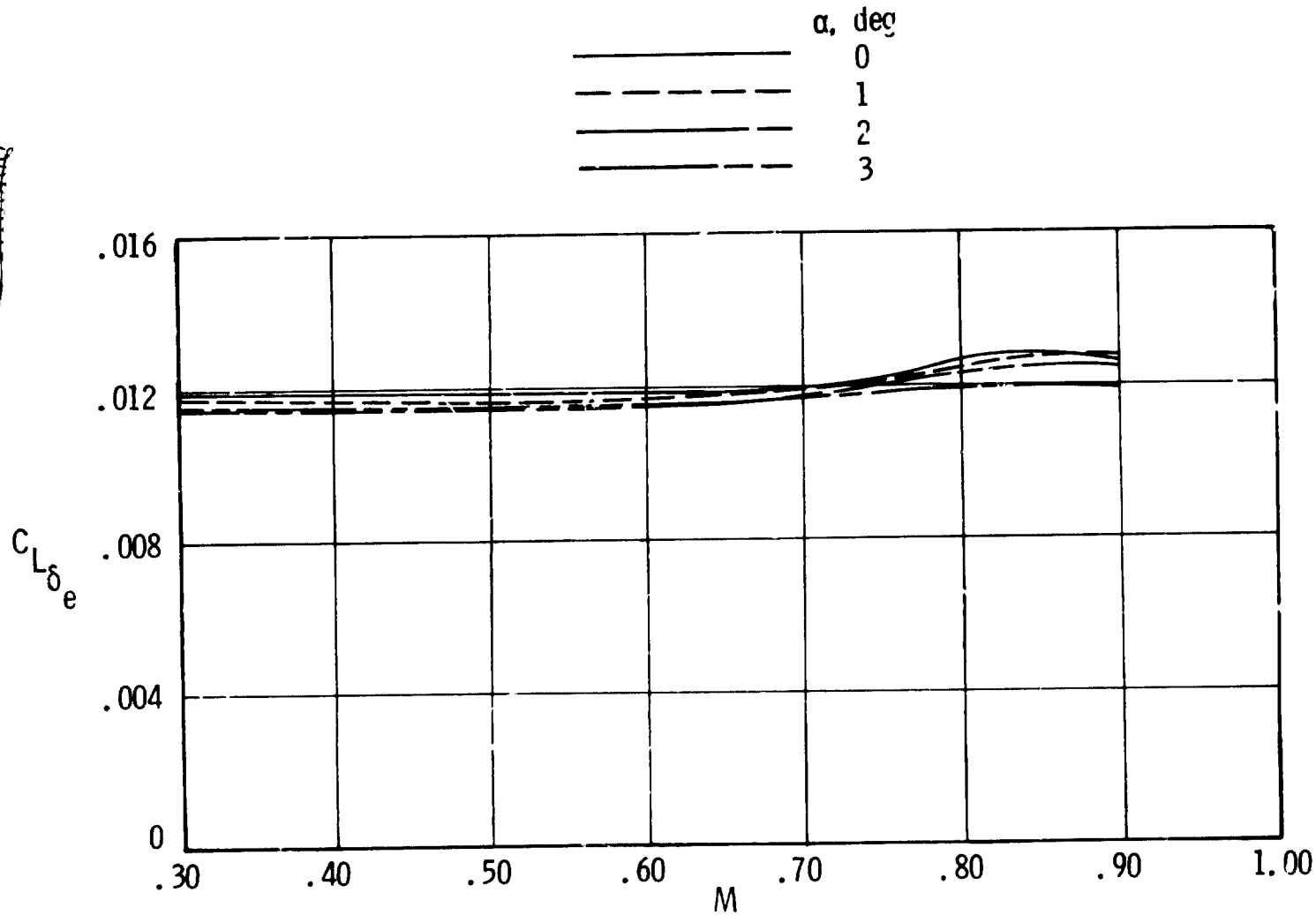

(C) Figure 25.- Variation of elevon effectiveness in lift with Mach number. Model configuration C; $-9^o \leq \delta_e \leq 3^o$; $\beta = 0^o$. (U)

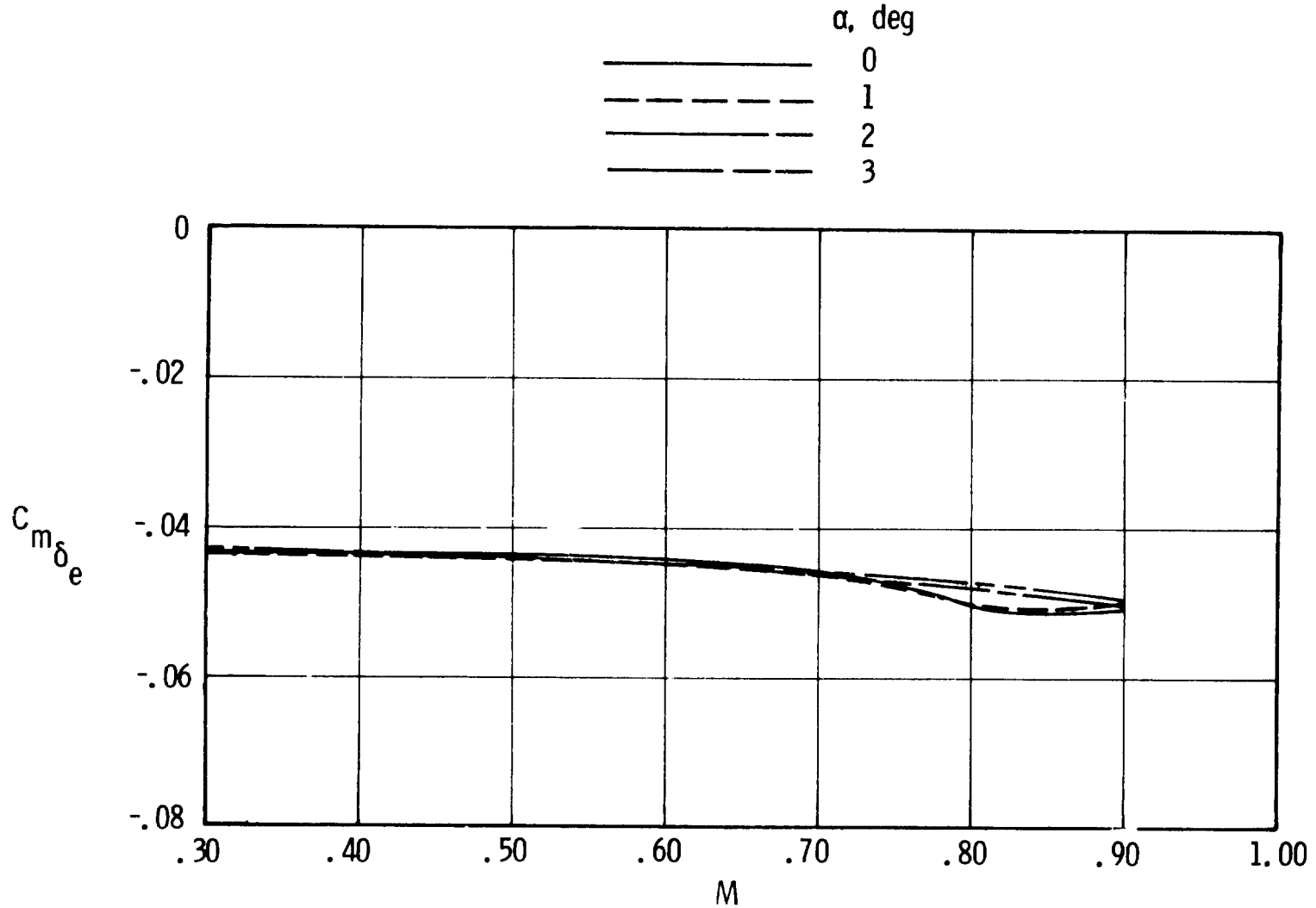

(C) Figure 26.- Variation of elevon effectiveness in pitching moment with Mach number. Model configuration C; $-9^{o} \leq \delta_e \leq 3^{o}$; $\beta = 0^{o}$. (U)

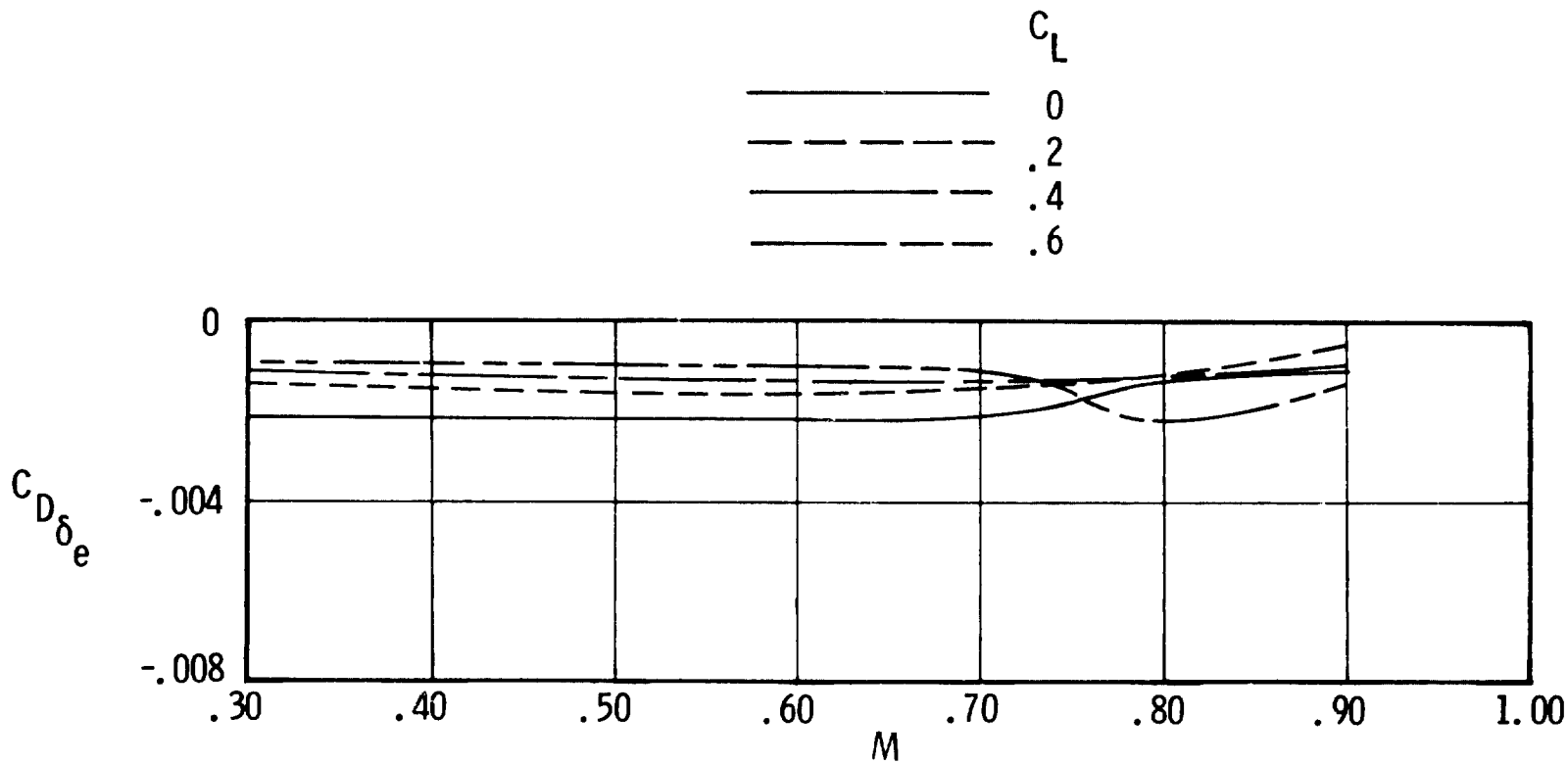

(C) Figure 27.- Variation of elevon effectiveness in drag with Mach number. Model configuration C; $-9^o \leq \delta_e \leq 3^o$; $\beta = 0^o$. (U)

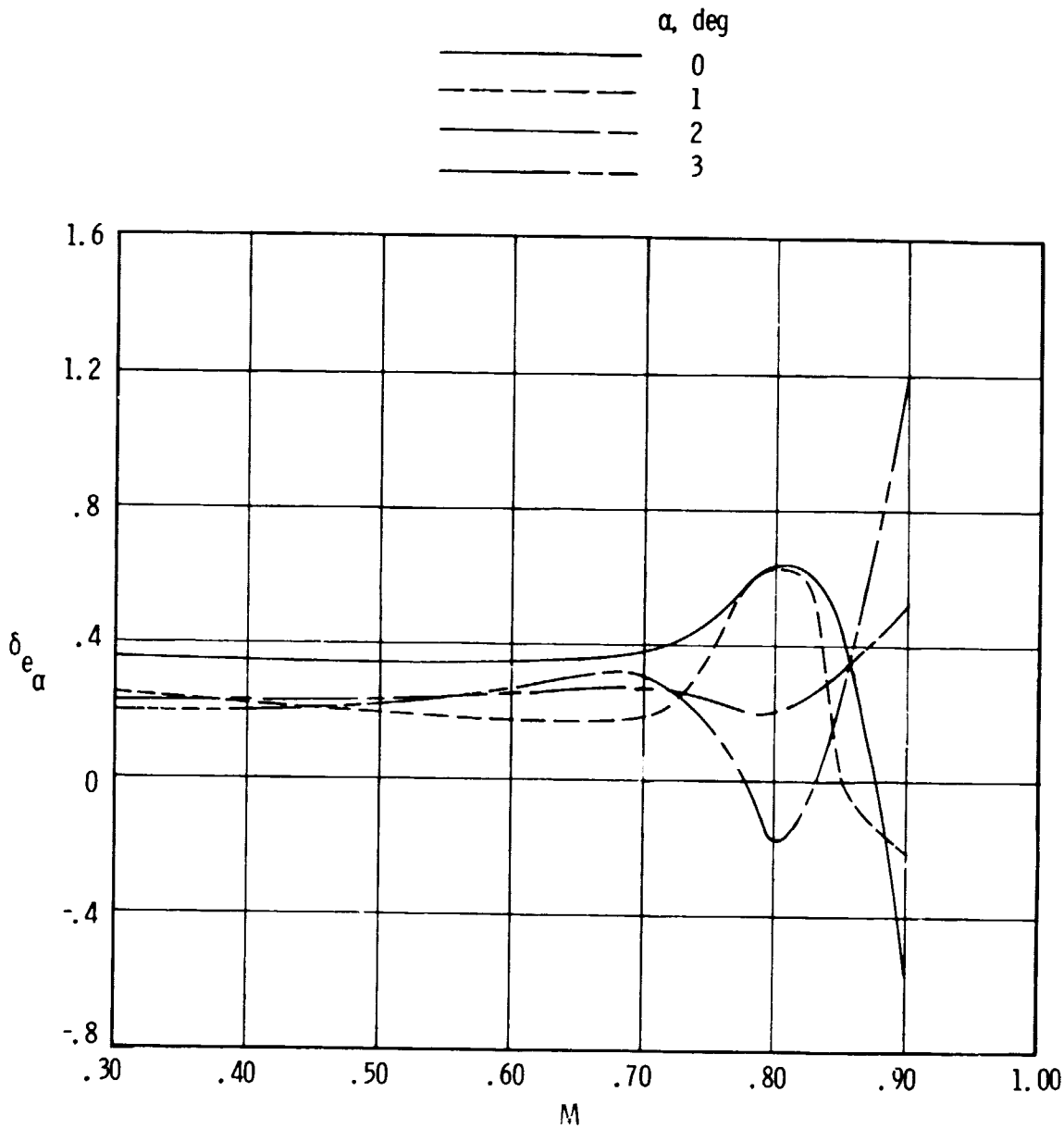

Figure 28.- Variation of pitch-control index with Mach number for model configuration C. (U)

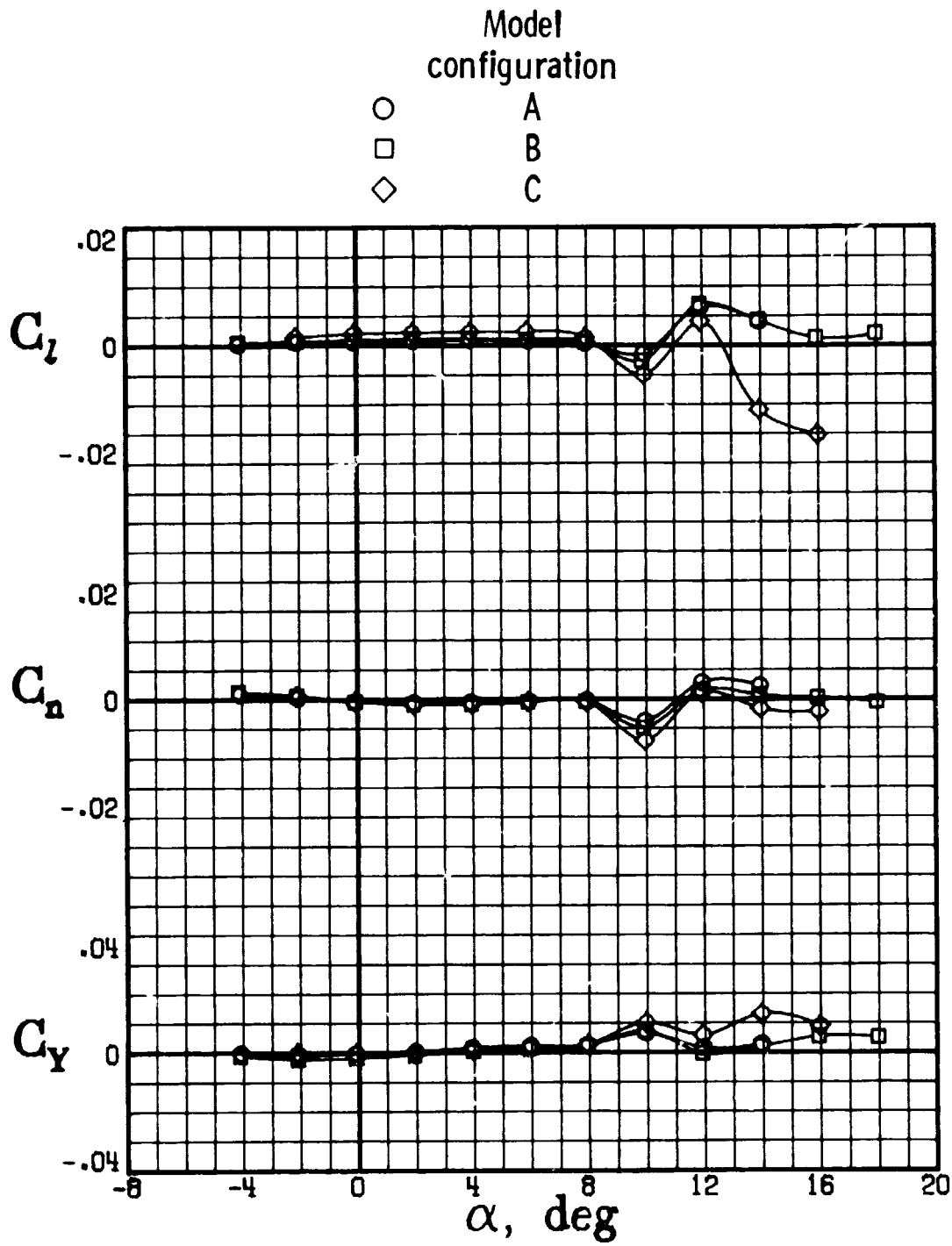

(a) M = 0.300.

Figure 29.- Effect of model configuration on lateral-directional aerodynamic characteristics. $\beta = 0^o$; $\delta_a = 0^o$; $\delta_r = 0^o$. (U)

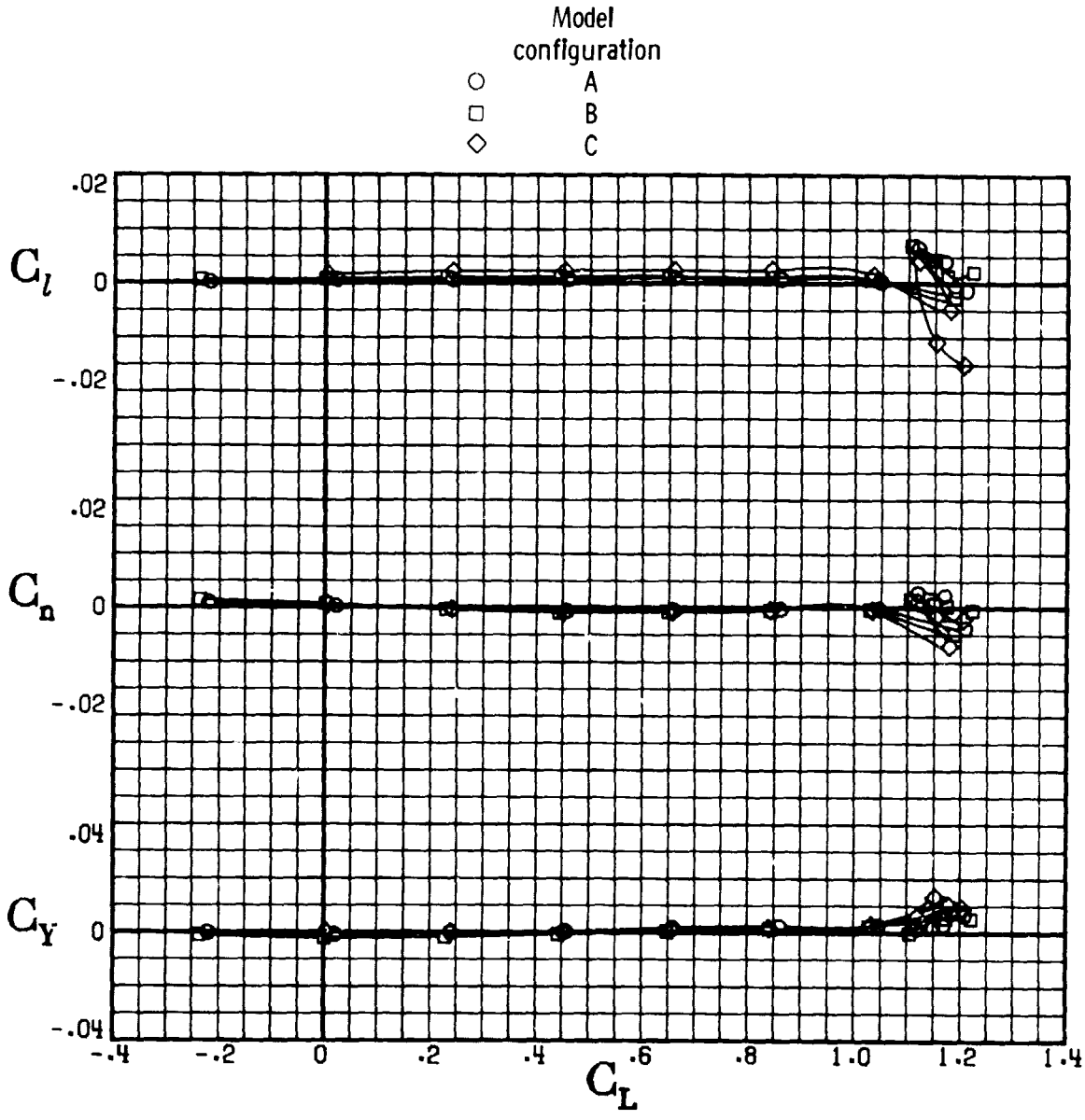

(a) Concluded.

(C) Figure 29.- Continued. (U)

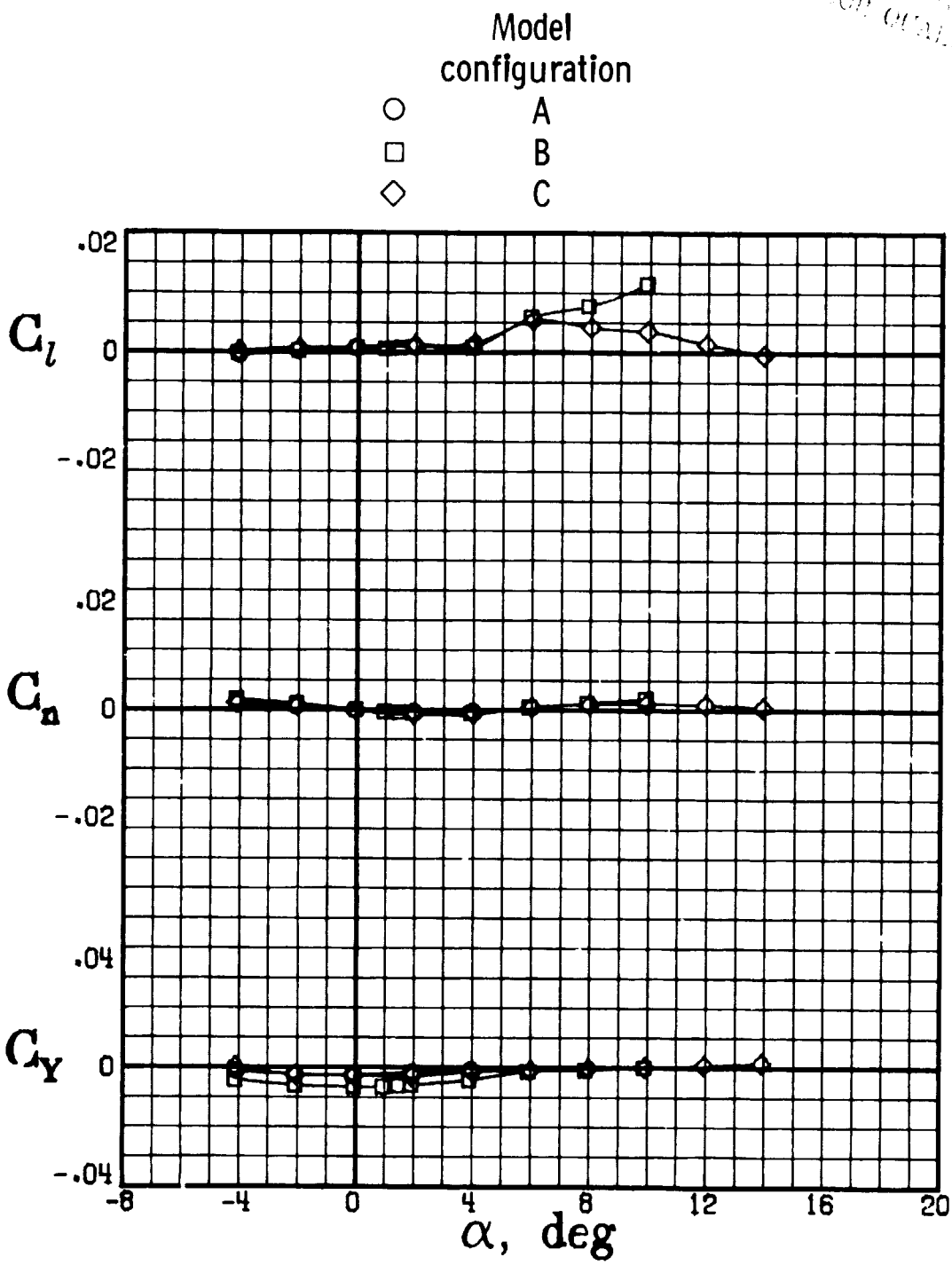

(b) M = 0.700.

Figure 29.- Continued. (U)

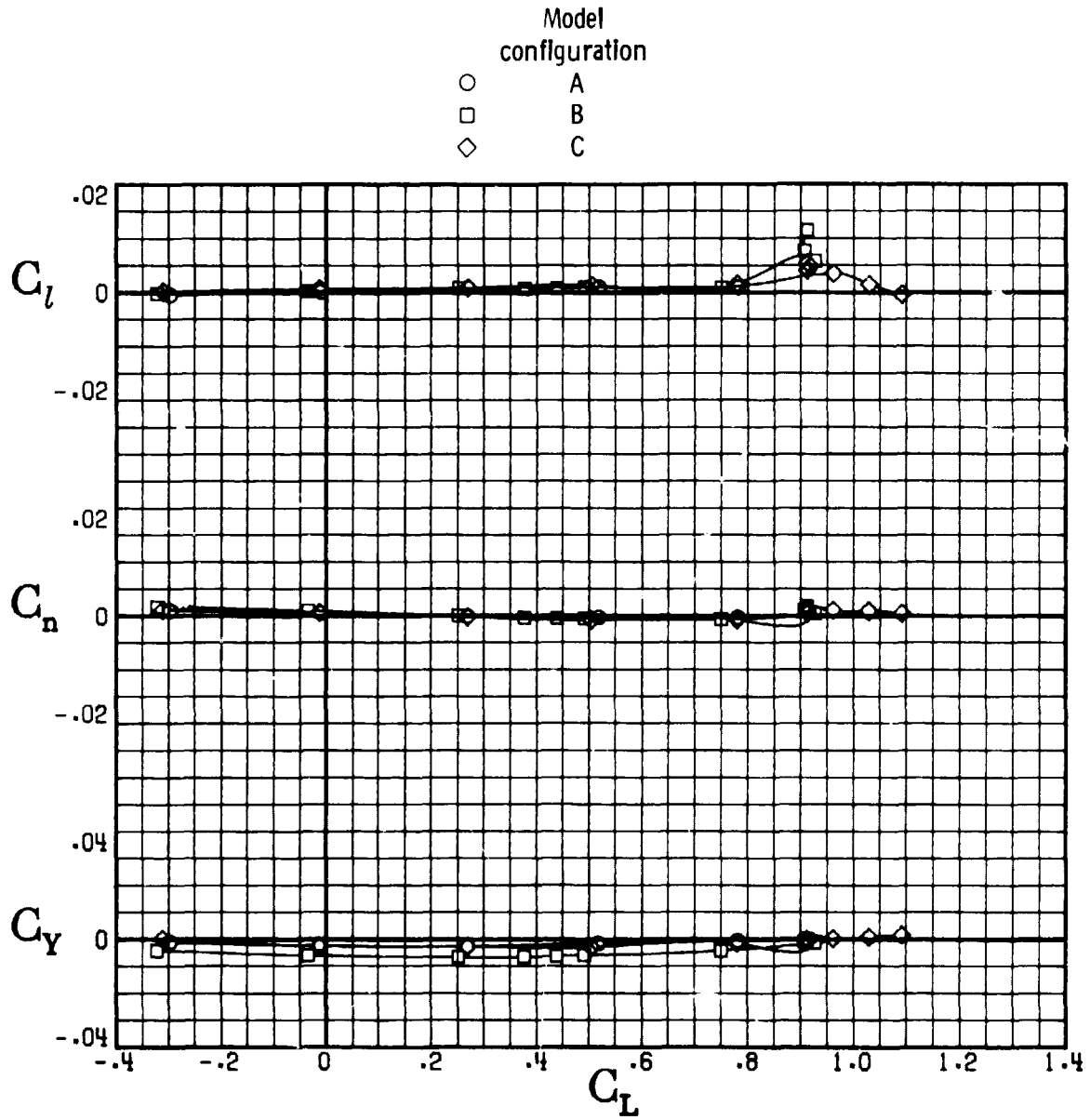

(b) Concluded.

Figure 29.- Continued. (U)

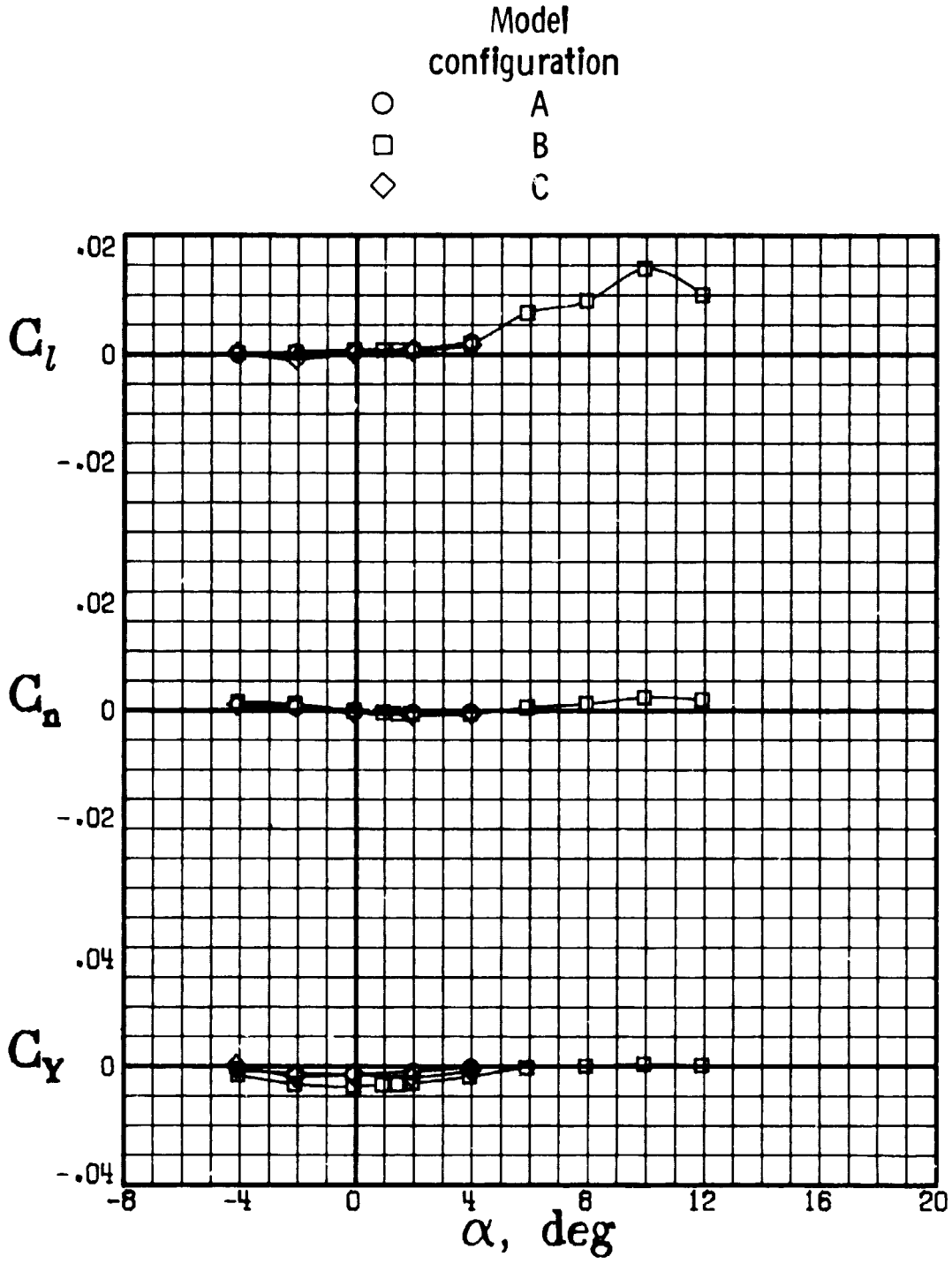

(c) M = 0.750.

Figure 29.- Continued. (U)

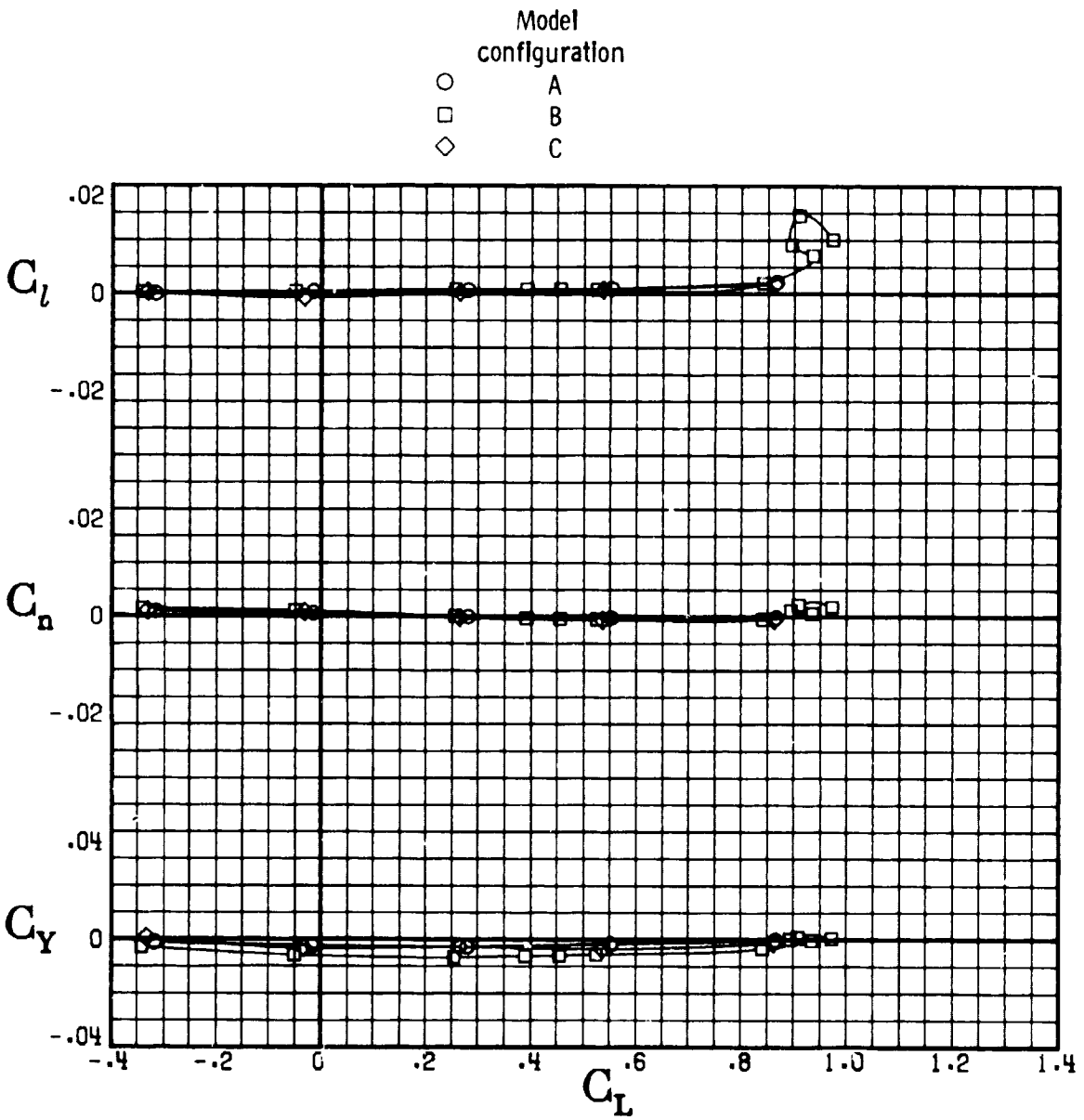

(c) Concluded.

Figure 29.- Continued. (U)

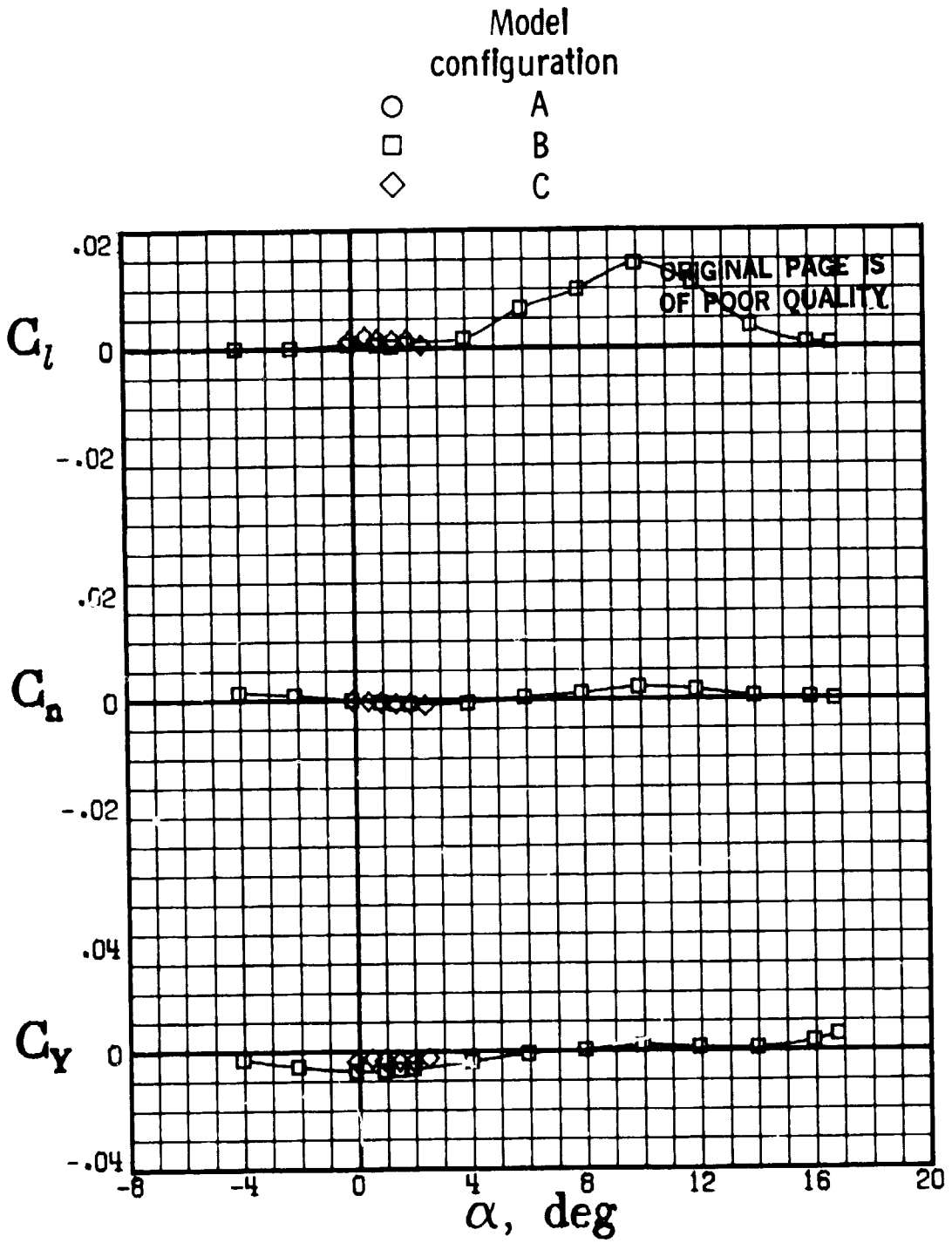

(d) M = 0.780.

Figure 29.- Continued. (U)

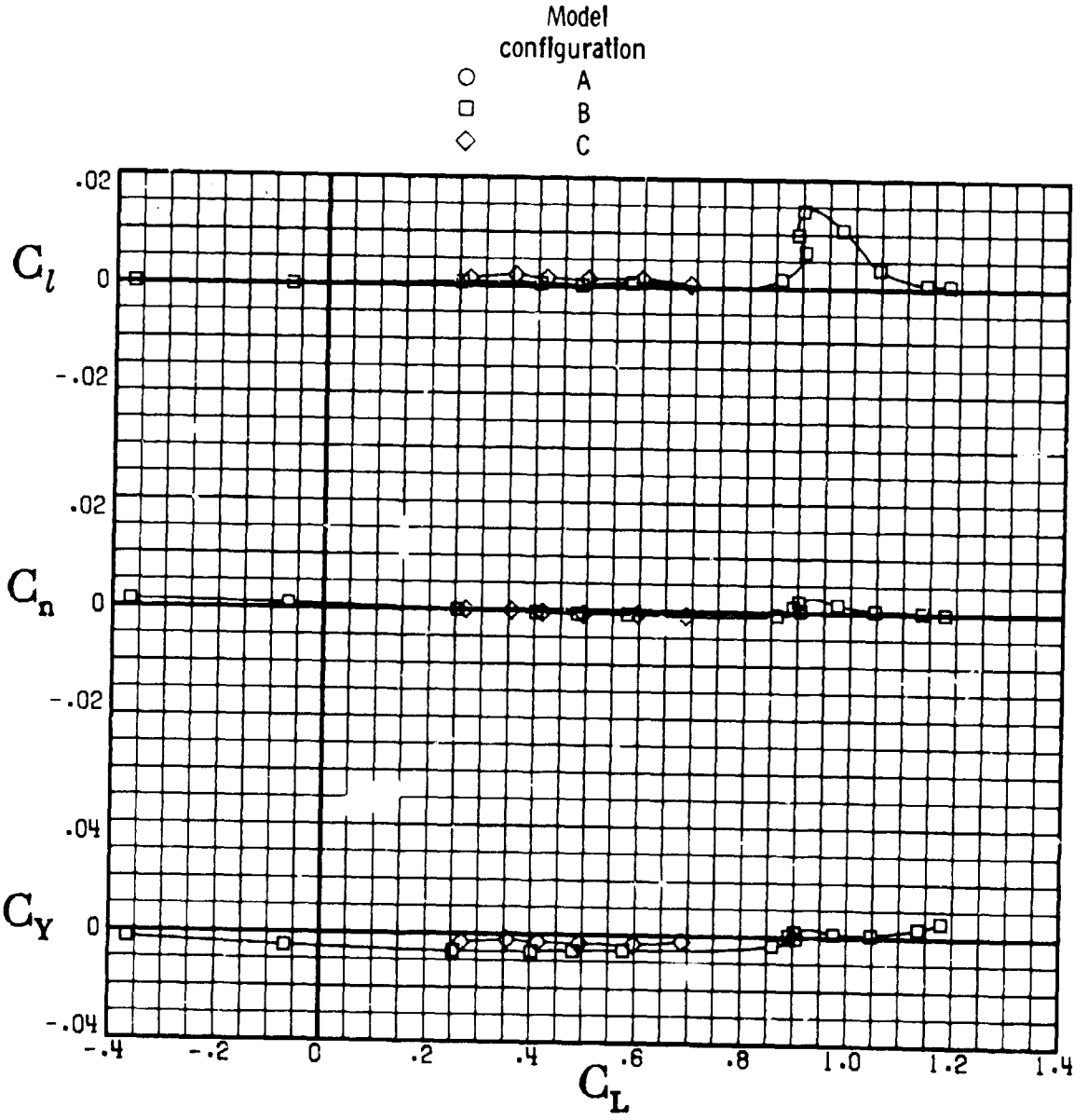

(d) Concluded.

Figure 29.- Continued. (U)

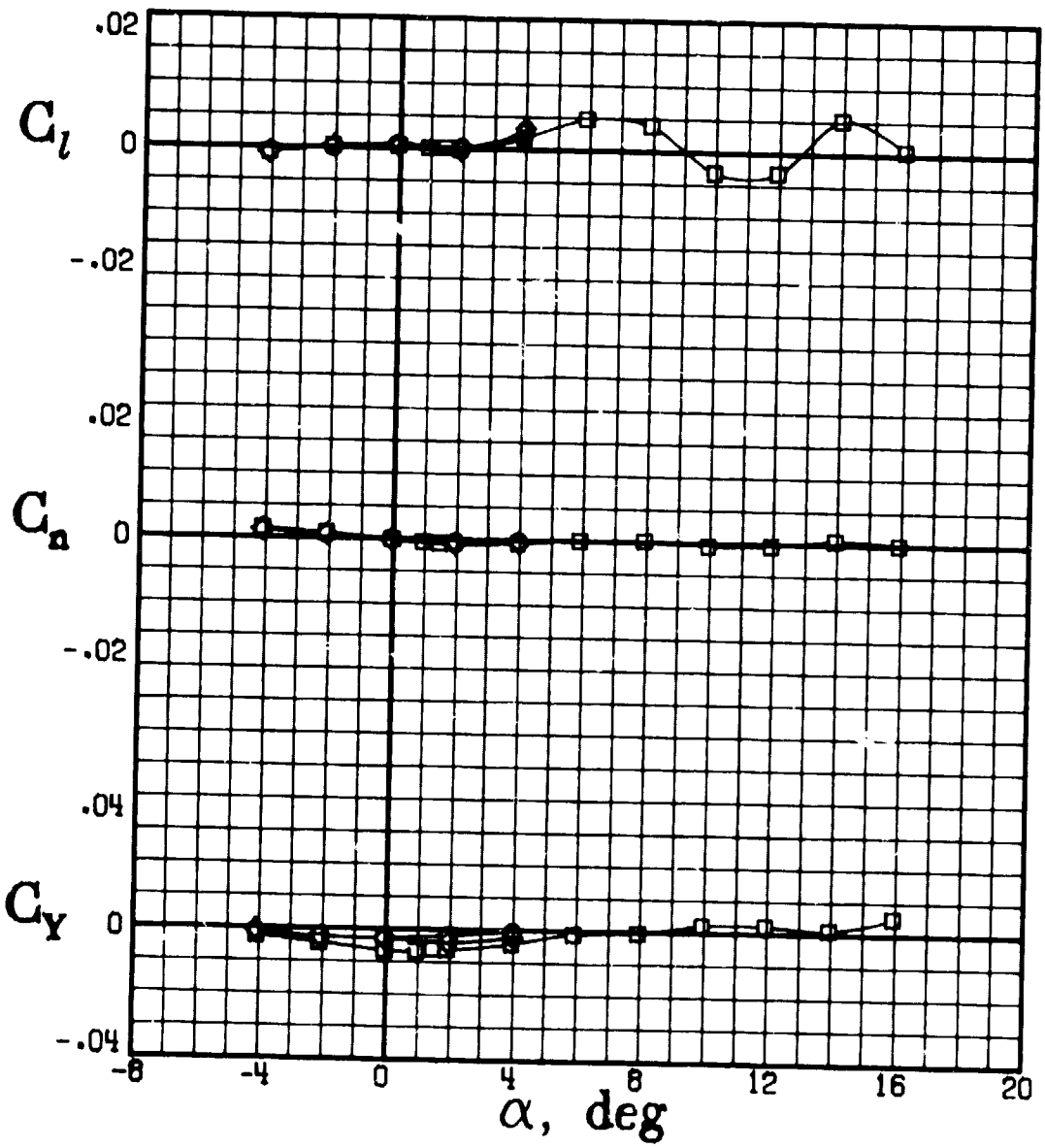

(e) M = 0.800.

Figure 29.- Continued. (U)

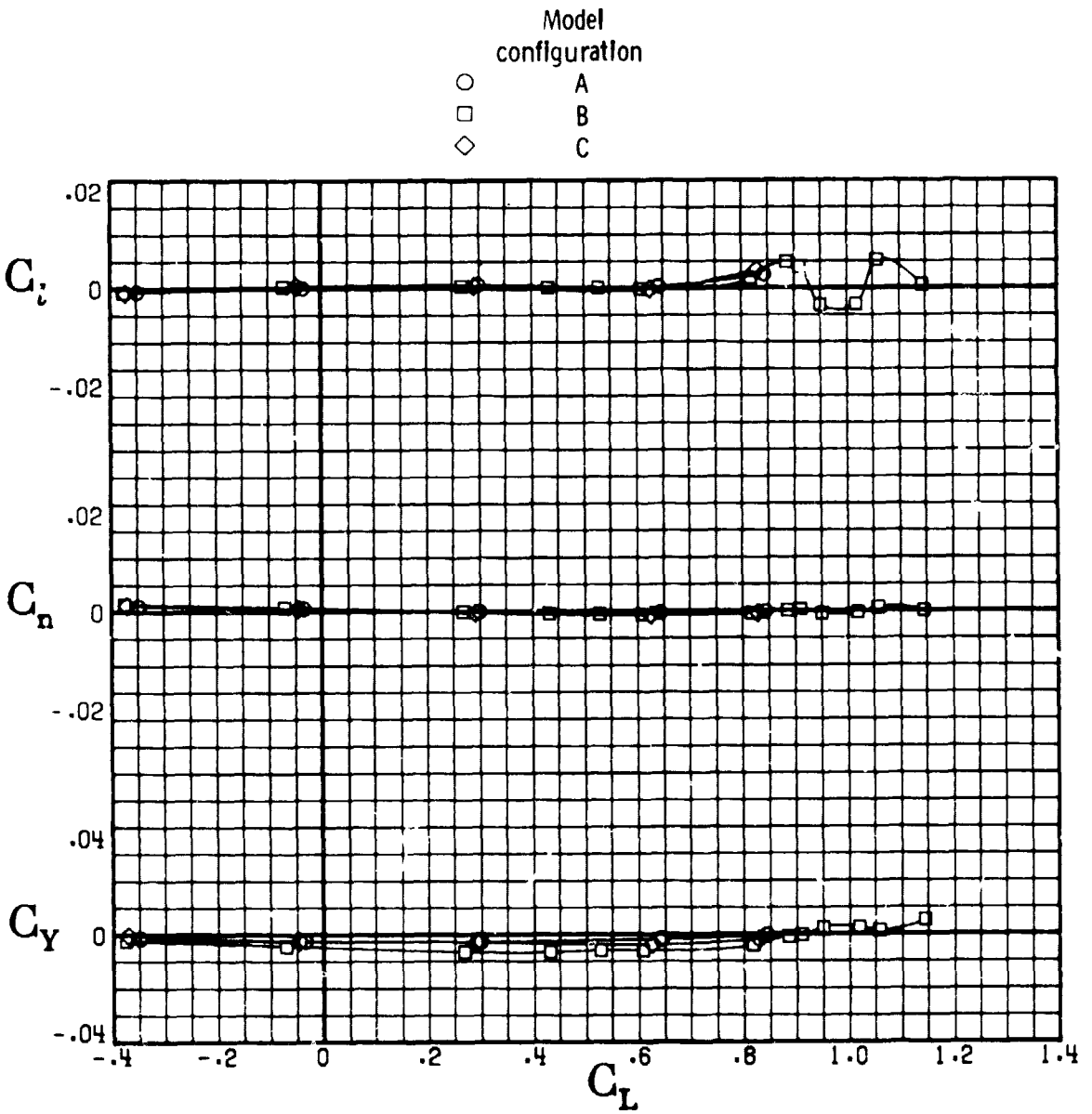

(e) Concluded.

Figure 29.- Continued. (U)

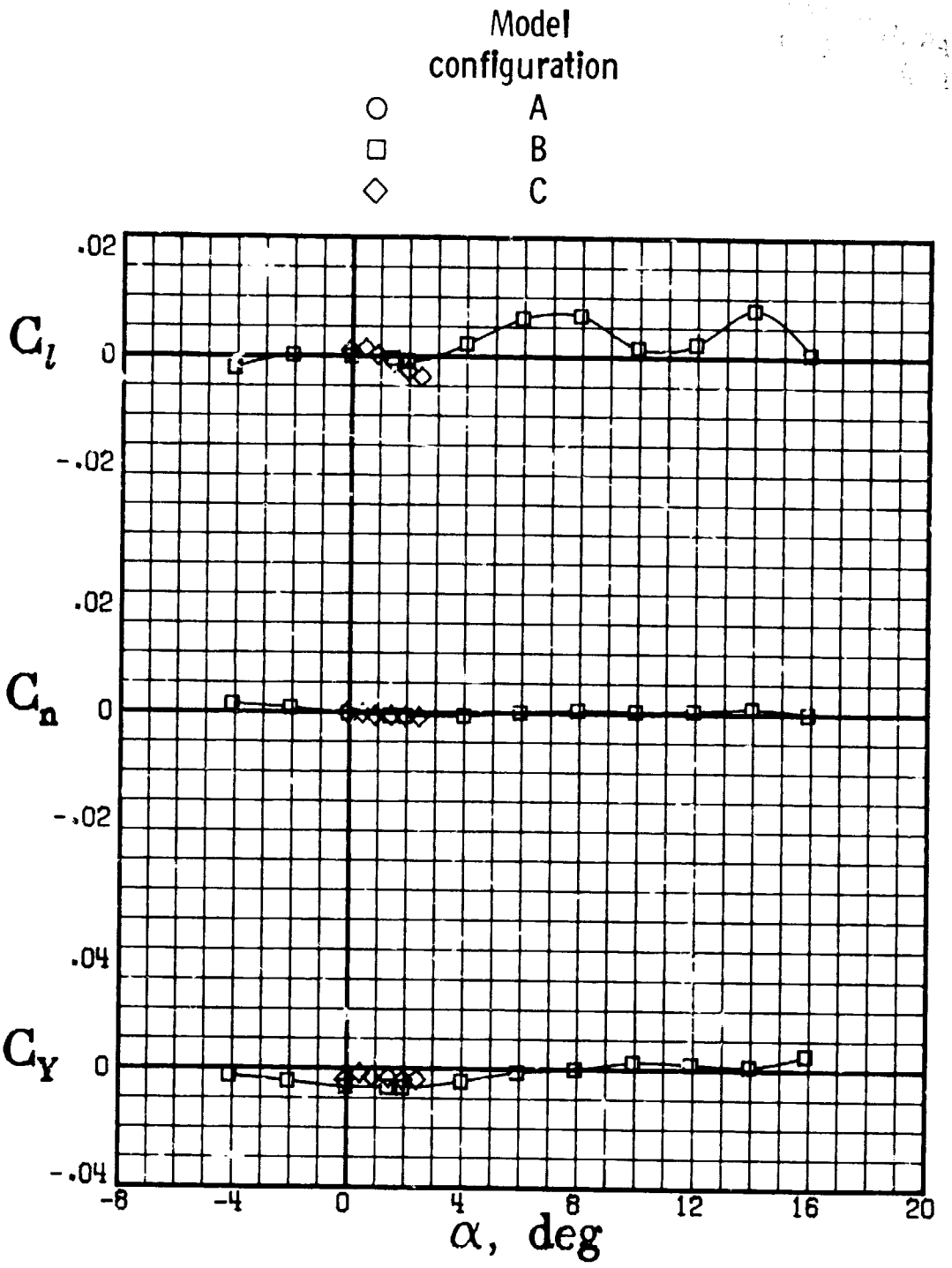

(f) M = 0.820.

Figure 29.- Continued. (U)

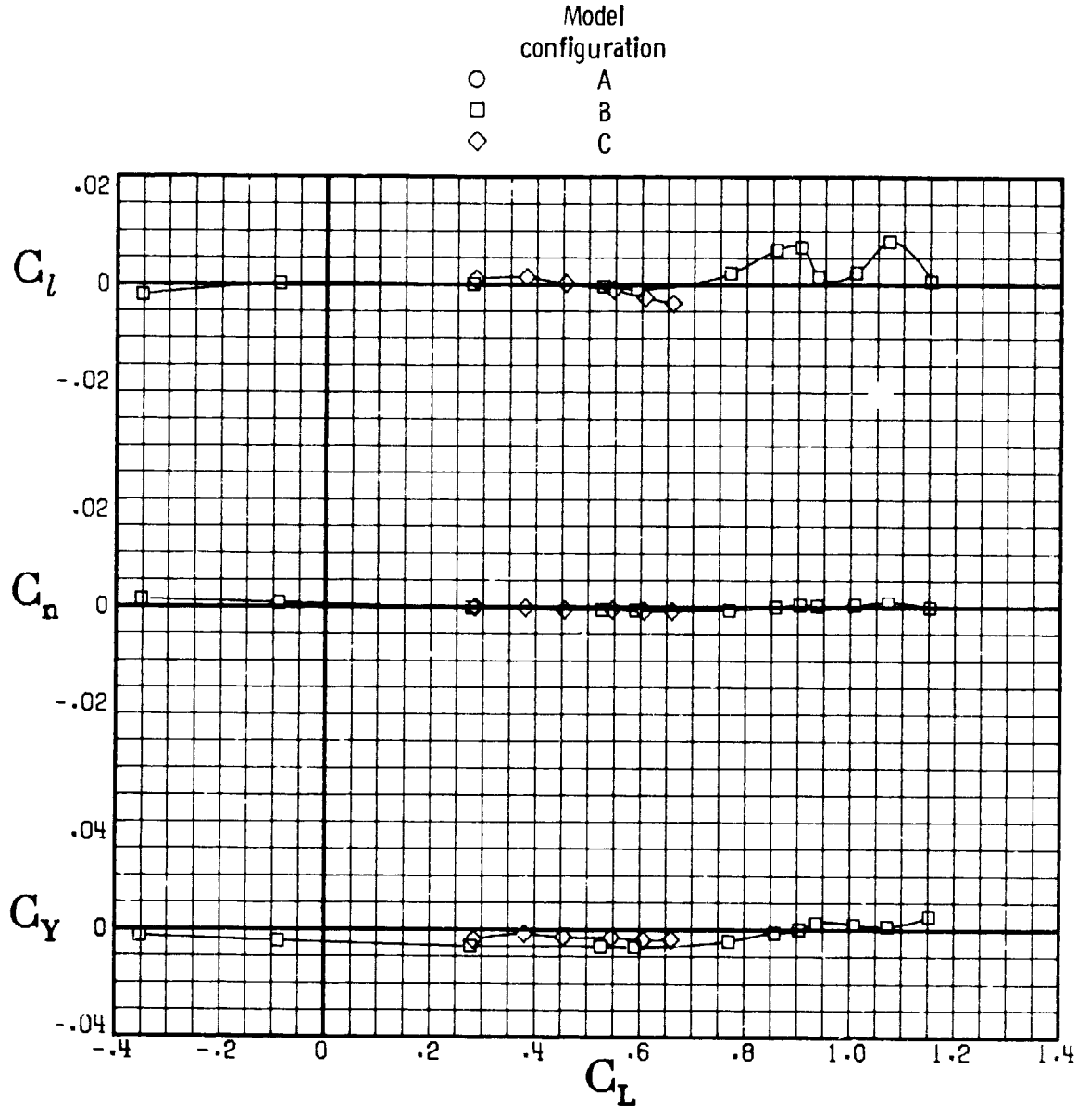

(f) Concluded.

Figure 29.- Continued. (U)

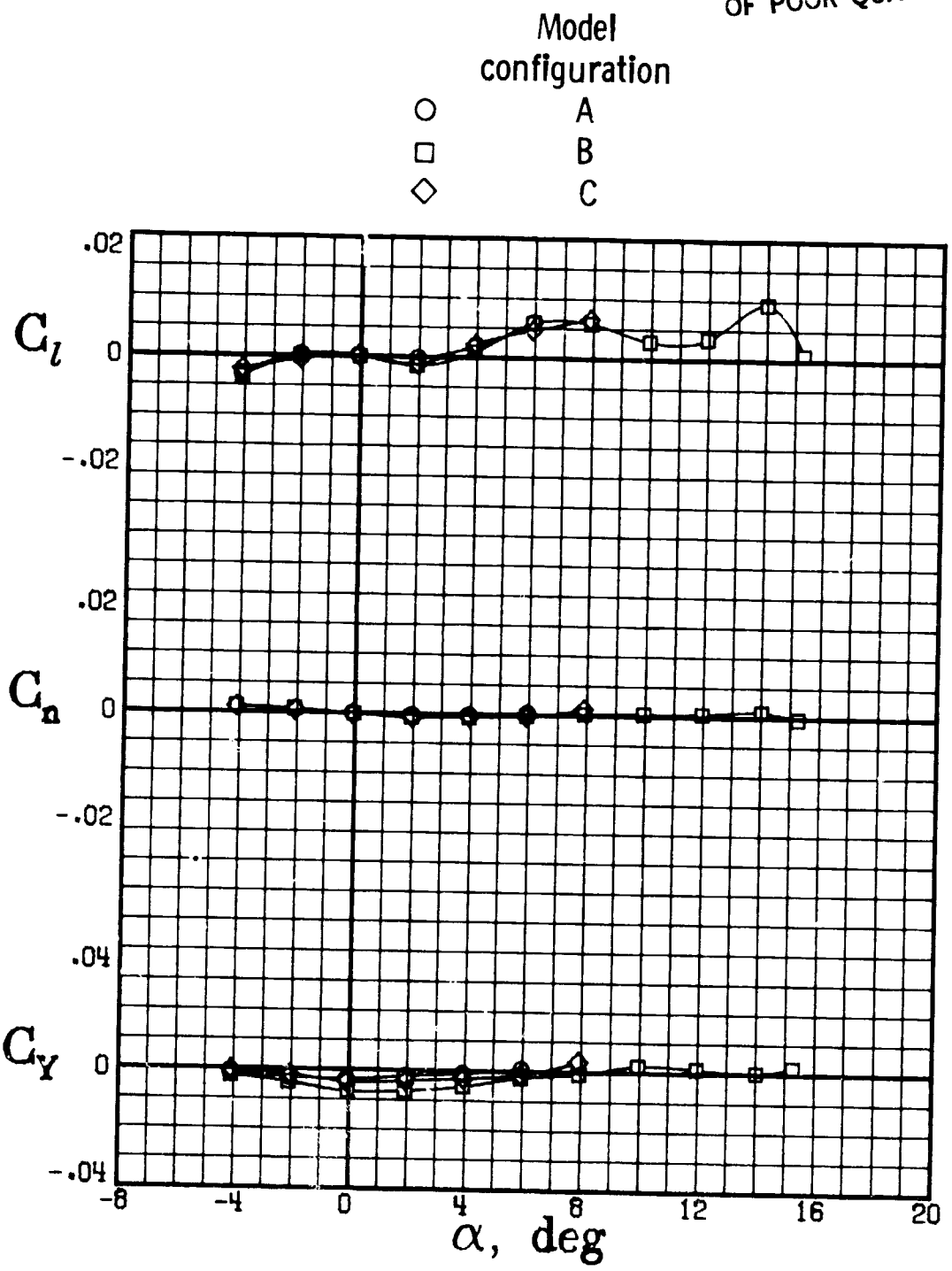

(g) M = 0.840.

Figure 29.- Continued. (U)

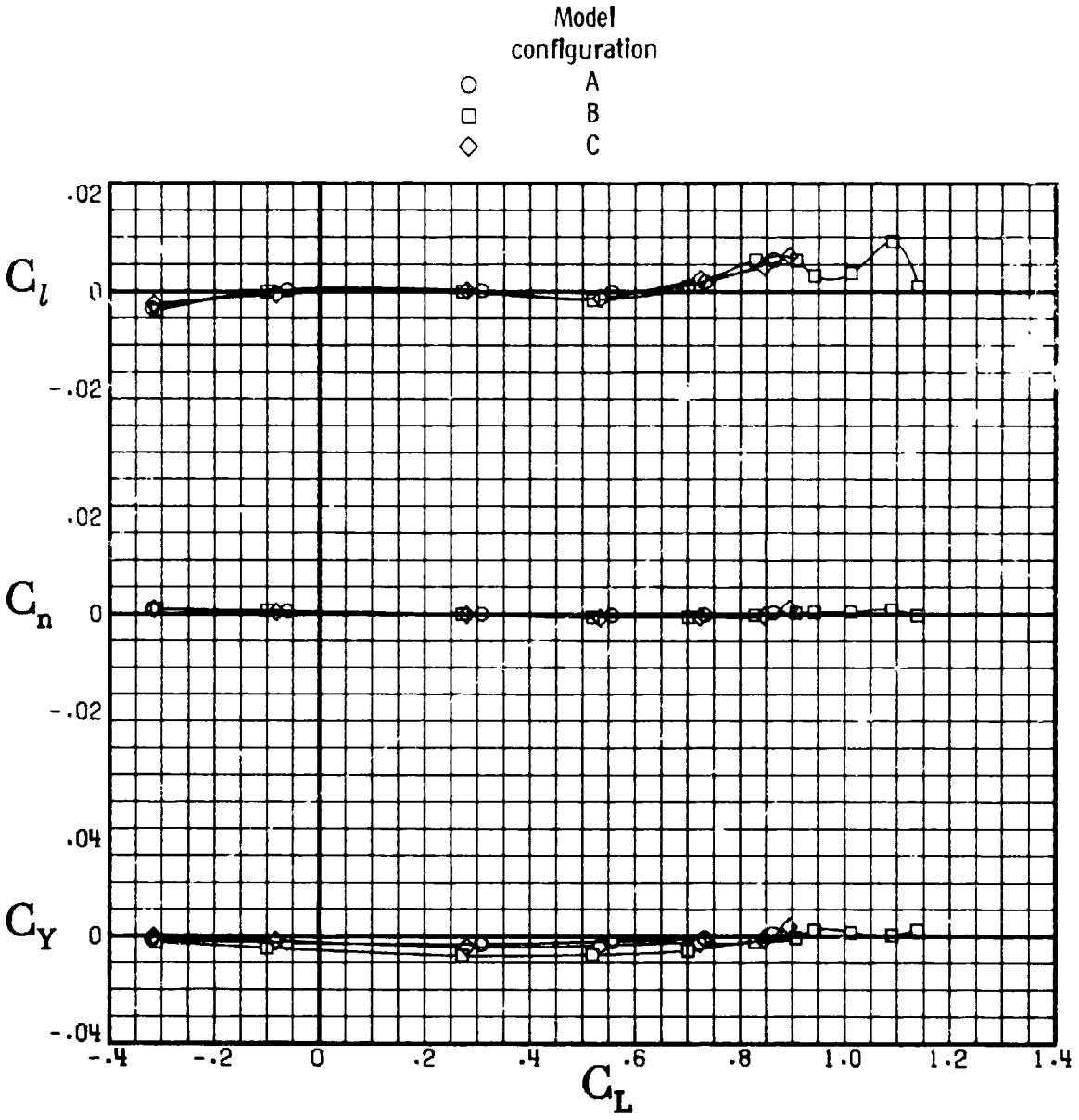

(g) Concluded.

Figure 29.- Continued. (U)

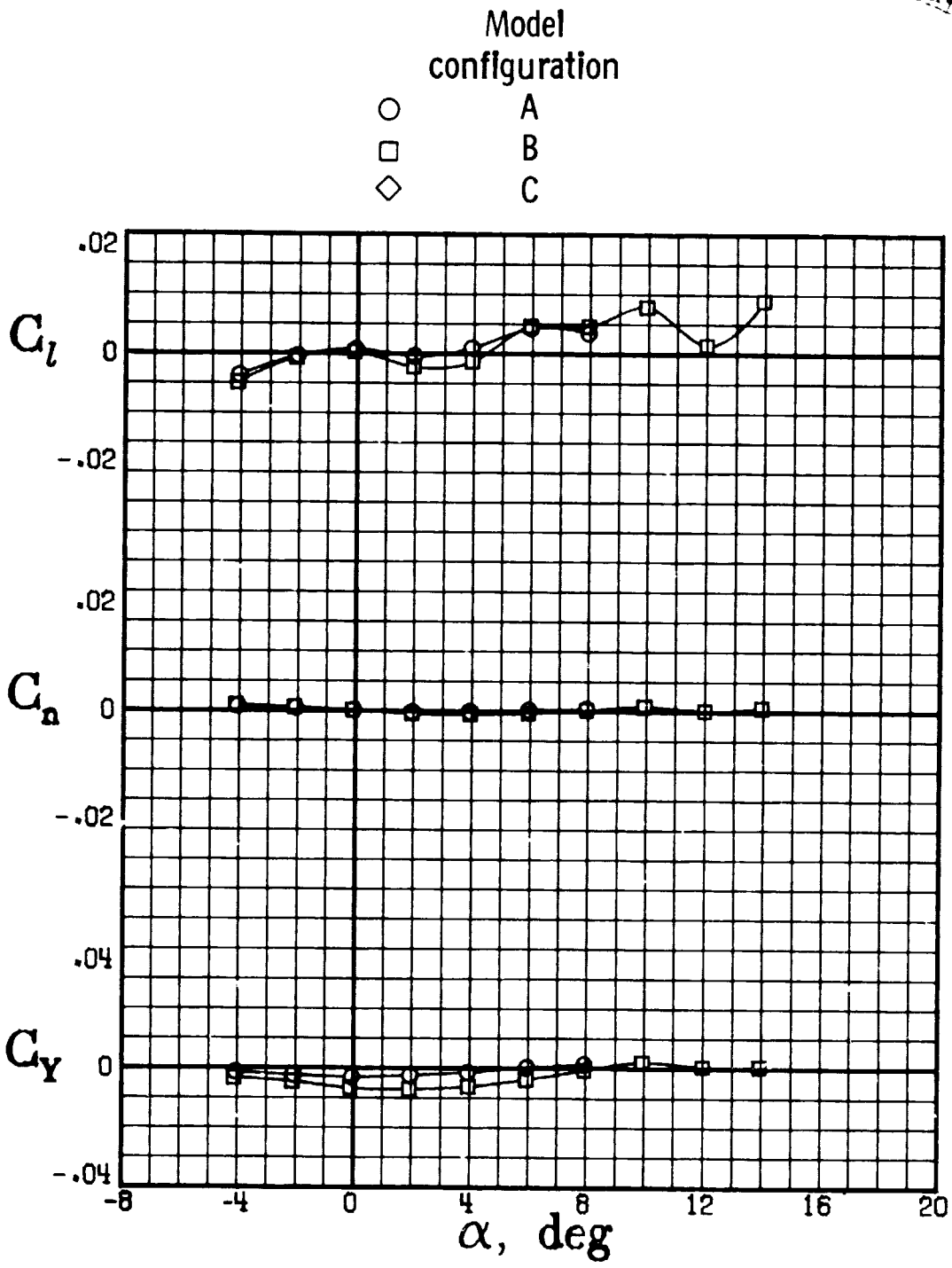

(h) M = 0.860.

Figure 29.- Continued. (U)

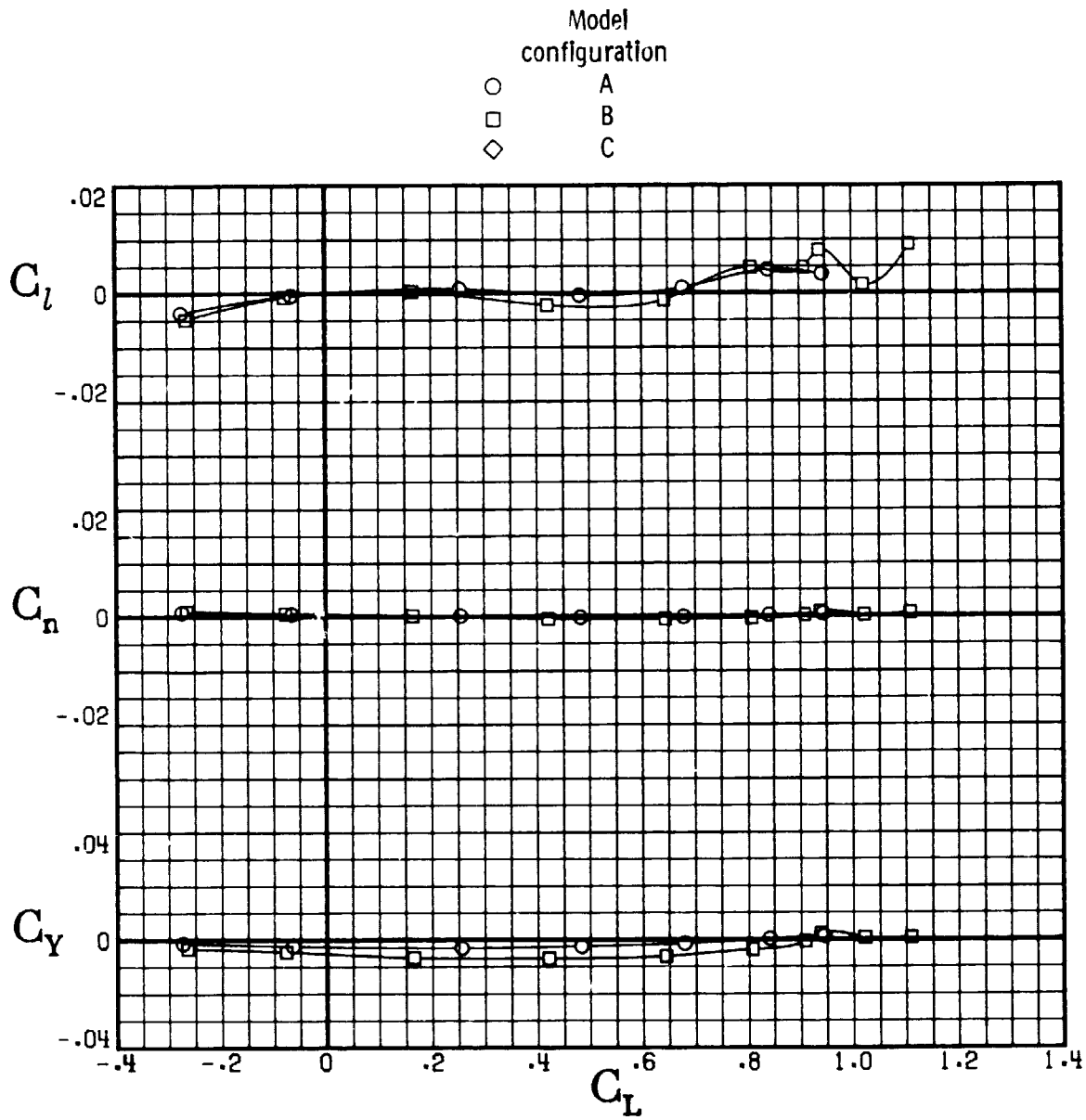

(h) Concluded.

Figure 29.- Continued. (U)

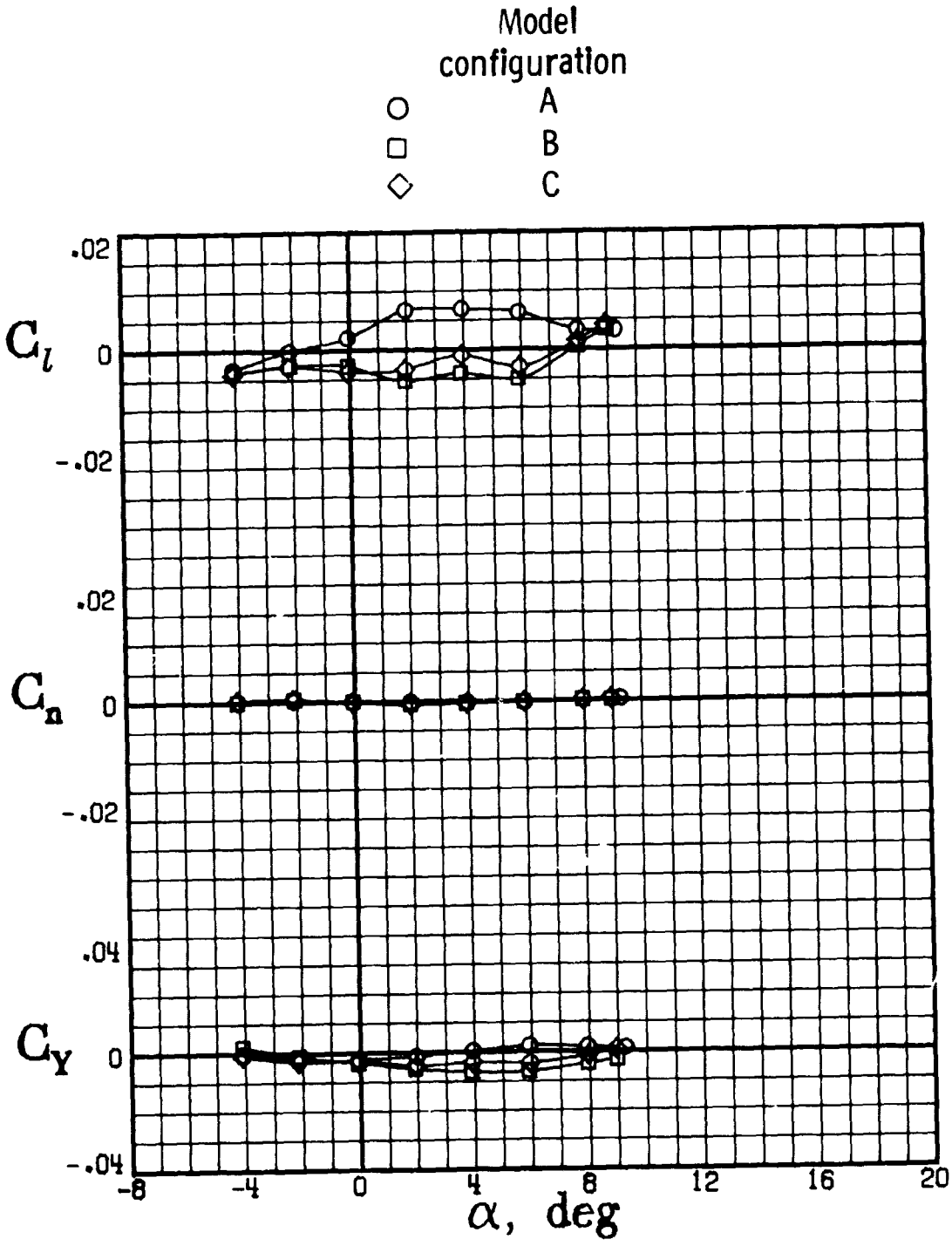

(i) M = 0.900.

Figure 29.- Continued. (U)

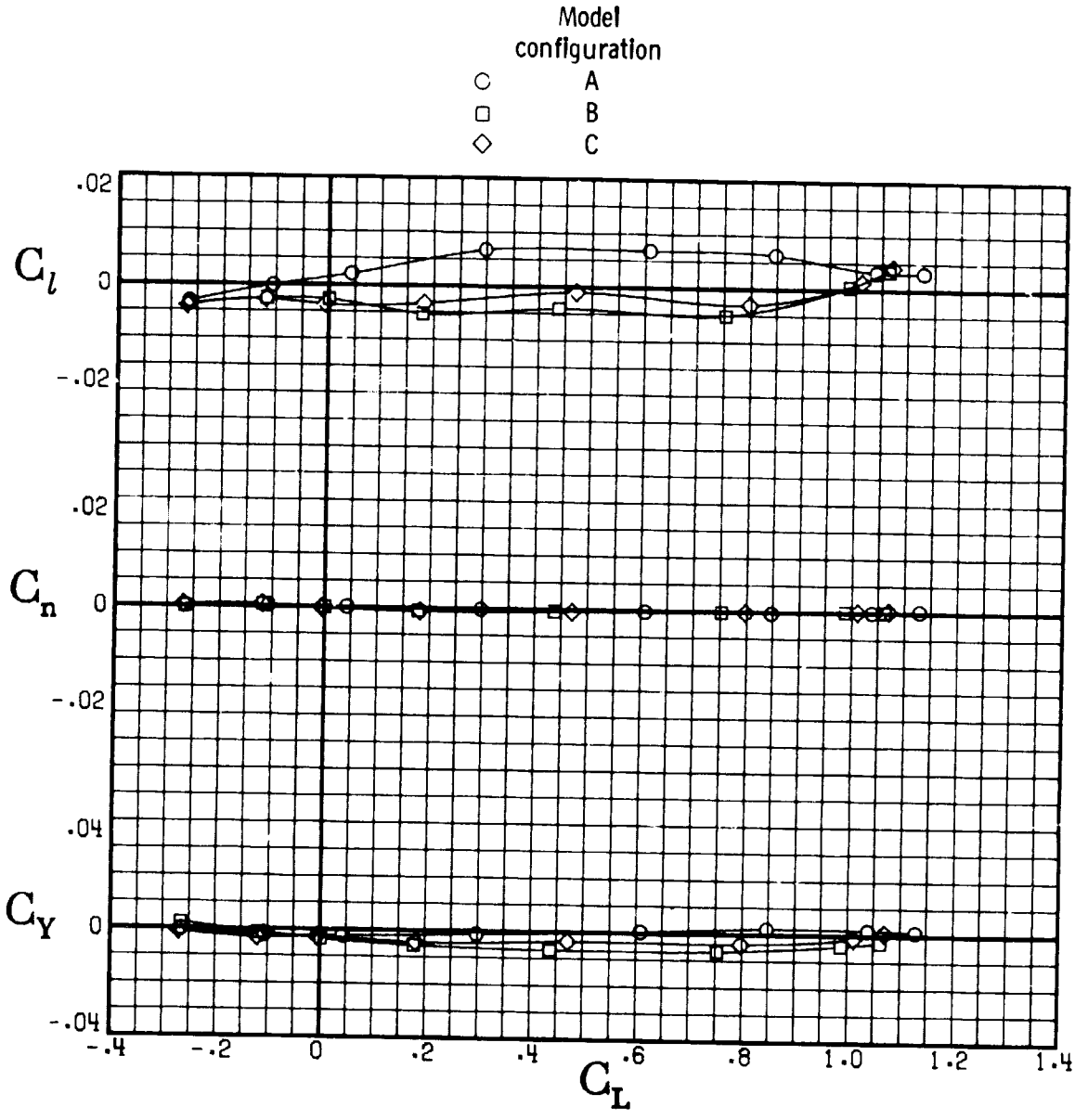

(i) Concluded.

Figure 29.- Continued. (U)

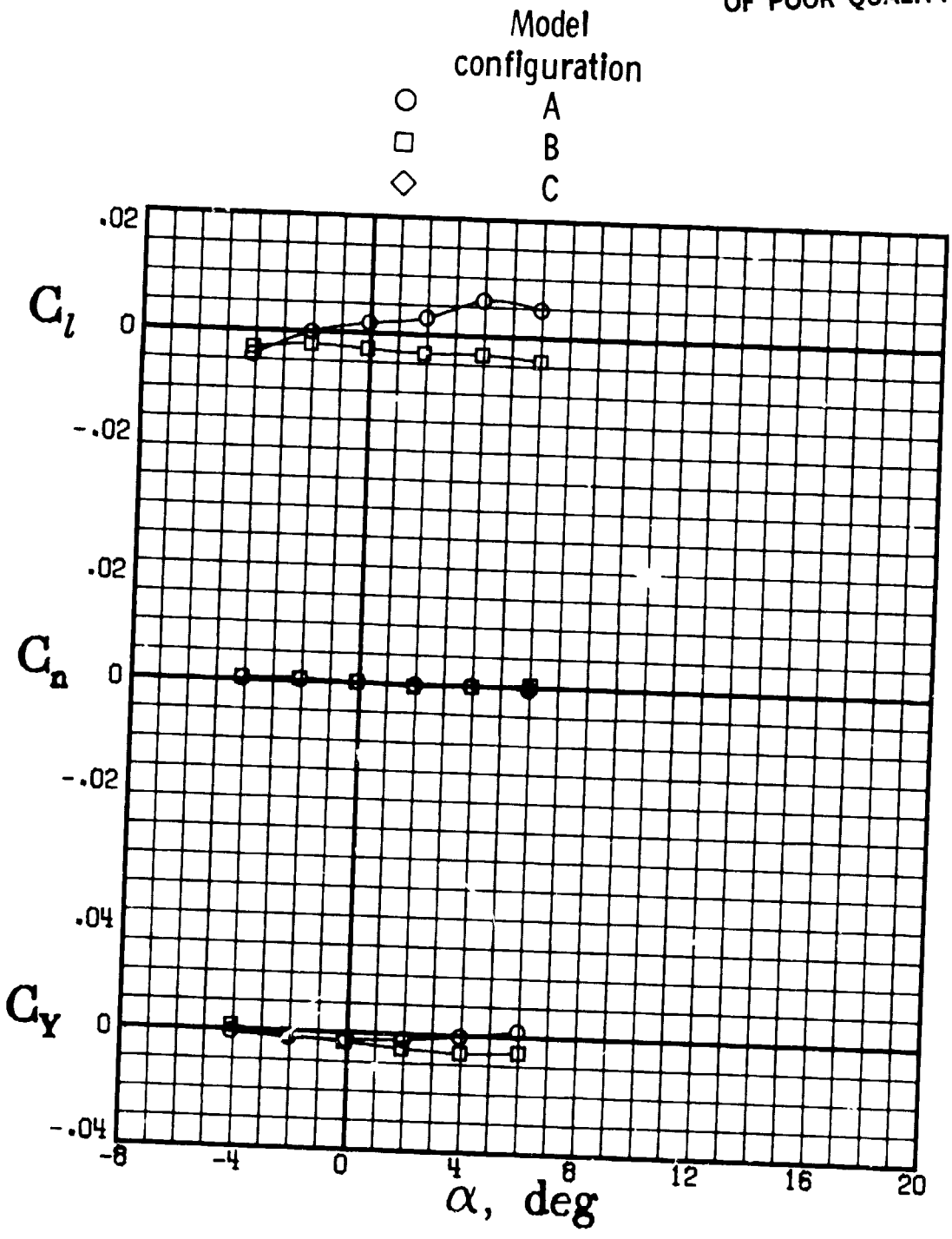

(j) M = 0.920.

Figure 29.- Continued. (U)

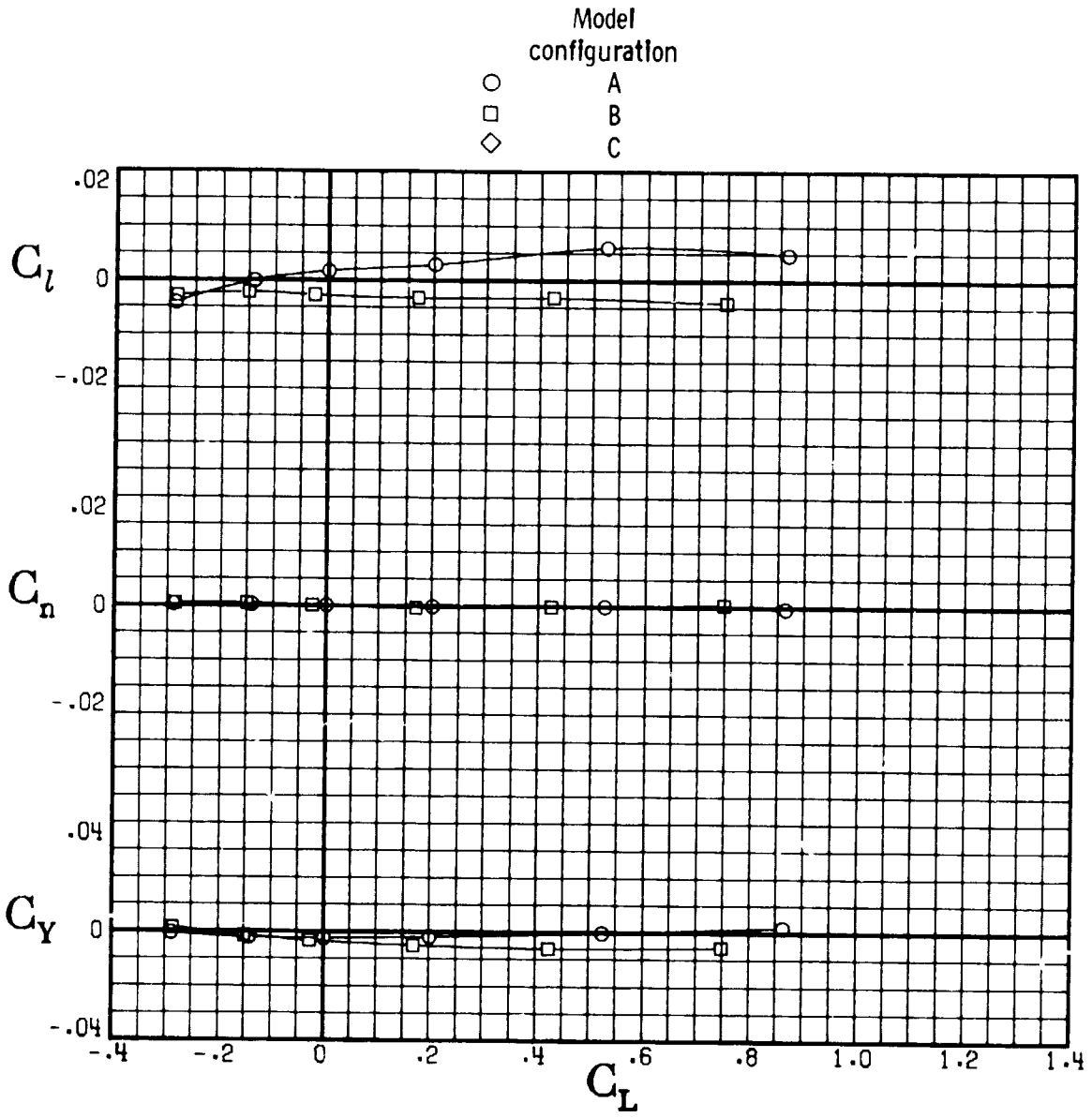

(j) Concluded.

Figure 29.- Concluded. (U)

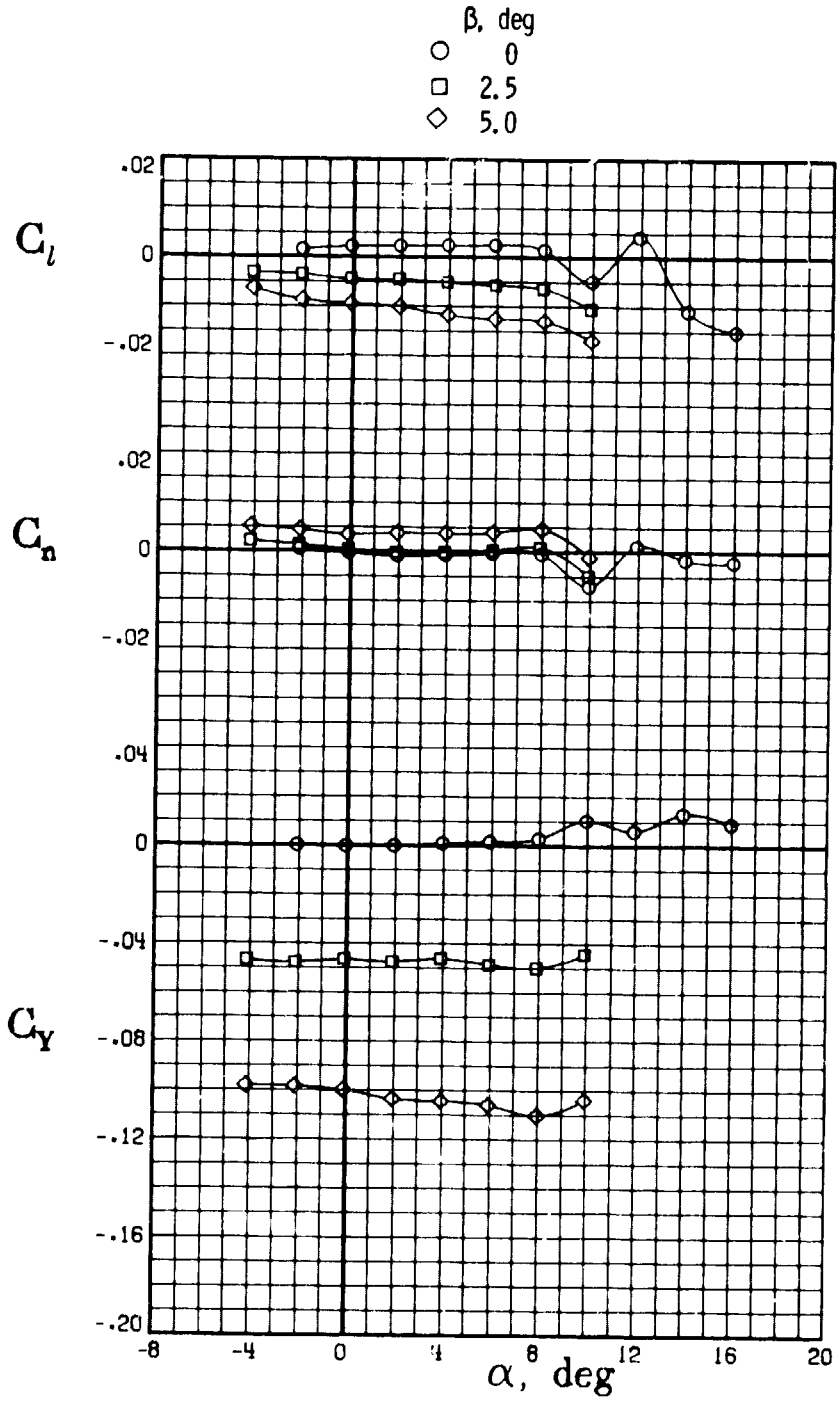

(a) M = 0.300.

Figure 30.- Effect of sideslip on lateral-directional aerodynamic characteristics for model configuration C. $\delta_e = 0^o$; $\delta_r = 0^o$. (U)

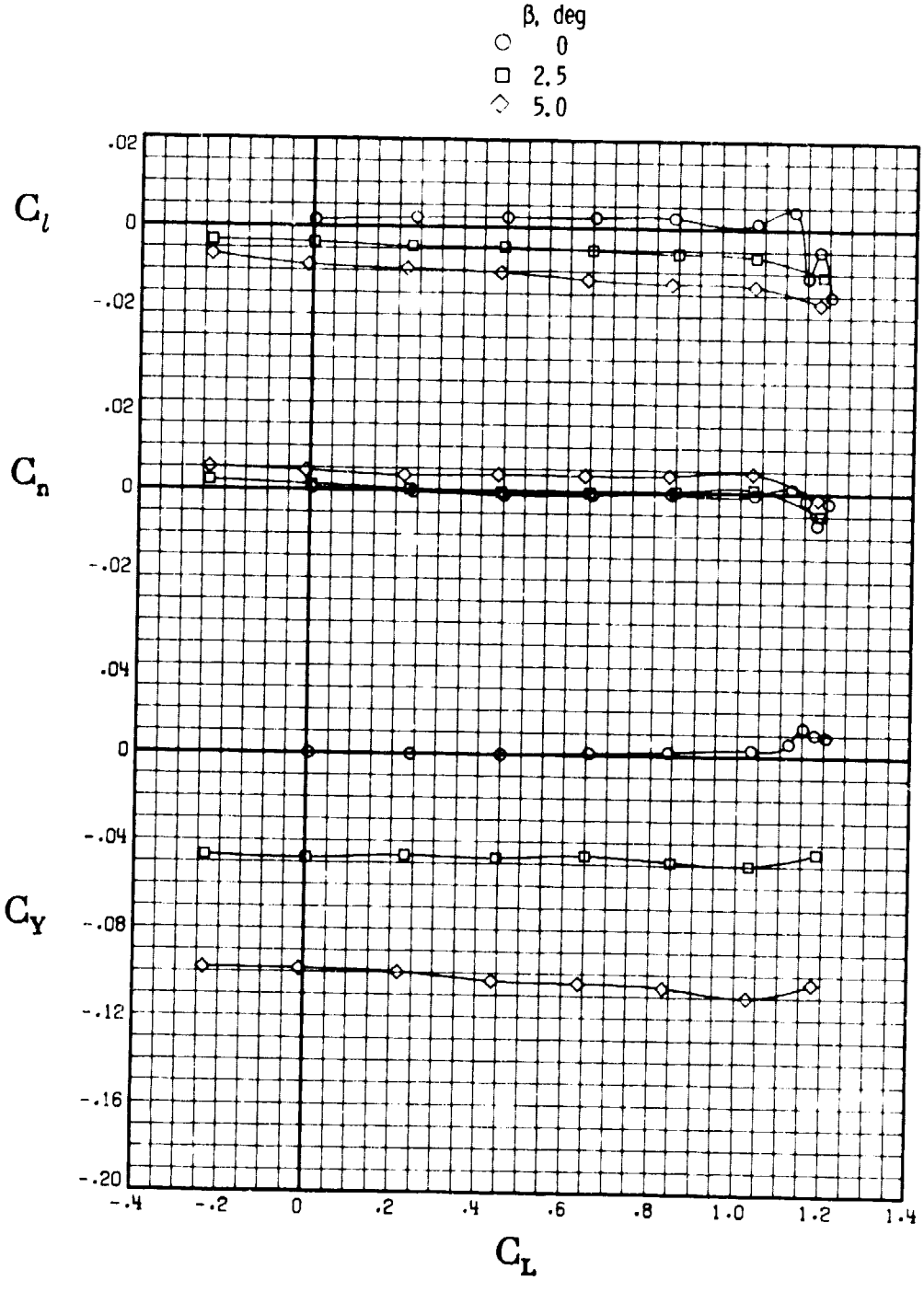

(a) Concluded.

Figure 30.- Continued. (U)

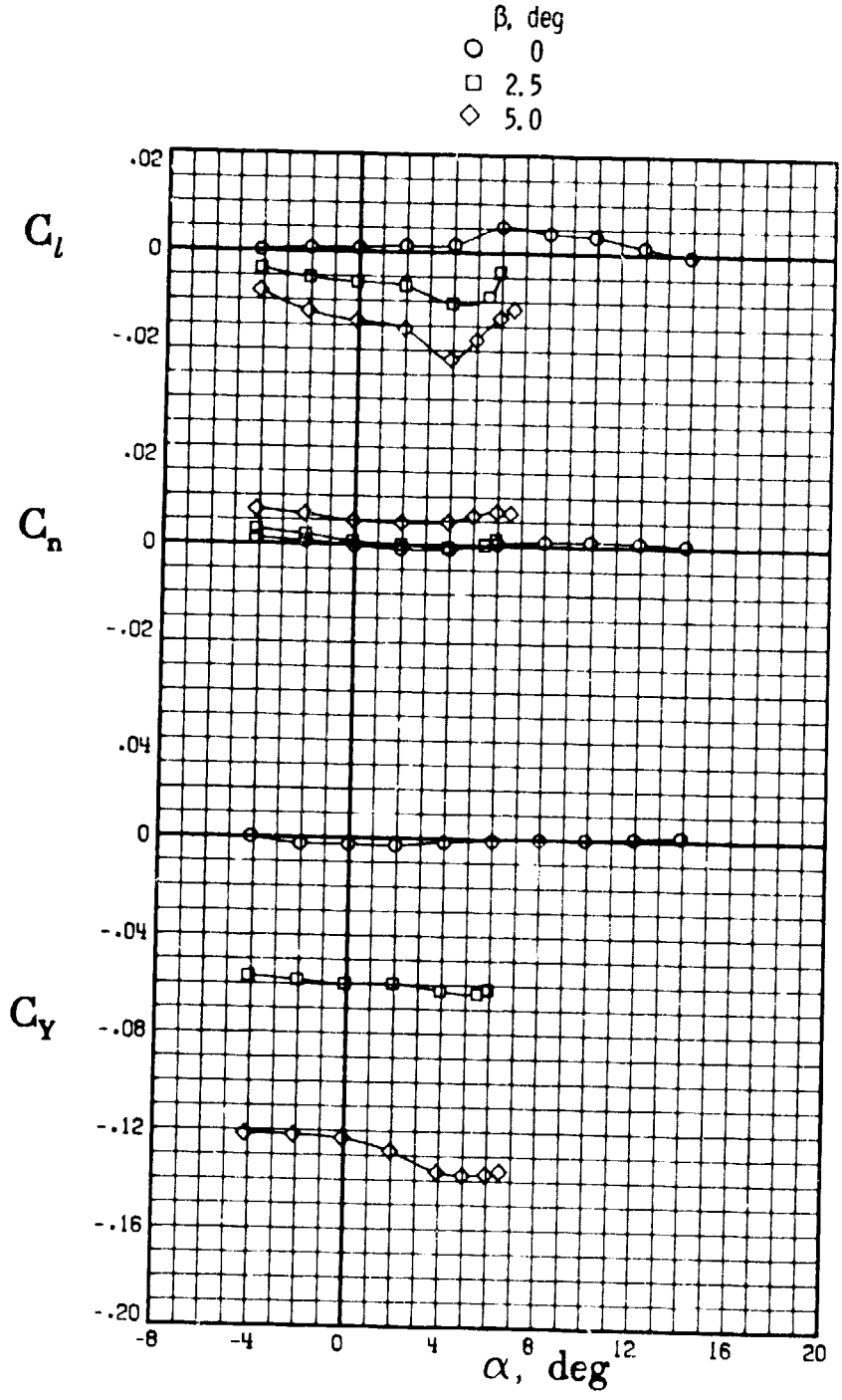

(b) M = 0.700.

Figure 30.- Continued. (U)

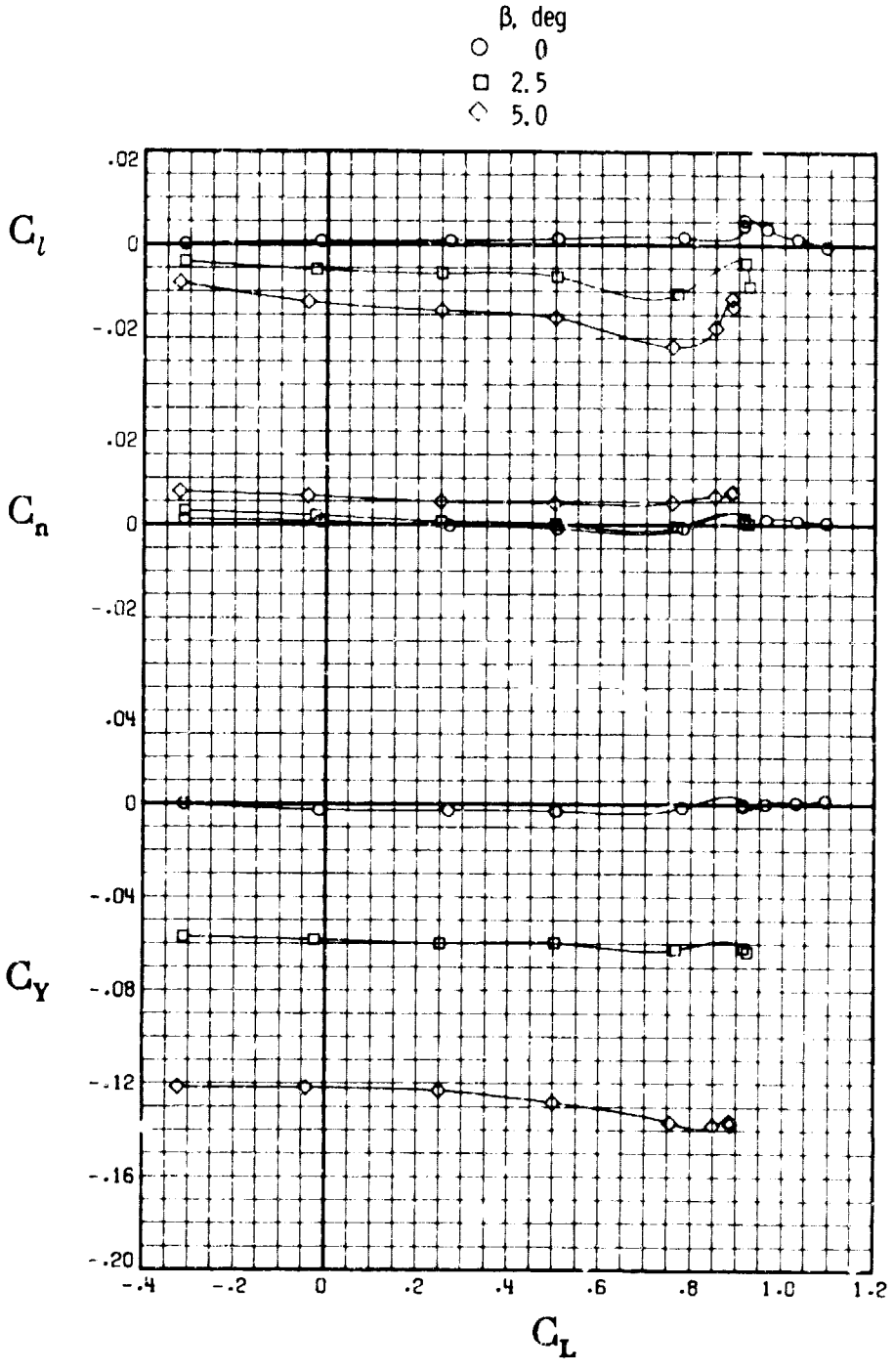

(b) Concluded.

Figure 30.- Continued. (U)

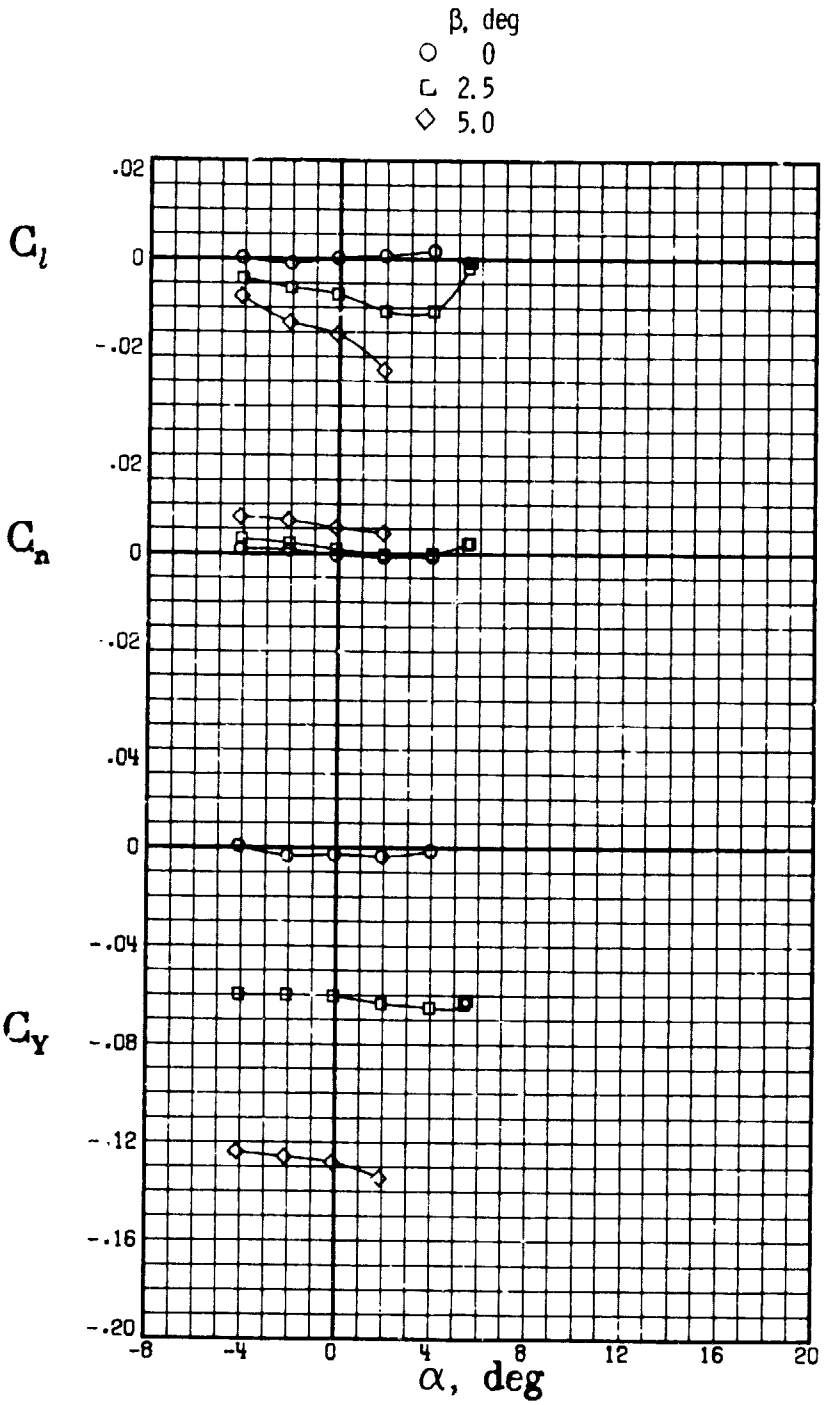

(c) M = 0.750.

Figure 30.- Continued. (U)

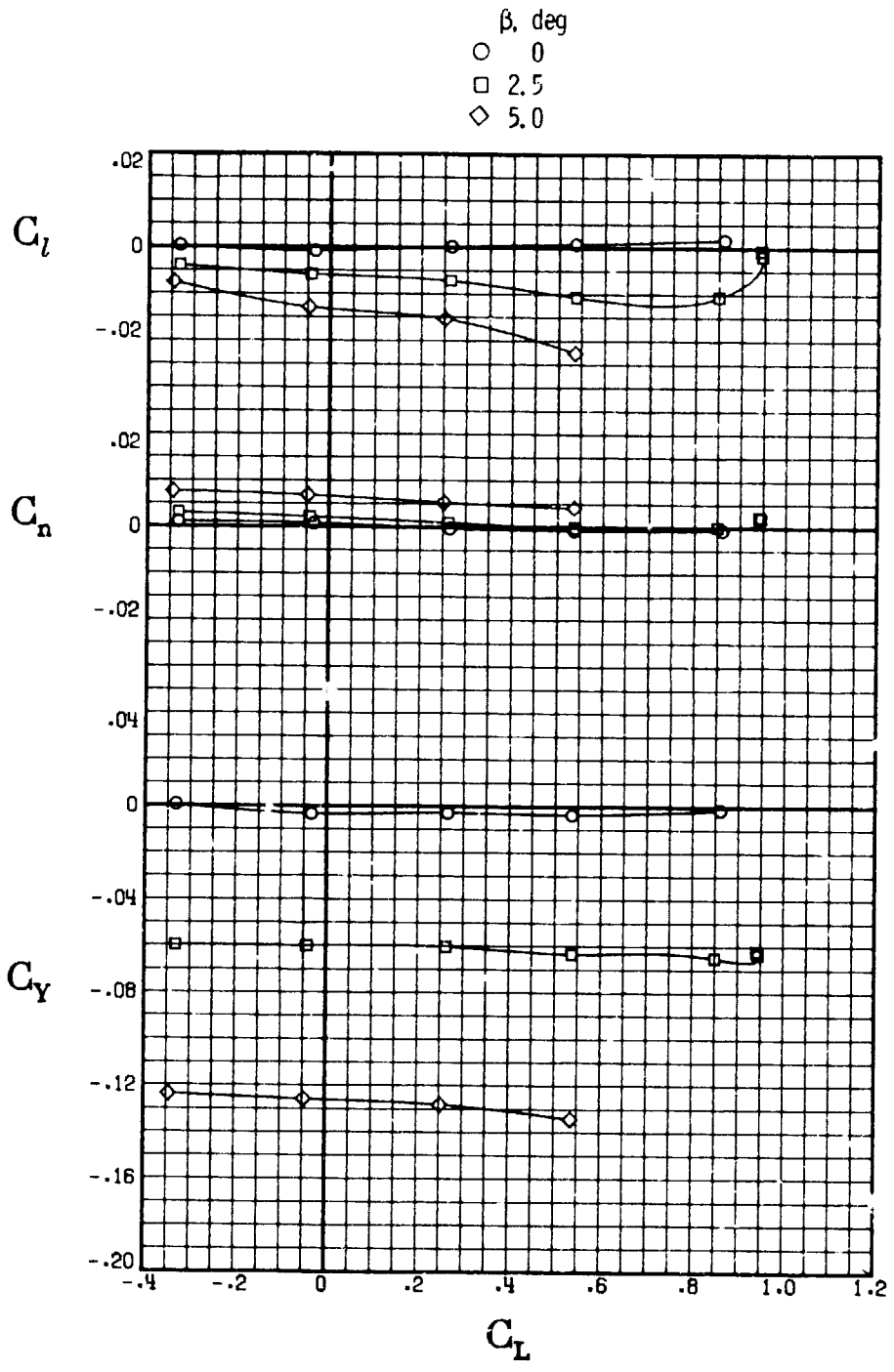

(c) Concluded.

Figure 30.- Continued. (U)

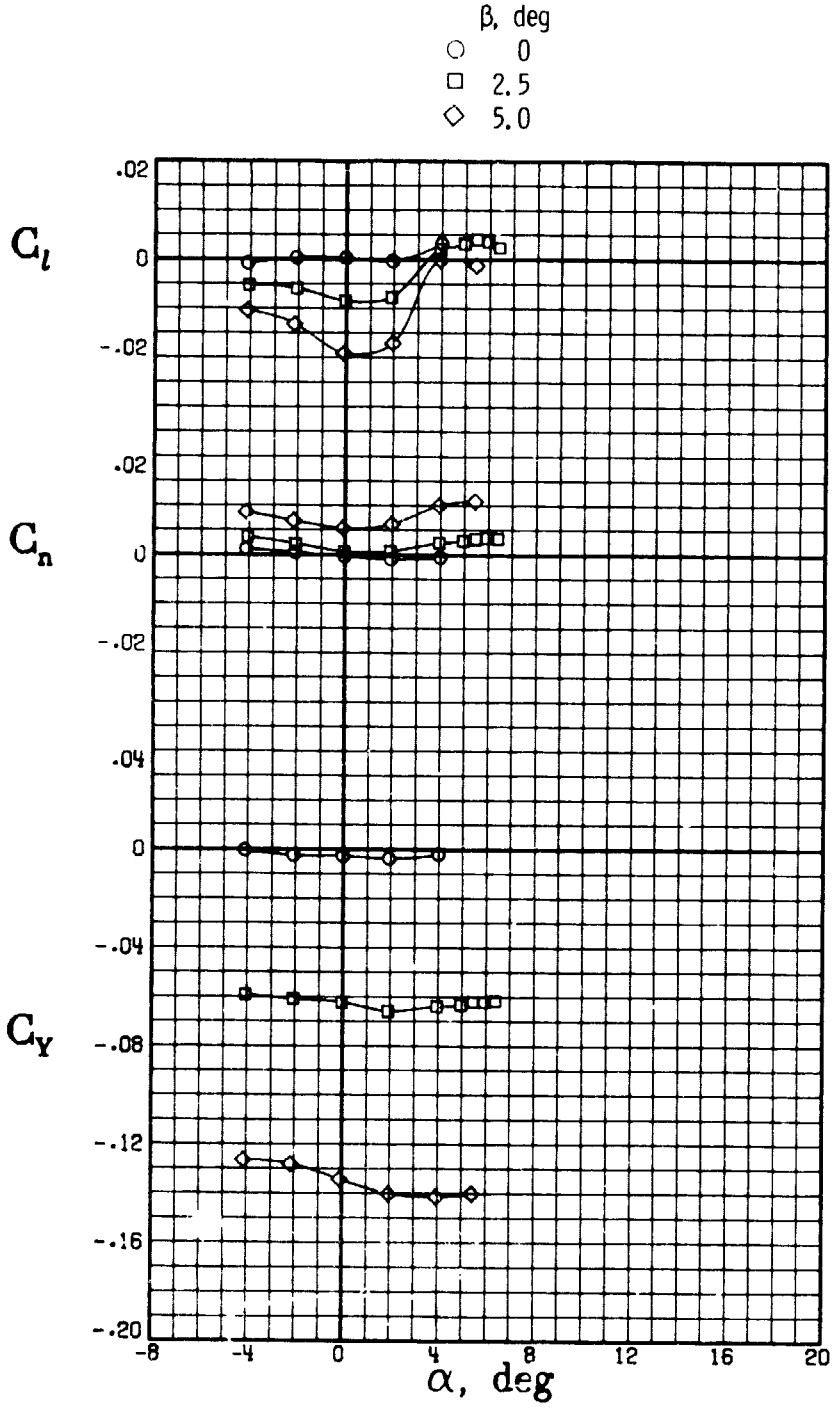

(d) M = 0.800.

Figure 30.- Continued. (U)

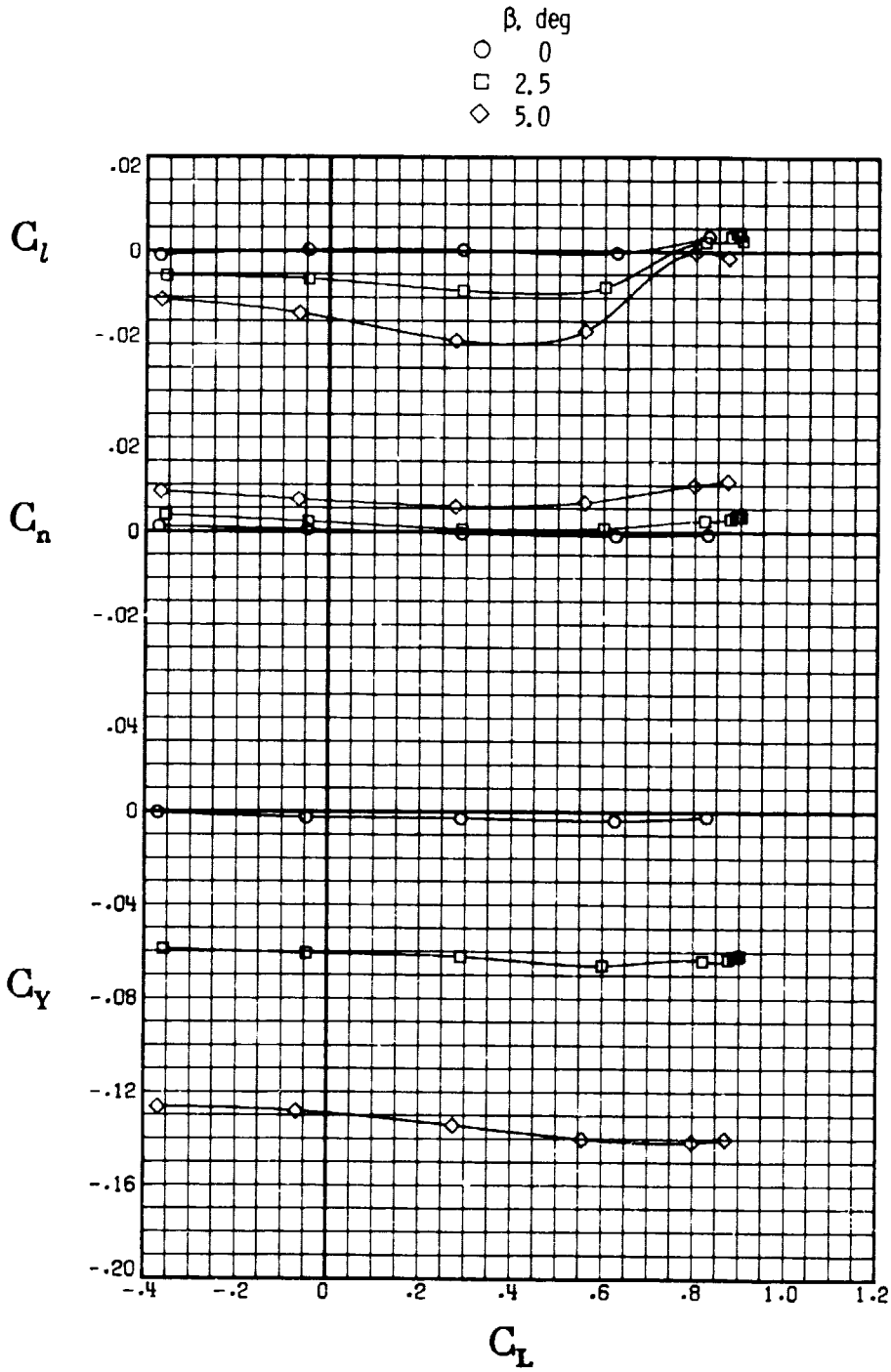

(d) Concluded.

Figure 30.- Continued. (U)

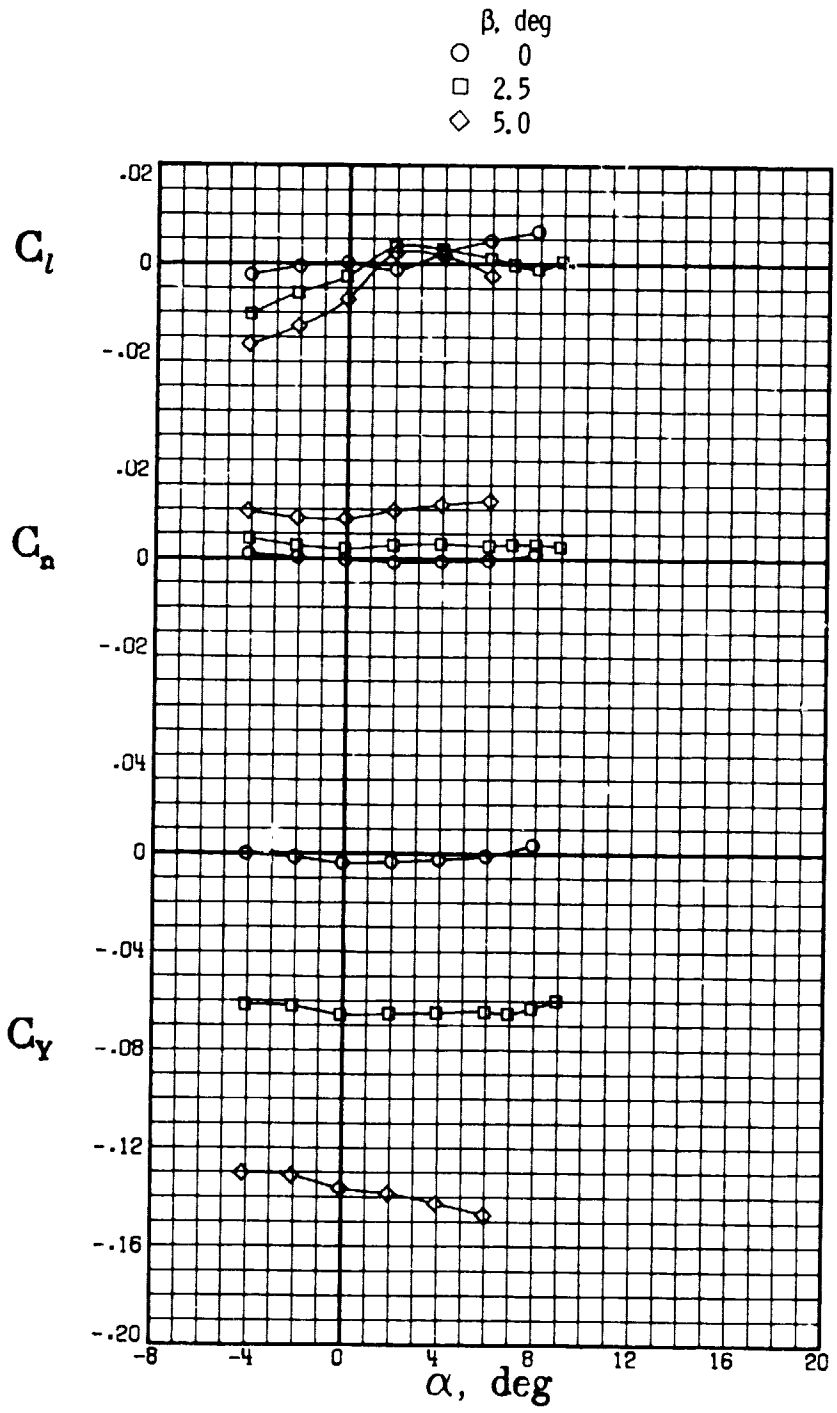

(e) M = 0.840.

Figure 30.- Continued. (U)

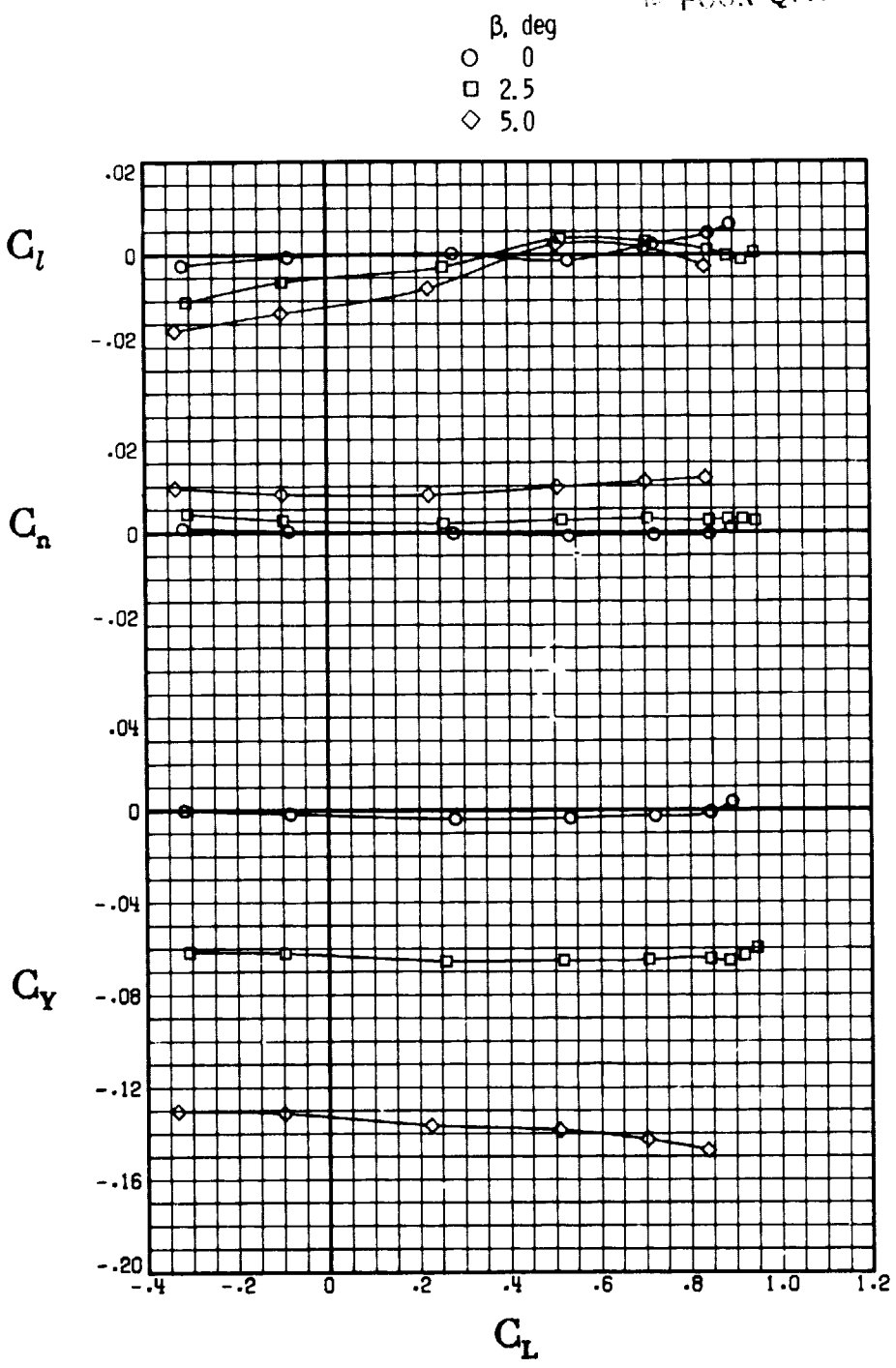

(e) Concluded.

Figure 30.- Continued. (U)

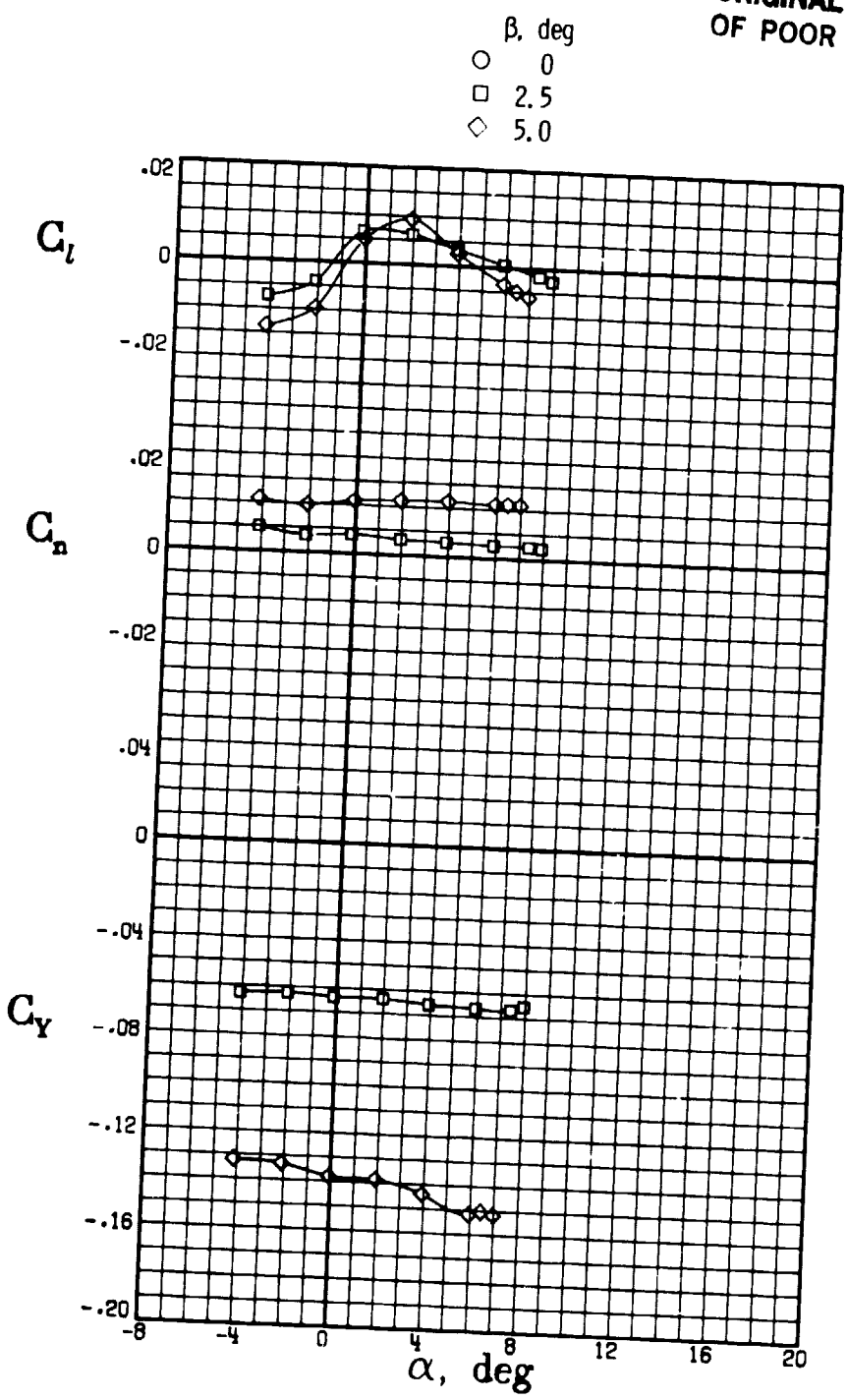

(f) M = 0.860.

Figure 30.- Continued. (U)

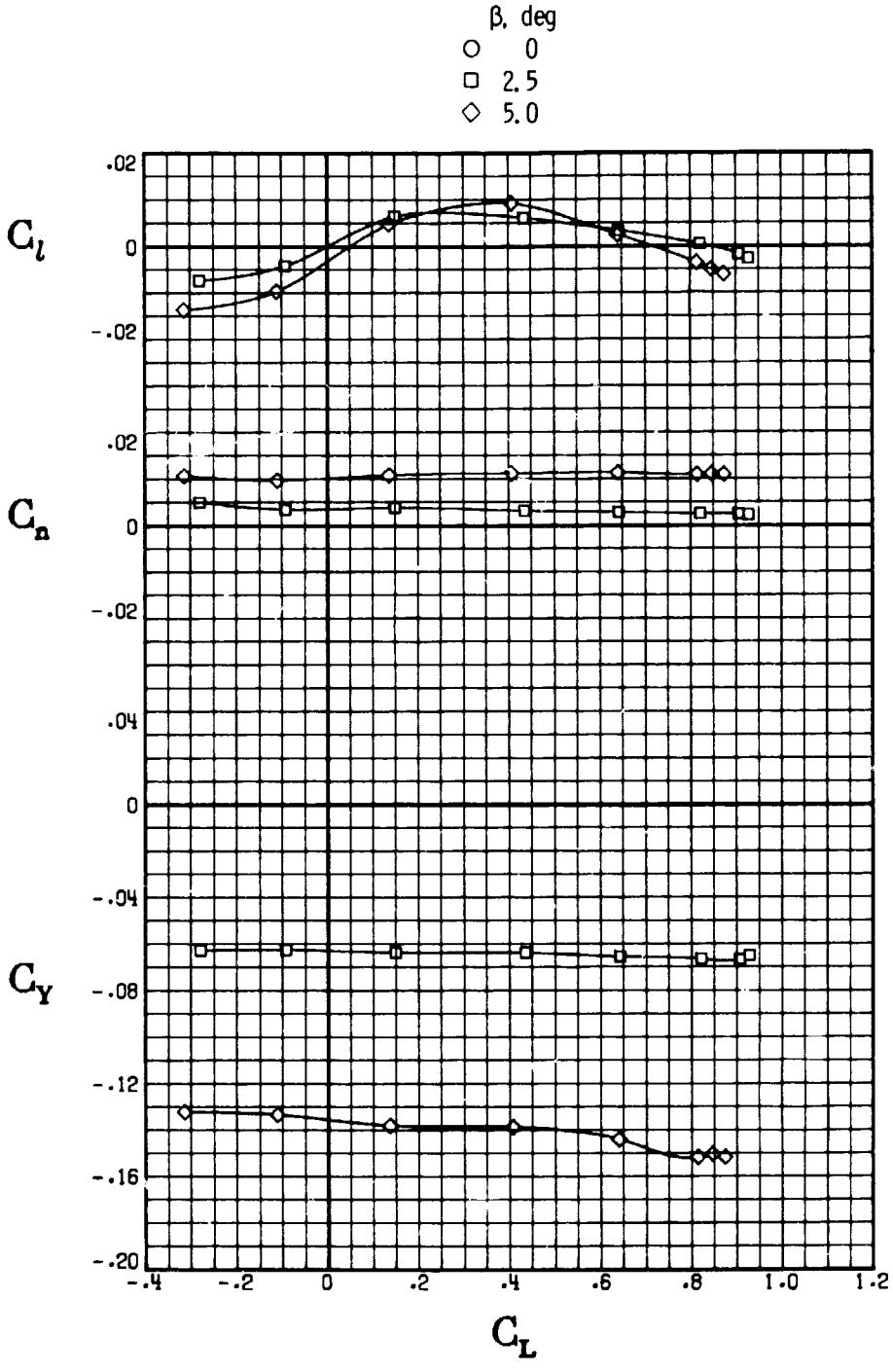

(f) Concluded.

Figure 30.- Continued. (U)

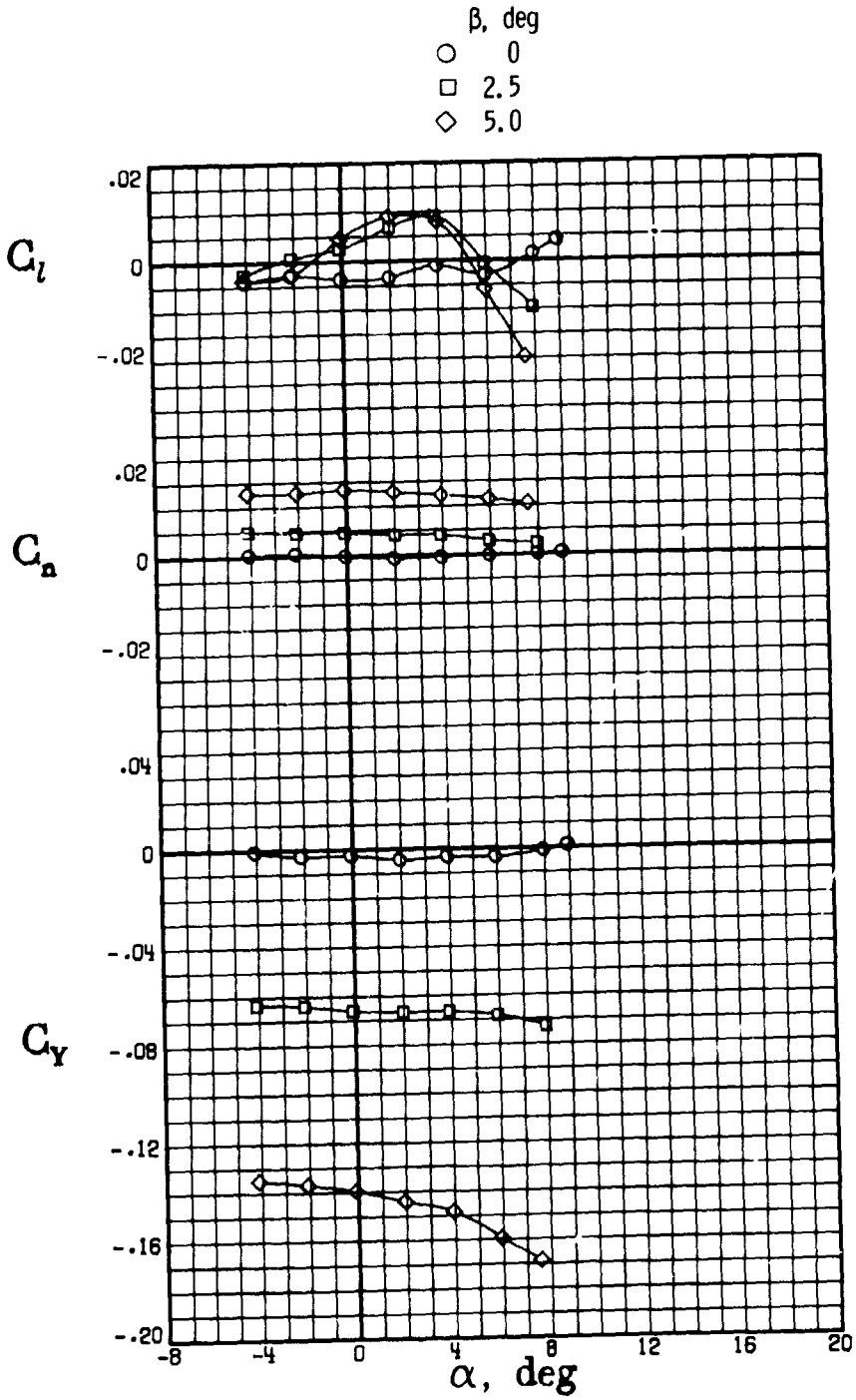

(g) M = 0.900.

Figure 30.- Continued. (U)

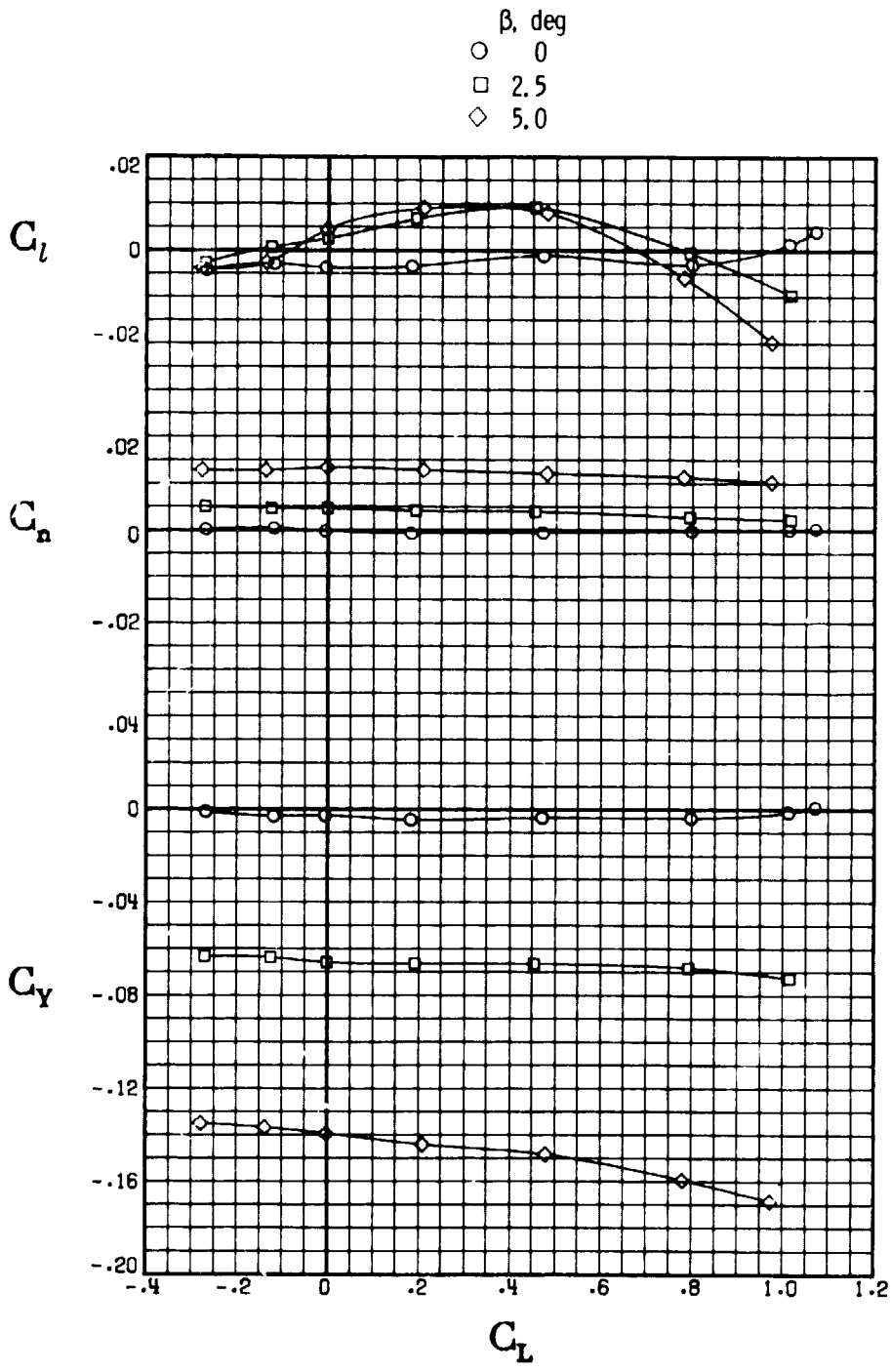

(g) Concluded.

Figure 30.- Continued. (U)

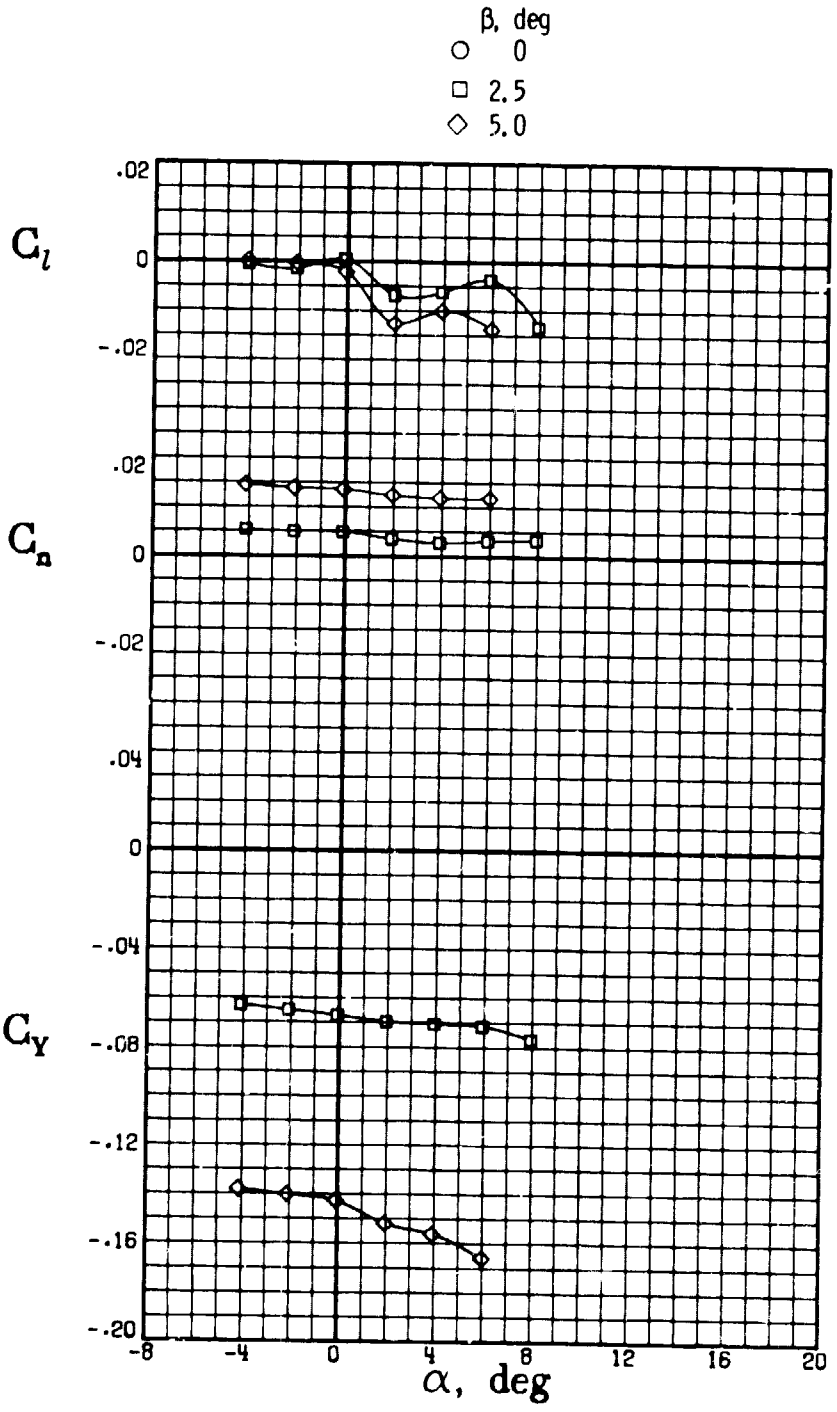

(h) M = 0.920.

Figure 30.- Continued. (U)

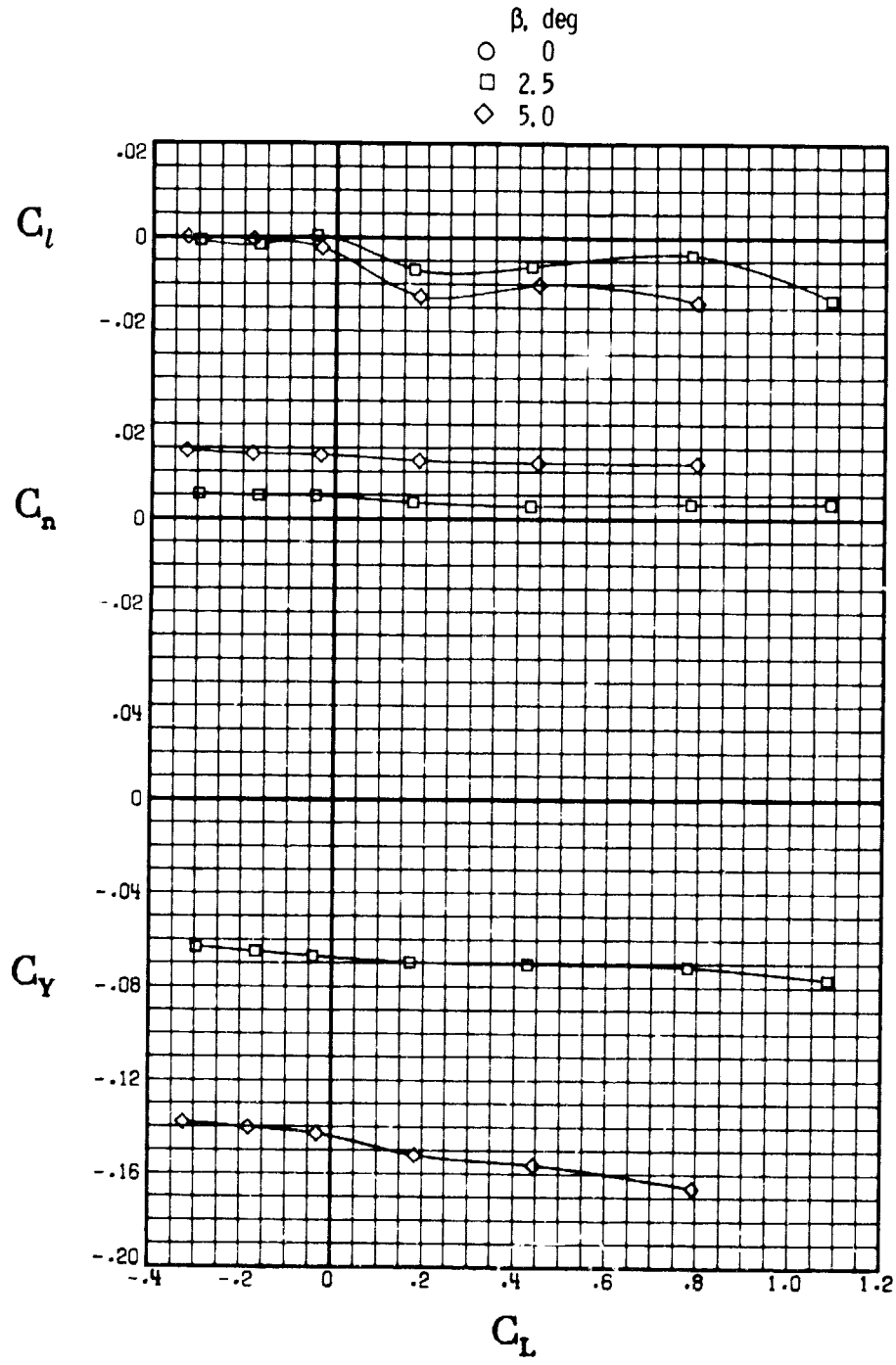

(h) Concluded.

Figure 30.- Concluded. (U)

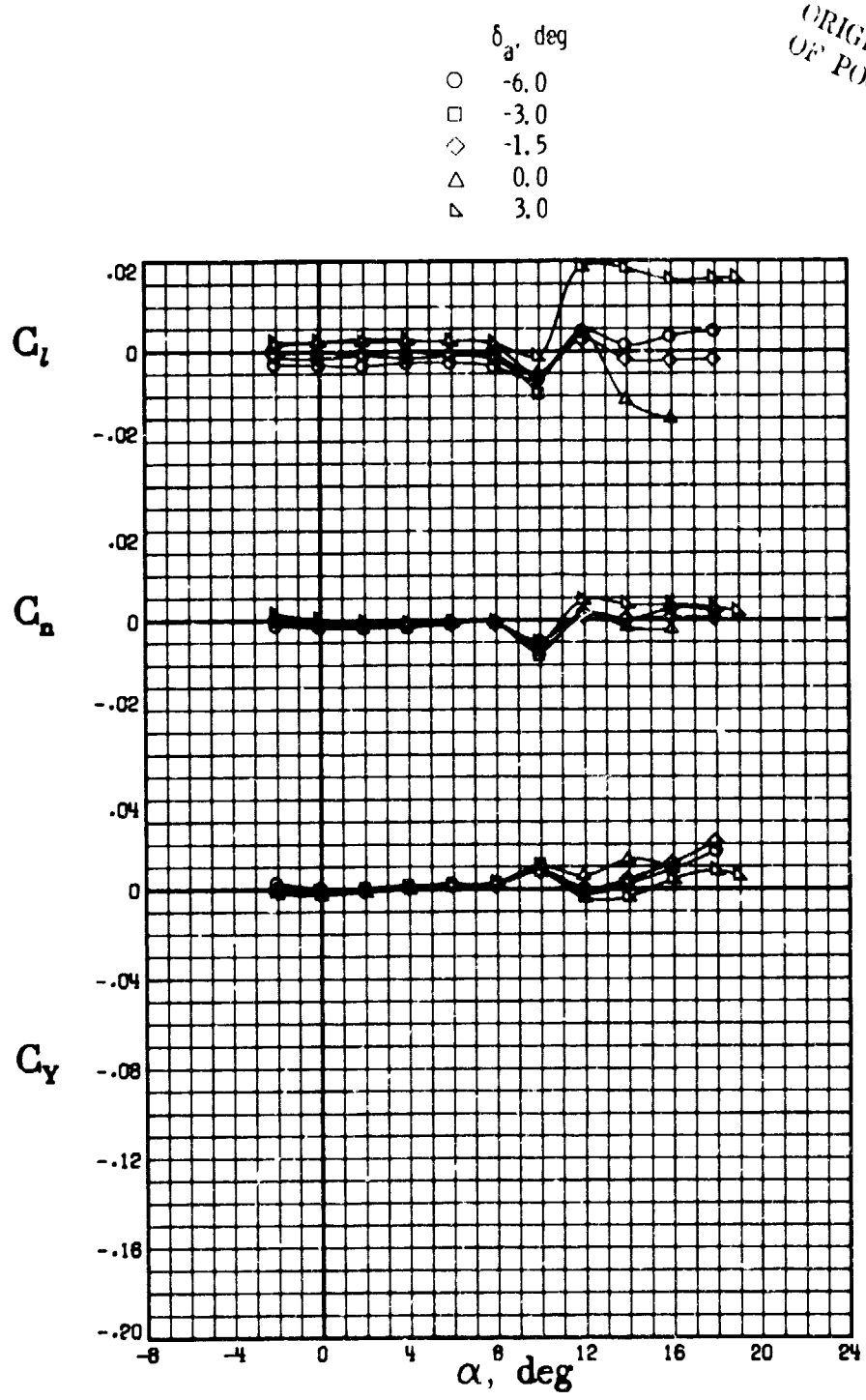

(a) M = 0.300.

(C) Figure 31.- Effect of roll control on lateral-directional aerodynamic characteristics for model configuration C. $\beta = 0^o$; $\delta_r = 0^o$. (U)

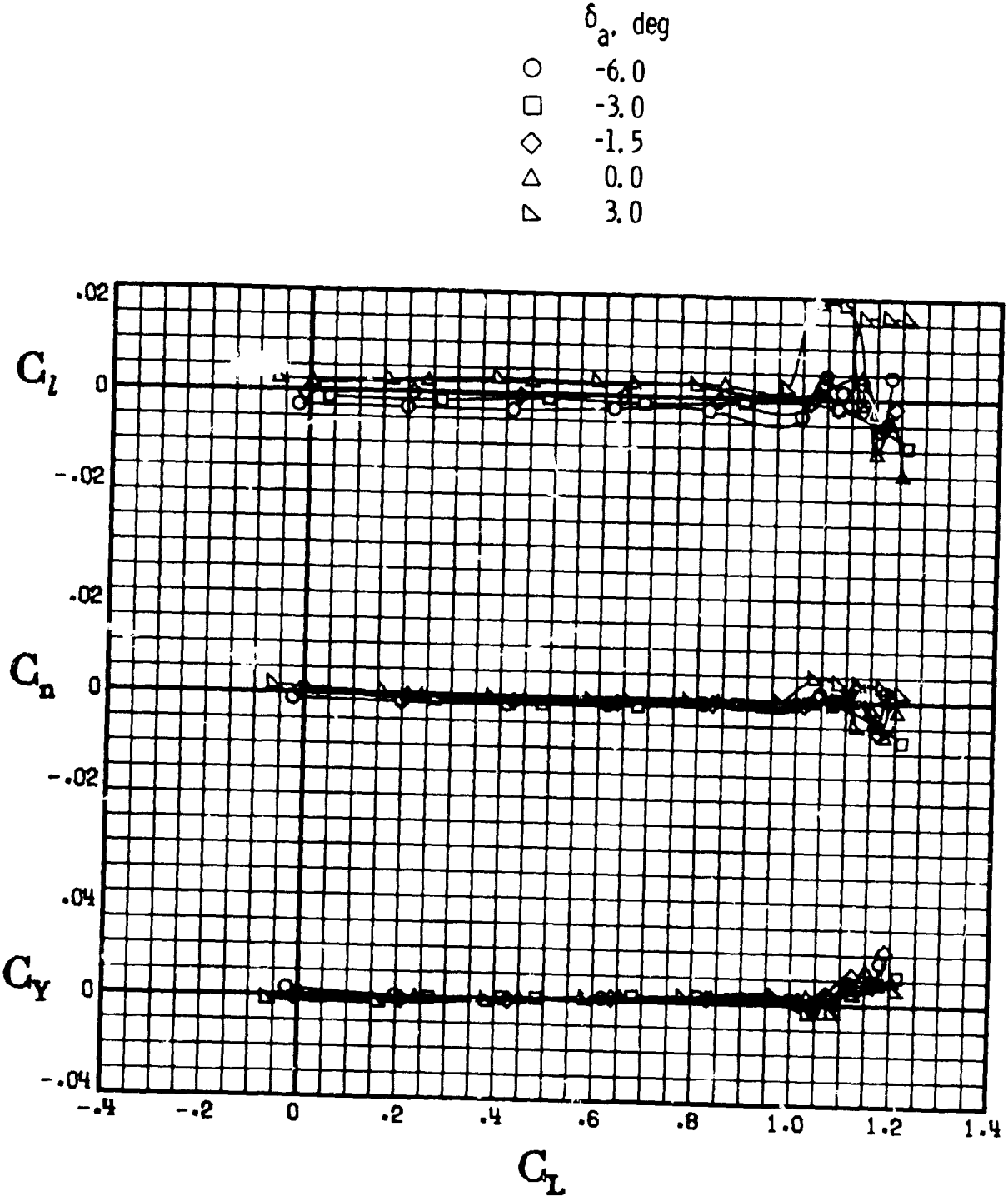

(a) Concluded.

Figure 31.- Continued. (U)

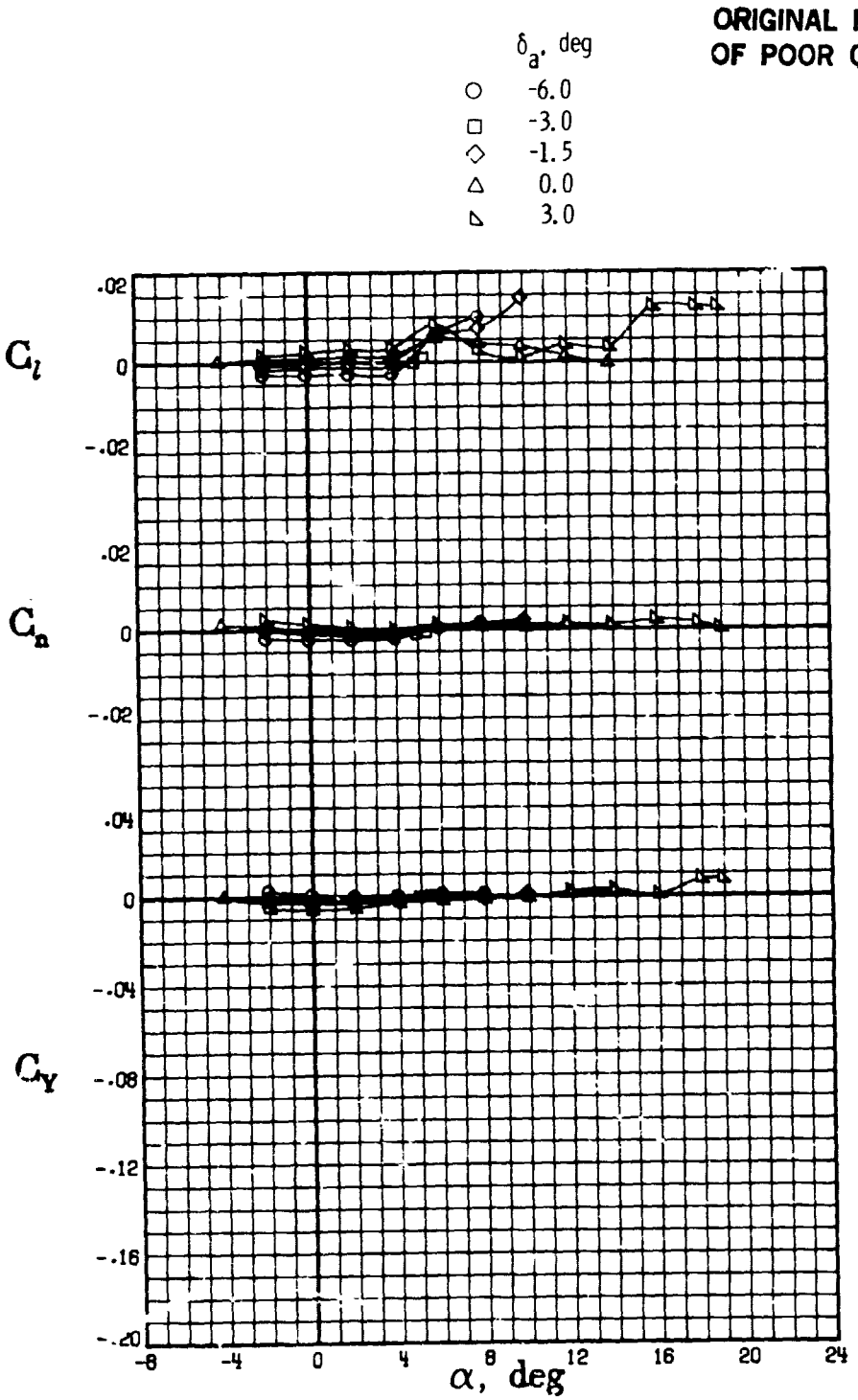

(b) M = 0.700.

Figure 31.- Continued. (U)

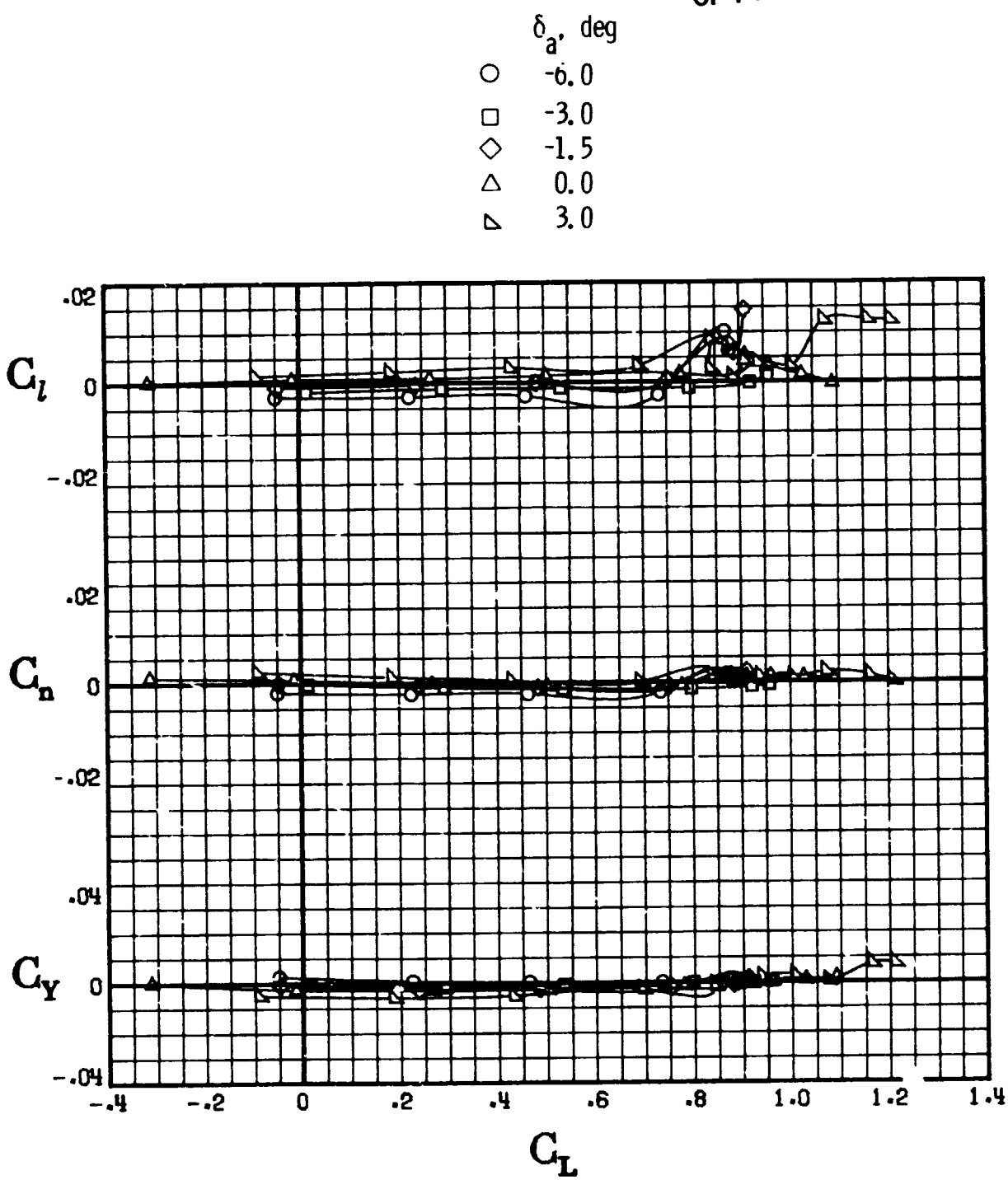

(b) Concluded.

Figure 31.- Continued. (U)

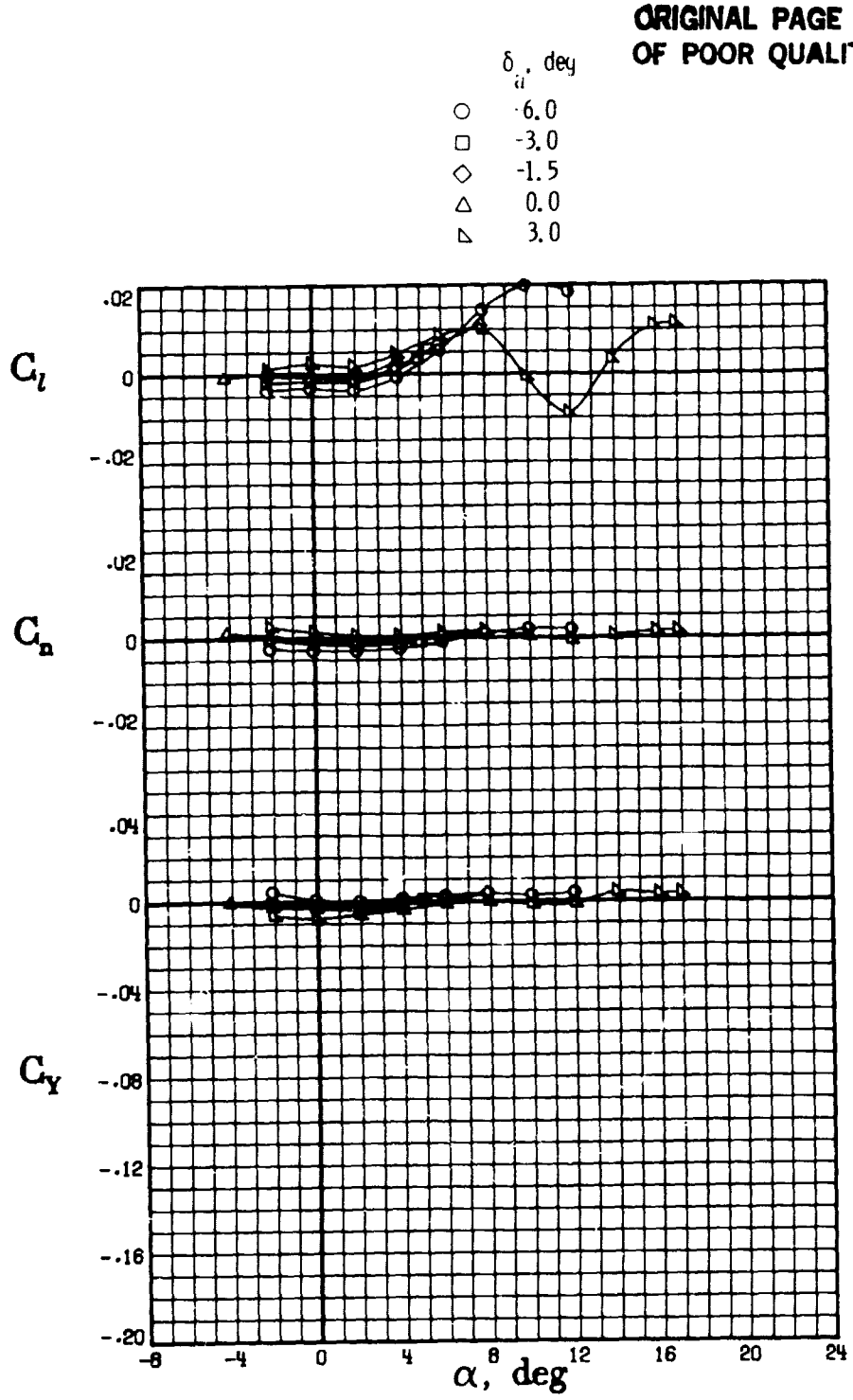

(c) M = 0.800.

(C) Figure 31.- Continued. (U)

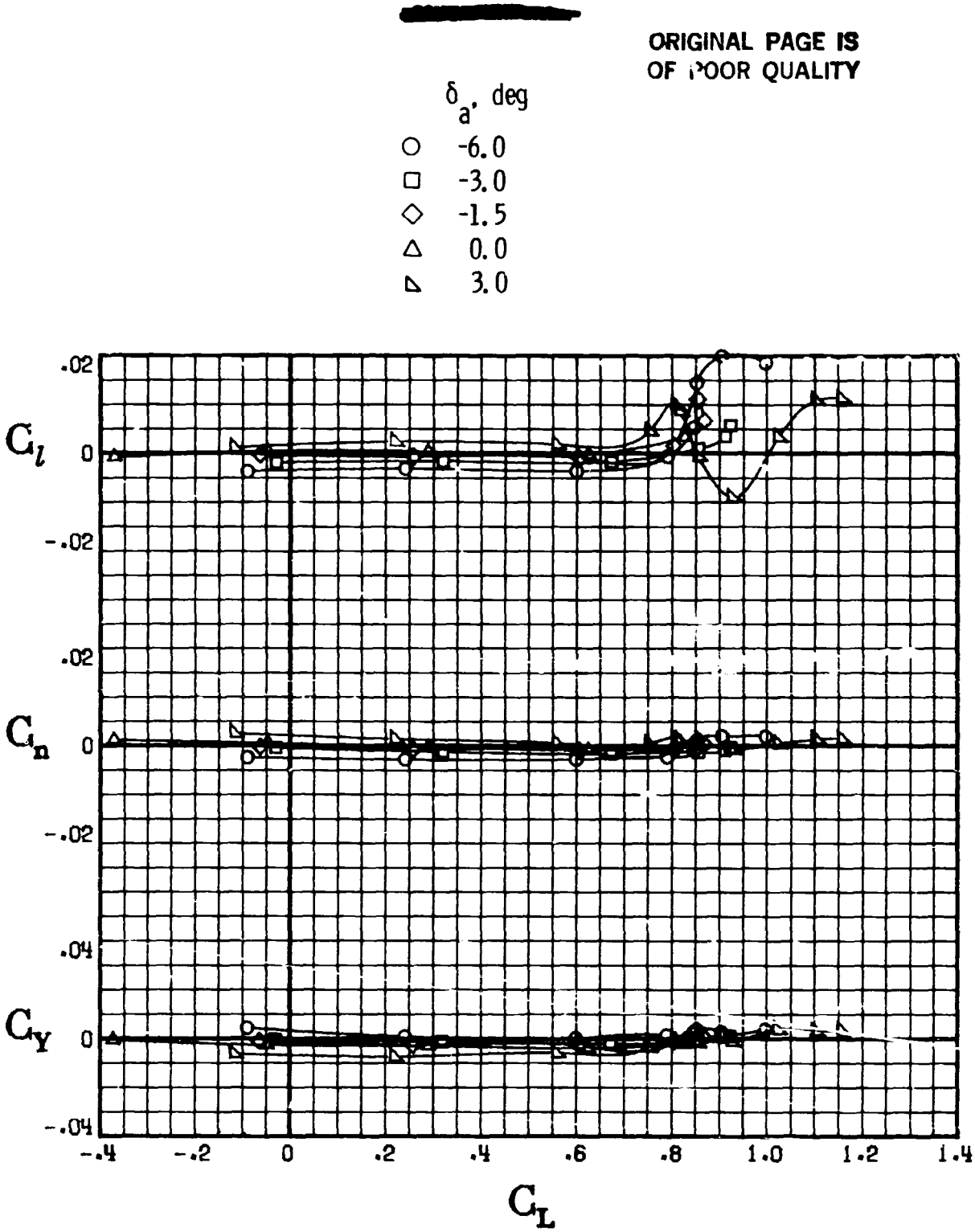

(c) Concluded.

Figure 31.- Continued. (U)

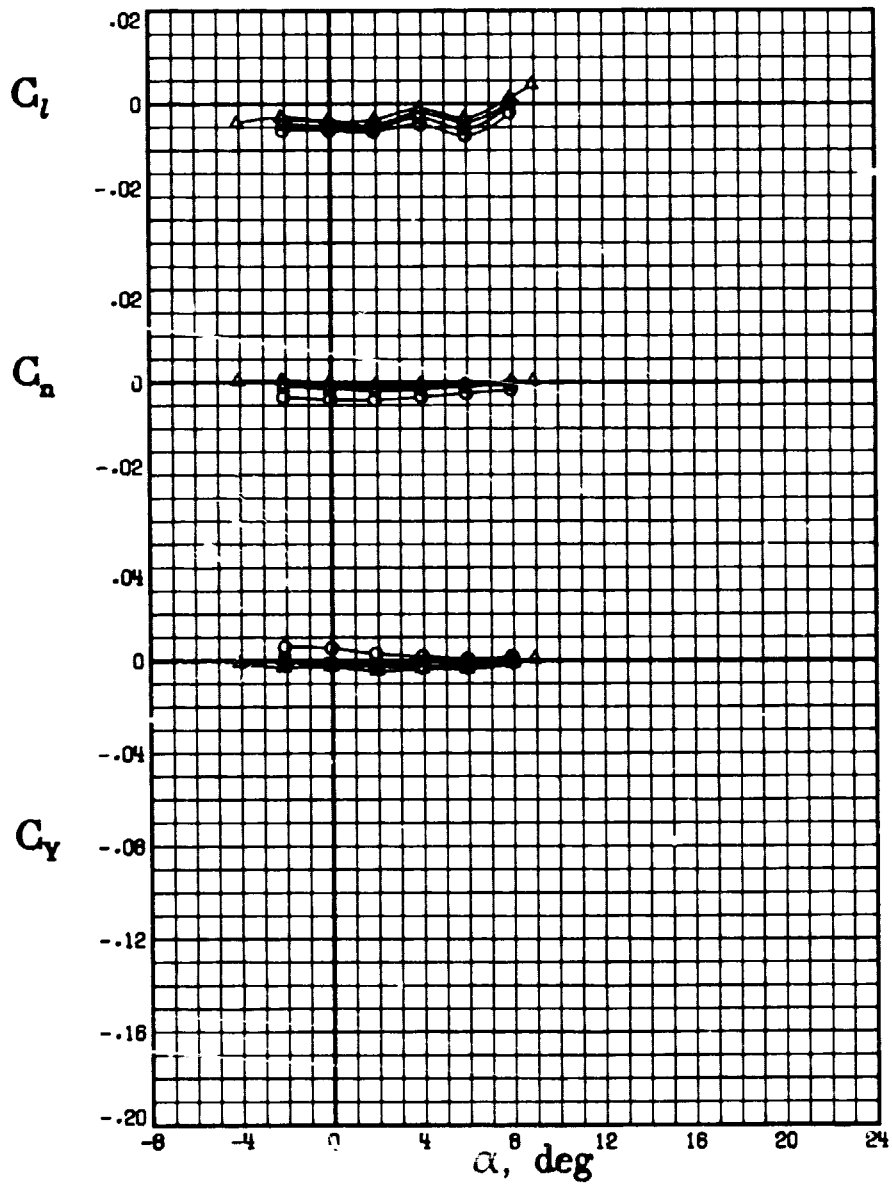

(d) M = 0.900.

Figure 31.- Continued. (U)

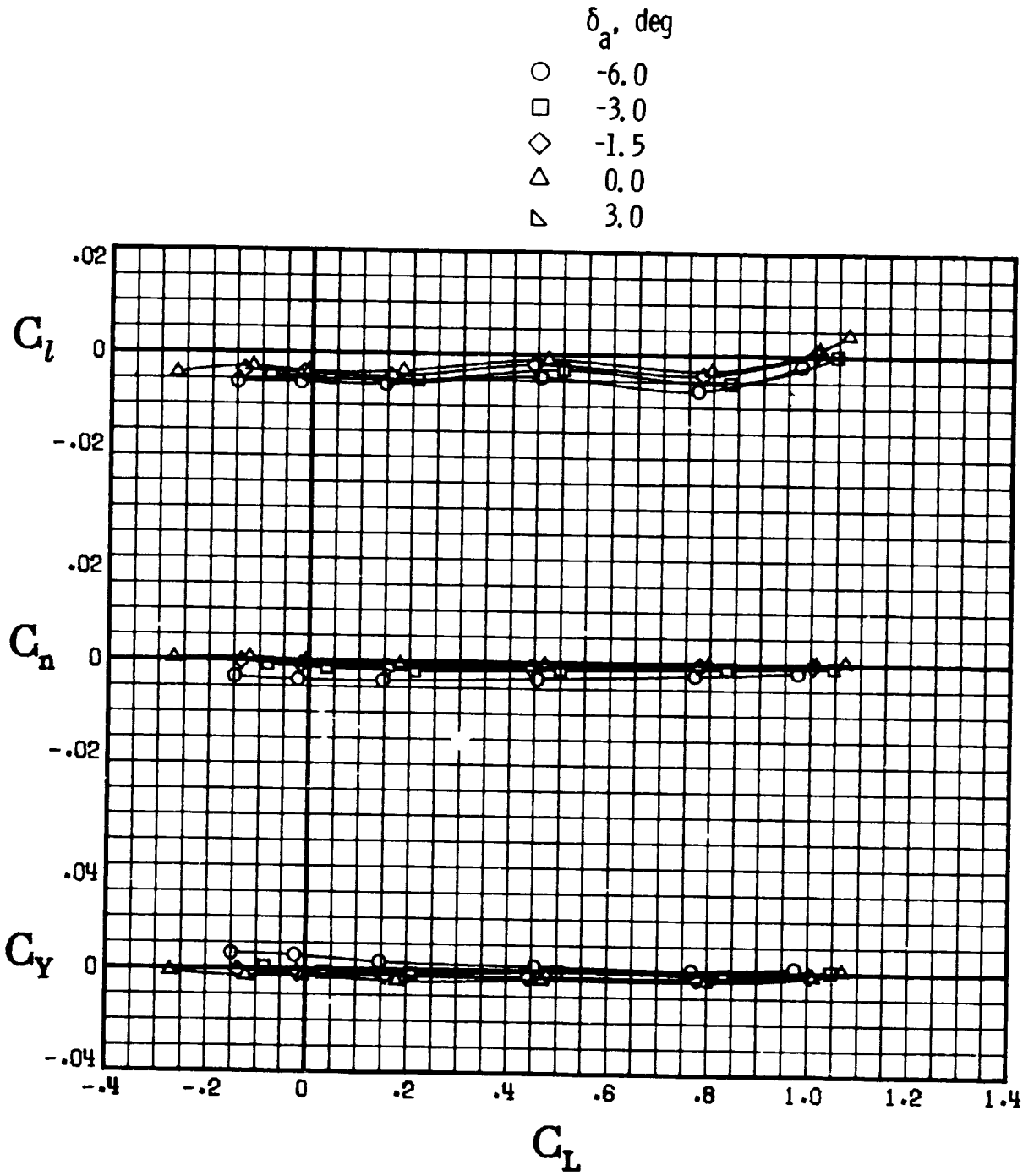

(d) Concluded.

Figure 31.- Concluded. (U)

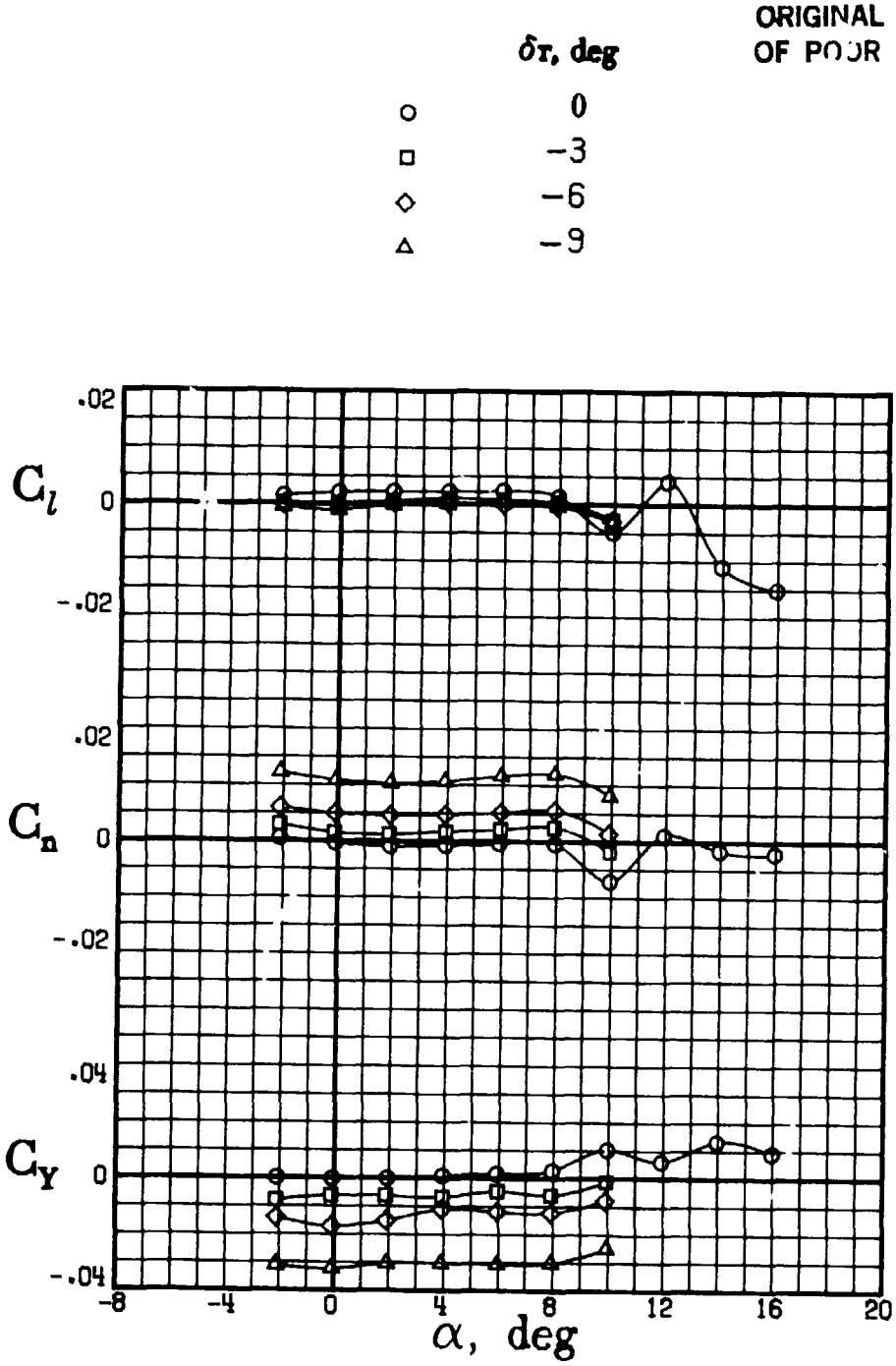

(a) M = 0.300.

Figure 32.- Effect of directional control on lateral-directional characteristics for model configuration C. $\delta_a = 0^o$; $\beta = 0^o$. (U)

	δr, deg
○	0
□	-3
◇	-6
△	-9

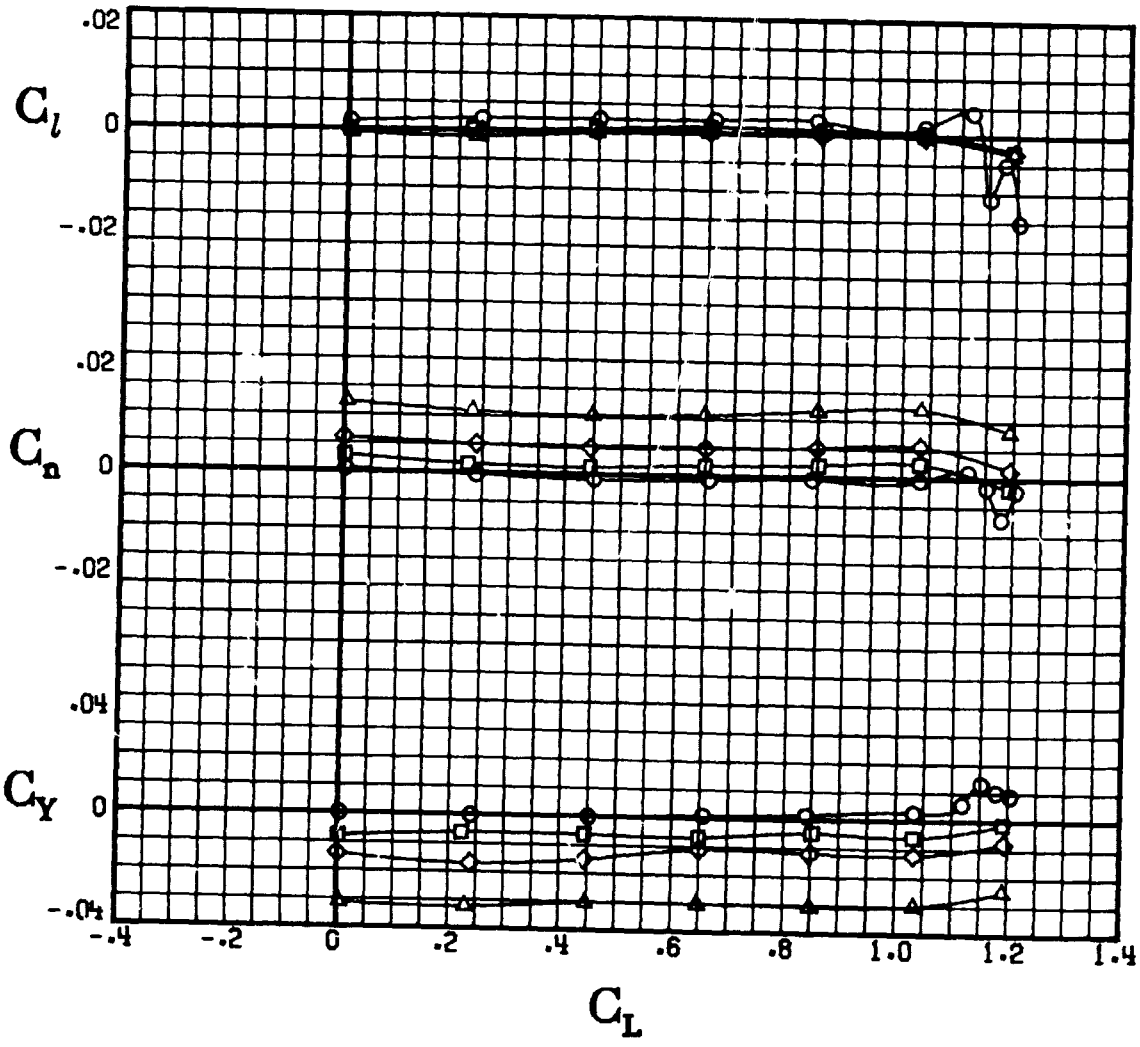

(a) Concluded.

Figure 32.- Continued. (U)

	δr, deg
○	0
□	-3
◇	-6
△	-9

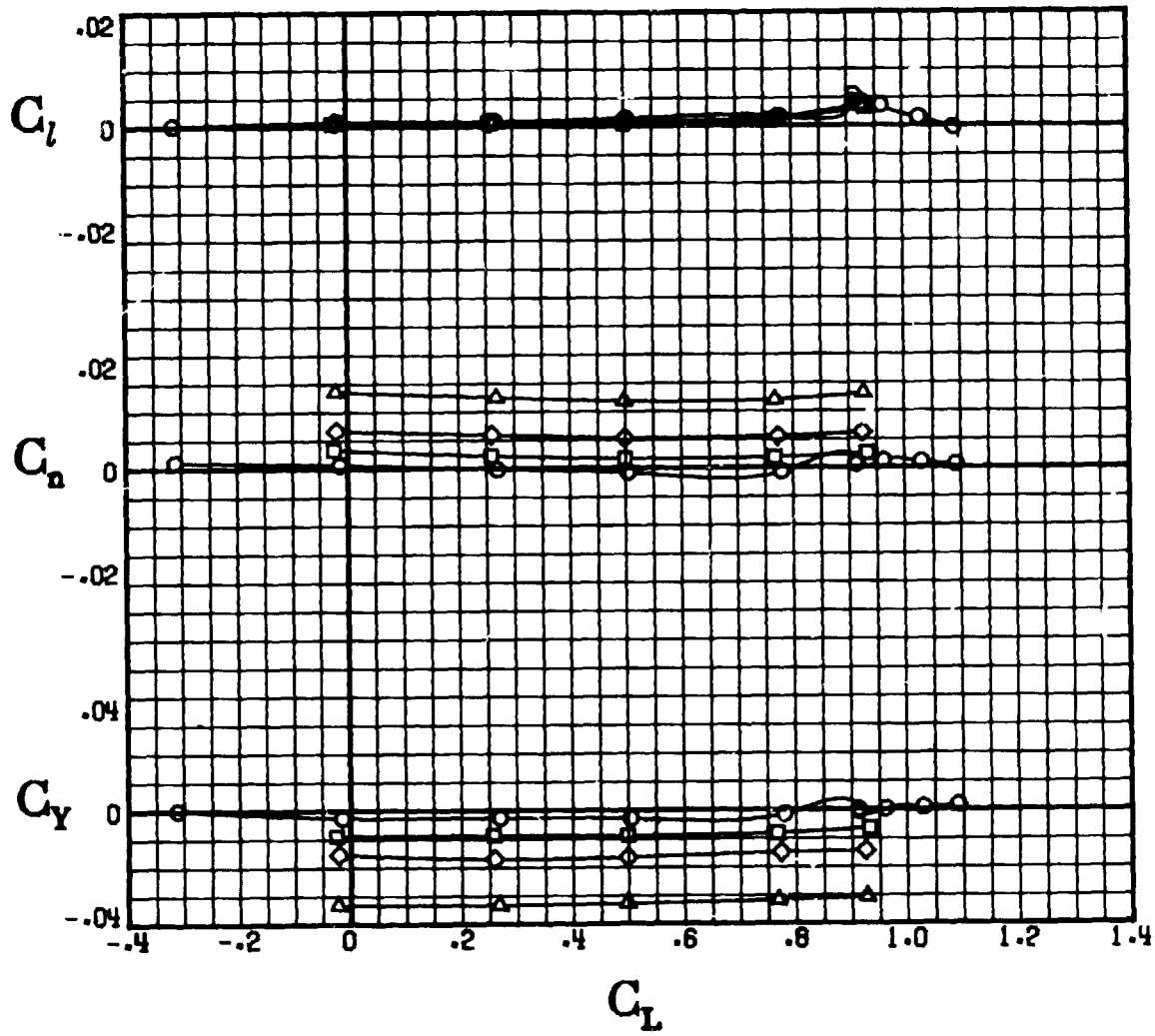

(b) M = 0.700.

Figure 32.- Continued. (U)

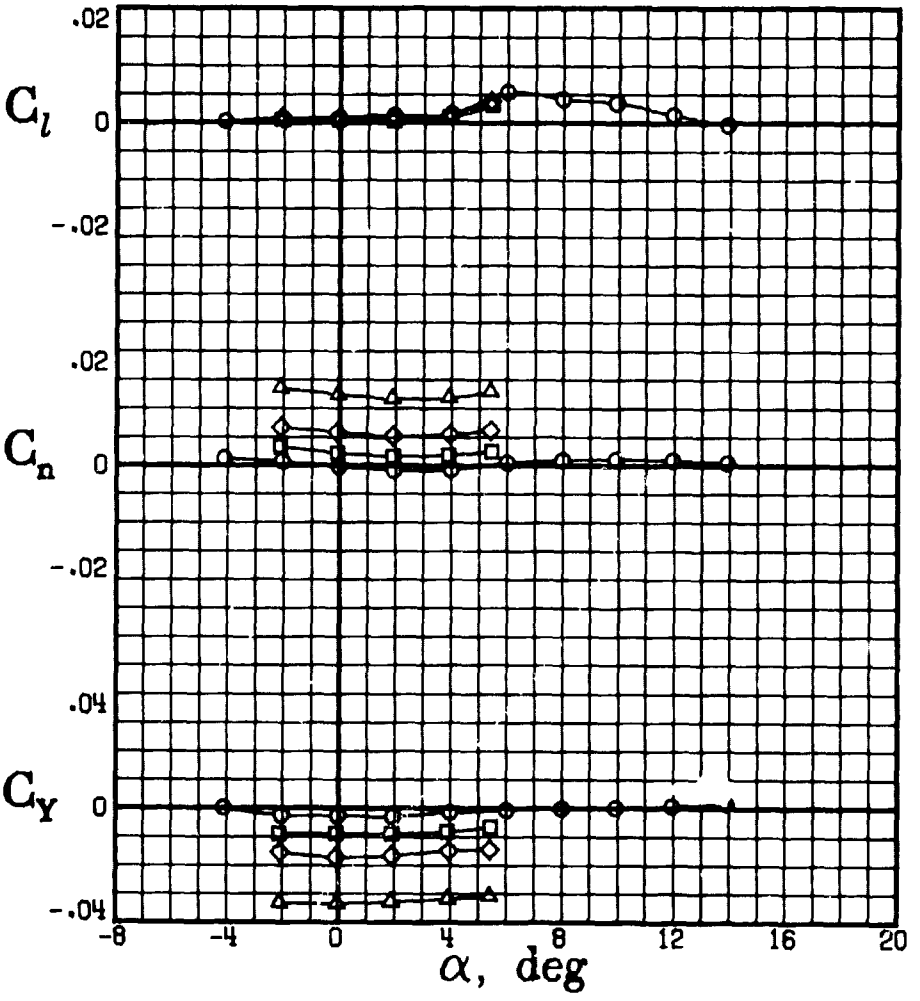

(b) Concluded.

Figure 32.- Continued. (U)

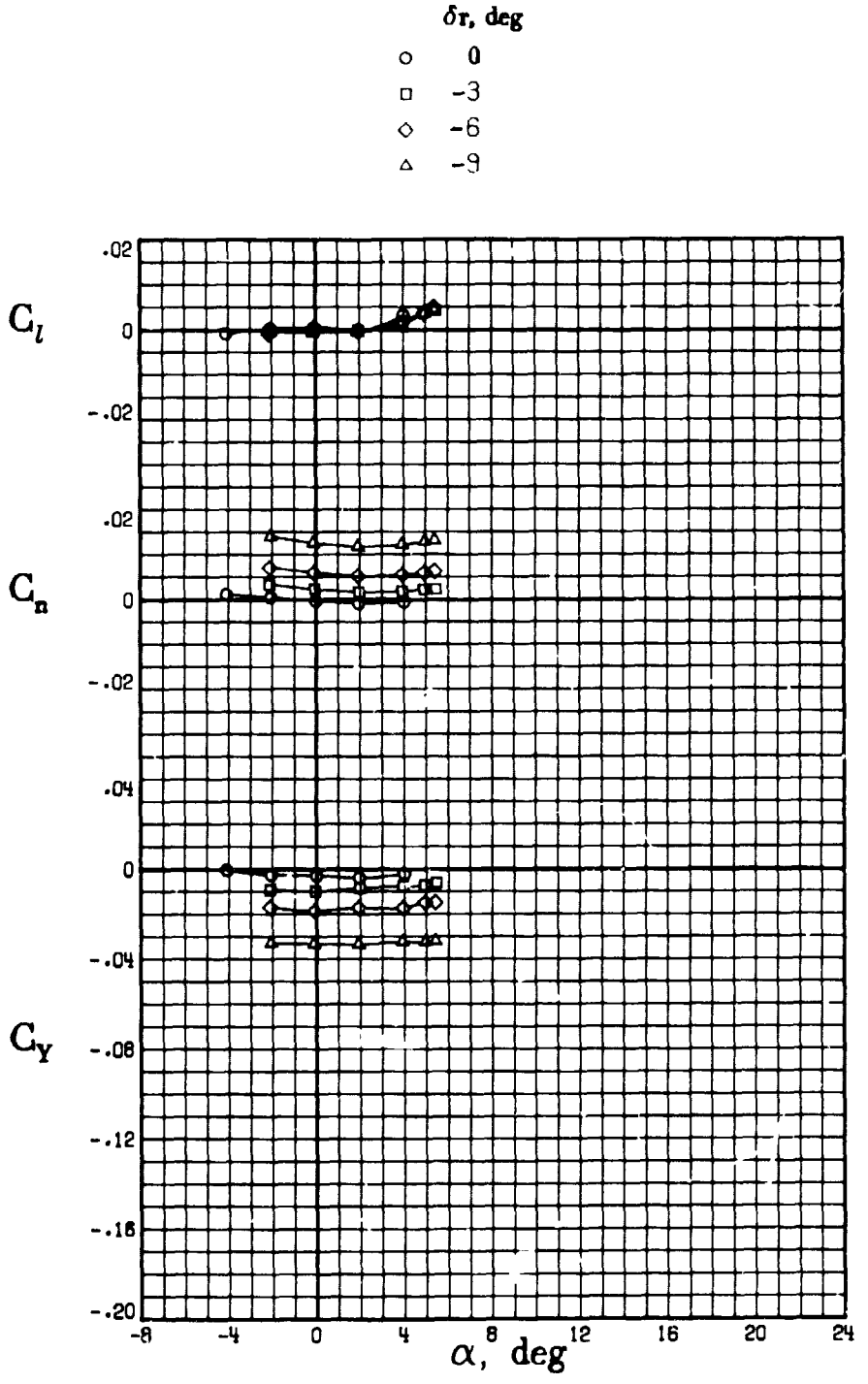

(c) M = 0.800.

Figure 32.- Continued. (U)

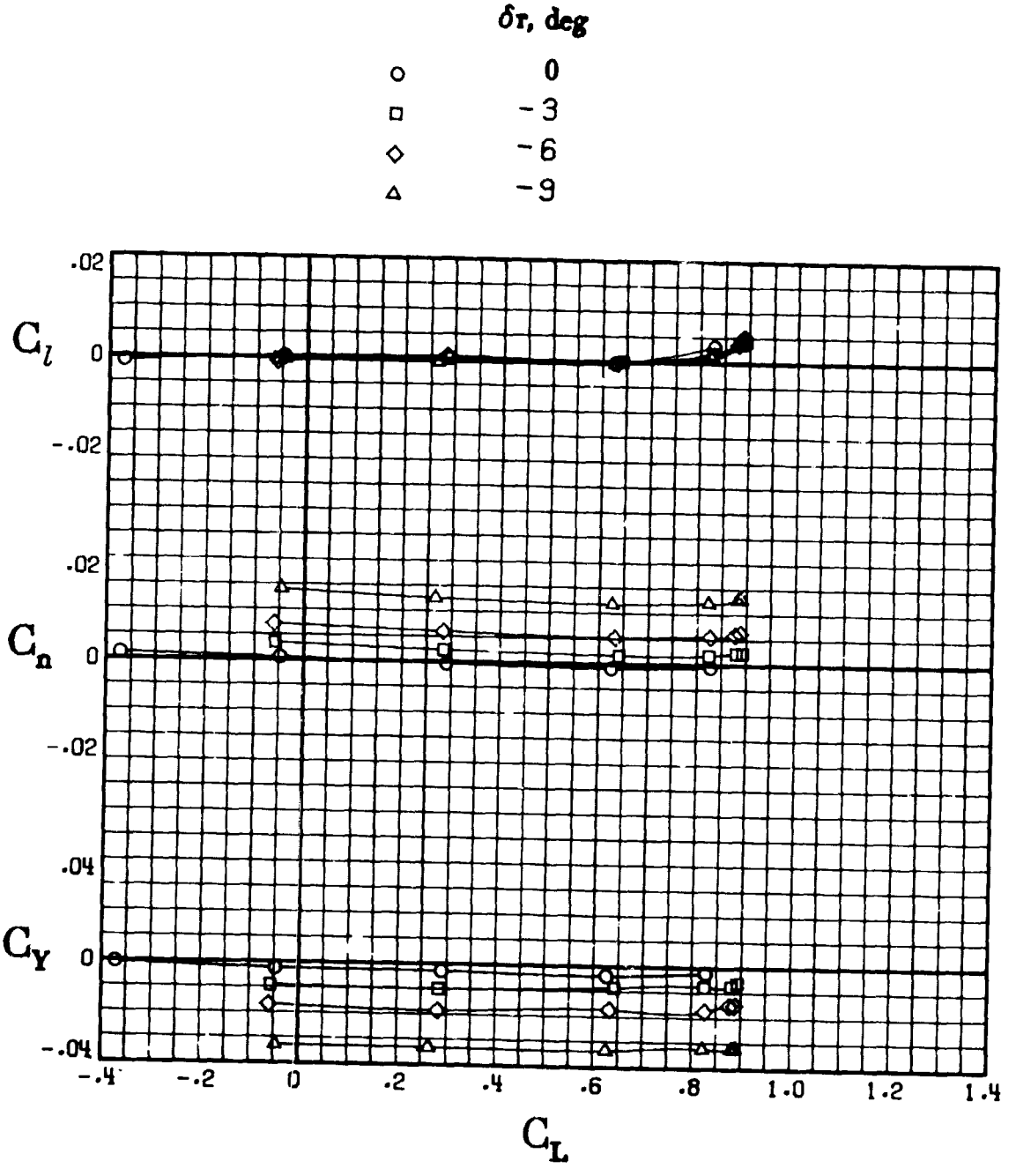

(c) Concluded.

Figure 32.- Continued. (U)

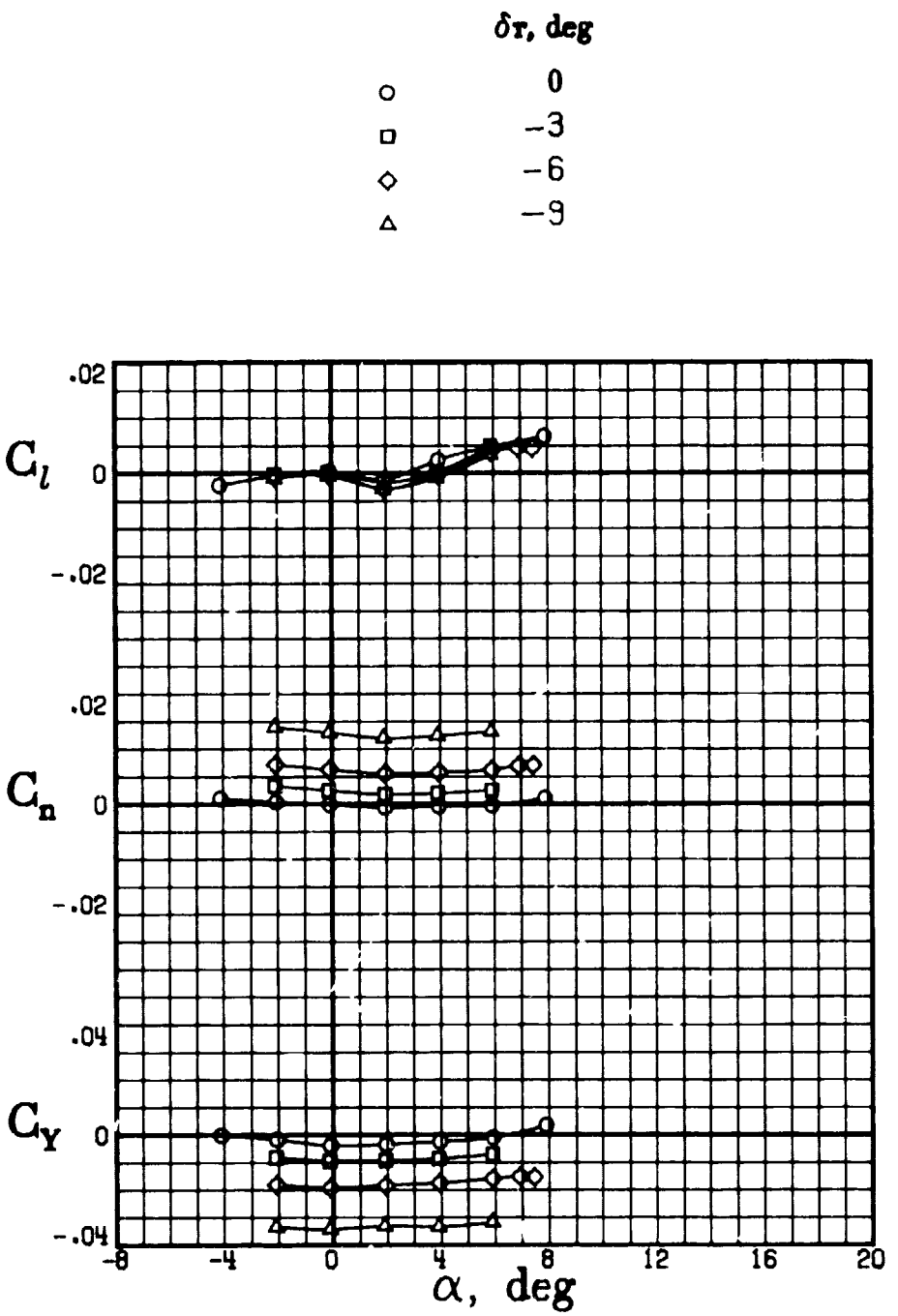

(d) M = 0.840.

Figure 32.- Continued. (U)

δ_r, deg
○ 0
□ −3
◇ −6
△ −9

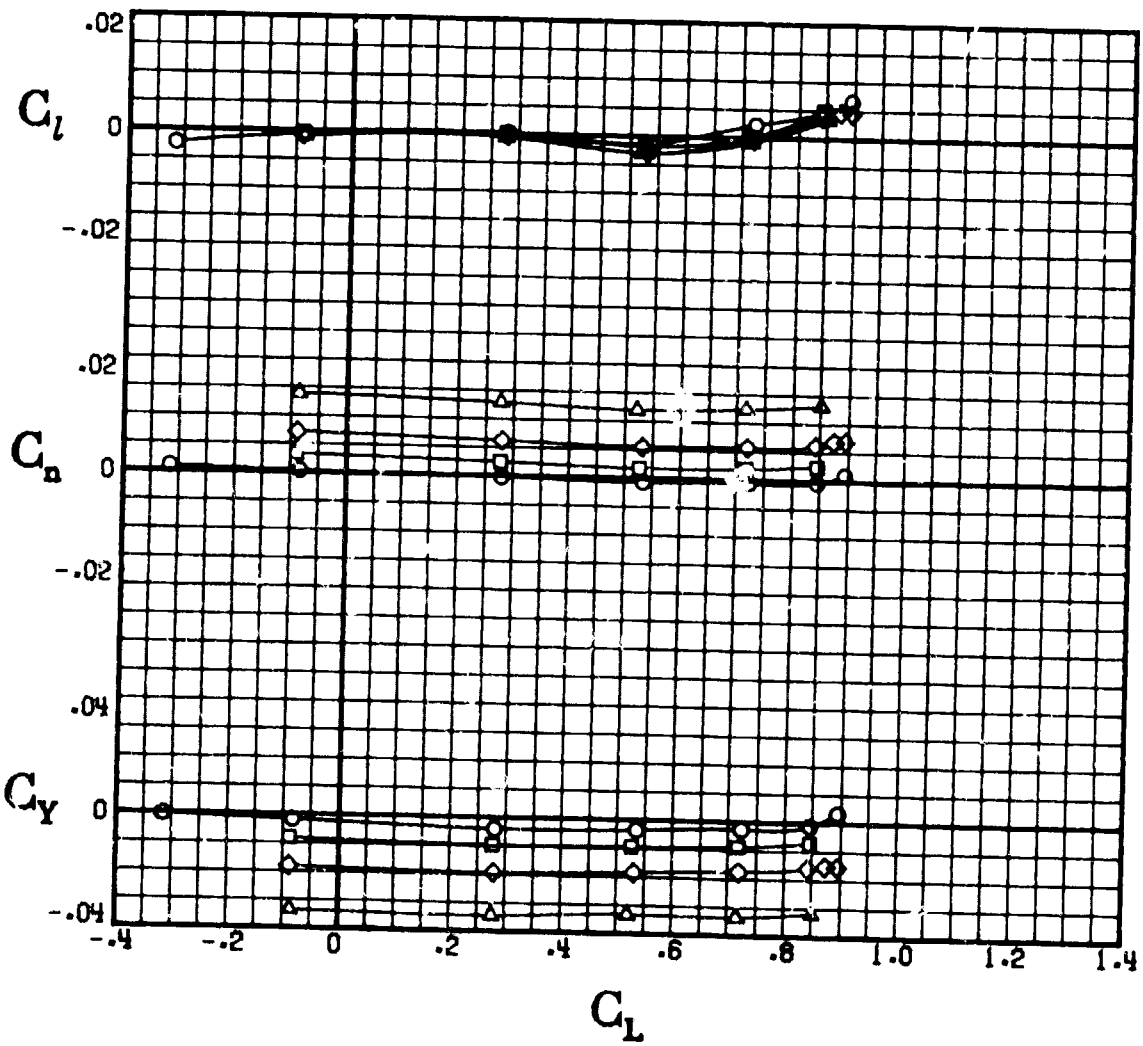

(d) Concluded.

Figure 32.- Continued. (U)

	δ_r, deg
○	0
□	−3
◇	−6
△	−9

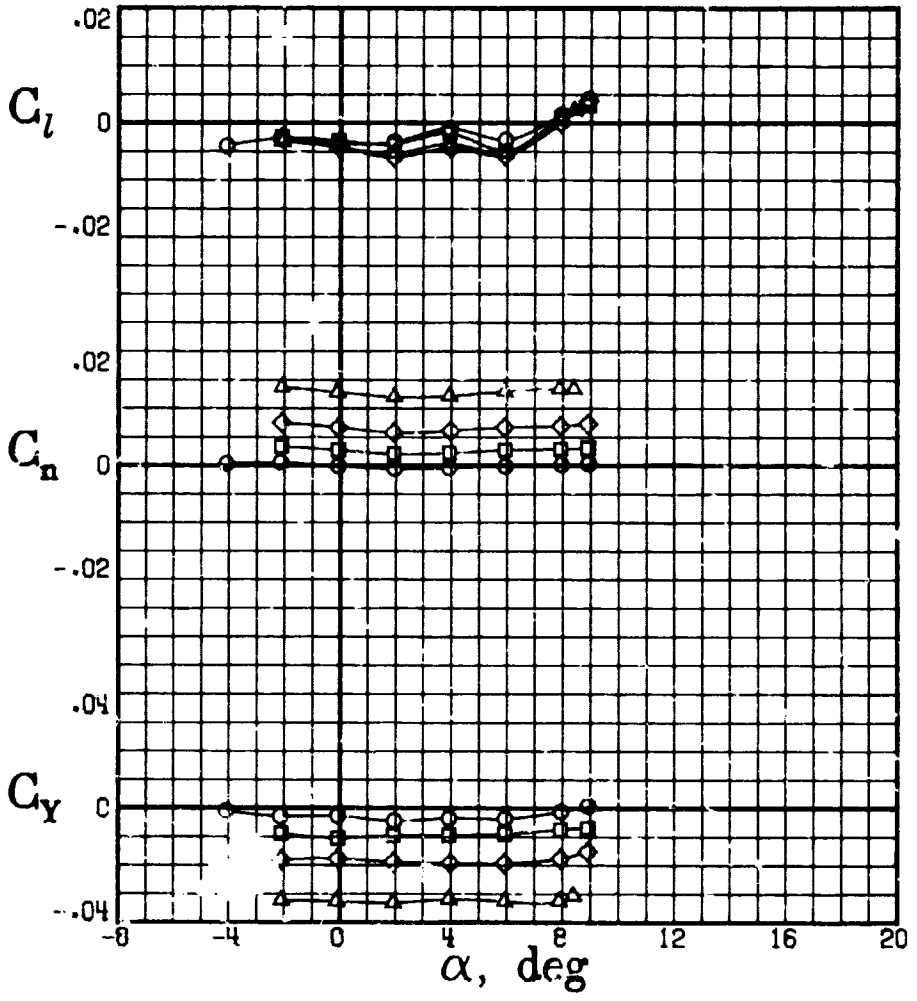

(e) M = 0.900.

Figure 32.- Continued. (U)

[redacted]

	δ_r, deg
○	0
□	−3
◇	−6
△	−9

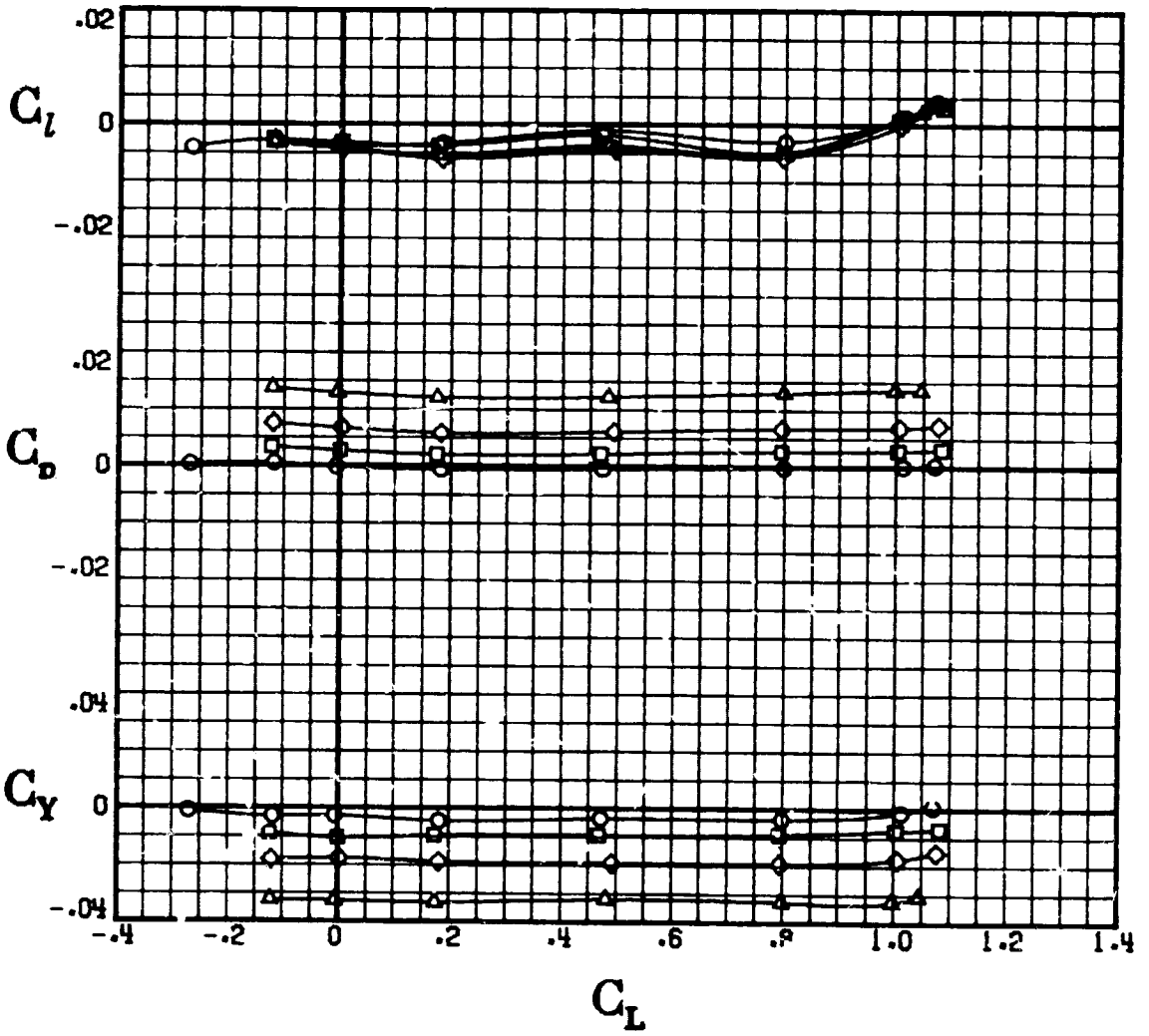

(e) Concluded.

[redacted] Figure 32.- Concluded. (U)

[redacted]

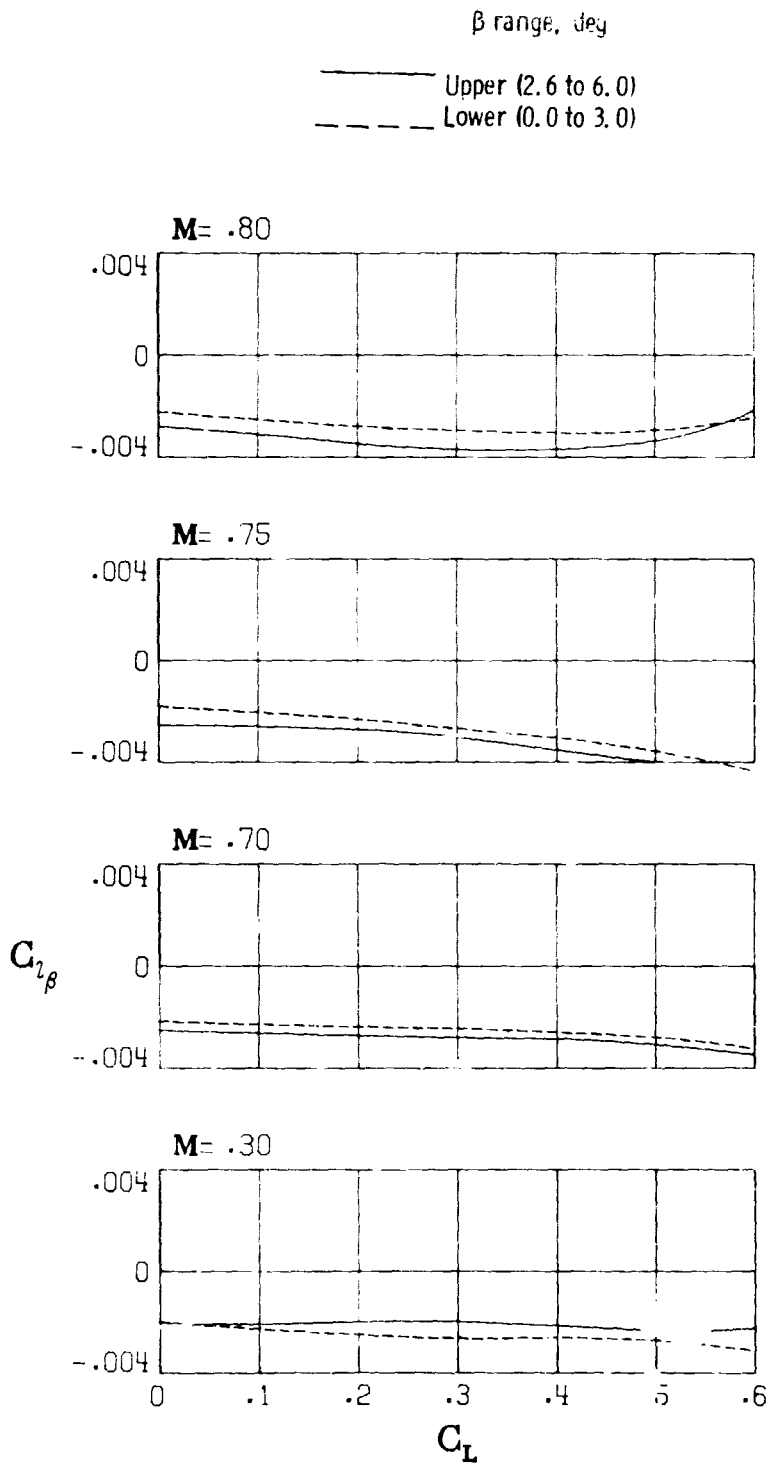

(a) Rolling-moment derivative.

Figure 33.- Variation of lateral-directional stability characteristics with lift coefficient for two ranges of sideslip angle. Model configuration C. (U)

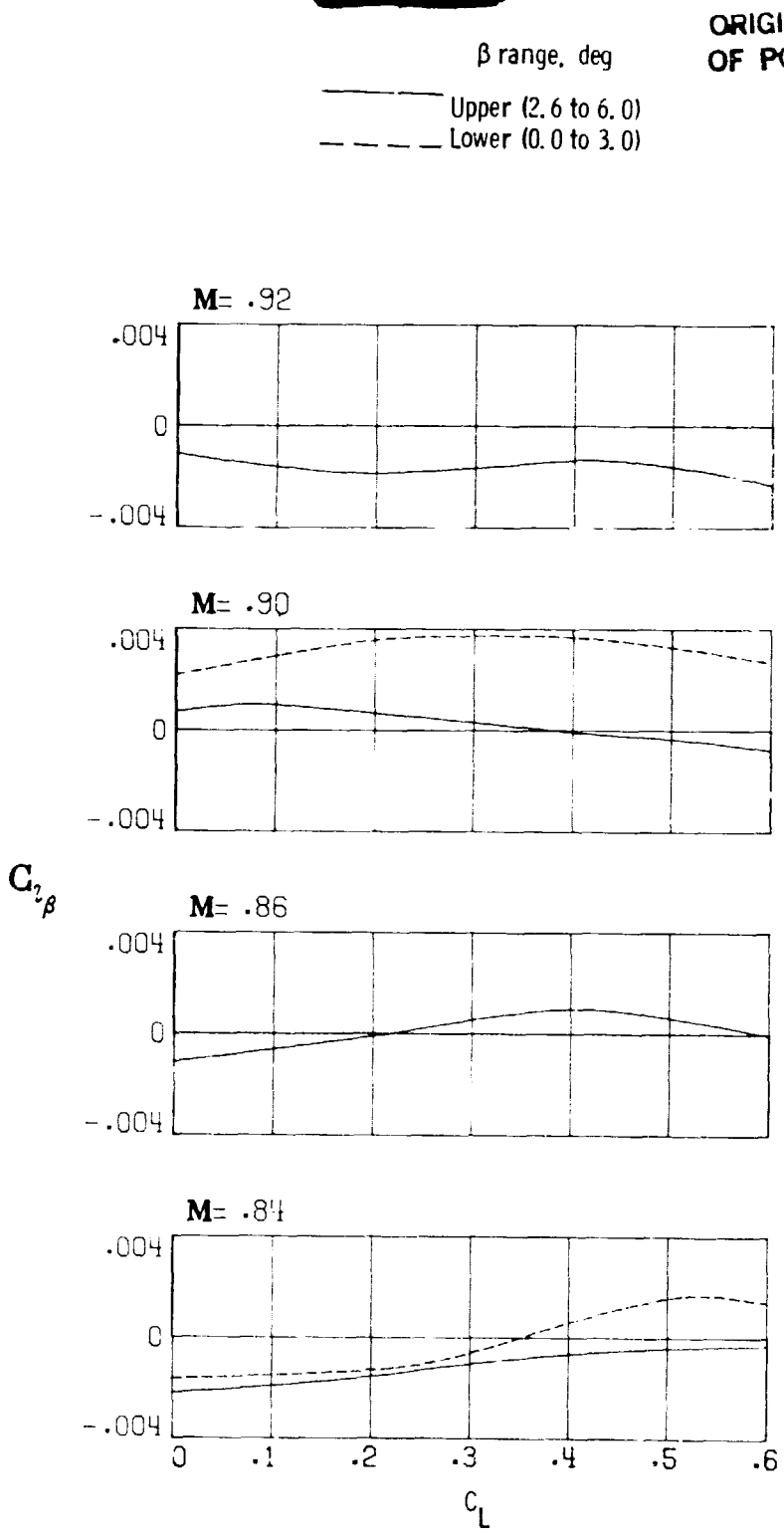

(a) Concluded.

Figure 33.- Continued. (U)

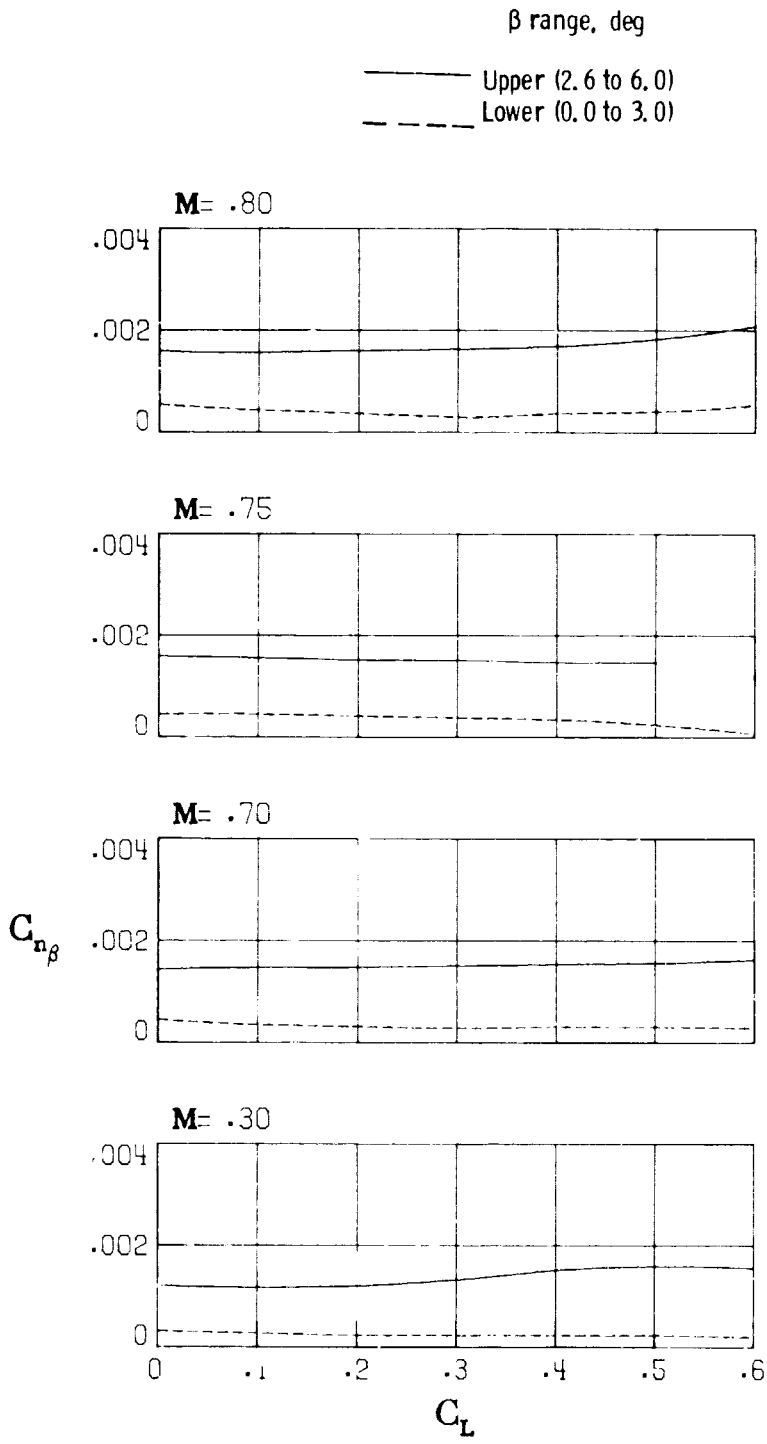

(b) Yawing-moment derivative.

Figure 33.- Continued. (U)

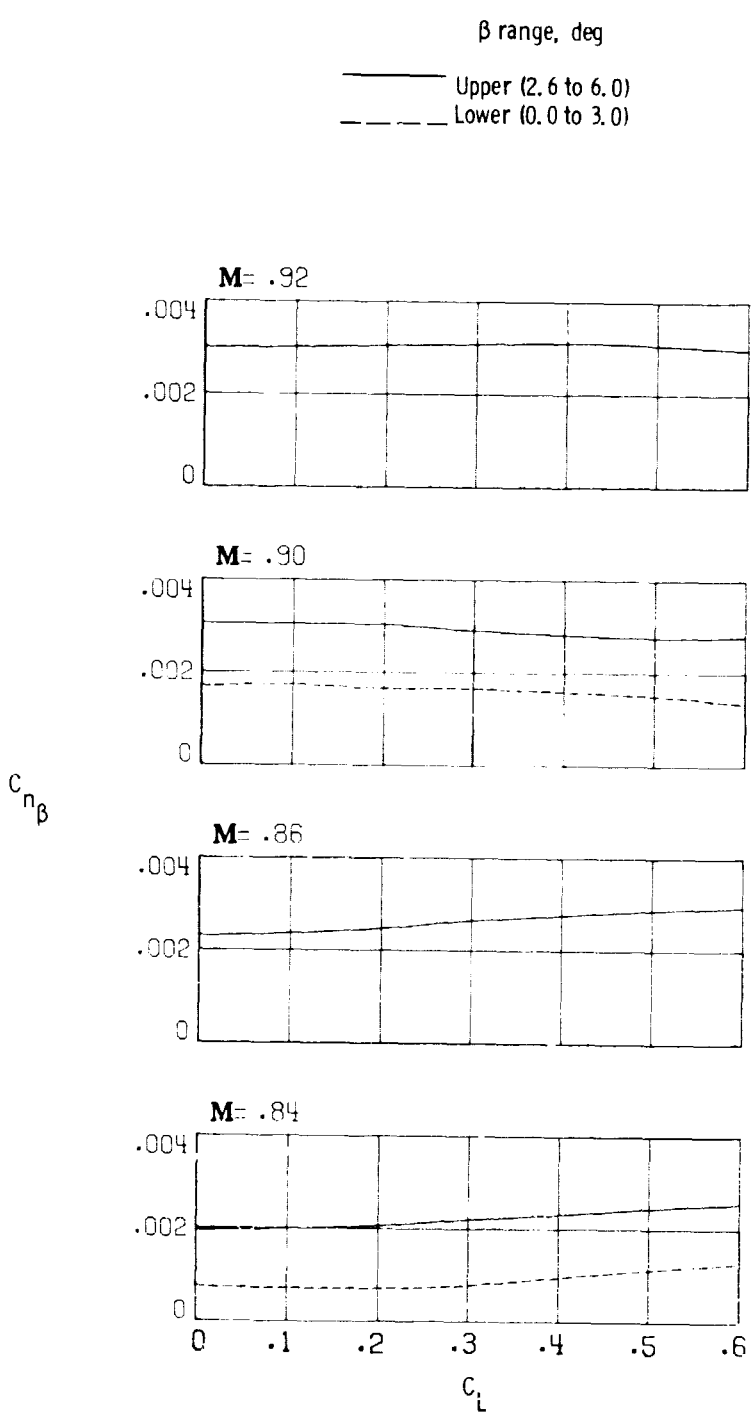

(b) Concluded.

Figure 33.- Continued. (U)

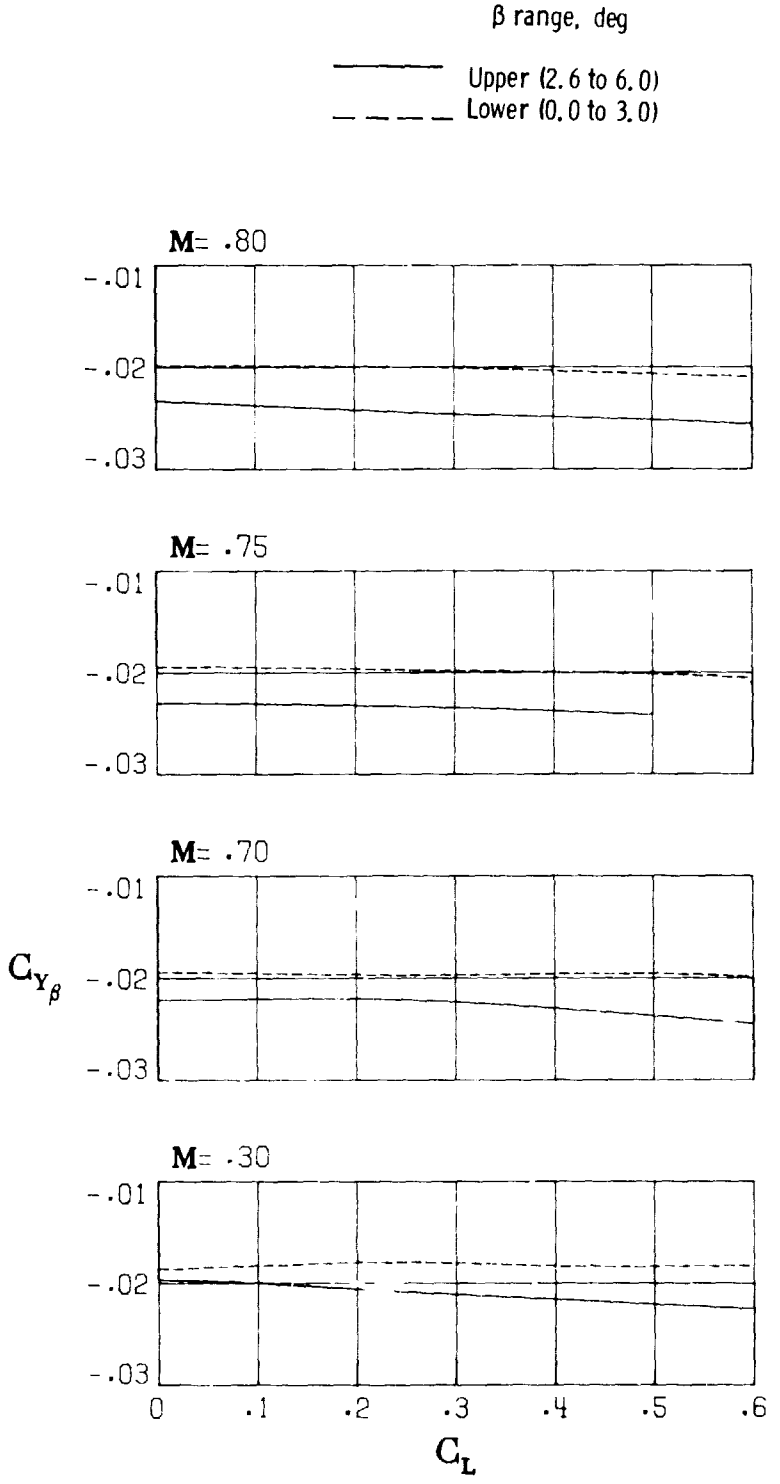

(c) Side-force derivative.

(C) Figure 33.- Continued. (U)

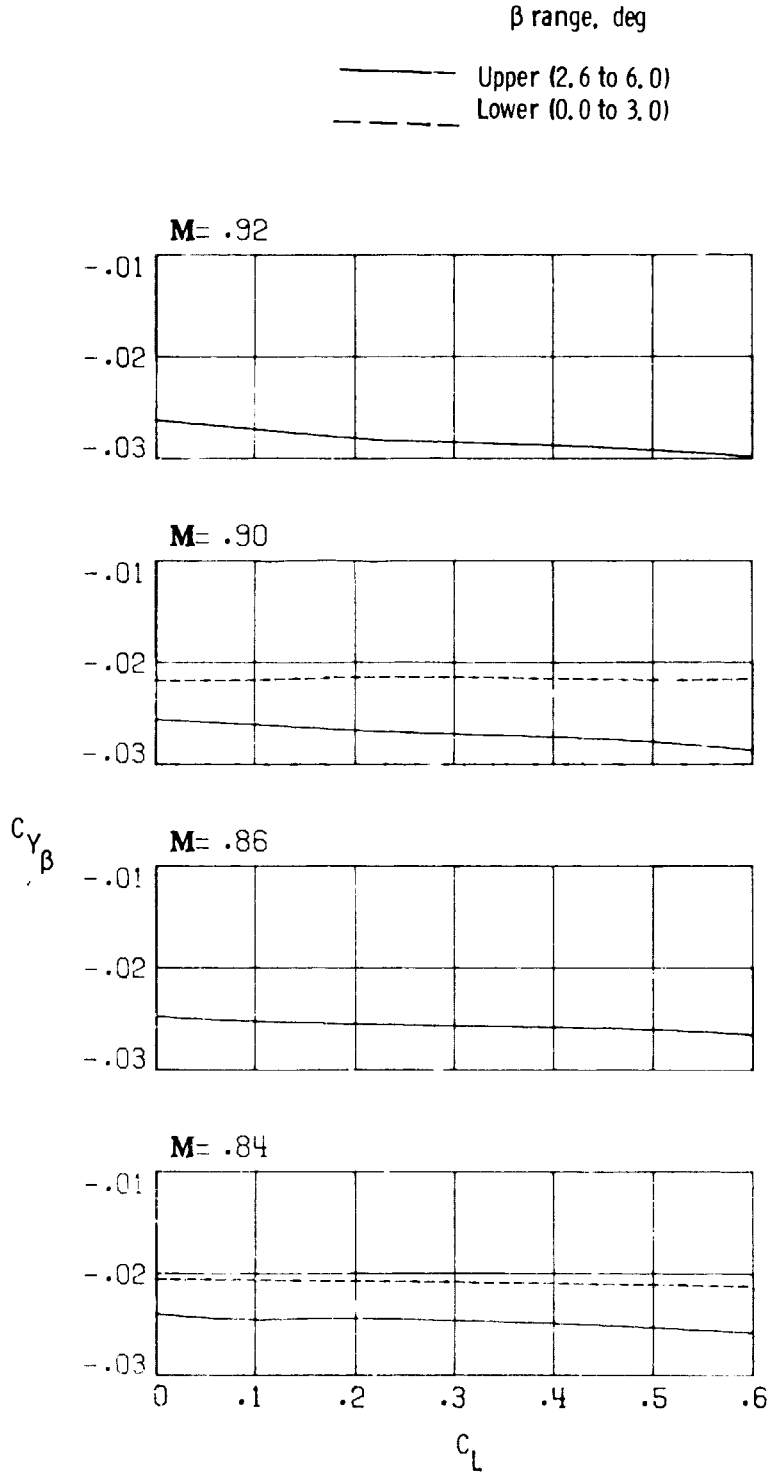

(c) Concluded.

Figure 33.- Concluded. (U)

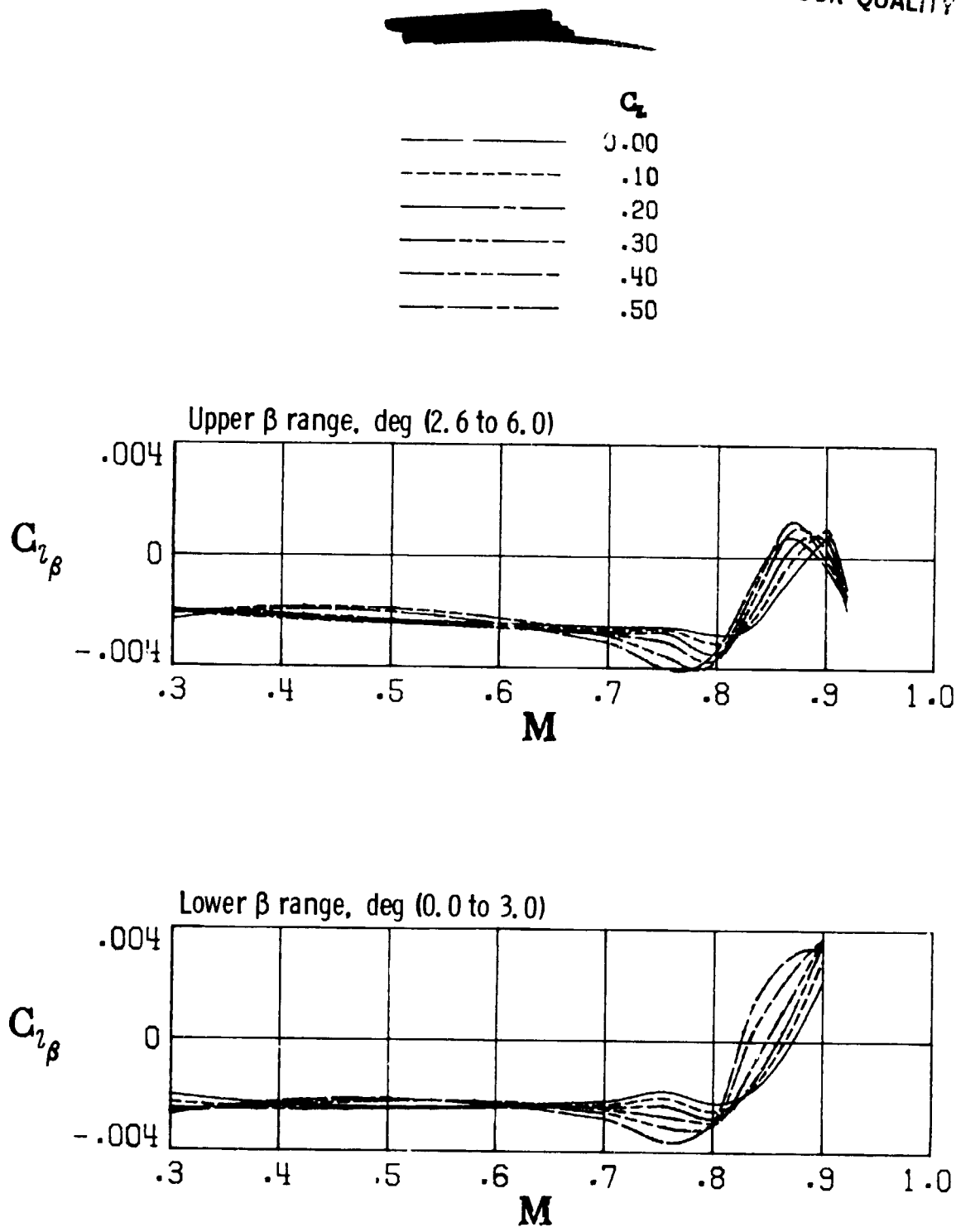

(a) Rolling-moment derivative.

Figure 34.- Variation of lateral-directional static stability characteristics with Mach number for two ranges of sideslip angle. Model configuration C. (U)

[redacted]

	α_s
———	0.00
- - - - - - - - - -	.10
——— - - ———	.20
——— - - - - ———	.30
——— - - - - ———	.40
——— - - - - ———	.50

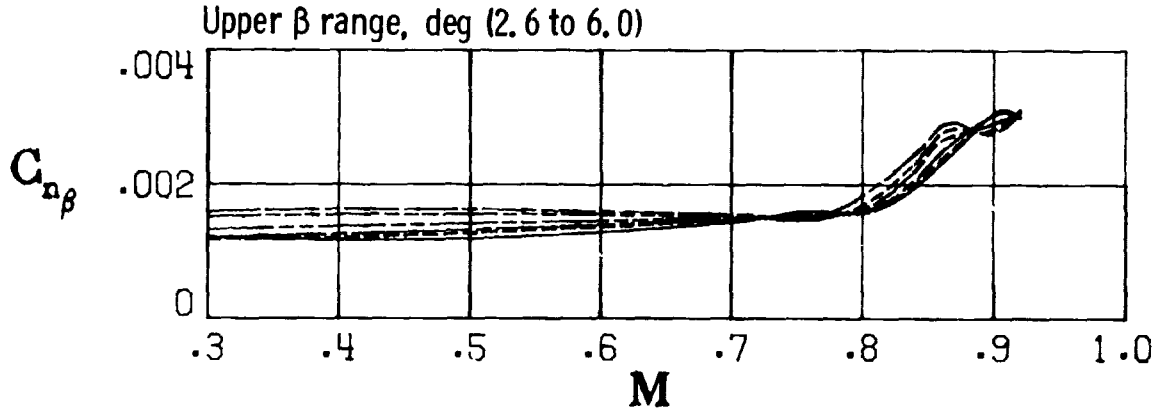

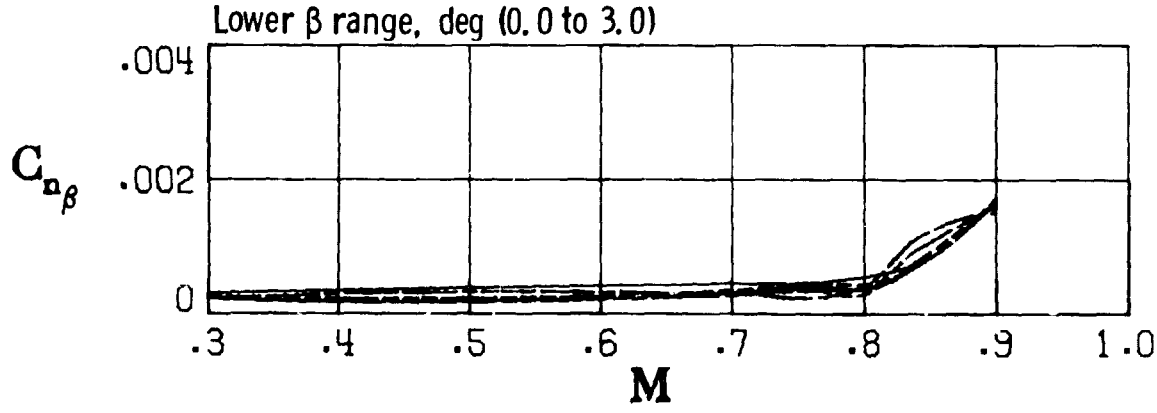

(b) Yawing-moment derivative.

[redacted] Figure 34.- Continued. (U)

[redacted]

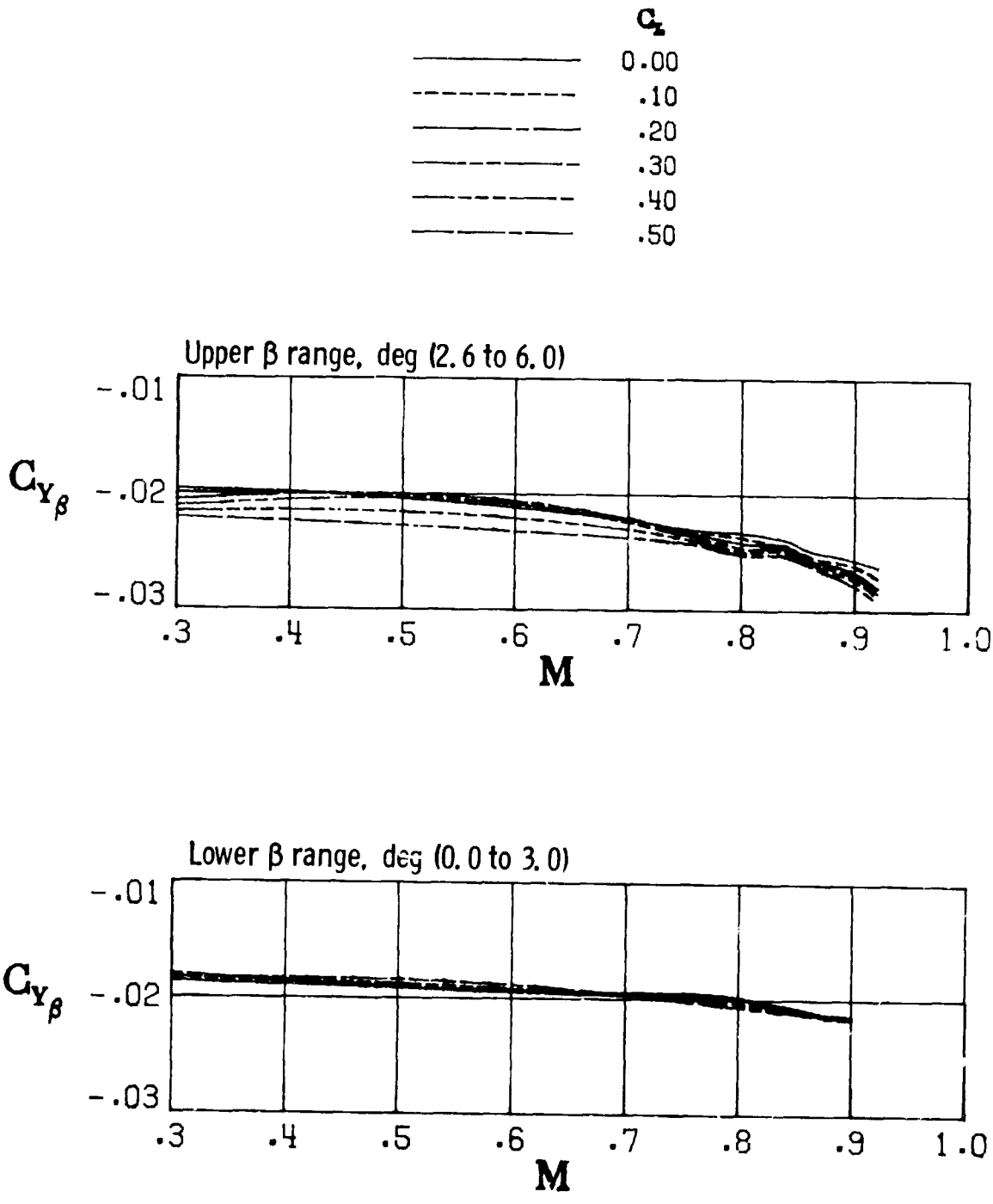

(c) Side-force derivative.

Figure 34.- Concluded. (U)

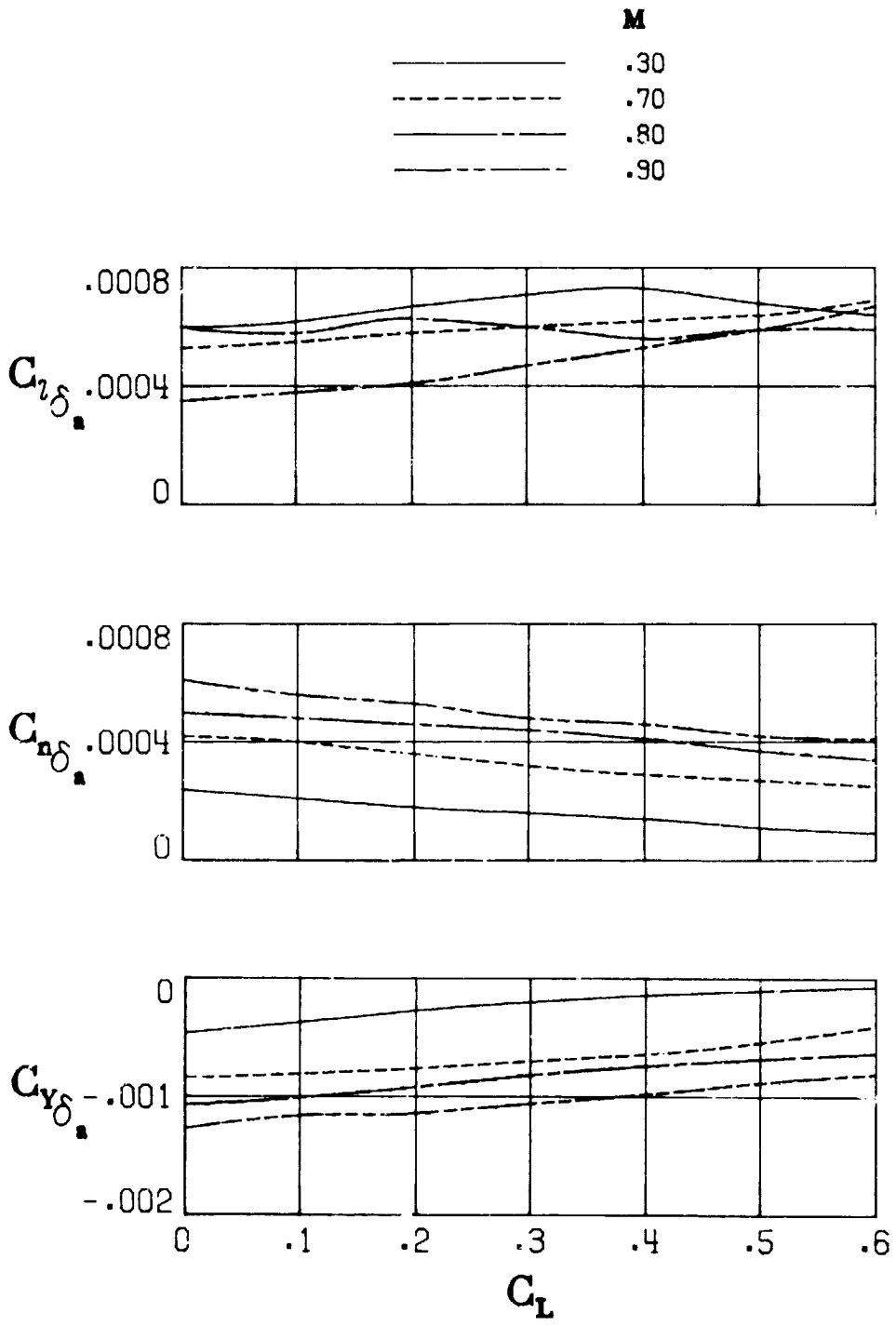

Figure 35.- Variation of roll-control derivatives (asymmetric elevon deflection) with lift coefficient for model configuration C. (U)

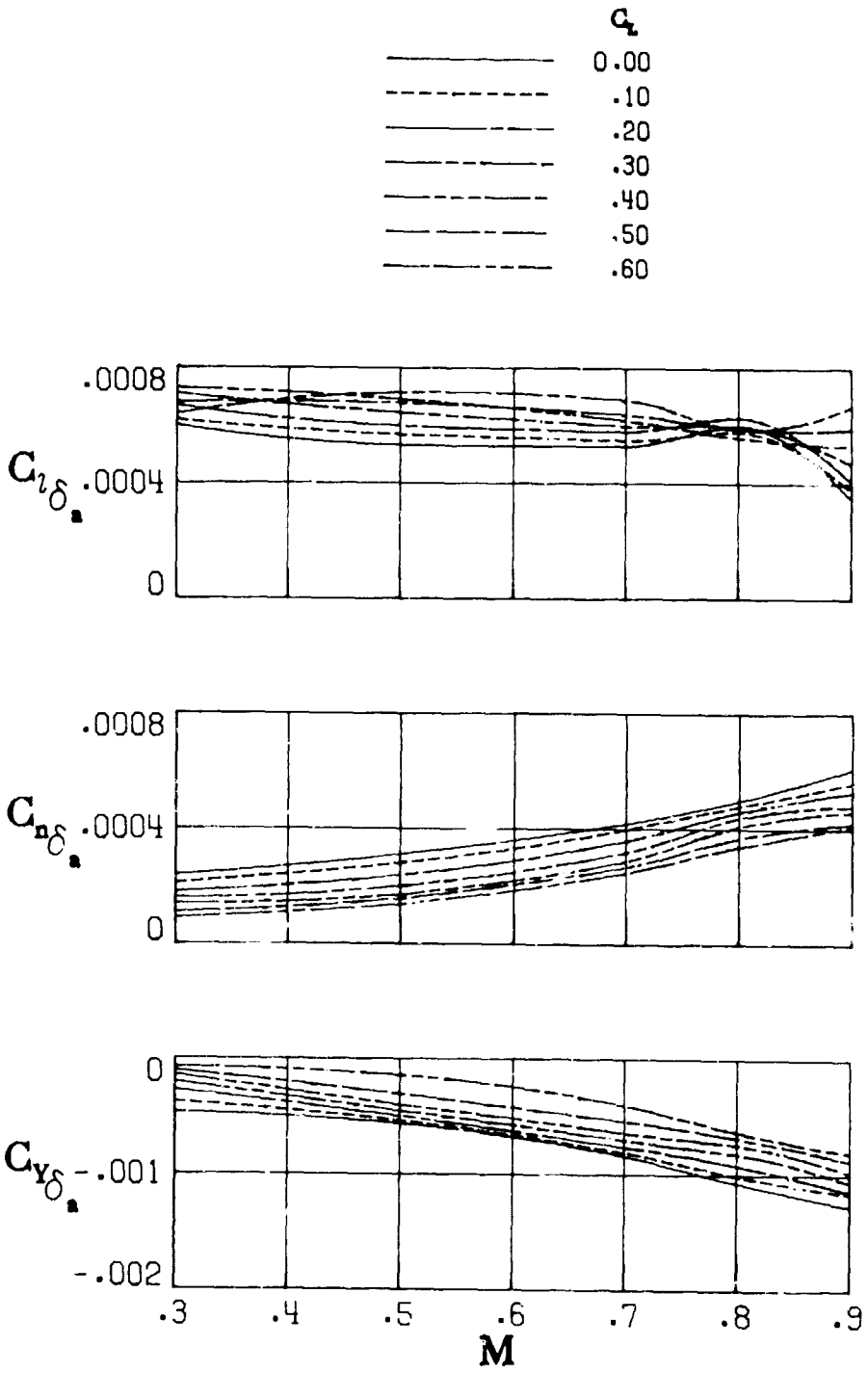

Figure 36.- Variation of roll-control derivatives (asymmetric elevon deflection) with Mach number for model configuration C. (U)

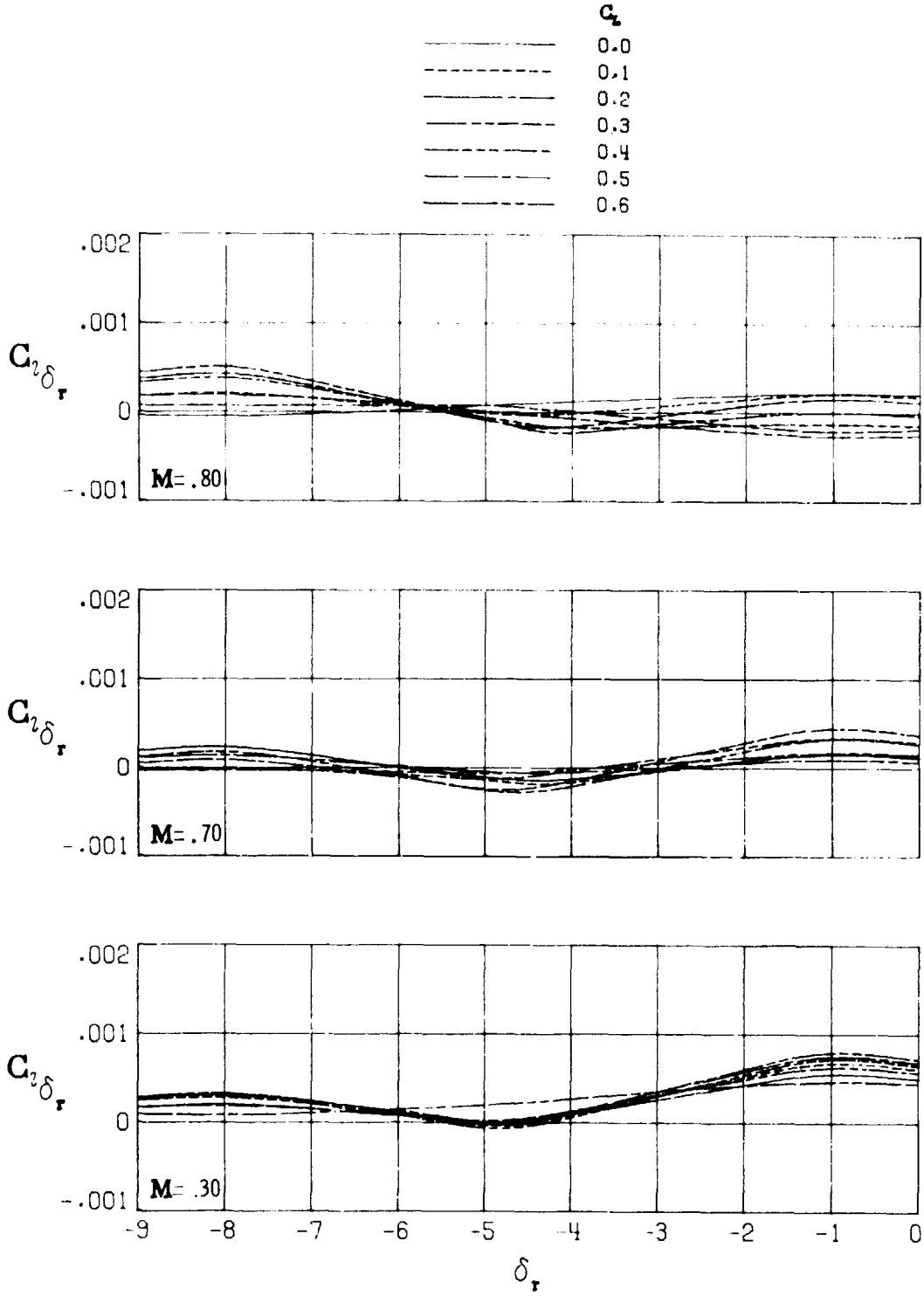

(a) Rolling-moment derivative.

Figure 37.- Variation of rudder-control derivatives with rudder deflection for model configuration C. (U)

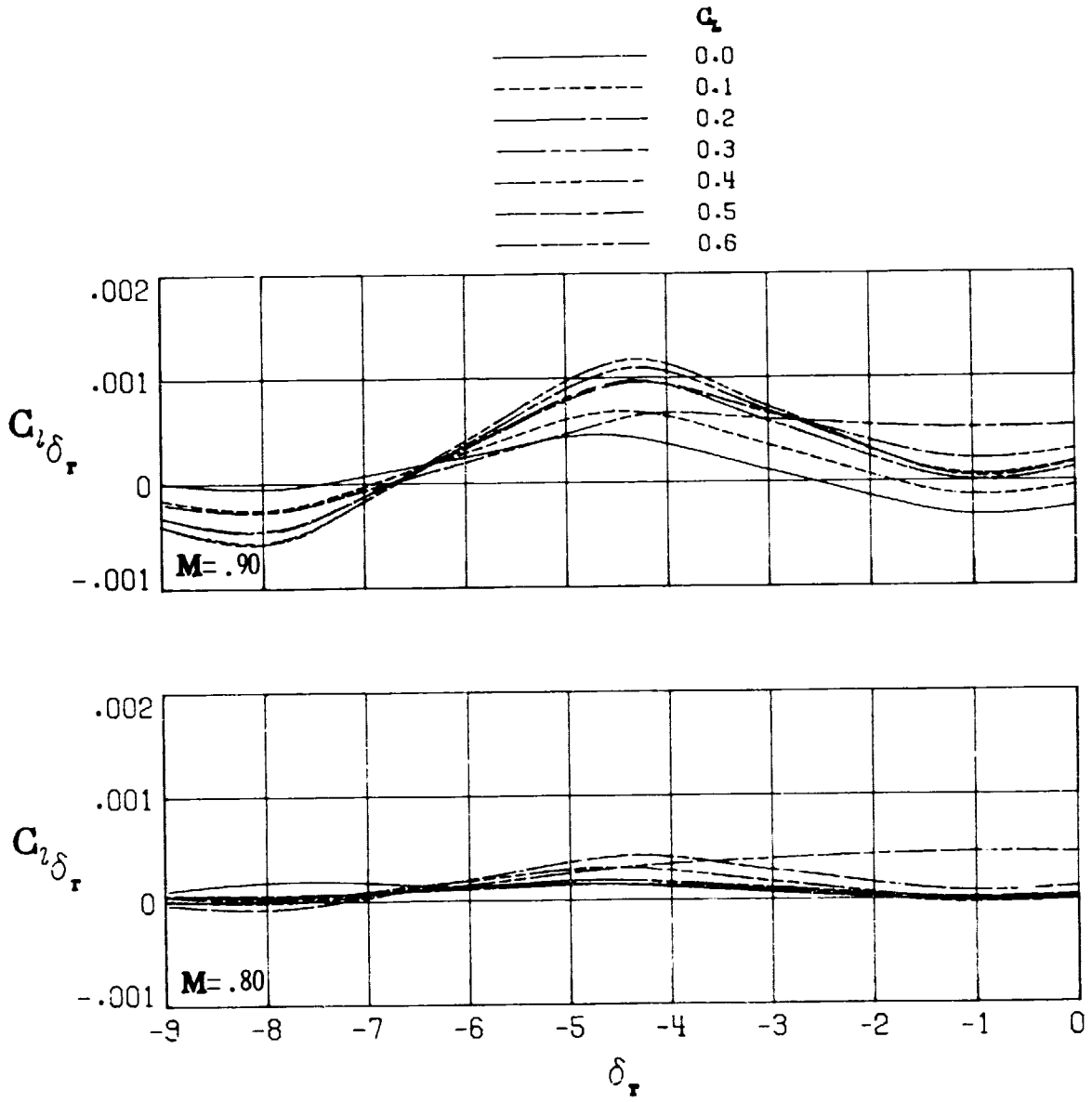

(a) Concluded.

Figure 37.- Continued. (U

C-3

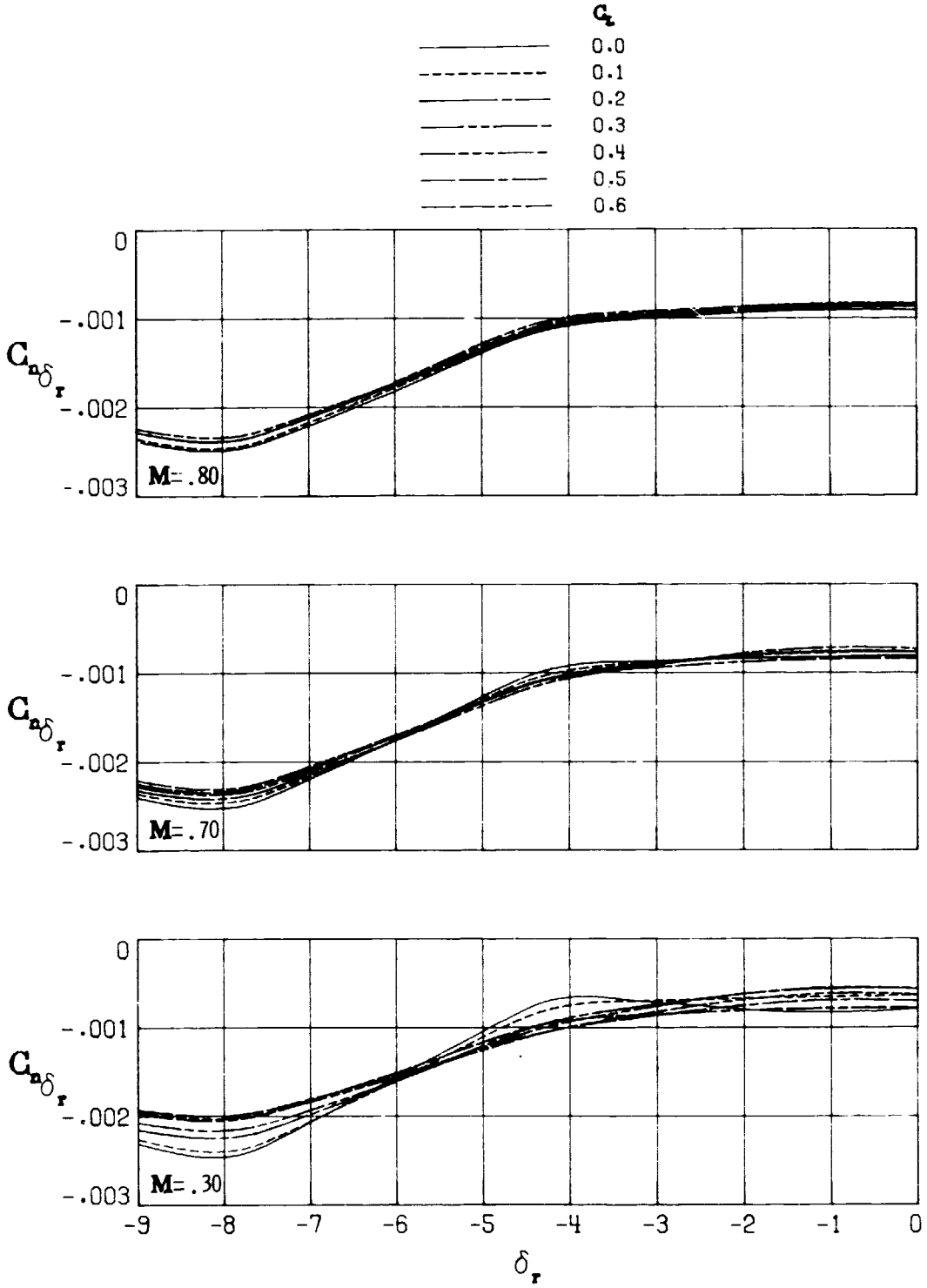

(b) Yawing-moment derivative.

Figure 37.- Continued. (U)

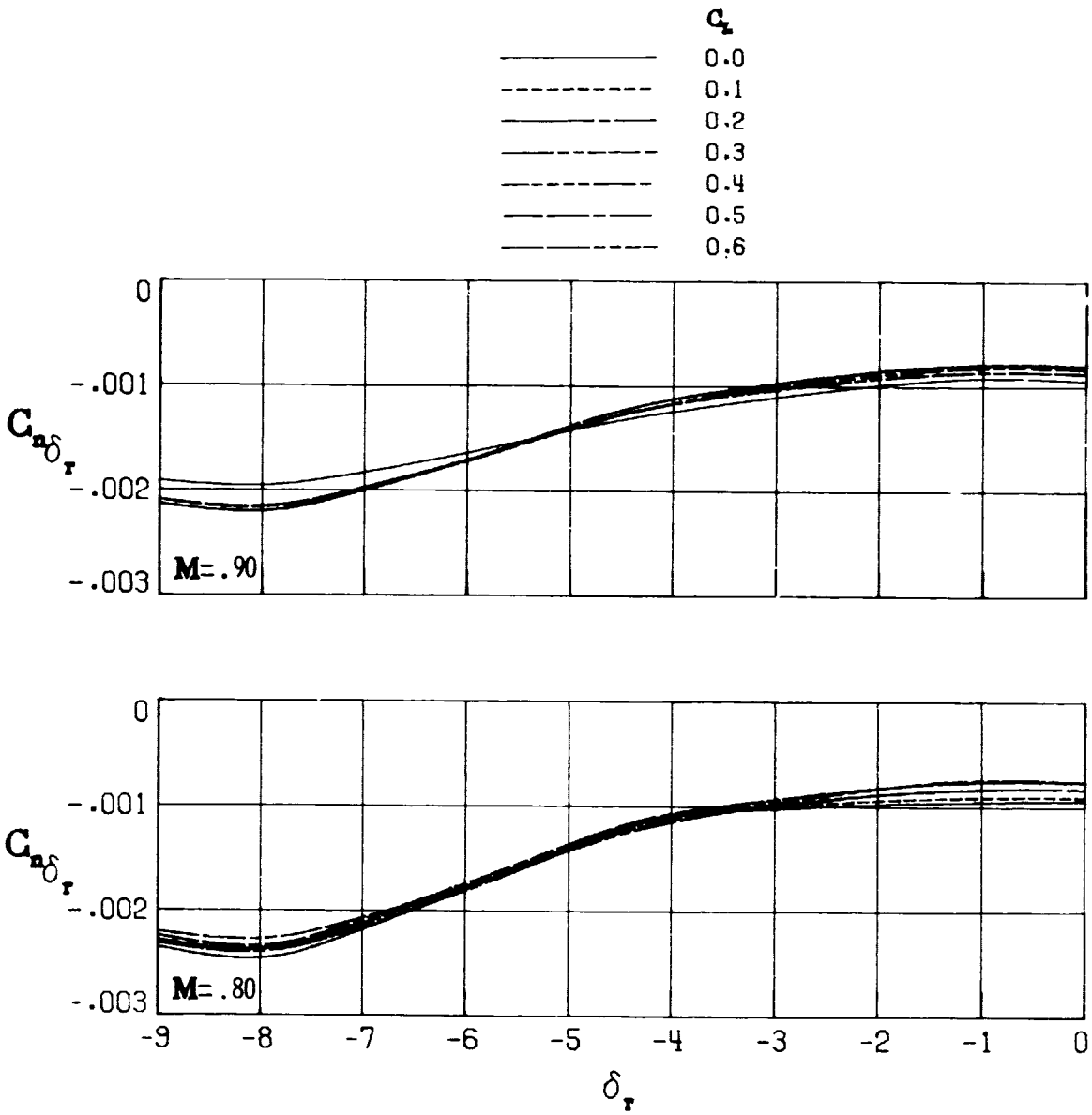

(b) Concluded.

Figure 37.- Continued. (U)

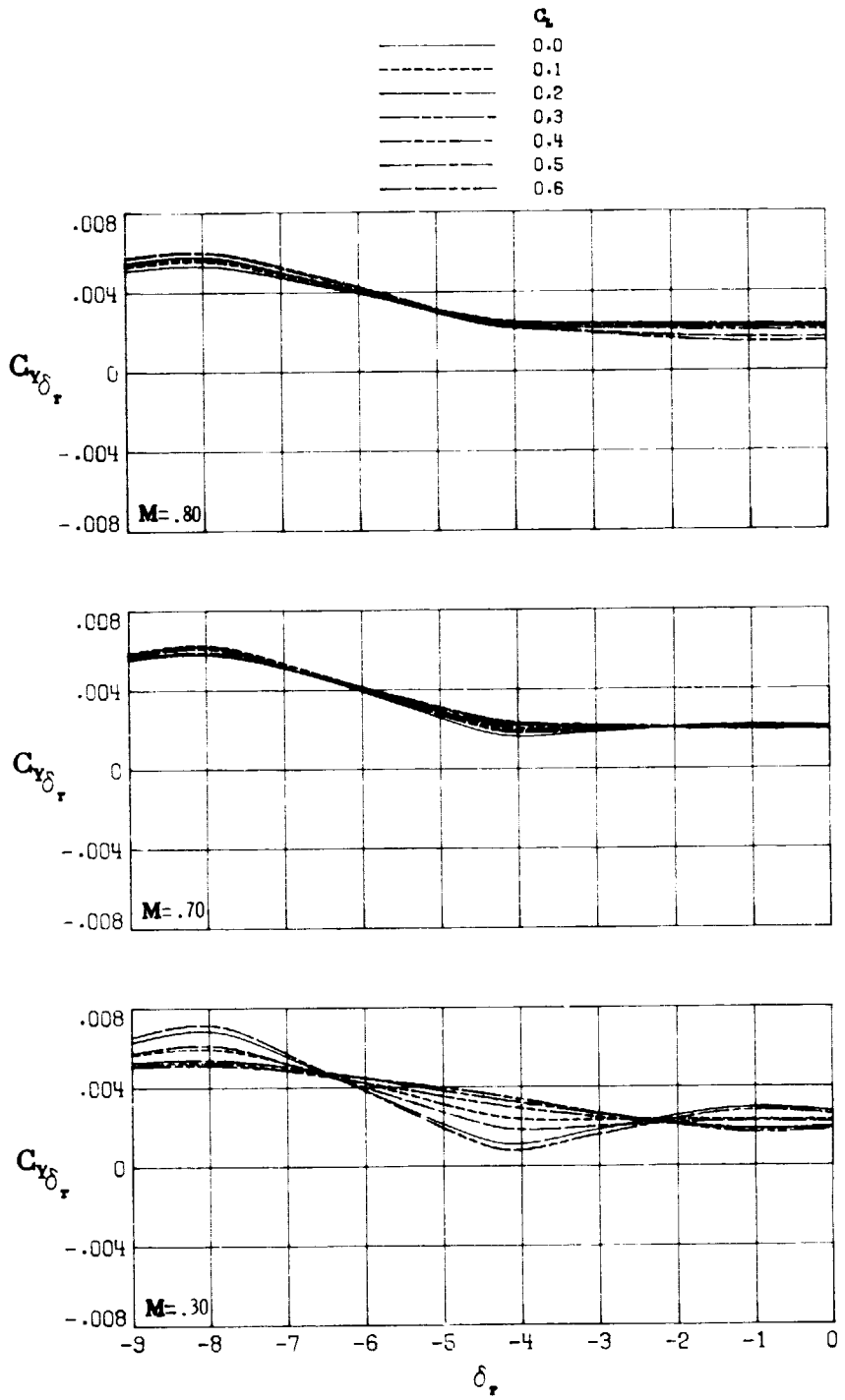

(c) Side-force derivative.

Figure 37.- Continued. (U)

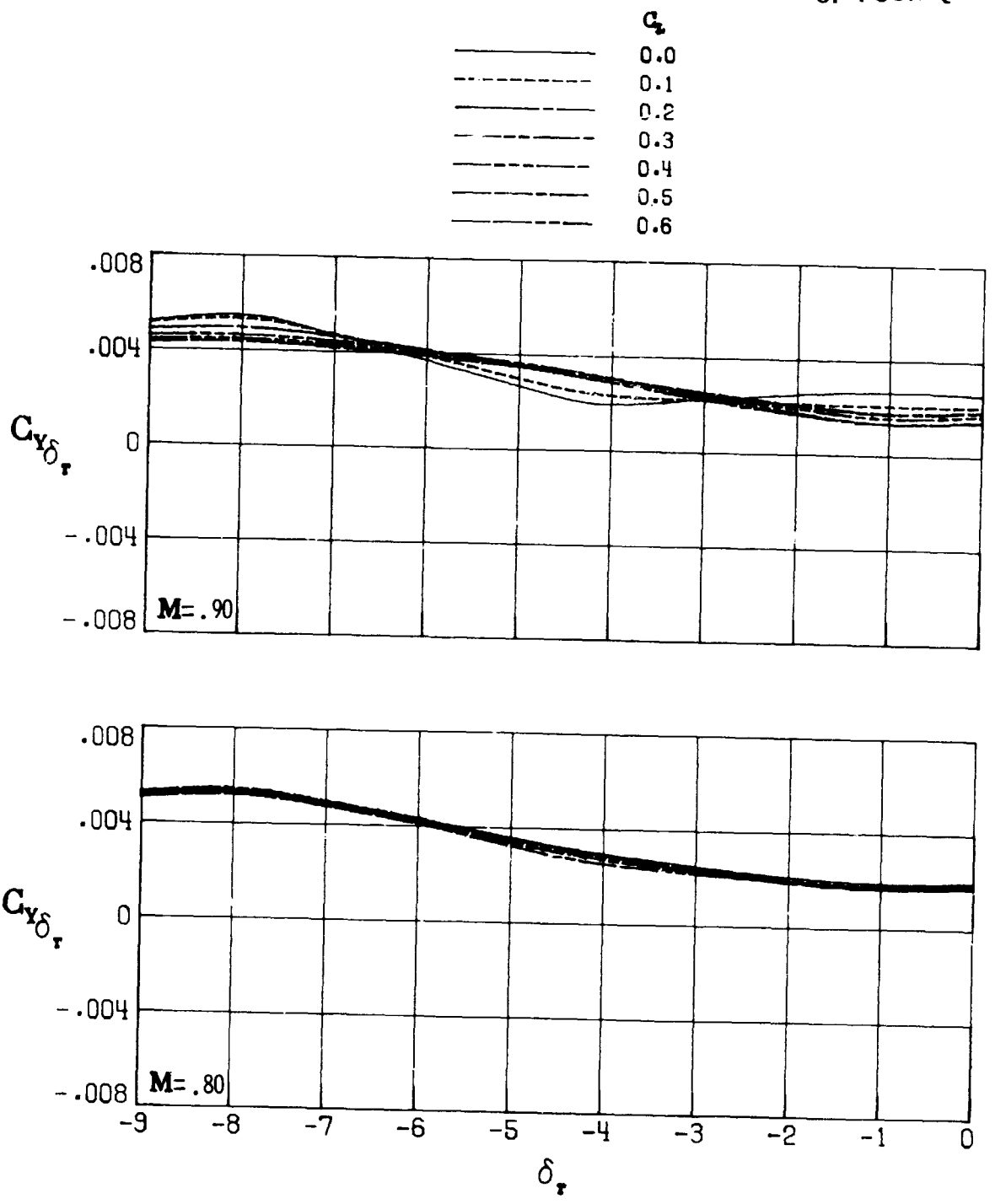

(c) Concluded.

Figure 37.- Concluded. (U)

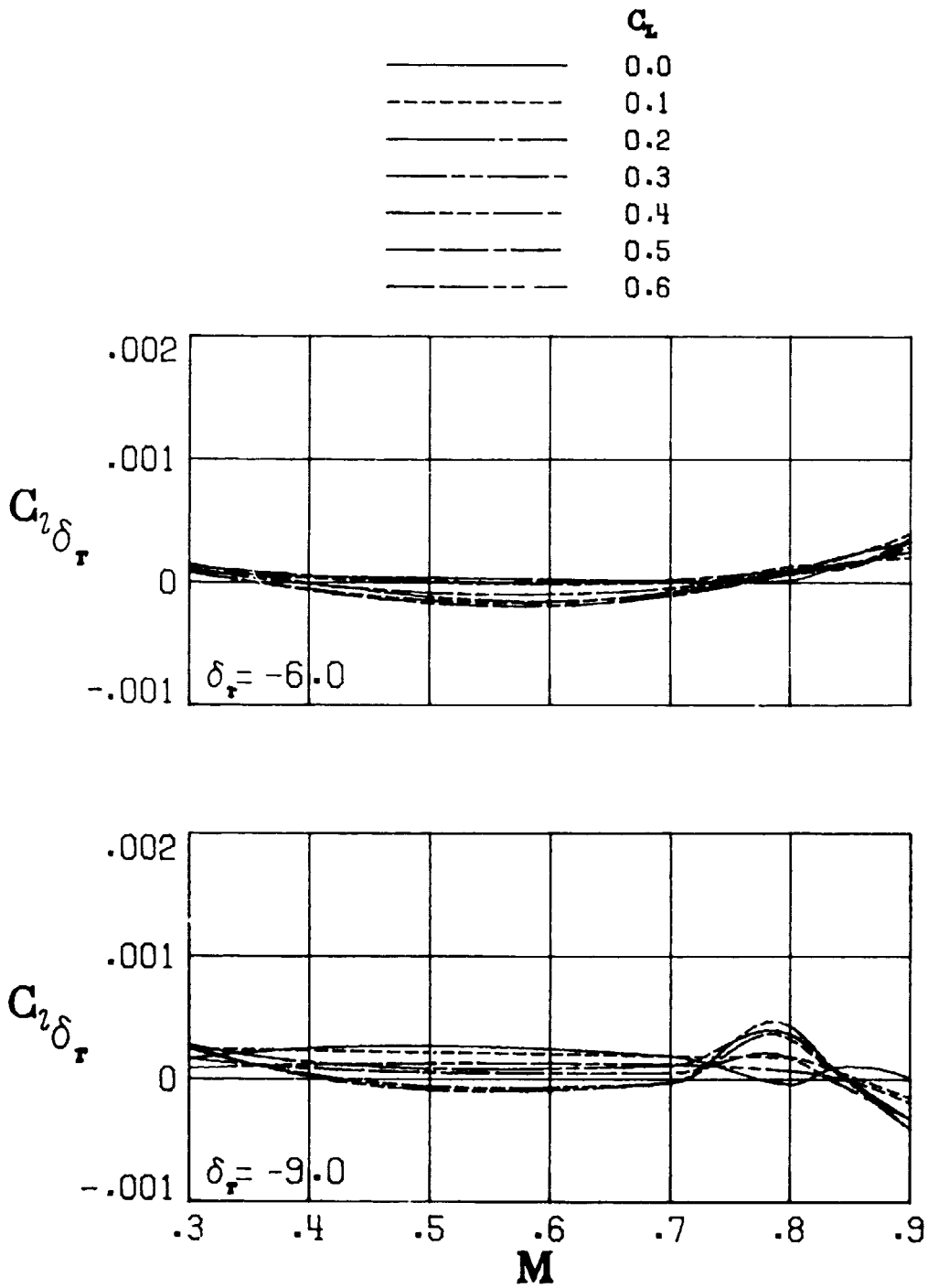

(a) Rolling-moment derivative.

Figure 38.- Variation of rudder-control derivatives with Mach number for four rudder deflection angles. Model configuration C. (U)

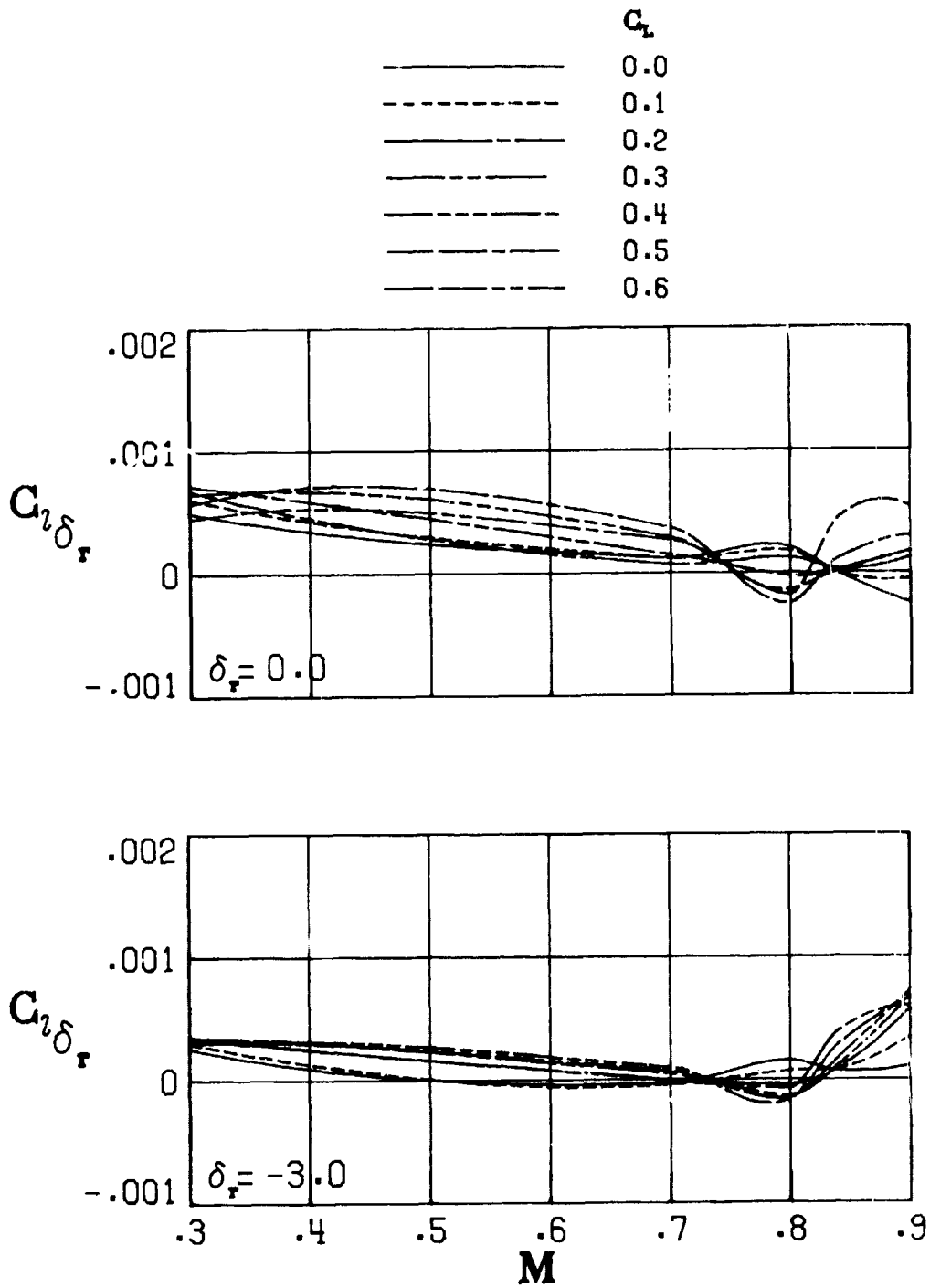

(a) Concluded.

Figure 38.- Continued. (U)

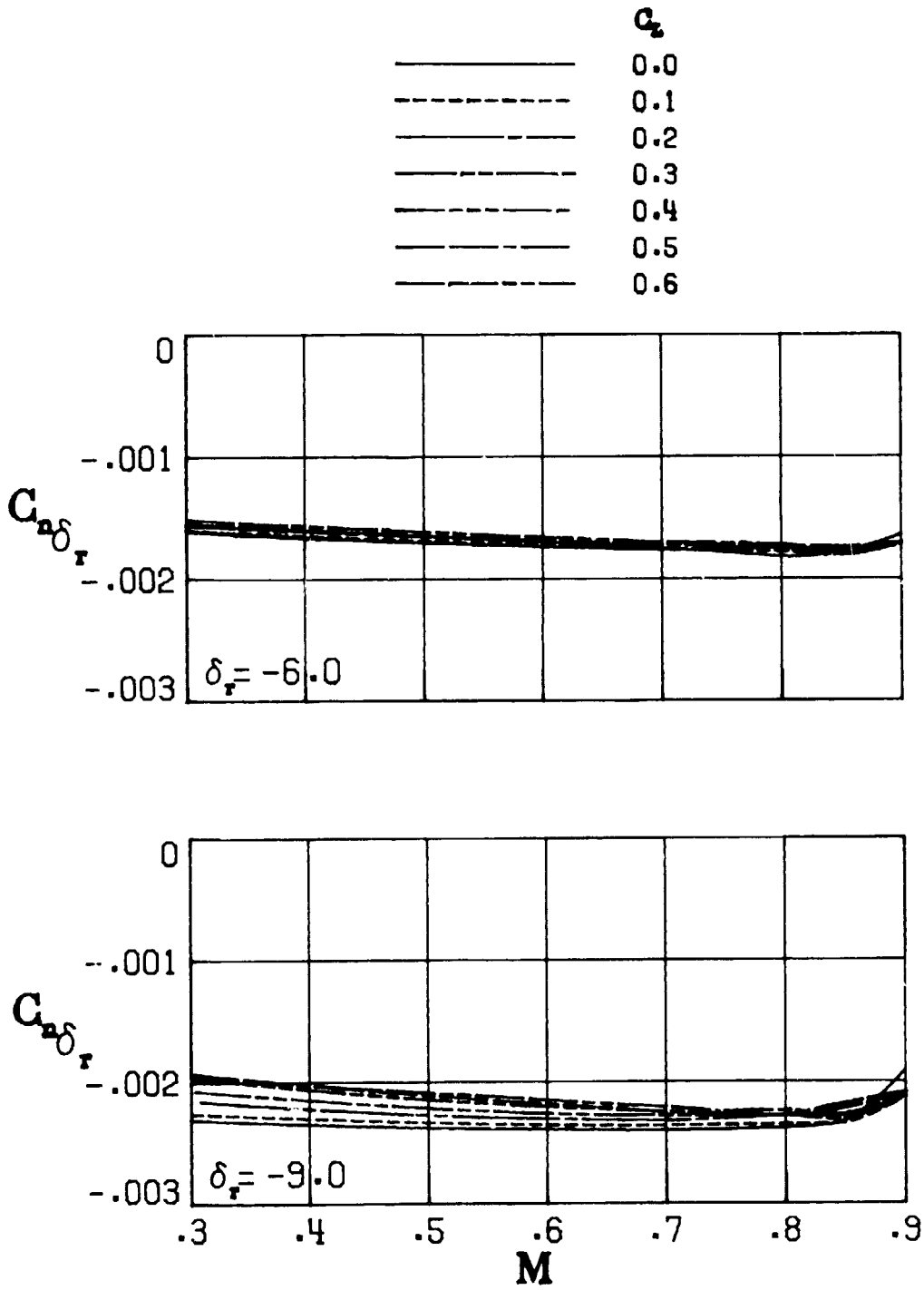

(b) Yawing-moment derivative.

(C) Figure 38.- Continued. (U)

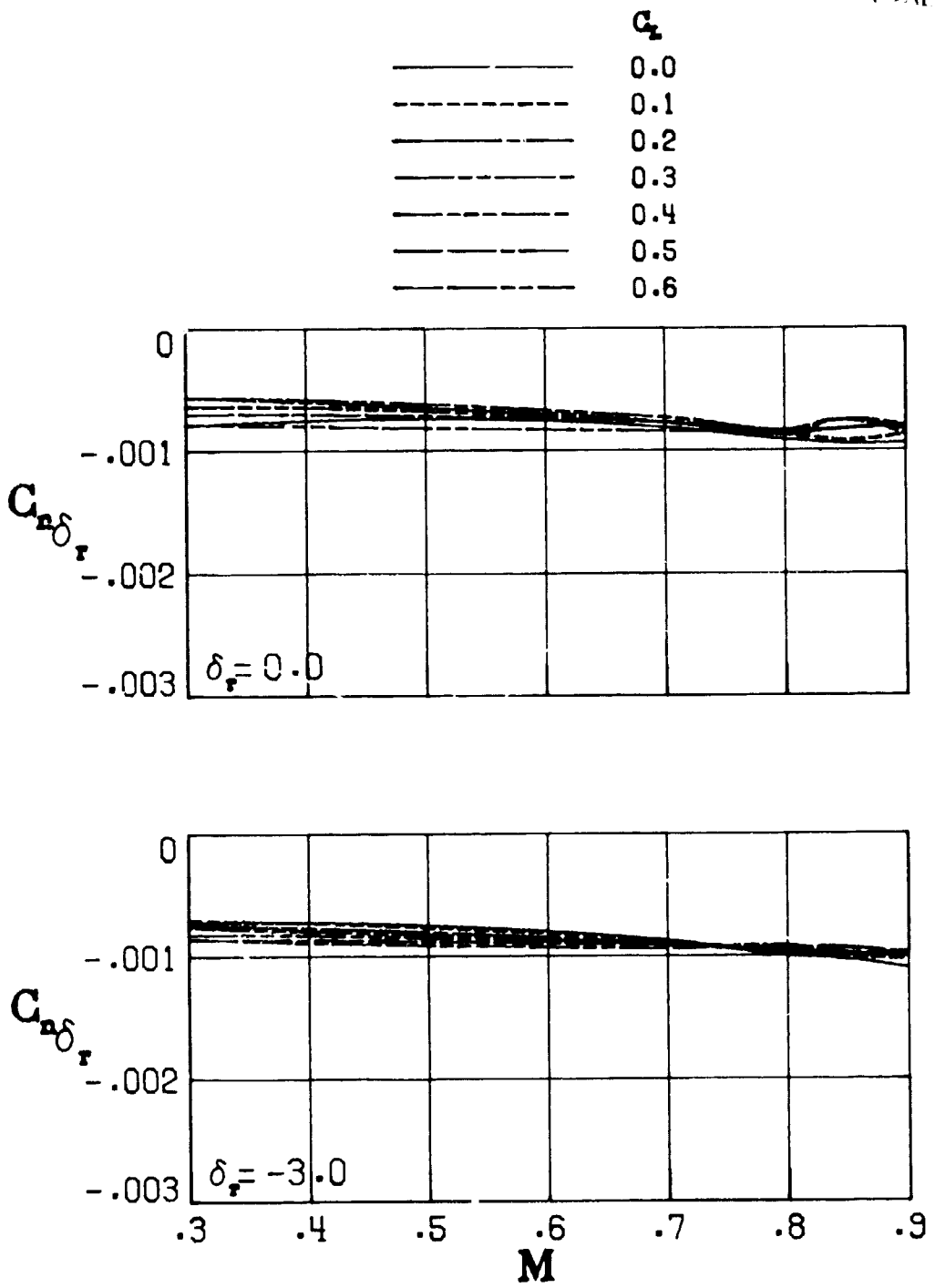

(b) Concluded.

Figure 38.- Continued. (U)

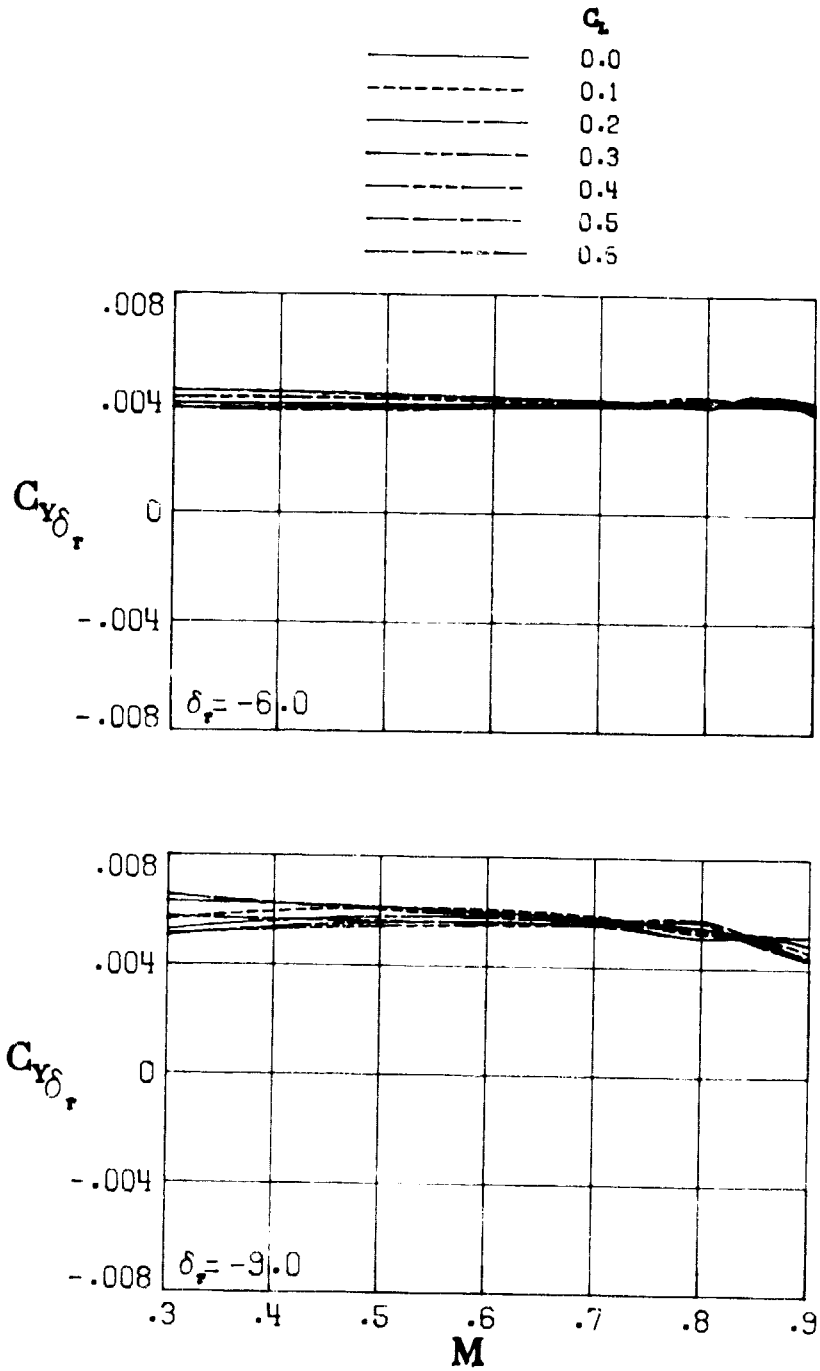

(c) Side-force derivative.

Figure 38.- Continued. (U)

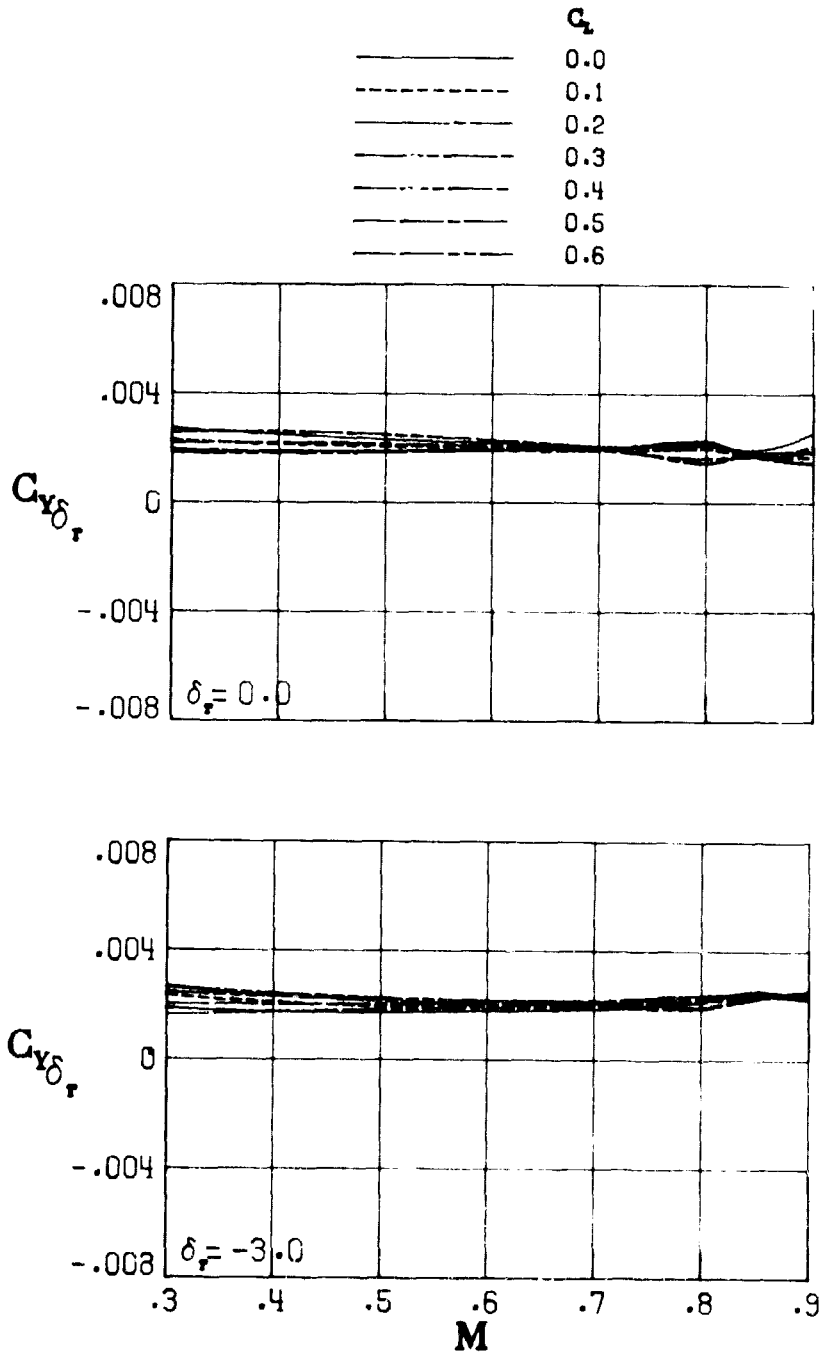

(c) Concluded.

Figure 38.- Concluded. (U)

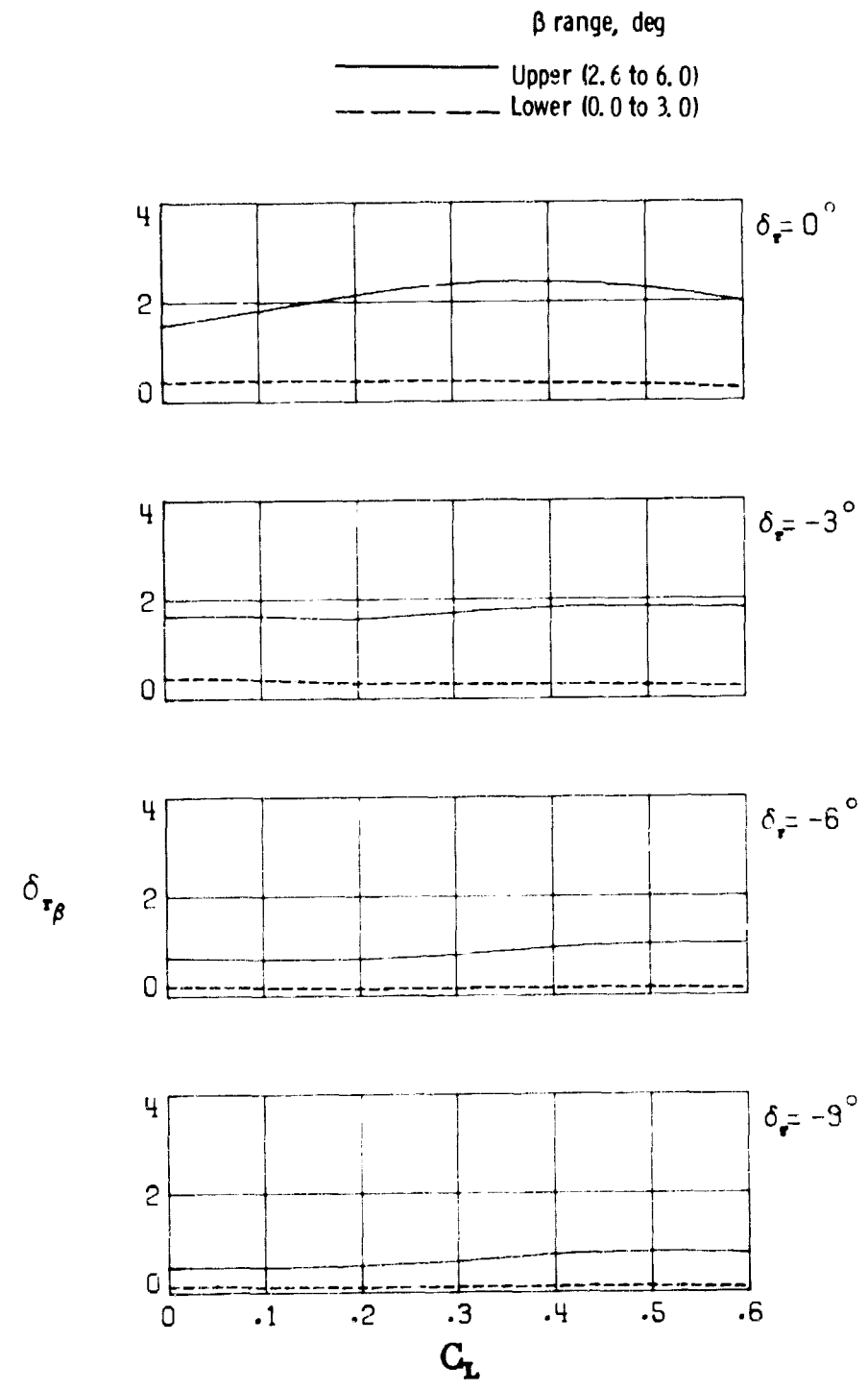

(a) M = 0.300.

Figure 39.- Variation of rudder-control index with lift coefficient for four rudder deflection angles. Model configuration C. (U)

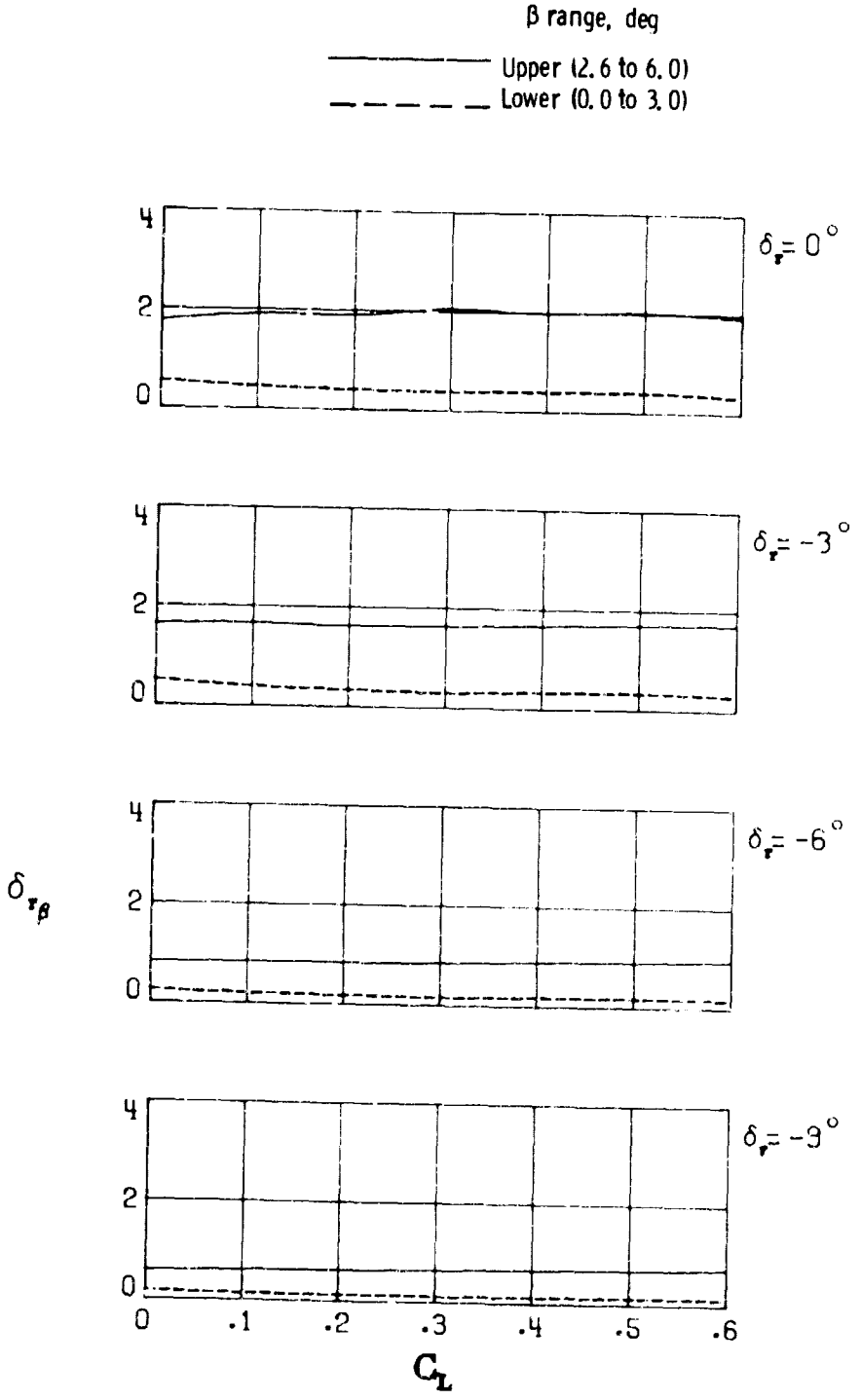

(b) M = 0.700.

Figure 39.- Continued. (U)

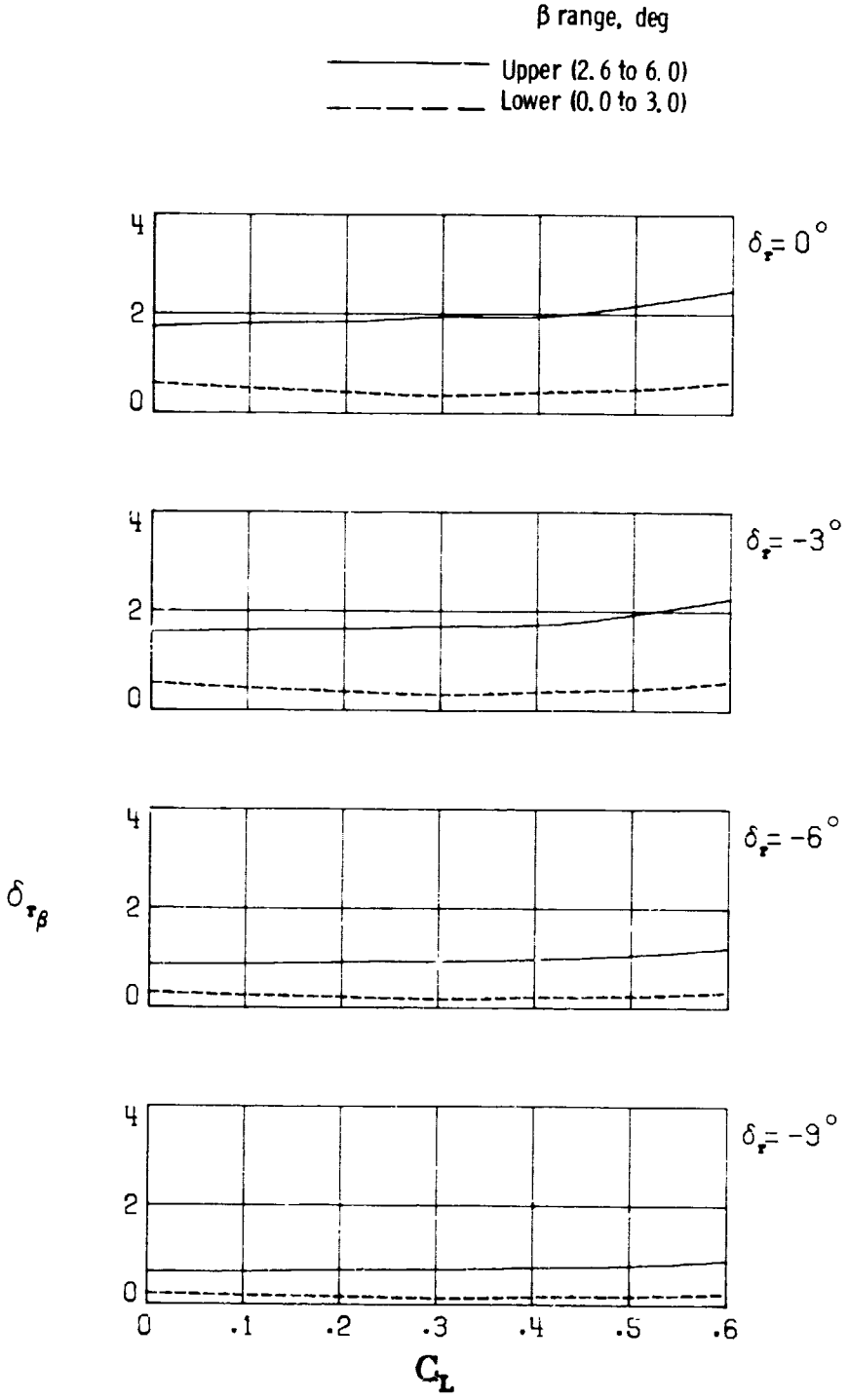

(c) M = 0.800.

Figure 39.- Continued. (U)

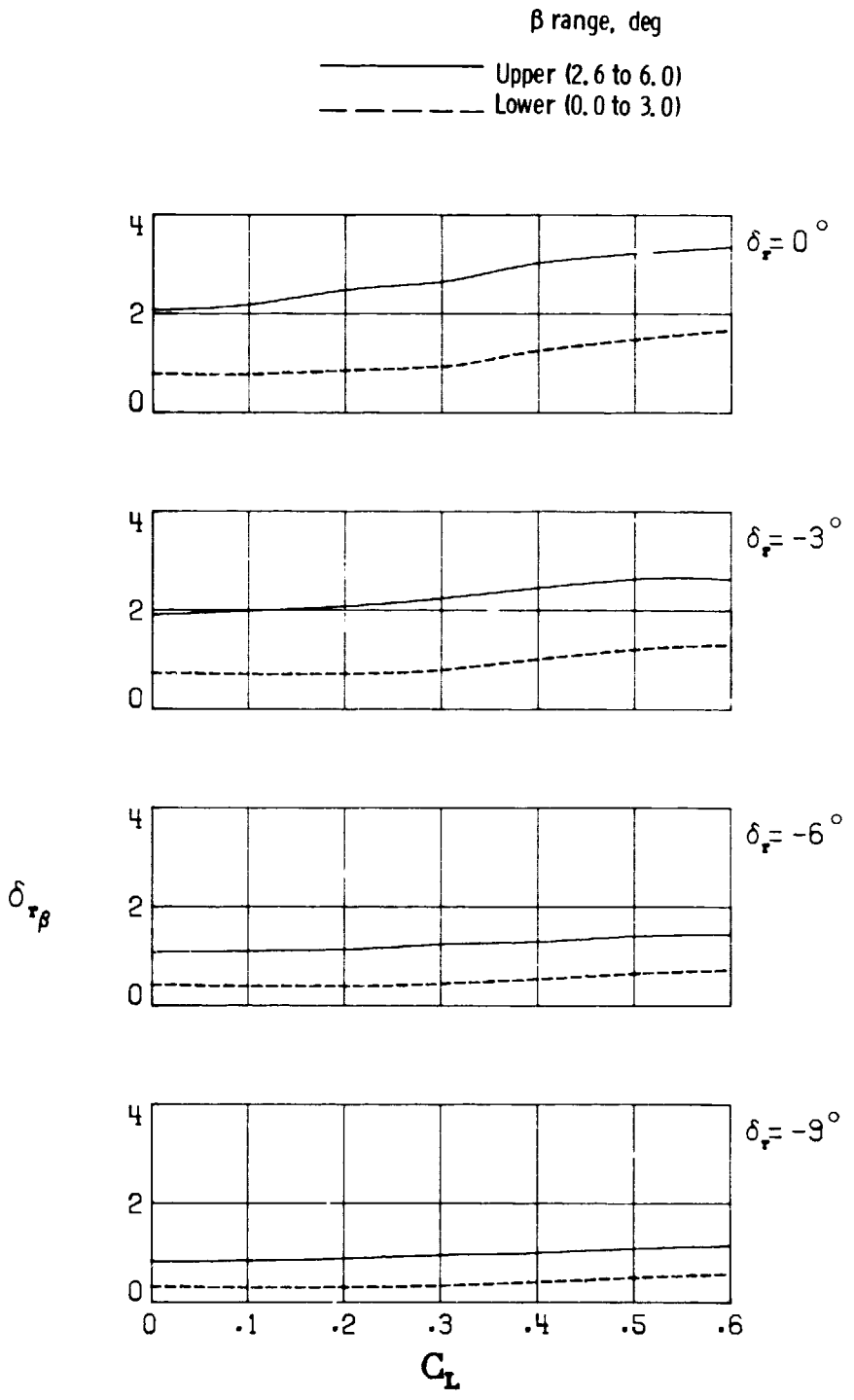

(d) M = 0.840.

Figure 39.- Continued. (U)

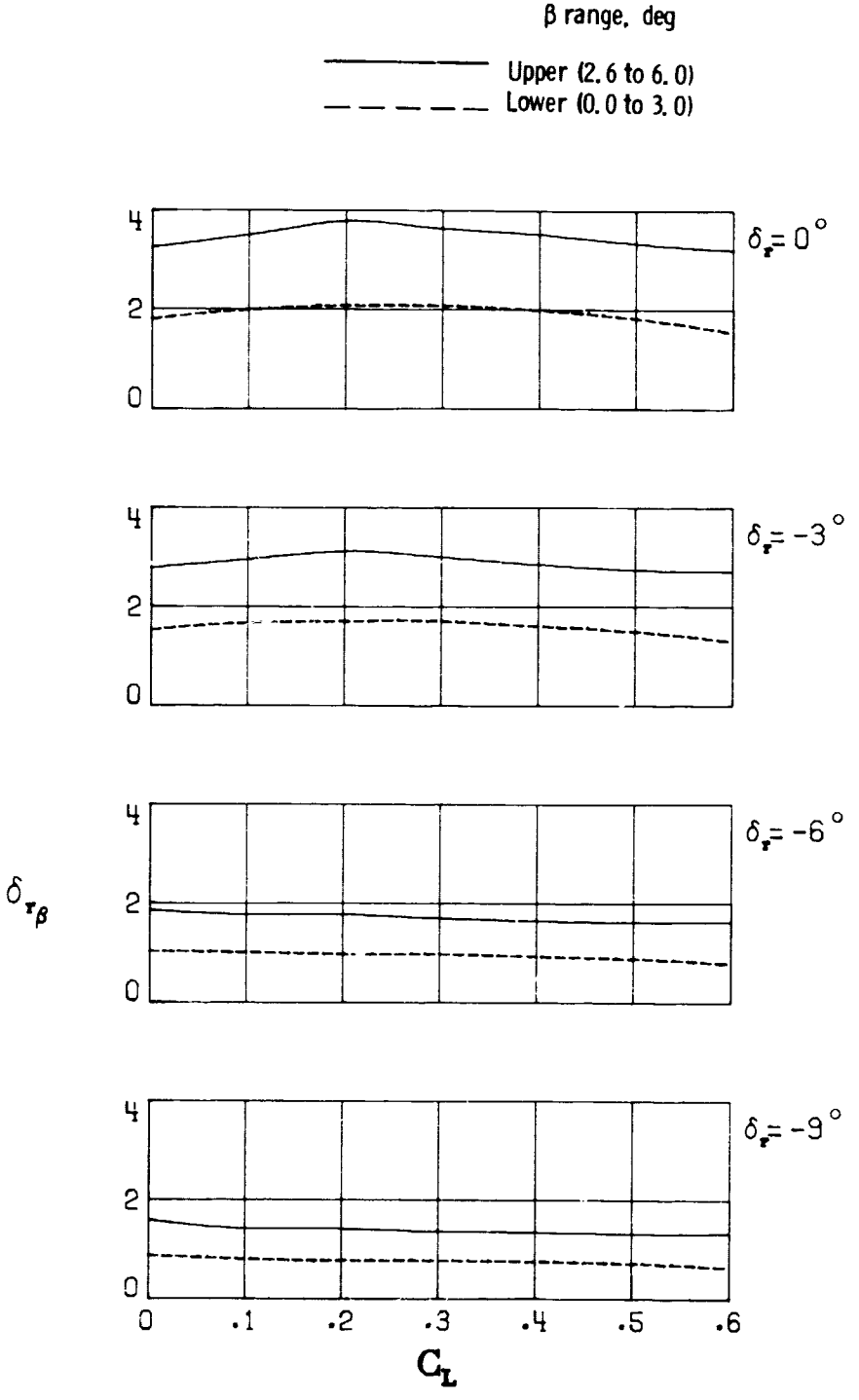

(e) M = 0.900.

Figure 39.- Concluded. (U)

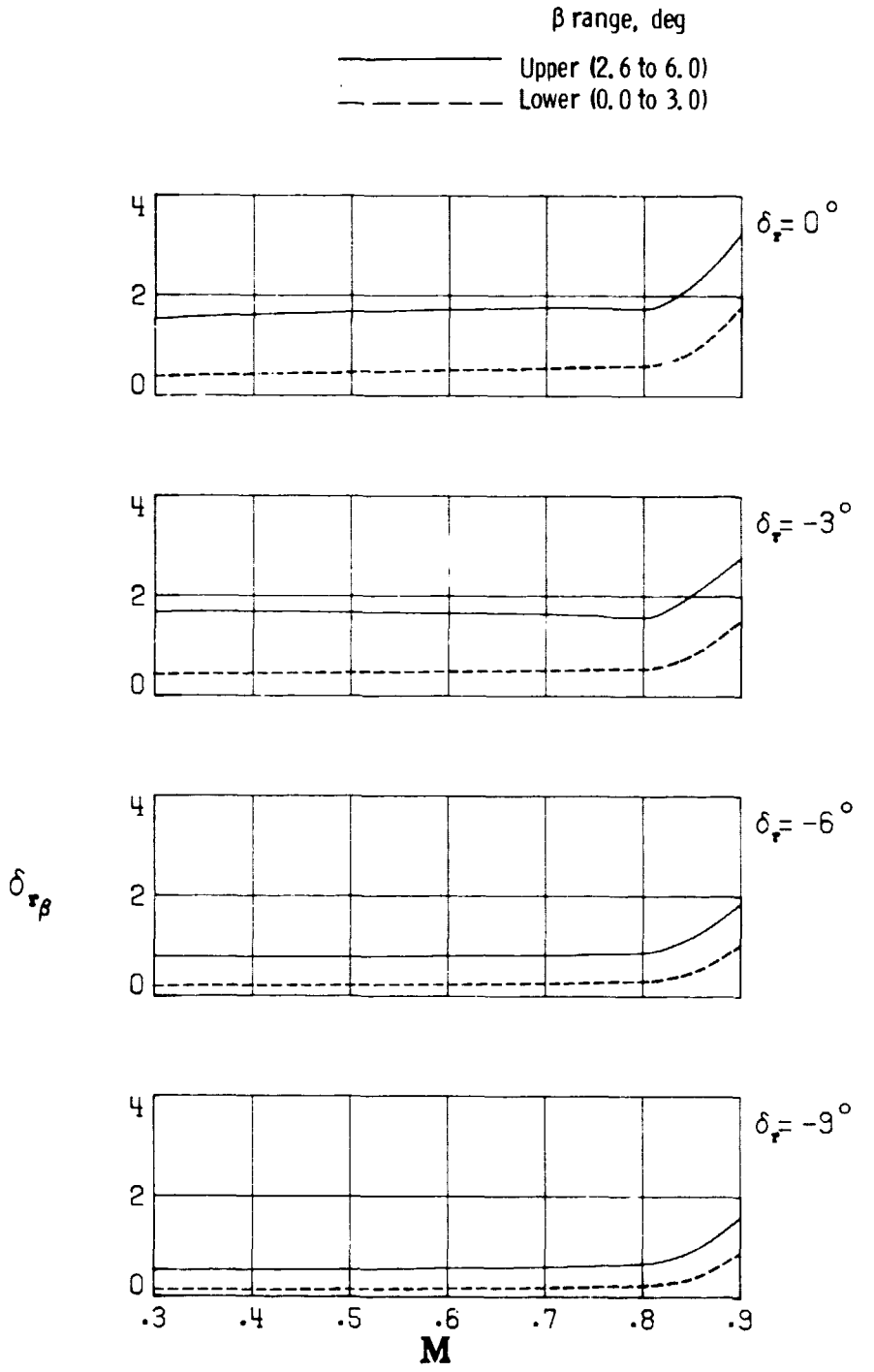

(a) $C_L = 0.0$.

Figure 40.- Variation of rudder-control index with Mach number for four rudder deflection angles. Model configuration C. (U)

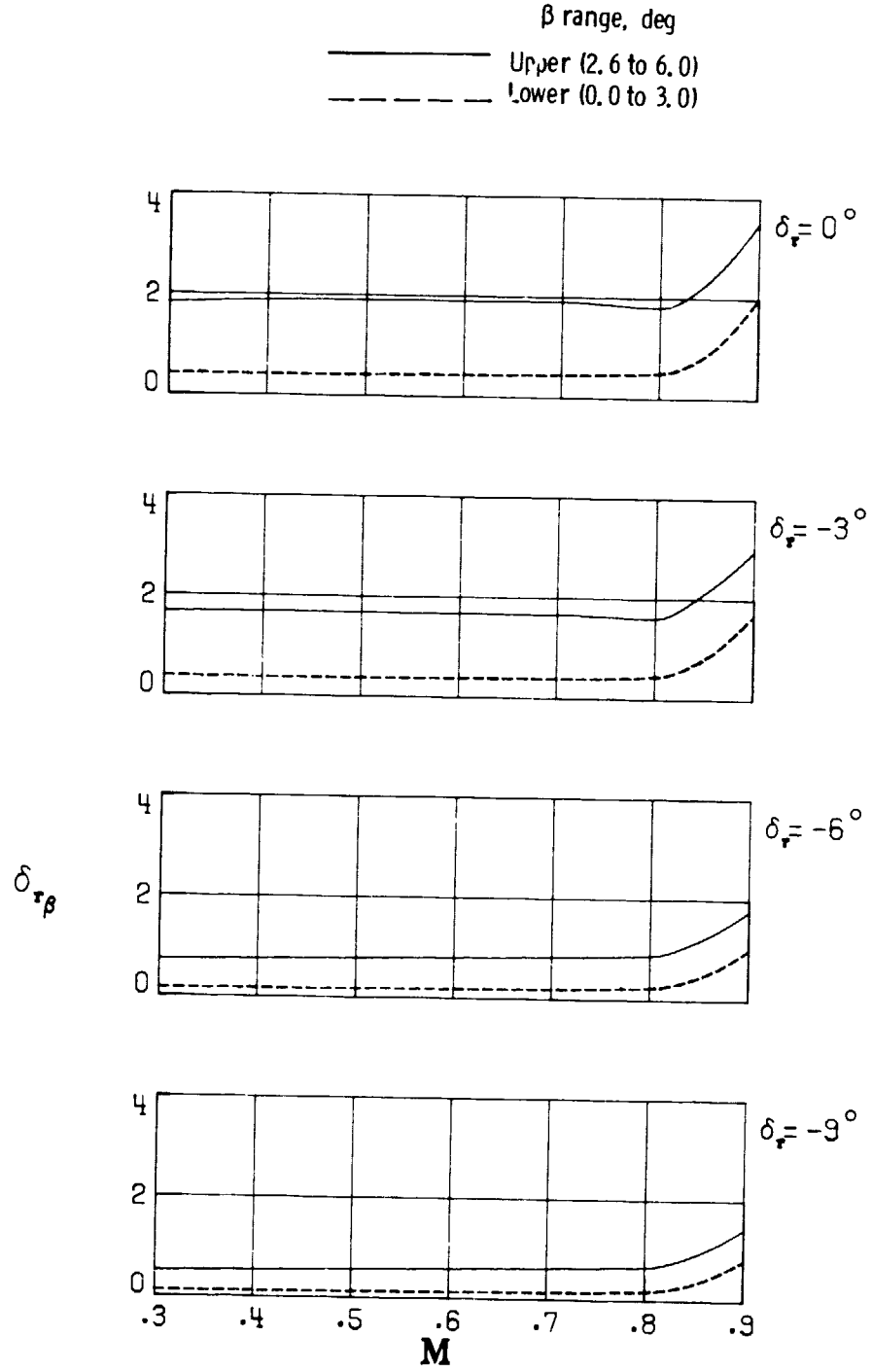

(b) C_L = 0.1.

Figure 40.- Continued. (U)

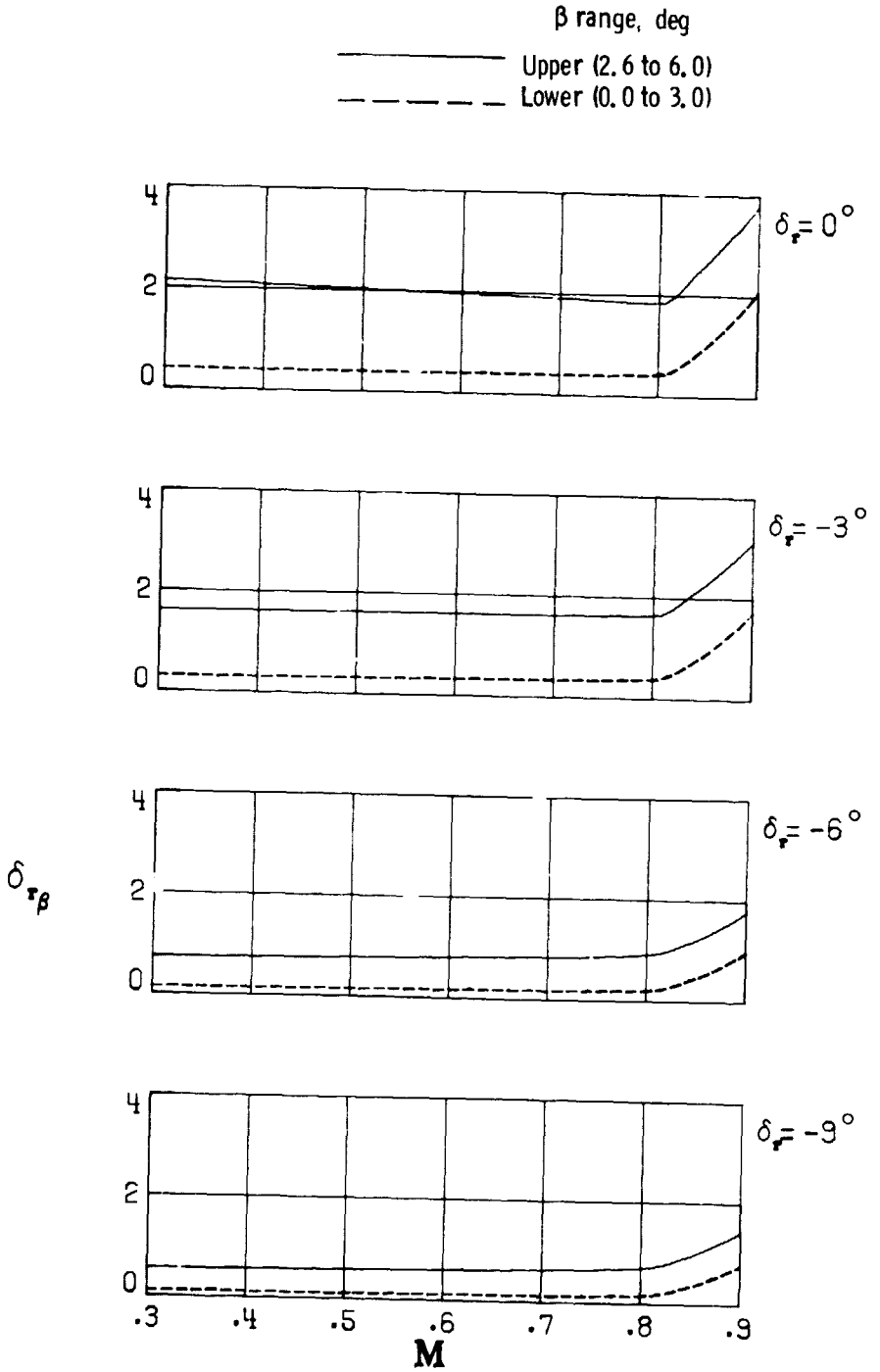

(c) $C_L = 0.2$.

Figure 40.- Continued. (U)

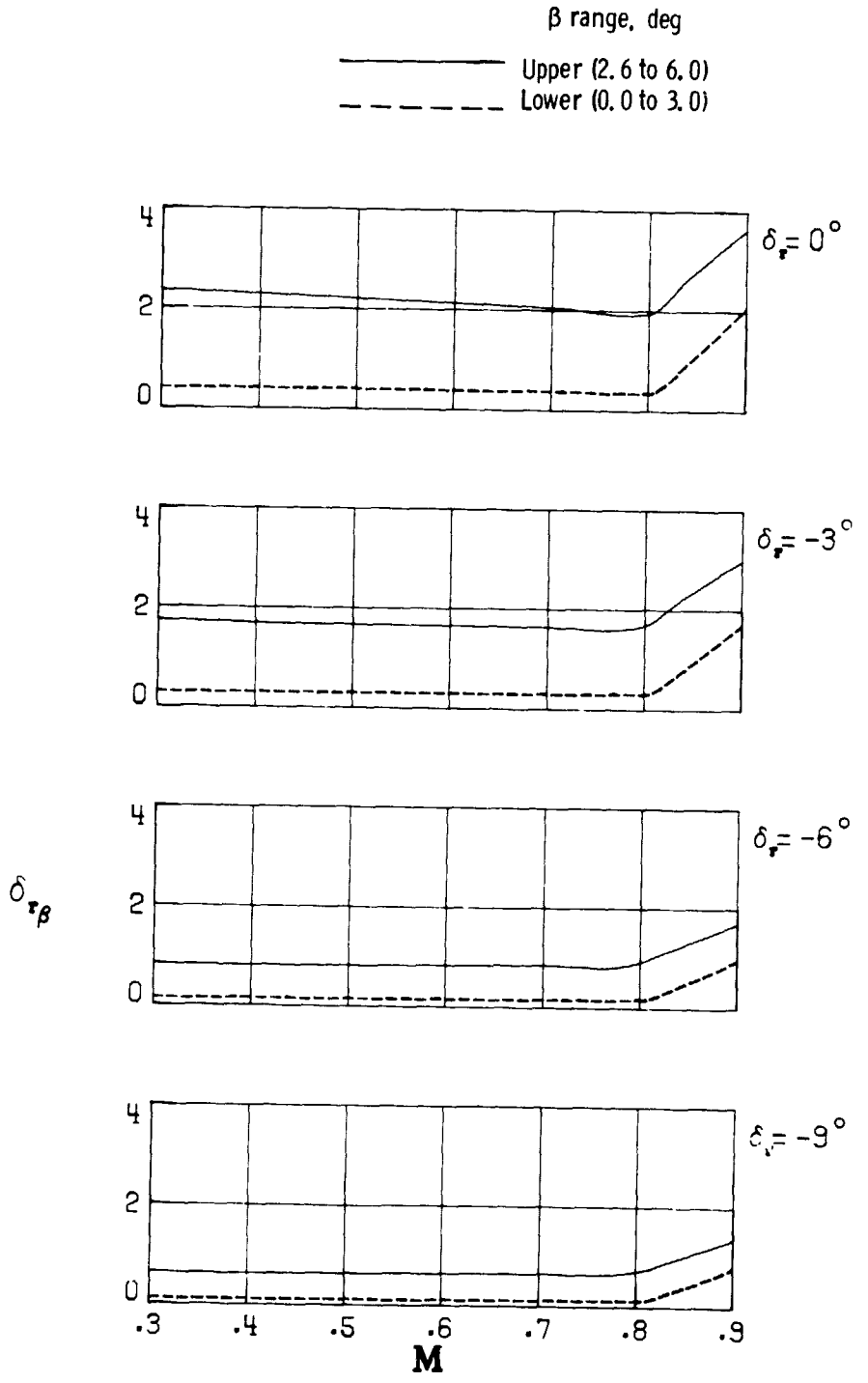

(d) C_L = 0.3.

Figure 40.- Continued. (U)

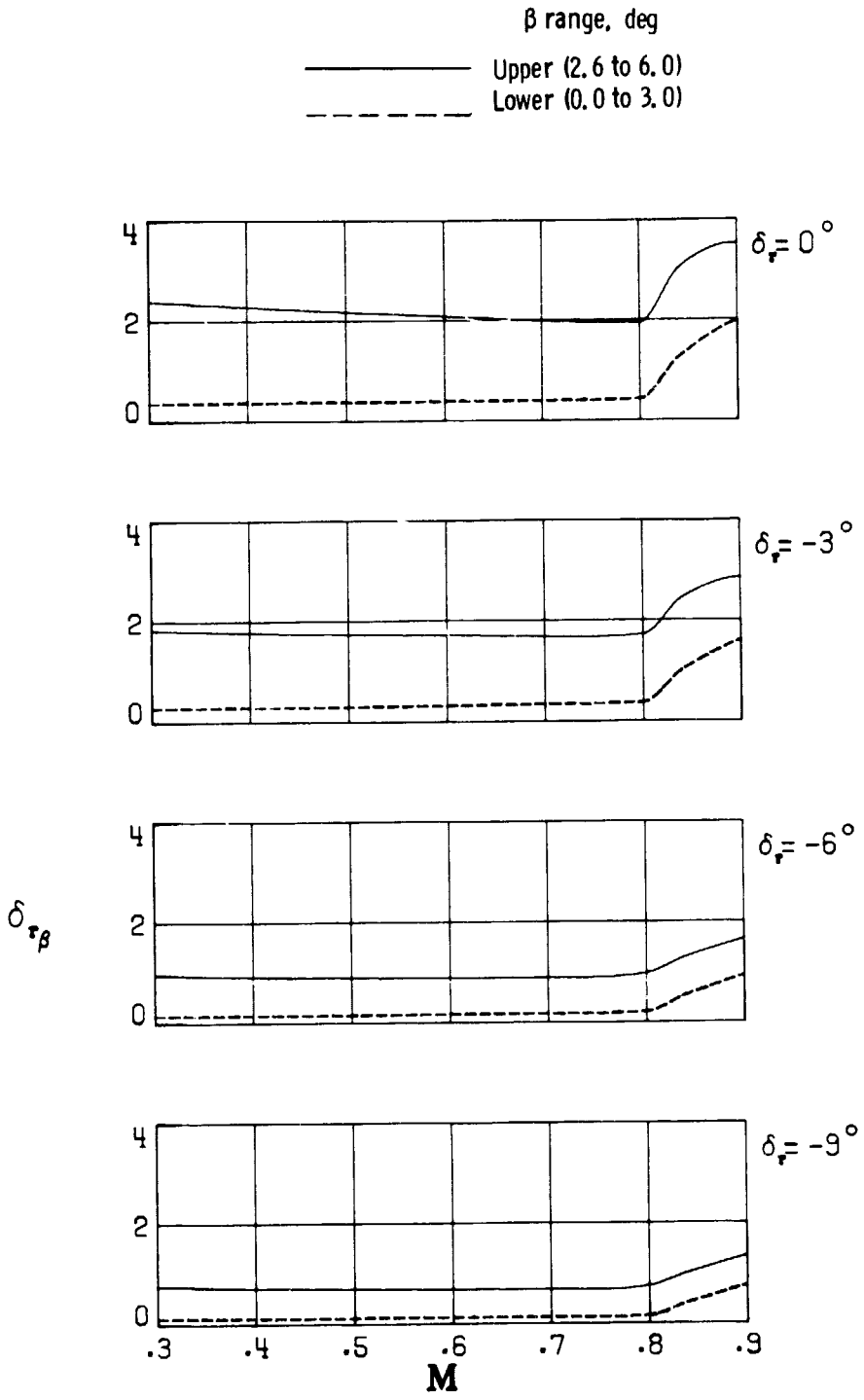

(e) $C_L = 0.4$.

(C) Figure 40.- Continued. (U)

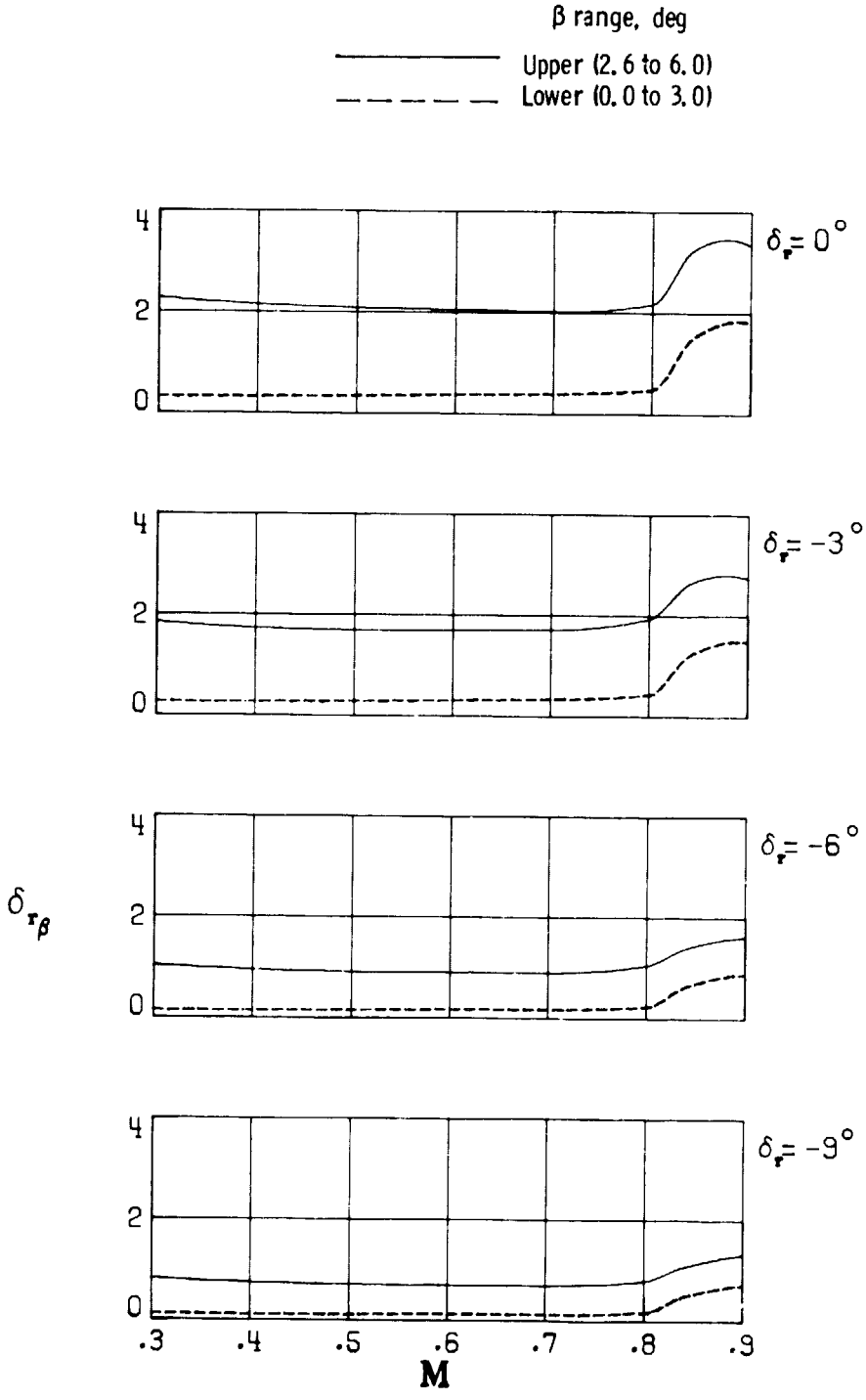

(f) C_L = 0.5.

Figure 40.- Continued. (U)

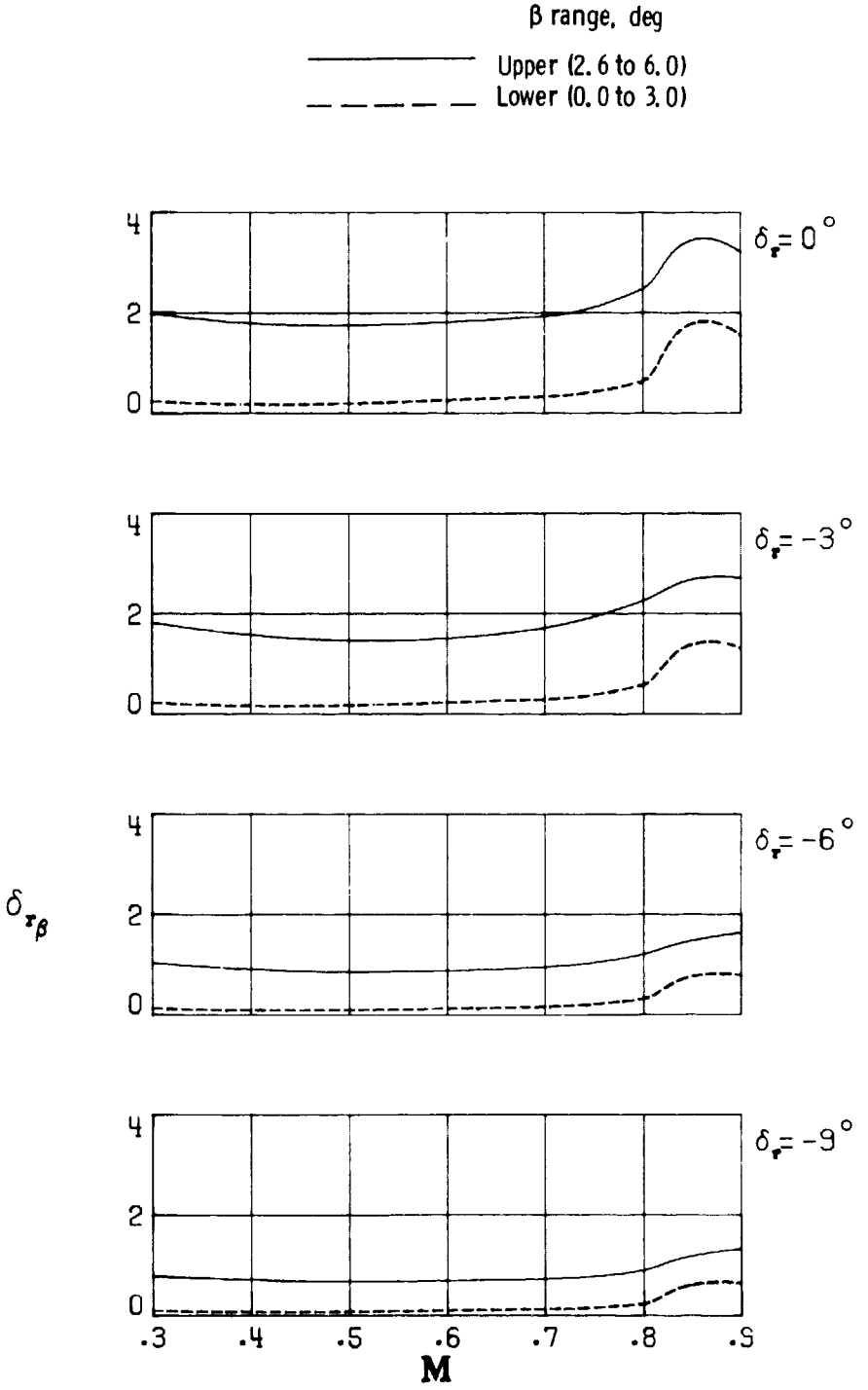

(g) $C_L = 0.6$.

Figure 40.- Concluded. (U)